

CAPTURE CROSS SECTIONS FOR THE ASTROPHYSICAL P PROCESS

By

Stephen J. Quinn

A DISSERTATION

Submitted to
Michigan State University
in partial fulfillment of the requirements
for the degree of

Physics - Doctor of Philosophy

2015

ABSTRACT

CAPTURE CROSS SECTIONS FOR THE ASTROPHYSICAL P PROCESS

By

Stephen J. Quinn

This dissertation includes the design and development of the Summing NaI (SuN) 4π γ -ray detector at the National Superconducting Cyclotron Laboratory to measure proton and α radiative capture reactions relevant in the astrophysical p process. Discussions of p-process nucleosynthesis, the relevant nuclear reaction theory, experimental details, and analysis procedures are included. All reaction measurements were performed at the Nuclear Science Laboratory of the University of Notre Dame. The commissioning experiments in both regular and inverse kinematics were done using known resonances in the $^{27}\text{Al}(p,\gamma)^{28}\text{Si}$ and $^{58}\text{Ni}(p,\gamma)^{59}\text{Cu}$ reactions, and the results agree well with previous literature values. The success of these proof-of-principle measurements marks the first time that the γ -summing technique has been implemented in inverse kinematics. Furthermore, in an effort to investigate the synthesis of the light p-process nuclei, the $^{74}\text{Ge}(p,\gamma)^{75}\text{As}$, $^{74}\text{Ge}(\alpha,\gamma)^{78}\text{Se}$, and $^{90,92}\text{Zr}(\alpha,\gamma)^{94,96}\text{Mo}$ reactions were measured and compared to theoretical calculations using the nuclear statistical model. It was found that the new $^{74}\text{Ge}(p,\gamma)^{75}\text{As}$ measurements cause an enhancement in the overproduction of ^{74}Se in p-process models, and that the updated $^{90}\text{Zr}(\alpha,\gamma)^{94}\text{Mo}$ reaction rate seems to confirm the p-process branching point at ^{94}Mo . Finally, the $^{58}\text{Ni}(\alpha,\gamma)^{62}\text{Zn}$ reaction was measured for its role in nucleosynthesis in type Ia supernovae. The measurements here lower the reaction rate used in astrophysical models, which leads to a 5% reduction in the calculated abundances of several isotopes. All of the measurements in this dissertation greatly reduce the uncertainty in the reaction cross section.

When the Yankees beat the Red Sox all is right in the world.

ACKNOWLEDGMENTS

This is my favorite section of all because it gives me an opportunity to thank everyone who contributed to this thesis. First of all, special thanks must go to my advisor, Artemis Spyrou, for her guidance, kindness, and support during my time in graduate school. I absolutely could not have worked with a better professor, a more brilliant scientist, or on a more interesting project, and I am extremely grateful for the many opportunities that she has given me that are far too numerous to list here. Thank you, Artemis! It has been a pleasure working alongside all of the SuN group members, including Jorge, Farheen, Alex, Debra, Alicia, and the many brilliant undergraduate students. In particular, I would like to single out Anna Simon for her countless contributions to this thesis. She has been an incredible source of information when I had little experience, as well as serving as a wonderful mentor and friend. Overall, it has been a pleasure to take part in the creation of the SuN group and it is wonderful to see the SuN detector shine as brightly as it is today.

The experiments comprising this thesis would not have been possible without the hard work of many scientists and they all deserve recognition. It is a large fear of mine that I will forget someone! At the NSCL, thanks to John Yurkon for his vast knowledge and patience in teaching me the art of target making, and thanks to Renan Fontus for designing the beam pipe for the SuN detector. I would also like to thank Sean Liddick, Jeromy, Chris, Nicki, and Scott for their time and assistance with DDAS; they are true superstars. At Notre Dame, thanks to the many graduate students who helped operate the accelerator, the technicians who assisted in the setup, and everyone who makes Notre Dame such a welcoming place for external experimenters. A special thanks is in order for Manöel Couder, Dan Robertson, Ed Stech, Wanpeng Tan, and Antonios Kontos for going above and beyond the call of duty, and

whose help was critical for a successful experimental campaign. At Hope College, I express my gratitude to Paul DeYoung, Graham Peaslee, and Dave Daugherty for their time and expertise with target thickness measurements. Additionally, I would like to thank Thomas Rauscher and Eduardo Bravo for their collaboration and contribution to this work.

I greatly appreciate the assistance of Professors Ed Brown, Jim Linnemann, Filomena Nunes, and Michael Thoennessen through their knowledge, questions, and, most of all, generosity in agreeing to give up their valuable time to serve on my guidance committee. I also would like to acknowledge the National Science Foundation, the Joint Institute for Nuclear Astrophysics, and the Michigan State University Graduate School for financial support.

Truthfully, my time in graduate school has been wonderful and I am very fortunate to have many friends that have made it so enjoyable. I will miss my officemates, roommates, teammates, and everyone from the daily lunches, Happy Hours, tailgates, and parties that have kept me laughing since I arrived at MSU. A “merci beaucoup” to Yari and Bazzy for their support and motivation during the more difficult first few years of trying to balance classes, exams, teaching, and research. Finally, and most importantly, I would like to thank my family. I have been incredibly blessed with unquestionably the greatest family of all time, and I would like to thank them for putting up with me. Thanks Mom and Dad for being such awesome role models, and thanks Lassu and Mollister for being my two favorite people in the world. As Yogi Berra would say, “I just want to thank everyone for making this day necessary.”

TABLE OF CONTENTS

LIST OF TABLES	ix
LIST OF FIGURES	xi
Chapter 1 Introduction	1
1.1 Elements	2
1.2 Abundances	4
1.3 Nucleosynthesis	6
1.3.1 Big Bang Nucleosynthesis	7
1.3.2 Quiescent Stellar Burning	7
1.3.3 Supernovae	8
1.3.4 Nuclear Statistical Equilibrium	10
1.3.5 Nucleosynthesis of the Heavy Elements	11
1.4 Production of the p Nuclei	14
1.4.1 ν p process	14
1.4.2 rp process	15
1.4.3 p process	15
1.4.4 Uncertainties	21
1.5 Looking Ahead	25
Chapter 2 Nuclear and Astrophysical Quantities	27
2.1 Cross Section	27
2.2 Stellar Reaction Rate	29
2.3 Astrophysical S factor	31
2.4 Gamow Window	33
2.5 Q value	35
Chapter 3 Theoretical Considerations	37
3.1 Resonant Reactions	37
3.1.1 In Stars	38
3.1.2 In the Laboratory	39
3.2 Nuclear Statistical Model	44
3.3 Reciprocity Theorem	49
Chapter 4 Experimental Techniques	53
4.1 Measuring the Cross Section	53
4.1.1 Activation	54

4.1.2	γ -Induced Reactions	55
4.1.3	In-Beam Methods	55
4.1.3.1	Angular Distributions Method	57
4.1.3.2	γ -Summing Technique	58
4.1.4	Techniques in Inverse Kinematics	60
4.2	Target Production and Characterization	62
4.2.1	Evaporation	62
4.2.2	Thickness Measurements	65
4.2.2.1	Experimental Details	67
4.2.2.2	Calibrations	69
4.2.2.3	RBS Analysis	70
4.2.2.4	ERD Analysis	72
4.3	Experimental Setup	76
4.3.1	Beam Production	77
4.3.2	Acceleration	79
4.3.3	Ion Selection	80
4.3.4	Experimental Endstation	82
Chapter 5 The SuN Detector		84
5.1	Design	84
5.2	Detection	86
5.3	Data Acquisition	89
5.3.1	PMT signals	90
5.3.2	NSCL DDAS	91
5.3.3	External Triggering	96
5.4	Radiation Source Testing	98
5.5	GEANT4 Simulation	101
Chapter 6 Analysis		107
6.1	Gain Matching and Calibration	107
6.2	Thresholds	114
6.3	Sum Peak Analysis	117
6.3.1	Isomeric states	119
6.3.2	Doppler reconstruction	121
6.4	γ -Summing Efficiency	123
Chapter 7 $^{27}\text{Al}(p,\gamma)^{28}\text{Si}$		128
Chapter 8 $^{74}\text{Ge}(p,\gamma)^{75}\text{As}$		135
Chapter 9 $^{58}\text{Ni}(\alpha,\gamma)^{62}\text{Zn}$		147

Chapter 10 Additional (α,γ) Measurements	158
10.1 $^{90}\text{Zr}(\alpha,\gamma)^{94}\text{Mo}$ Results	161
10.2 $^{92}\text{Zr}(\alpha,\gamma)^{96}\text{Mo}$ Results	163
10.3 $^{74}\text{Ge}(\alpha,\gamma)^{78}\text{Se}$ Results	165
10.4 Discussion	166
10.4.1 $^{90}\text{Zr}(\alpha,\gamma)^{94}\text{Mo}$	168
10.4.2 $^{92}\text{Zr}(\alpha,\gamma)^{96}\text{Mo}$	170
10.4.3 $^{74}\text{Ge}(\alpha,\gamma)^{78}\text{Se}$	172
10.5 Conclusions	173
Chapter 11 Measurements in Inverse Kinematics	175
Chapter 12 Summary and Outlook	182
Appendices	187
Appendix A Energy Filter Algorithm	188
Appendix B GEANT4 Detector Construction	191
Appendix C Creating SuN's ROOT files	198
References	202

LIST OF TABLES

Table 4.1	Beam energies and energy calibrations used at HIBAL	69
Table 4.2	Target thicknesses	73
Table 5.1	SuN's energy resolution to various experimental γ -ray peaks	103
Table 6.1	List of γ -ray transitions used to calibrate SuN	113
Table 6.2	Gain matching multiplication factors for each of SuN's PMTs	114
Table 6.3	Energy calibrations for each of SuN's segments	115
Table 6.4	Average emission angles for Doppler reconstruction	122
Table 6.5	Doppler correction factors for each segment	122
Table 7.1	Resonance strength results for the $^{27}\text{Al}(p,\gamma)^{28}\text{Si}$ reaction	133
Table 8.1	Experimental results for the $^{74}\text{Ge}(p,\gamma)^{75}\text{As}$ reaction	139
Table 8.2	New reaction rates for the $^{74}\text{Ge}(p,\gamma)^{75}\text{As}$ reaction	143
Table 9.1	Cross sections for the $^{58}\text{Ni}(\alpha,\gamma)^{62}\text{Zn}$ reaction	150
Table 9.2	Stellar reactivities for the $^{58}\text{Ni}(\alpha,\gamma)^{62}\text{Zn}$ reaction	155
Table 9.3	REACLIB parameters for the $^{58}\text{Ni}(\alpha,\gamma)^{62}\text{Zn}$ reaction	155
Table 9.4	Impact of the $^{58}\text{Ni}(\alpha,\gamma)^{62}\text{Zn}$ reaction on nucleosynthesis in SNIa	156
Table 10.1	Experimental results for the $^{90}\text{Zr}(\alpha,\gamma)^{94}\text{Mo}$ reaction	162
Table 10.2	Experimental results for the $^{92}\text{Zr}(\alpha,\gamma)^{96}\text{Mo}$ reaction	163

Table 10.3	Experimental results for the $^{74}\text{Ge}(\alpha,\gamma)^{78}\text{Se}$ reaction	166
Table 10.4	New reaction rates for the $^{90}\text{Zr}(\alpha,\gamma)^{94}\text{Mo}$ reaction	170
Table 11.1	Resonance strengths from measurements in inverse kinematics	179

LIST OF FIGURES

Figure 1.1	Chart of nuclides	3
Figure 1.2	Solar abundances	6
Figure 1.3	Stellar burning layers inside a massive star	9
Figure 1.4	s and r neutron capture processes	13
Figure 1.5	Temperature and density profile of O/Ne layers in SNII	16
Figure 1.6	Simplified p-process reaction flow	17
Figure 1.7	Normalized overproduction factors for the p nuclei	20
Figure 1.8	Seed abundances for the p process	22
Figure 1.9	Effect of stellar temperature on the production of the p nuclei	23
Figure 1.10	Effect of stellar mass on the production of the p nuclei	23
Figure 1.11	Effect of reaction rates on the production of the p nuclei	24
Figure 2.1	Front view of uniformly placed circular targets	27
Figure 2.2	Cartoon of particles impinging onto a target	30
Figure 2.3	The Gamow peak	34
Figure 2.4	Binding energies per nucleon	35
Figure 3.1	A Breit-Wigner resonance	42
Figure 3.2	General level scheme for a forward and reverse reaction	51
Figure 4.1	General level scheme of a radiative capture reaction	56

Figure 4.2	γ -summing effect of a calorimeter	59
Figure 4.3	The RBS technique	66
Figure 4.4	General layout of the HIBAL scattering chamber	68
Figure 4.5	SIMNRA fit to a gold-on-glass measurement	70
Figure 4.6	SIMNRA fits to RBS spectra of nine different targets	71
Figure 4.7	SIMNRA fit to the RBS spectrum of the ^{74}Ge target	72
Figure 4.8	SIMNRA calculations of the titanium hydride foil	74
Figure 4.9	Wrinkles in the titanium hydride foil	75
Figure 4.10	Final SIMNRA calculations of the titanium hydride foil	76
Figure 4.11	The Nuclear Science Laboratory at Notre Dame	77
Figure 4.12	The experimental endstation	82
Figure 5.1	The SuN detector	85
Figure 5.2	Typical signal from one of SuN's PMTs	89
Figure 5.3	Diagram of SuN's data acquisition system	90
Figure 5.4	Digital trapezoidal filter for a step function	93
Figure 5.5	Response of DDAS to SuN's signals	95
Figure 5.6	Simplified decay scheme for ^{137}Cs and ^{60}Co	98
Figure 5.7	^{137}Cs source spectrum	99
Figure 5.8	^{60}Co source spectrum	100
Figure 5.9	Position dependence of SuN's γ -summing efficiency	101
Figure 5.10	Visualization of SuN's GEANT4 simulation	102
Figure 5.11	Energy resolution of SuN vs. γ -ray energy	104

Figure 5.12	Simulated γ -summing efficiencies for various detectors	106
Figure 5.13	SuN's detection efficiency for a single γ ray	106
Figure 6.1	PMT spectra for room background and a ^{137}Cs source	108
Figure 6.2	2D plot of left PMT vs. right PMT for a ^{60}Co source	109
Figure 6.3	Effect of different gain matchings	111
Figure 6.4	Gain matching SuN's segments using a ^{60}Co source	112
Figure 6.5	SuN's threshold	116
Figure 6.6	Sum peak analysis	118
Figure 6.7	Average emission angles for Doppler reconstruction	123
Figure 6.8	Simulated hit pattern for a 10 MeV sum peak	125
Figure 6.9	Hit pattern method to determine γ -summing efficiency	126
Figure 6.10	Systematic trends of hit pattern and efficiency	127
Figure 7.1	Total γ -summed spectrum for the $^{27}\text{Al}(p,\gamma)^{28}\text{Si}$ reaction	129
Figure 7.2	Sample level scheme of ^{28}Si	130
Figure 7.3	Segment spectrum for the $^{27}\text{Al}(p,\gamma)^{28}\text{Si}$ reaction	131
Figure 7.4	Excitation function for the $^{27}\text{Al}(p,\gamma)^{28}\text{Si}$ reaction	132
Figure 7.5	Resonance strength results for the $^{27}\text{Al}(p,\gamma)^{28}\text{Si}$ reaction	133
Figure 8.1	Nuclear chart for the $^{74}\text{Ge}(p,\gamma)^{75}\text{As}$ reaction	136
Figure 8.2	Sum peaks for the $^{74}\text{Ge}(p,\gamma)^{75}\text{As}$ reaction	137
Figure 8.3	Linear background with and without including the isomeric state	138
Figure 8.4	Cross section results for the $^{74}\text{Ge}(p,\gamma)^{75}\text{As}$ reaction	140

Figure 8.5	New reaction rates for the $^{74}\text{Ge}(p,\gamma)^{75}\text{As}$ reaction	143
Figure 8.6	Effect of the $^{74}\text{Ge}(p,\gamma)^{75}\text{As}$ reaction on ^{74}Se production in SNII . .	145
Figure 9.1	Nuclear chart for the $^{58}\text{Ni}(\alpha,\gamma)^{62}\text{Zn}$ reaction	148
Figure 9.2	SuN's spectra for the $^{58}\text{Ni}(\alpha,\gamma)^{62}\text{Zn}$ reaction	149
Figure 9.3	Cross section results for the $^{58}\text{Ni}(\alpha,\gamma)^{62}\text{Zn}$ reaction	152
Figure 9.4	Sensitivity plot for the $^{58}\text{Ni}(\alpha,\gamma)^{62}\text{Zn}$ reaction	153
Figure 10.1	Reaction rates for the photodissociation of ^{94}Mo	160
Figure 10.2	Sum peak for the $^{90}\text{Zr}(\alpha,\gamma)^{94}\text{Mo}$ reaction	162
Figure 10.3	Sum peak for the $^{92}\text{Zr}(\alpha,\gamma)^{96}\text{Mo}$ reaction	164
Figure 10.4	Sum peak for the $^{74}\text{Ge}(\alpha,\gamma)^{78}\text{Se}$ reaction	165
Figure 10.5	Cross section results for the $^{90}\text{Zr}(\alpha,\gamma)^{94}\text{Mo}$ reaction	169
Figure 10.6	Cross section results for the $^{92}\text{Zr}(\alpha,\gamma)^{96}\text{Mo}$ reaction	171
Figure 10.7	Cross section results for the $^{74}\text{Ge}(\alpha,\gamma)^{78}\text{Se}$ reaction	173
Figure 11.1	SuN's spectra for the $p(^{27}\text{Al},\gamma)^{28}\text{Si}$ reaction	177
Figure 11.2	Yield curve for the $p(^{27}\text{Al},\gamma)^{28}\text{Si}$ reaction	178
Figure 11.3	SuN's spectra for the $p(^{58}\text{Ni},\gamma)^{59}\text{Cu}$ reaction	180
Figure 11.4	Yield curve for the $p(^{58}\text{Ni},\gamma)^{59}\text{Cu}$ reaction	180
Figure A.1	A digitized signal and its baseline	189
Figure A.2	Response of the tau-corrected energy filter	190

Chapter 1

Introduction

It is fascinating to think that the chemical elements that make up our bodies and the world around us have extraterrestrial origins. The lightest elements, hydrogen and helium (along with trace amounts of lithium), can be traced as far back as a few seconds to a few minutes after the Big Bang approximately 13.8 billion years ago, when the universe first cooled. If it were not for the creation of stars around 100 million years after the Big Bang, there would be no heavier elements. Instead, stars act as enormous nuclear reactors that combine the hydrogen and helium building blocks into all of the elements that exist today. Not only do stars generate the elements, but they may also spew them out into the neighboring universe during their lifetimes. The ejected material can then be used in the formation of the next generation of stars. It is through this cycle of stellar birth and death that the elements of the universe are continually produced and mixed together and, ultimately, have contributed to the existence of life as we know it today.

The motivation of this thesis work is one of origin, specifically improving the understanding of the origin of the elements. This is a fundamental question, but one that is complex in nature and involves the interplay of several diverse research fields. The present dissertation represents a small contribution to the ongoing effort at a complete description of the synthesis of the elements.

1.1 Elements

In total, there are less than 100 naturally occurring chemical elements. Each element is comprised of small units known as atoms, and atoms are in turn comprised of a dense nuclear core of positive protons and chargeless neutrons surrounded by a negative cloud of electrons. An element is defined by the number of protons in its nucleus, and there are different versions, called isotopes, that differ in the number of neutrons. Approximately 3000 isotopes have been discovered and it is thought that there may be over 7000 total possible combinations of protons and neutrons that could make up a nucleus [1]. Remarkably, out of these 7000 possible nuclei, less than 300 are known to be stable. The other nuclei, if given enough time, eventually decay into a stable nucleus. Thus, the complex world that we live in is made up of less than 300 nuclear building blocks along with their electrons. Nuclei can be conveniently displayed in a chart as in Fig. 1.1, with each nucleus plotted according to its unique number of protons and neutrons. The stable nuclei are commonly referred to as the valley of stability. The notation for labeling each isotope is ${}^A_Z\text{X}_N$, where X is the chemical symbol of the element, Z is the number of protons, N is the number of neutrons, and $A=Z+N$ is the atomic mass number. Each isotope can be uniquely identified in the form ${}^A\text{X}$, for example the carbon isotope with six protons and six neutrons is labeled ${}^{12}\text{C}$. The nuclei of ${}^1\text{H}$ and ${}^4\text{He}$ often receive special nicknames with ${}^1\text{H}$ being labeled p because it consists of only one proton, and ${}^4\text{He}$ being labeled an α -particle for historical classification reasons.

Experimental observations indicate that isotopes with certain “magic numbers” of protons and neutrons exist in an especially stable configuration compared to their neighboring isotopes [2]. For example, magic nuclei are more tightly bound and therefore require larger

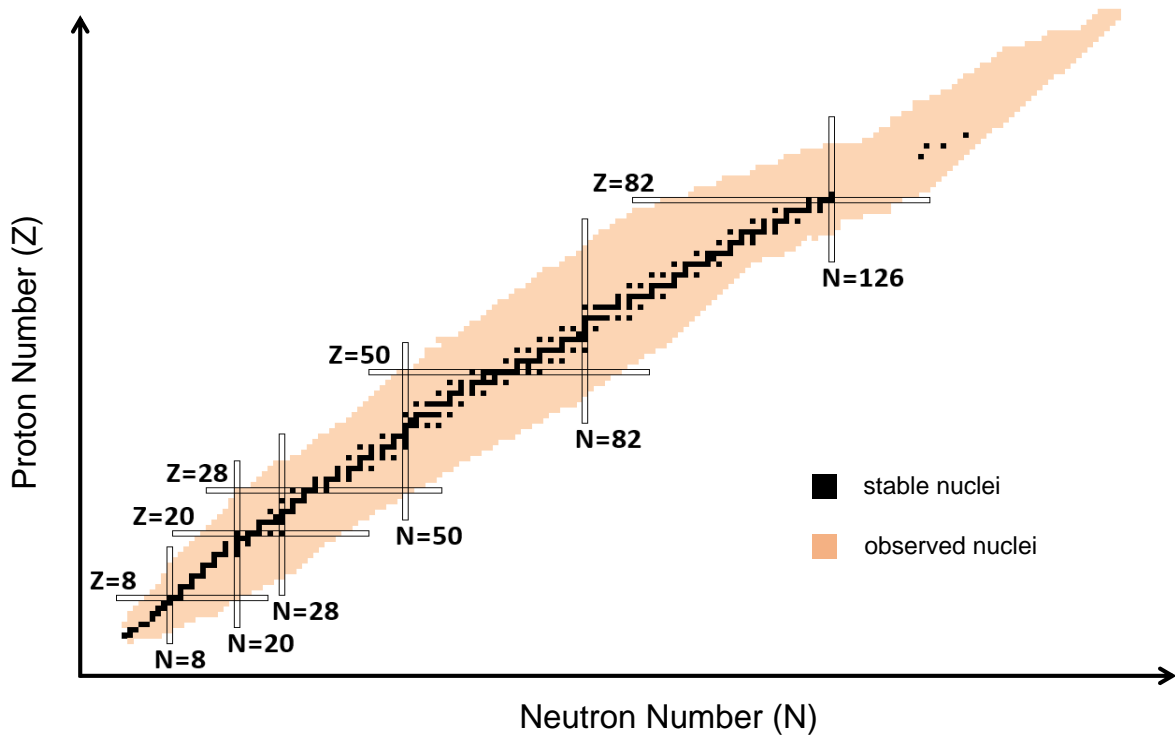


Figure 1.1: (For interpretation of the references to color in this and all other figures, the reader is referred to the electronic version of this thesis.) Nuclear chart with proton number along the y-axis and neutron number along the x-axis. Stable nuclei are indicated with black boxes and the observed radioactive isotopes are indicated with shaded boxes. There are also thousands of nuclei beyond what is plotted here that are expected to exist and are yet to be discovered. The lines on the chart indicate nuclear magic numbers.

amounts of energy to excite or completely remove a proton or neutron from the nucleus. The experimentally observed magic numbers at 8, 20, 28, 50, 82, and 126 were successfully predicted by the nuclear shell model in 1949 [3, 4]. In the same way that electrons fill atomic shells with closed shells correspond to the noble gases, in the nuclear shell model protons and neutrons fill nuclear shells with magic numbers appearing at the closed shells. The location of the magic numbers on the nuclear chart is indicated in Fig. 1.1.

1.2 Abundances

In order to understand the synthesis of the elements, it is necessary to know what elements exist in the universe and their relative quantity compared to each other. Any potential description of the production of the elements must match the observed abundance pattern, and any feature present in the abundance pattern is a clue to the stellar processes that are taking place.

The most complete and accurate elemental abundances are from our solar system and are known as the solar abundances. The solar abundances are similar to other sites in the universe, but many differences exist due to different evolutionary histories. The solar abundances serve as the standard to which all abundance patterns are compared. Since the solar system formed from the collapse of a gaseous nebula of approximately uniform composition, all objects are expected to have approximately the same elemental abundance pattern. However, planets like the Earth have undergone many chemical separation processes since their formation [5] and solar abundances are instead derived from two main sources; observations of the Sun by astronomers and analysis of meteorites by cosmochemists.

Astronomers deduce abundances from stars by identifying and analyzing the electromagnetic waves emitted at unique frequencies by the elements near the stellar surface. From these spectral lines, models of the stellar atmosphere and interior are used to calculate abundances [6]. For the Sun these observations are primarily taken from the photosphere because this is the deepest layer of the Sun that can be observed directly, but additional information on a few elements can be deduced from events like solar winds, solar flares, solar energetic particles, and through helioseismology (see Ref. [7] and references therein). On the other hand, cosmochemists measure elemental abundances directly by chemical analysis

of meteorites. Many of the meteorites that have been recovered on the Earth have undergone significant changes since their formation 4.5 billion years ago, but there have been 5 meteorites discovered, known as CI carbonaceous chondrites, which are expected to have maintained the majority of their initial chemical composition [8].

Having two separate and complementary sources of solar abundances is important because more information is available than just using one source alone. For example, meteorites are expected to be lacking some of their initial composition of elements like hydrogen, oxygen, and the noble gases as they form gases which escape from the meteorite, and the Sun is expected to be lacking in elements like lithium which get processed by the Sun. For the elements which can be compared in both meteorites and the Sun, their abundances typically agree remarkably well to within 10%. The comparison is done by normalizing the abundances from both meteorites and the Sun to 10^6 silicon atoms. Additionally, solar isotopic abundances are usually derived from the elemental abundances by using the isotopic ratios found on the Earth, for example using data from Ref. [9]. However, there have been small variations in isotopic composition observed between the Earth and other parts of the solar system due to mass fractionation, and care must be taken when assigning solar isotopic abundances [10].

There are several compilations of solar abundances from the first detailed work [11] to more recent works [10, 7] (along with subsequent updates), and a plot based on the data from Lodders [7] is displayed in Fig. 1.2. The lightest elements, hydrogen and helium, are by far the most abundant elements in the solar system, while the next lightest elements, lithium, beryllium, and boron, have relatively low abundances. The elements from carbon to scandium have a general trend of decreasing abundance with increasing mass, and then there is a spike in the abundances around iron which is known as the iron peak. The elements

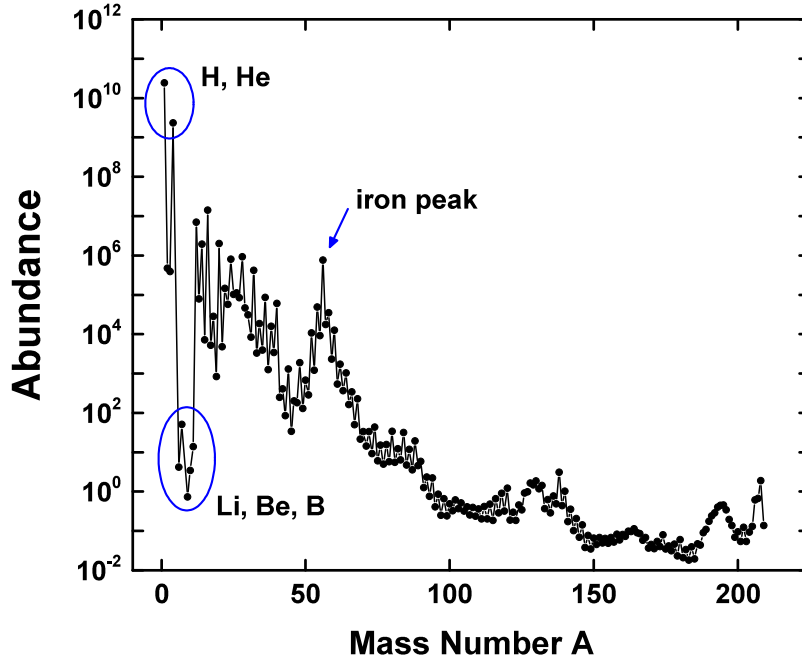


Figure 1.2: Abundances of the nuclides in the solar system based on the data from Lodders [7]. The abundances are normalized to 10^6 silicon atoms.

beyond the iron peak have very low abundances and show maxima in the ranges of mass 110-150 and 180-210.

1.3 Nucleosynthesis

The creation of the chemical elements in the universe is called nucleosynthesis. The modern view of nucleosynthesis began with two seminal papers by Burbidge, Burbidge, Fowler, and Hoyle (B2FH) [12] and Cameron [13] in 1957, which were based on existing ideas and the available abundance patterns of the time. In the nearly 60 years since, the interplay of the diverse research fields of astronomy, cosmochemistry, theoretical astrophysics, and nuclear physics have advanced our understanding of the origin of the elements. There are many astrophysical processes, thousands of nuclear reactions, and countless details that will be

glossed over in this section in favor of generality. In the following Section 1.4, more details will be given on the specific nucleosynthesis process that is most directly related to this dissertation.

1.3.1 Big Bang Nucleosynthesis

The first second of the universe was a period of remarkable expansion and change with extreme energies causing particles to pop into and out of existence. After a few seconds, the universe had cooled enough for quarks to form free protons and neutrons, and a few minutes later the universe had cooled enough to allow protons and neutrons to combine into heavier nuclei. The free neutrons were quickly scooped up into nuclei (mostly helium) creating abundances of roughly 75% hydrogen and 25% helium, which are approximately what is observed in the universe today. Trace amounts of lithium and beryllium were also produced, but no heavy elements could be built up at this point because of the lack of stable isotopes with mass numbers 5 and 8 and the insufficient densities preventing much nuclear fusion from taking place [14]. This is contrary to an earlier proposal that all the elements were produced as a result of the Big Bang [15].

1.3.2 Quiescent Stellar Burning

Over the course of 100 million years after the Big Bang, gas clouds in the universe began to collapse to form the first stars, a process that still takes place today. As material collects, the gravitational pressure leads to increased temperature and density at the core and eventually nuclear fusion begins. The energy released as a result of the nuclear fusion opposes the gravitational pressure of the star in hydrostatic equilibrium. This is known as quiescent

stellar burning. At first, hydrogen is converted into helium in the core of the star via the pp chain or the CNO cycle. Stars spend the majority of their lifetime in this main sequence stage, but eventually the hydrogen fuel runs low and the gravitational pressure causes the star to collapse and the core to increase in temperature. The mass of the star determines its evolution and if the star is massive enough, high enough temperatures will be reached that the next stage of stellar burning in the core occurs, which converts helium into carbon via the triple- α reaction in the red giant stage. Depending on the mass of the star, the sequence of burning stages in the core at increasingly higher temperatures and shorter timescales continues with carbon burning, neon burning, oxygen burning, and silicon burning. The previous burning stages do not stop but continue in outer shells of the star in an onion-like structure as shown in Fig. 1.3. The quiescent burning stages of stars can produce elements up to those around iron where the sequence stops because the nuclei in the iron region are energetically the most tightly bound (see Sec. 2.5). Additional fusion reactions beyond the iron region are mostly endothermic and do not release energy to withstand the gravitational pressure of the star [16].

1.3.3 Supernovae

A supernova is the explosion of a star, which causes the release of huge amounts of energy and particles into the universe. Supernovae are classified into two groups based on the presence of hydrogen absorption lines in their spectra, with type I having no hydrogen lines and type II having hydrogen lines. There are several subcategories of these two main classification groups, and this thesis focuses on nucleosynthesis in supernovae type Ia (SNIa) and supernovae type II (SNII).

SNII occur at the end of quiescent stellar burning of a massive star. At first the inert

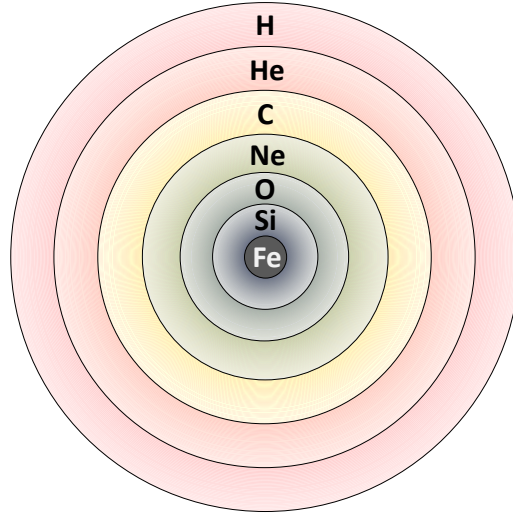


Figure 1.3: Simplified picture of a massive star that has undergone all of the burning stages in the core. The burning layers are not drawn to scale.

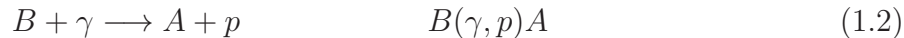
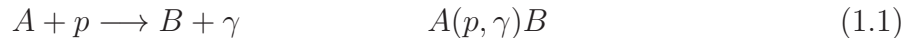
iron core is supported by the pressure of the degenerate electrons. However, once the core reaches approximately 1.4 times the mass of the Sun, electron degeneracy pressure can no longer support the star and the gravitational pressure causes the core to collapse under its own weight (the Chandrasekhar limit). For this reason SNII are also referred to as core collapse supernovae. The collapsing core causes the outer layers of the star to fall inwards. Once the infalling material strikes the collapsed core it rebounds outward in a shock wave. The outward propagating shock wave disrupts the star into a supernova and causes explosive nucleosynthesis to occur. Most of the outer layers get blown off in the explosion, leaving behind a neutron star or a black hole [17].

Whereas SNII involve only a single star, SNIa are thought to occur in a binary star system, where at least one of the stars is a white dwarf made out of carbon and oxygen. Carbon-oxygen white dwarves are formed from stars which are not massive enough to ignite carbon burning in their cores, and therefore end their quiescent stellar burning lifetimes after helium burning. Because there is limited energy released from nuclear reactions to

counteract the gravitational pressure, white dwarves are incredibly dense objects supported by electron degeneracy pressure. White dwarves by themselves do not become supernovae, but if they have a nearby star as a companion they may accrete mass from the neighboring star until they reach the Chandrasekhar limit of approximately 1.4 times the mass of the Sun. At this point, the carbon ignites and the burning quickly spreads throughout the star causing it to explode as a supernova and leave no remnant behind. It is not yet known whether SNIa consist of a white dwarf and a different type of star (single degenerate), two white dwarfs that collide (double degenerate), or possibly some other scenario. As with all types of supernovae, SNIa involve several explosive nucleosynthesis processes [18].

1.3.4 Nuclear Statistical Equilibrium

At high enough temperatures, the material inside a star can quickly reach a point where all forward and reverse reactions are in equilibrium, except for the reactions involving neutrinos, which are chargeless subatomic particles that typically escape from the star. For example, in equilibrium the rate that species A captures a proton to form species B is exactly equal to the rate that species B is photodissociated into species A plus a free proton. These type of reactions, which will be used throughout the remainder of this thesis, can be denoted as follows:



When all species are in equilibrium with each other, this is known as nuclear statistical equilibrium (NSE). Typical temperatures to achieve NSE in stellar environments are larger than 5 GK and such extreme temperatures are reached in the innermost layers of stars when

they explode as supernovae. While in NSE the abundance of each isotope can be determined from a relatively small number of parameters, including nuclear properties like mass and spin, and stellar properties like temperature, density, and neutron-to-proton ratio of the material [19]. In NSE, the highest temperatures favor free nucleons and lower temperatures favor isotopes that are energetically the most bound (have the highest binding energy). Therefore, in a supernovae the material that reaches NSE first breaks down into free protons, neutrons, and α particles due to the initial high temperatures. As the material expands and cools, the free nucleons combine to form mostly iron-peak nuclei due to their high binding energy. The neutron-to-proton ratio of the stellar material determines which isotopes in the iron region are the most abundantly produced [16]. Because supernovae spew the majority of their mass into the universe, the iron-peak nuclei existing in our solar system are nearly all a result of NSE.

If the expansion of the material undergoing NSE in the supernova occurs very rapidly, then the triple- α reaction can drop out of equilibrium before all the free α particles can combine into heavier nuclei. Such a scenario is known as α -rich freeze-out of NSE, and it leaves a quasi-equilibrium group of heavier nuclei [20]. The final composition of the material is iron-peak nuclei and free α particles. Further discussion of α -rich freeze-out of NSE is contained in Chapter 9.

1.3.5 Nucleosynthesis of the Heavy Elements

The elements beyond the iron peak cannot all be produced through nuclear fusion reactions and must be produced in some other fashion. Since neutrons are chargeless and not repelled by the positive nucleus, the majority of these heavy nuclei are produced by neutron captures on existing nuclei inside of stellar environments. There are two main neutron capture pro-

cesses that contribute: the slow (s) neutron capture process [21] and the rapid (r) neutron capture process [22]. As their names indicate, the two processes are distinguished by the speed of neutron capture. For a lower abundance of neutrons, the capture reactions occur slowly enough that any unstable nucleus that is produced has time to decay back into a stable nucleus before the next neutron capture. This is known as the s process and is expected to occur in the helium-shell burning, red giant phase of a star's life. For a large flux of neutrons, as is expected in a supernova explosion or the collision of two neutron stars, the neutron capture reactions occur very rapidly and produce very neutron-rich radioactive nuclei before decaying back into stable nuclei. This is known as the r process. Fig. 1.4 includes the nucleosynthesis pathway of the s and r processes. The spikes in the abundance pattern in Fig. 1.2 around mass 110 – 150 and 180 – 210 are signatures of the s and r processes.

While the s and r processes synthesize the majority of the heavy isotopes, there exists a group of stable isotopes that cannot be produced by either neutron capture process. These “p nuclei” lie on the neutron-deficient side of the valley of stability ranging from ^{74}Se up to ^{196}Hg (see Fig. 1.4). There are 35 p nuclei in total, but several of the isotopes are expected to have contributions from the s and r processes and are not always classified as p nuclei. With the exception of $^{92,94}\text{Mo}$ and $^{96,98}\text{Ru}$, the isotopic abundances of the p nuclei are very low compared to their more neutron-rich neighbors, typically contributing less than 1% to the total elemental abundance. Several potential astrophysical sites have been proposed for the creation of the p nuclei and a discussion of these scenarios follows in Sec. 1.4.

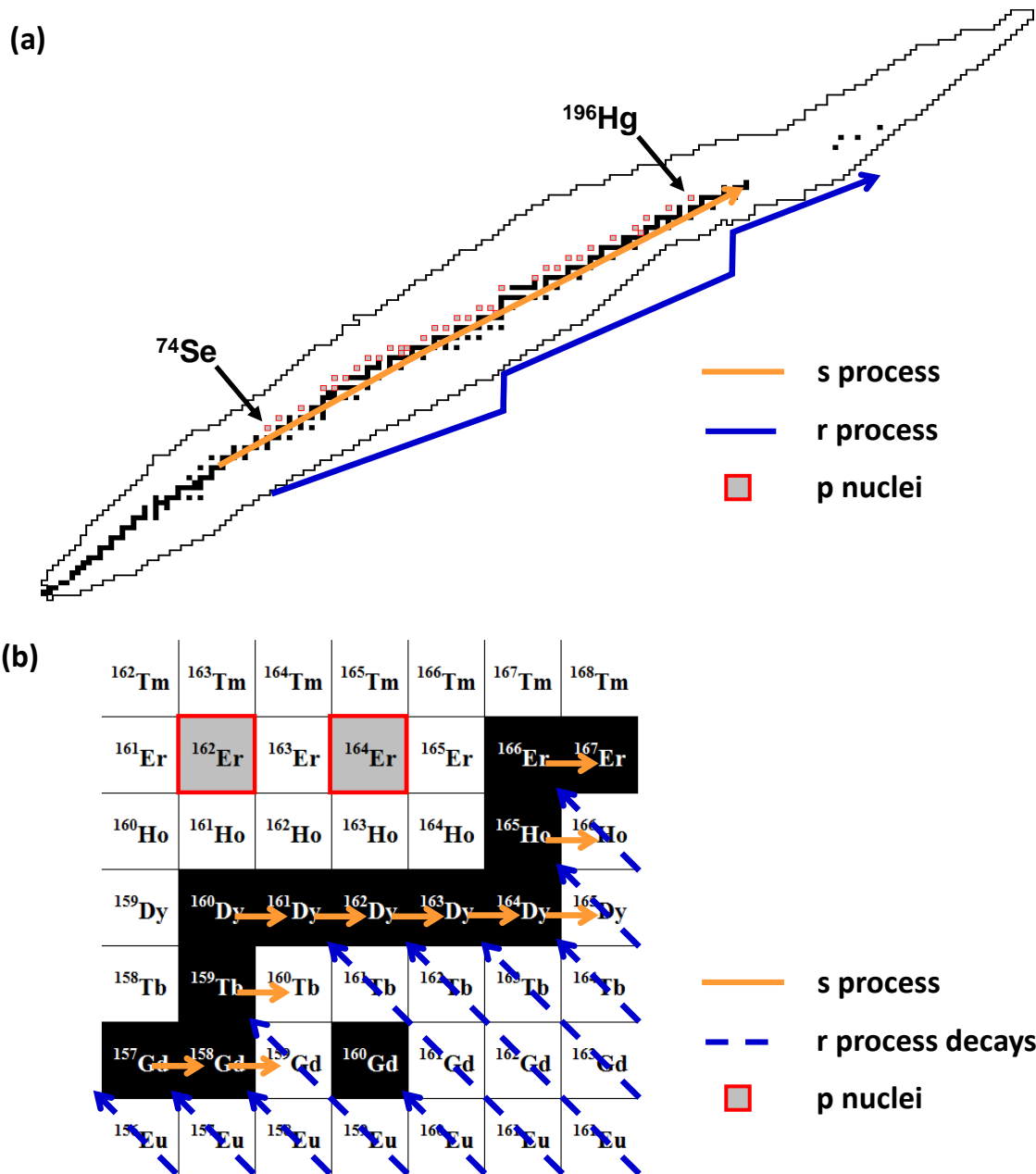


Figure 1.4: Nuclear chart showing the pathways for the s and r neutron capture processes, with a zoomed in view on the bottom. The s and r processes produce the majority of the stable isotopes heavier than iron, except for the 35 p nuclei which are shielded from β^- decay by the valley of stability.

1.4 Production of the p Nuclei

In the influential B2FH paper [12], the authors first noticed the need for an alternative astrophysical process to explain the production of the p nuclei. They termed it the “p process” and proposed the scenario of proton capture reactions on preexisting s- and r-process nuclei at high temperatures inside the hydrogen shell of a massive star when it explodes as a type II supernova. However, it was later shown that the high temperatures and densities required to produce the p nuclei in this fashion are not reached in the hydrogen shell [23]. More recently, two alternative explosive processes involving proton captures were identified as likely candidates for synthesizing some of the less massive p nuclei; the νp process [24, 25, 26] and the rp process [27].

1.4.1 νp process

The νp process is expected to occur in a type II supernova, when a massive star explodes ejecting its outer layers and leaving behind a neutron star [24]. The innermost layers of the ejecta are proton rich and undergo a series of proton captures as the material expands. The material expands very rapidly, however, and this provides only a short timescale for reactions to occur. Thus, the creation of elements with heavier mass gets inhibited by waiting point nuclei, for which proton capture is inhibited and the reaction flow has to wait for the relatively long decay time before continuing. However, in the process of forming the neutron star, neutrinos are radiated outward and can be captured by the large number of free protons to create neutrons. It is the capture of these newly produced neutrons on the waiting point nuclei which allows the flow of nucleosynthesis to bypass the long decays and produce elements with heavier mass. It has been shown that the νp process may produce

nuclei up to mass 152 under certain supernova conditions [28]

1.4.2 rp process

The rp process requires a hydrogen-rich environment at high temperatures to lead to rapid proton captures that synthesize higher mass nuclei. Such conditions can be reached in a binary star system with a donor star accreting hydrogen and helium from its atmosphere onto its neutron star partner. As the material builds up on the neutron star's surface, instabilities can cause an X-ray burst, which leads to high enough temperatures for the rp process to occur [29]. The rp process can reach up to mass 110 at the endpoint in the proton-rich isotopes of tellurium [30], but it is not clear whether the material in the X-ray burst escapes the gravitational field of the neutron star to contribute to the changing chemical history of the universe [31].

1.4.3 p process

While the νp process and rp process can synthesize some of the less massive p nuclei, there is an astrophysical scenario that can produce the p nuclei across the entire mass range. Instead of proton captures creating more massive nuclei, the dominant reactions are photodisintegrations that knock out nucleons from existing nuclei and produce the p nuclei as a result. The preexisting nuclei in the star, referred to as seed nuclei, can originate from the s- and r-process material expelled from other stars or can be freshly produced through the s process in the star of interest. All objects emit radiation depending on their temperature through blackbody radiation, and for temperatures higher than about 1.8 GK the blackbody radiation from the star is at high enough energies to knock out protons, neutrons, and α -particles

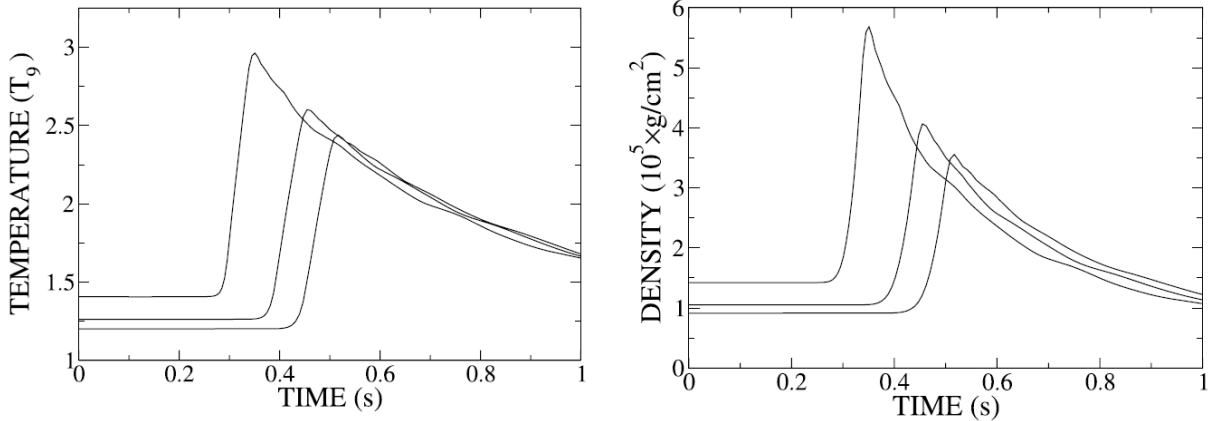


Figure 1.5: Figure from Ref. [37] showing the temperature and density of the O/Ne layer as the shockwave passes through. The curves represent different depths of the O/Ne layer.

in (γ,p) , (γ,n) , and (γ,α) reactions, respectively. It is important that the temperatures do not reach higher than about 3.3 GK, however, so that the heavier nuclei are not completely photodissociated into iron peak nuclei.

The conditions of having existing seed nuclei and temperatures between 1.8 and 3.3 GK are reached naturally in the oxygen and neon (O/Ne) layers of a massive star (see Fig. 1.3). For the more massive stars the temperatures may be already high enough for photodissociations to occur in the presupernova phase [32, 33], but the largest effect is expected to occur in the type II supernova when the shockwave passes through the O/Ne layers [34]. The term “p process” from the original B2FH publication has stuck, although (perhaps more appropriately) it is also referred to as the γ process in literature because of the prevalence of photodisintegration reactions. Nice reviews of the p process can be found in Ref. [35] and Ref. [36].

Fig. 1.5 shows the temperature and density of the O/Ne layer as the shock wave propagates through. There is a very rapid rise followed by an exponential decrease in temperature and density. A maximum temperature between 1.8 and 3.3 GK is reached for various depths

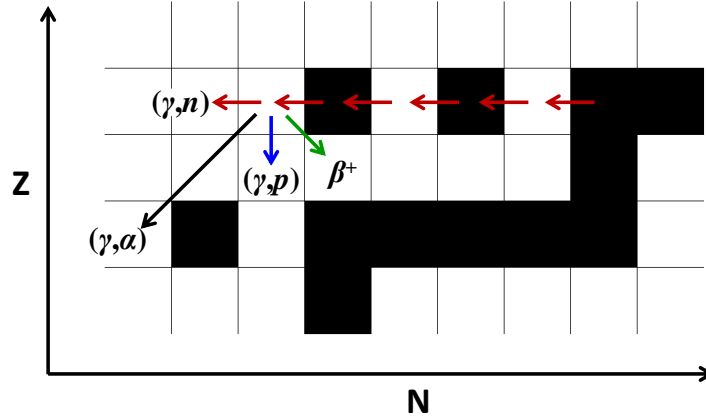


Figure 1.6: Section of the nuclear chart showing an example reaction flow for the p process.

in the O/Ne layer. Fig. 1.6 shows a simplified reaction flow of the p process for only one seed nucleus. In reality the flow proceeds through a complex network of reactions that compete at different temperatures. As mentioned, the seed nuclei have already been produced by a previous s- or r- process event. At first, the most probable reactions are (γ, n) reactions which cause the flow of mass from the stable seed nuclei into unstable nuclei. For each (γ, n) reaction that occurs, the nuclei become increasingly neutron deficient and eventually the (γ, p) or (γ, α) reactions will occur at a higher rate. (γ, α) reactions are typically more significant for the heavier elements while (γ, p) reactions are key contributors to the formation of the lighter p nuclei [35]. There are also proton capture reactions that play a role for the lighter masses. The isotope in each elemental chain where the (γ, p) or (γ, α) reaction rate is comparable to the (γ, n) rate is called the branching point, and its location is critical for understanding the flow of mass in the p process [38]. The branching point shifts the reaction flow to a new elemental chain where the photodisintegration reactions continue. Once the temperature cools and the photodisintegration reactions slow, the competition of the β^+ decays of unstable nuclei also become important. Eventually all unstable nuclei will β^+ decay back to stability.

It should be emphasized that Fig. 1.6 represents the initial reaction flow from only one seed nucleus. Inside of the supernova, all preexisting s and r nuclei are taking part in the photodisintegrations. In total, the p process includes over 20,000 reactions on approximately 2000 nuclei. These include (γ,p) , (γ,n) , and (γ,α) reactions, their inverse capture reactions, and β^+ decays. It is also important to note that the majority of the reactions involve radioactive isotopes.

Reaction network calculations of the p process have been performed by various authors for a range of stellar masses and compositions [39, 40, 35, 37, 41]. The stellar parameters used in these reaction networks are determined from hydrodynamical simulations of the environment of massive stars (see Ref. [40] and references therein). In these p-process models, the massive star is divided into mass layers and reaction network calculations are performed in each layer. For example, Ref. [37] divided the O/Ne of the star into 14 layers. It is also necessary to use accurate initial seed abundances, stellar parameters such as temperature and density, and nuclear properties such as reaction rates, masses, and decay rates. Any uncertainty in the input physics contributes to the uncertainty in the production of the p nuclei in the models. A discussion of these uncertainties is presented in Sec. 1.4.4. After performing the calculation, it is desirable to compare the abundances of the p nuclei produced in the model to the solar abundances. However, this comparison cannot be done directly because the solar abundances contain a mixture of many nucleosynthesis processes and the models are focused only on the p process. Instead, what is typically done is to check whether or not the models produce the p nuclei in the correct ratios [40]. First, the total mass of each p nucleus produced in the calculation is compared to what its total mass would be if it was present in

the correct solar abundance. This ratio is known as the overproduction factor

$$\langle F_i \rangle = \frac{m_i}{M_{model} X_{i\odot}} \quad (1.3)$$

where m_i is the produced mass of a p nucleus over all the mass layers the model, M_{model} is the total mass of all the mass layers in the model, and $X_{i\odot}$ is the solar abundance mass fraction of the p nucleus. Then, the average overproduction factor for the 35 p nuclei is calculated by

$$F_0 = \frac{1}{35} \sum_{i=1}^{35} \langle F_i \rangle . \quad (1.4)$$

Comparing the overproduction factor of each p nucleus to the average overproduction factor is a convenient way to check if the model reproduces the p nuclei in the correct solar abundance ratios. This quantity $\langle F_i \rangle / F_0$ is called the normalized overproduction factor, and if all the p nuclei were produced in the correct ratio, the normalized overproduction factor for each p nucleus would be equal to 1. The p nuclei with values above 1 are overproduced by the calculation compared to the other p nuclei, and p nuclei with values below 1 are underproduced.

Fig. 1.7 shows a typical result of the normalized overproduction factor for each p nucleus from a calculation by Ref. [37], and all other models show a similar pattern. Overall, the majority of the calculated p-nuclei abundances agree to within a factor of 2-3 of the observations. The most notable discrepancy is the underproduction of $^{92,94}\text{Mo}$ and $^{96,98}\text{Ru}$, which is a problem because they are the most abundant of the p nuclei and make up to 14% of the total elemental abundance. If the p process scenario is correct it should be able to predict the correct abundances for the most abundant isotopes. However, as previously mentioned the νp process (Sec. 1.4.1) and rp process (Sec. 1.4.2) may be able to contribute to the pro-

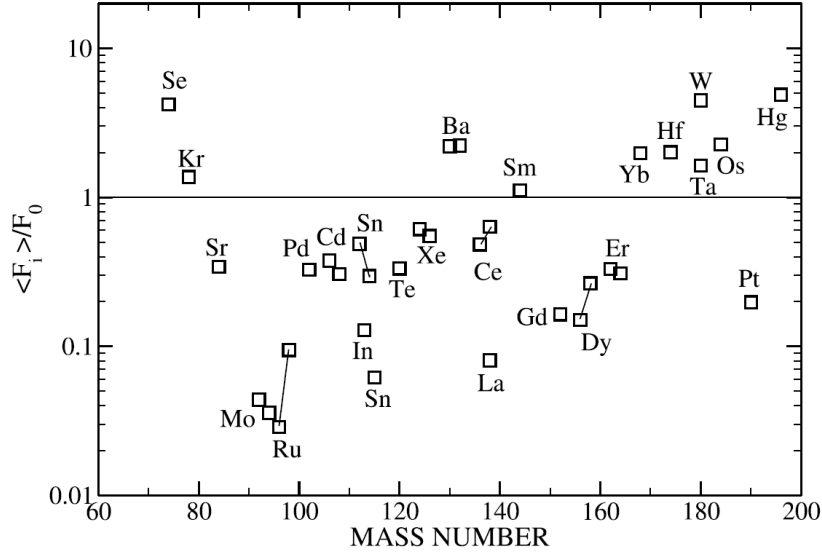


Figure 1.7: Normalized overproduction factor for the calculated abundance of each p nucleus plotted against mass number. Plot is taken from Ref. [37]

duction of the lighter p nuclei and may help explain this discrepancy. Also underproduced by the p process calculation are ^{113}In , ^{115}Sn , and ^{138}La . Possible explanations are that ^{113}In and ^{115}Sn may have contributions from the s and r processes [42, 43], and ^{138}La can be produced through neutrino reactions [44, 45]. While the majority of the light p nuclei are underproduced, ^{74}Se is surprisingly overproduced. Thus far the overproduction of ^{74}Se has remained a mystery and a nuclear physics measurement related to the ^{74}Se abundance can be found in Chapter 8.

In addition to type II supernovae, the p process is expected to occur in type Ia supernovae [46]. In this scenario, material enriched in s nuclei is accreted from a companion star onto a white dwarf star. Once the white dwarf reaches its maximum mass, known as the Chandrasekhar mass, it explodes as a type Ia supernova and some of the material reaches the correct temperatures for the p process to occur. Earlier models of this scenario saw the same underproduction in light p-process nuclei as in the O/Ne layer of type II super-

novae [47, 48]. However, a more recent attempt using a two-dimensional model matches the solar abundances of the light p-process nuclei by using large enhancements of the s nuclei prior to the explosion [49].

1.4.4 Uncertainties

There are several sources of uncertainty in the production of the p nuclei via the p process, including uncertainties in the stellar environment and nuclear physics data both before and during the p process. Even before the supernova occurs, it is necessary to understand the development of the pre-supernova star, especially the abundances of the seed nuclei. These abundances depend on the initial composition of the star, the nuclear reactions contributing to the s process, and how the seed nuclei get mixed and transformed prior to the explosion. Fig. 1.8 shows the spread in abundances of the s nuclei as a result of some of these uncertainties. Both varying the initial composition of the star (left panel) and the reaction rates (right panel) in a s-process simulation lead to different distributions of the seed nuclei. Additionally, it has been shown that the uncertainties in the $^{22}\text{Ne}(\alpha, n)^{25}\text{Mg}$ [50, 51] and $^{12}\text{C}(\alpha, \gamma)^{16}\text{O}$ [40] reactions have a significant impact on the result of p-process calculations due to their effect on the initial composition of the p-process layers of massive stars. The important contributions of both reactions take place during the helium burning stage. The $^{22}\text{Ne}(\alpha, n)^{25}\text{Mg}$ reaction is the main source of neutrons for the s process during helium burning, while the $^{12}\text{C}(\alpha, \gamma)^{16}\text{O}$ reaction determines the composition of the carbon-oxygen core and its later evolution. Reducing the uncertainty on both of these reactions will lead to more accurate p-process calculations.

In addition to the uncertainty in the abundances of seed nuclei, the stellar environment during the supernova also contributes uncertainties to the p process. For example, the

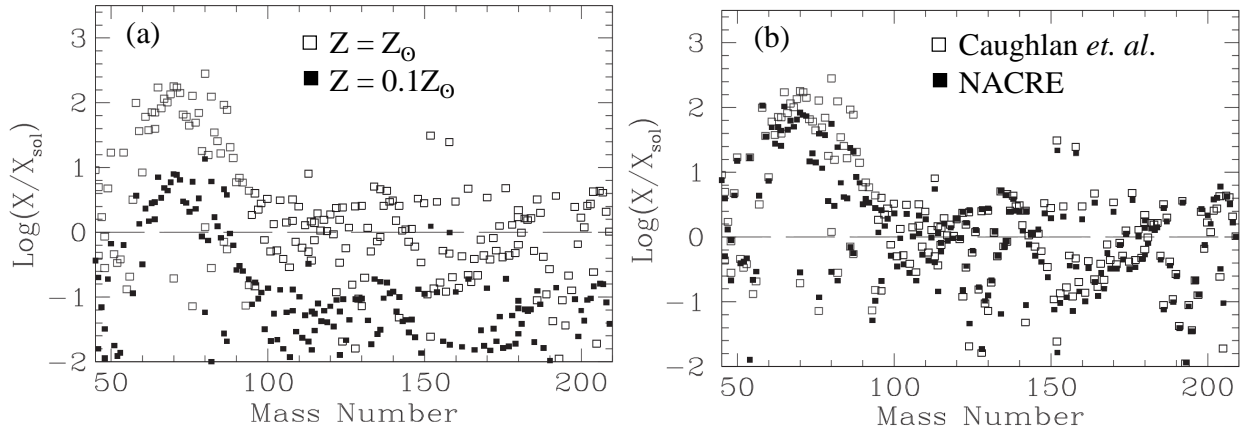


Figure 1.8: Figures from Ref. [35] showing the abundances of the s nuclei at the end of the helium burning stage and how they depend on (a) the initial metallicity of the star (b) the reaction rates used in the s-process calculations. The initial metallicities used were solar and 10% solar, and the different rates used were from Ref. [52] and Ref. [53].

temperature and density profile of the stellar layers during the explosion are critical for determining which p nuclei are produced. This can be seen in Fig. 1.9 from Ref. [37], which shows how sensitive the p process is to the maximum temperature that a stellar layer reaches during the explosion. Shifting the maximum temperature of a layer by a tenth of a GK can have a huge effect on which p nuclei get produced due to the change in rate of photodisintegration reactions. Because the mass of the star and its composition are key factors in determining the properties of the supernova explosion, the uncertainty in initial stellar masses and metallicities are also important considerations. Fig 1.10 from Ref. [40] shows how stellar masses ranging between 13-25 times the mass of the Sun lead to very different results for the p process. In the universe, there is a distribution of massive stars with different masses and metallicities which undergo the p process and mix different quantities and ratios of the p nuclei into the interstellar medium. Because the solar abundances are a mixture of all these different sources of p nuclei, another uncertainty in the production of the p nuclei is the distribution of the various massive stars [40].

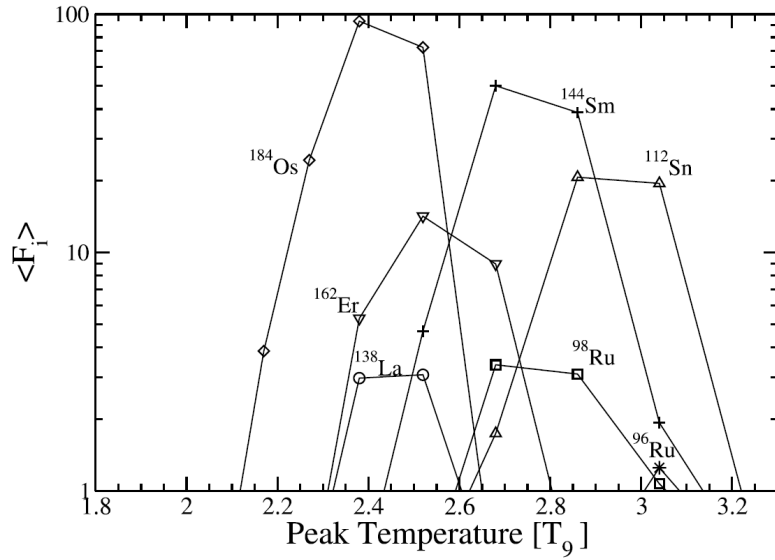


Figure 1.9: Figure from Ref. [37] showing the overproduction factor of selected p nuclei as a function of the peak temperature of the stellar layer reached during the supernova explosion.

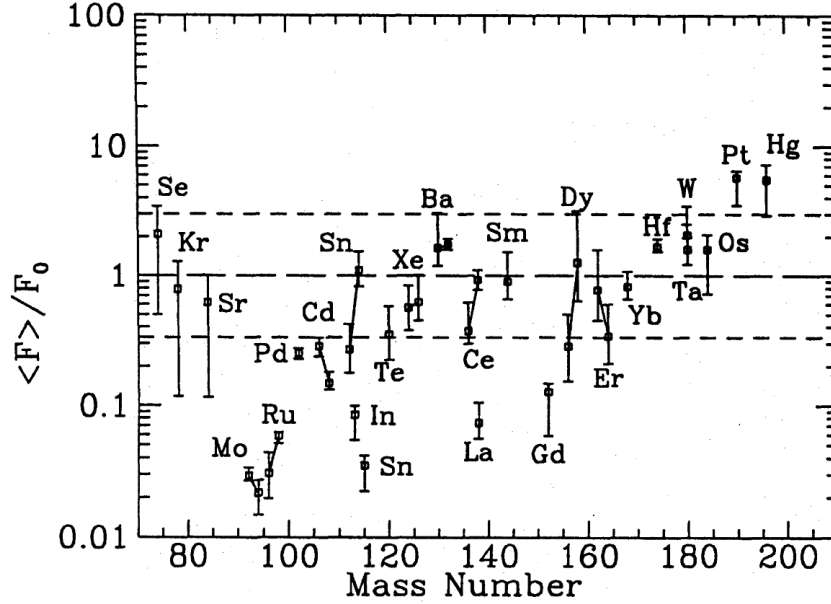


Figure 1.10: Figure from Ref. [40] showing the normalized overproduction factor of the p nuclei for supernova explosions of stars with mass in the range between 13-25 times the mass of the Sun. The vertical bar for each nucleus indicates the spread in p-nuclei abundances as a result of the various stellar masses.

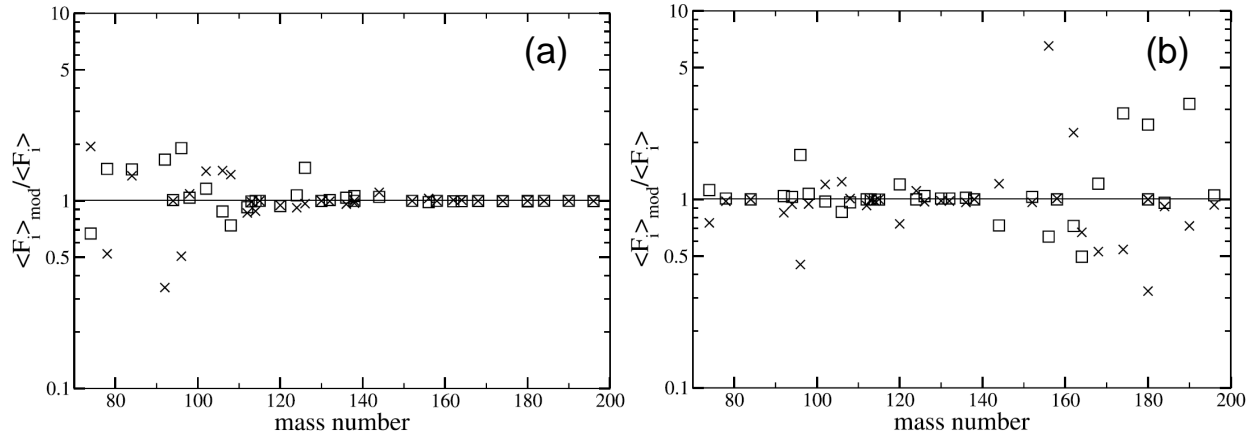


Figure 1.11: Figure from Ref. [37] showing the ratio of p-nuclei abundances calculated with rates modified by a factor of three up and down compared to the standard rate. (a) Modified proton-induced reactions and their inverse reactions. (b) Modified α -induced reactions and their inverse reactions.

A final crucial uncertainty in the p process is the nuclear physics reaction rates used in the p process models. As previously mentioned, the p process involves over 20,000 reactions on 2000 nuclei with the majority of the reactions involving radioactive isotopes. Thus far, very little experimental data exists for reactions relevant to the p process [36] and instead all astrophysical models rely heavily on theoretical calculations of reaction rates. These theoretical rates can have uncertainties of up to a factor of three. Fig. 1.11 shows the effect of varying all proton-induced (left panel) and α -induced (right panel) reaction rates and their inverse rates up and down by a factor of three. The uncertainties in reaction rates for reactions involving protons have the largest impact on the production of the lighter p nuclei, and the uncertainties in reactions involving α particles have the largest impact on the production of the heavier p nuclei.

Reducing the uncertainty in the nuclear physics reaction rates to improve p-process calculations is the main focus of this dissertation. Since it is not realistic to measure all 20,000 reactions, an interested experimentalist has two goals. The first goal is to measure as many p

process reactions as possible at the relevant astrophysical energies to put constraints on the theoretical calculations. Ideally the constraints would allow the theoretical calculations to predict the other unknown reactions more accurately. The second goal is to identify which reactions are the most critical for the production of the p nuclei. While there are many reactions occurring, only a few have a large impact on the final result. There have been two publications which have identified some of the most important reactions in the p process. Rapp et al. [37] performed a sensitivity study which varied reactions up and down by a factor of 3 (approximately equal to the theoretical uncertainty) and investigated which reactions led to the largest change in the abundances of the p nuclei. The other publication by Rauscher [38] contains a model independent study identifying the location of the p-process branching points which are critical to know for accurately understanding the flow of the p process to lighter mass. This dissertation contains the development of a new detector and expansion of an existing experimental technique in an effort to measure some of these critical reactions and improve the accuracy of p-process calculations.

1.5 Looking Ahead

The remainder of this dissertation contains the story of the development of a new detector to measure reactions relevant to the production of the p nuclei as well as results from the first experiments with the detector. In Chapter 2 important quantities in nuclear physics and astrophysics will be introduced. In Chapter 3 the most relevant nuclear reaction theories for this work will be presented. In Chapter 4 an overview of available experimental techniques and the methods used for this project will be provided. In Chapter 5 the design and testing of the primary detector will be discussed. In Chapter 6 the steps which were taken in the

analysis of the data will be demonstrated. In Chapters [7](#), [8](#), [9](#), [10](#), and [11](#) the results for the measurements of individual nuclear reactions will be presented, including the extension of the experimental technique to measurements in inverse kinematics. Finally, in Chapter [12](#) a summary and outlook for this dissertation will be provided.

Chapter 2

Nuclear and Astrophysical Quantities

2.1 Cross Section

This dissertation contains the measurement of the reaction cross section for several different nuclear reactions. To introduce this important nuclear physics quantity let's start with the classical treatment using the carnival game of throwing a dart at a wall of balloons as our example. If you hit a balloon, it will hopefully pop and you will win the prize of your choosing. Let's assume that all balloons are spheres of the same size and that you have decent aim so that your throws are always within the wall of balloons. We will say that your throws hit the wall within a circle of area A which is less than the total area of the wall (see Fig. 2.1). The probability that a balloon is hit is given by the ratio of the area covered by

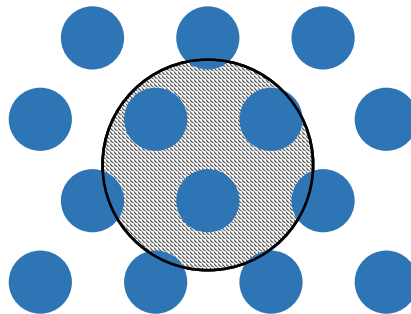


Figure 2.1: Front view of uniformly placed circular targets. The large grey circle represents the area in which projectiles strike the targets.

the balloons to the area A :

$$P_{\text{success}} = \frac{\text{area covered by balloons}}{\text{area covered by darts}} = \frac{N_b \pi r^2}{A} = \frac{N_b}{A} \sigma \quad (2.1)$$

where N_b is the number of balloons within your throwing accuracy, N_b/A is the areal density, and $\sigma = \pi r^2$ is the cross-sectional area covered by one balloon. If you throw a large number of darts (N_d) then the number of prizes you can expect to win is

$$N_{\text{prizes}} = N_d P_{\text{success}} = N_d \frac{N_b}{A} \sigma . \quad (2.2)$$

Thus, the cross section of the balloons can be calculated by

$$\sigma = \frac{N_{\text{prizes}}}{N_d N_b/A} = \frac{N_{\text{reactions}}}{N_{\text{projectiles}} N_{\text{targets}}/A} \quad (2.3)$$

where we made the change in variables from darts to projectiles, balloons to targets, and prizes to reactions. This same equation will be used throughout the dissertation to calculate the nuclear cross sections. Before moving on there are two important things to notice from Eq. 2.1; the cross section is directly related to the probability of an interaction occurring, and the cross section quantity has units of area.

In this example, the cross section is simply equal to the physical area that a balloon takes up $\sigma = \pi r^2$. Thus in the classical mechanics understanding, the cross section of a nuclear reaction would be given by the cross-sectional area of the nucleus, which for uranium is approximately equal to 10^{-24} cm^2 . Scientists have designated this value of 10^{-24} cm^2 as 1 barn (b). However, at the small nuclear scale there are quantum mechanical effects and

instead of the simple value of πr^2 the cross section has an energy dependence

$$\sigma \propto \pi \lambda^2 = \pi \frac{\hbar^2}{2\mu E} \quad (2.4)$$

where λ is the reduced de Broglie wavelength, \hbar is the reduced Planck constant, μ is the reduced mass equal to $m_1 m_2 / (m_1 + m_2)$, and E is the center of mass energy of the projectile and target system. In addition to the expected $1/E$ energy dependence of the cross section, there are several other factors that may inhibit the nuclear reaction from taking place. For example, the Coulomb barrier related to the nuclear charge and the centrifugal barrier related to the nuclear angular momentum are important factors in determining the cross section. In conclusion, the reaction cross section may be thought of as the effective area of the nucleus in a reaction. Typical cross sections measured in this thesis range from 10^{-6} b (1 μ b) to 10^{-3} b (1 mb).

2.2 Stellar Reaction Rate

In order to understand the energy generation and synthesis of the elements inside of stellar environments, it is necessary to know the rate at which nuclear reactions are taking place. The stellar reaction rate depends on the abundance of each type of nuclei inside of the star, the reaction cross section between them, and their relative energy. If we consider a stellar gas of particles in a volume (say it has area A and depth x), along with a flux of particles with relative speed v (see Fig. 2.2) then we can derive an expression for the reaction rate per unit volume per time starting from Eq. 2.2:

$$N_R = N_1 \frac{N_2}{A} \sigma \quad \longrightarrow \quad \frac{N_R}{V t} = \frac{N_1}{V} \frac{N_2}{A x} \sigma \frac{x}{t} \quad (2.5)$$

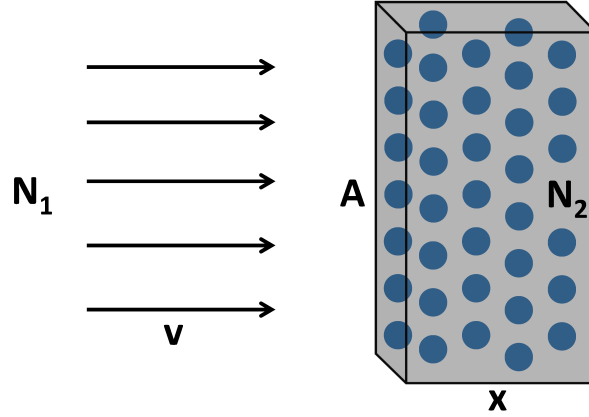


Figure 2.2: A number of particles N_1 and velocity v impinging on a number of particles N_2 within a volume that has area A and depth x .

where we first divided by the volume V and the time t and then multiplied by a convenient factor of $x/x = 1$. The quantity N_x/V is the number density of the interacting particles with units of number of particles per unit volume, and can be written simply as n_x . Since the cross section depends on energy and therefore on velocity, it immediately follows that the reaction rate is equal to

$$r_{12} = n_1 n_2 \sigma(v) v . \quad (2.6)$$

Inside of stellar environments the nuclei do not all have the same relative velocities but instead have a distribution of velocities, described by the probability function $\phi(v)$. Folding in this distribution as well as taking into account reactions involving identical particles, the reaction rate can be written

$$r_{12} = \frac{n_1 n_2}{1 + \delta_{12}} \int_0^\infty \phi(v) \sigma(v) v dv \quad (2.7)$$

where the Kronecker symbol δ_{12} is 0 for reactions between different nuclei and 1 for reactions between identical nuclei. The number density of reaction pairs is given by $n_1 n_2 / (1 + \delta_{12})$

and the reaction rate per particle pair is given by

$$\langle \sigma v \rangle = \int_0^\infty \phi(v) \sigma(v) v dv . \quad (2.8)$$

In a stellar plasma, nuclei are nondegenerate and nonrelativistic particles and thus move with velocities given by the Maxwell-Boltzmann distribution

$$\phi(v) = 4\pi v^2 \left(\frac{\mu}{2\pi kT} \right)^{3/2} \exp\left(\frac{-\mu v^2}{2kT} \right) \quad (2.9)$$

where k is the Boltzmann constant and T is the temperature of the stellar plasma. Combining the Maxwell-Boltzmann distribution with Eq. 2.8 and making the change of variables from relative velocity to center of mass energy $E = \mu v^2/2$, the reaction rate per particle pair can be written

$$\langle \sigma v \rangle = \sqrt{\frac{8}{\pi\mu(kT)^3}} \int_0^\infty \sigma(E) E \exp\left(\frac{-E}{kT} \right) dE . \quad (2.10)$$

2.3 Astrophysical S factor

The nuclear reactions in stellar environments take place at energies which are typically too low for charged particles to get close enough for the attractive nuclear strong force to fuse the particles together. Instead the electric repulsion of the two positive nuclei create a Coulomb barrier

$$V_C = \frac{Z_1 Z_2 e^2}{r} \quad (2.11)$$

with $Z_x e$ equal to the charge of the nuclei. For relative energies below the Coulomb barrier, charged particle reactions would not occur except for the quantum mechanical tunneling

effect. At energies well below the Coulomb barrier the probability of tunneling through the barrier is given by

$$P_{\text{tunnel}} = \exp(-2\pi\eta) \quad \text{with} \quad \eta = \frac{Z_1 Z_2 e^2}{\hbar v} \quad (2.12)$$

where η is called the Sommerfeld parameter.

The effect of the Coulomb barrier and the expected $1/E$ dependence of the cross section as introduced in Eq. 2.4 motivate the writing of the nuclear reaction cross section as

$$\sigma(E) = \frac{1}{E} \exp(-2\pi\eta) S(E) \quad (2.13)$$

where $S(E)$ is the astrophysical S factor. Because much of the energy dependence of the cross section has been factored out, $S(E)$ represents all of the nuclear effects in the cross section and is a smoothly varying function of energy. Due to the reduced energy dependence of $S(E)$ compared to the cross section it is much more useful to use $S(E)$ to extrapolate to lower energies. Nuclear reactions taking place in stellar environments typically occur at low energies, where the cross section for charged particle capture is very low due to the low probability of tunneling through the Coulomb barrier. Experimental data is often obtained at higher energies where the higher cross section makes the measurement more feasible, and then the data is extrapolated down to the lower astrophysical energies. It is more useful to extrapolate using $S(E)$ than $\sigma(E)$.

2.4 Gamow Window

Plugging the S factor (Eq. 2.13) into the reaction rate (Eq. 2.10) gives

$$\langle \sigma v \rangle = \sqrt{\frac{8}{\pi\mu(kT)^3}} \int_0^\infty \exp(-2\pi\eta) S(E) \exp\left(\frac{-E}{kT}\right) dE . \quad (2.14)$$

Changing the Sommerfeld parameter to a function of energy via $E = \mu v^2/2$ and introducing the constant term $E_G = 2\mu(\pi Z_1 Z_2 e^2/\hbar)^2$ the integral becomes

$$\langle \sigma v \rangle = \sqrt{\frac{8}{\pi\mu(kT)^3}} \int_0^\infty \exp\left(-\sqrt{\frac{E_G}{E}}\right) S(E) \exp\left(\frac{-E}{kT}\right) dE . \quad (2.15)$$

Since $S(E)$ is a smoothly varying function of energy, the energy dependence of the integrand is dominated by the two exponential terms. The term arising from the probability to penetrate through the Coulomb barrier approaches zero as the energy approaches zero, and the term arising from the tail of the Maxwell-Boltzmann distribution approaches zero for large energies. Thus, when multiplying the two terms together there is a sweet spot in the middle which creates a peak in the integrand. This is known as the Gamow peak and it gives rise to the range of energies, known as the Gamow window, over which the majority of nuclear reactions take place inside of stellar environments. The Gamow peak can be seen in Fig. 2.3.

The energy at the maximum of the Gamow peak can be found by solving for the point at which the derivative of the integrand of Eq. 2.15 equals zero. Before taking the derivative, $S(E)$ is taken to be constant and factored outside of the integral. This leads to a value of

$$E_{max} = \left(\frac{E_G(kT)^2}{4}\right)^{1/3} . \quad (2.16)$$

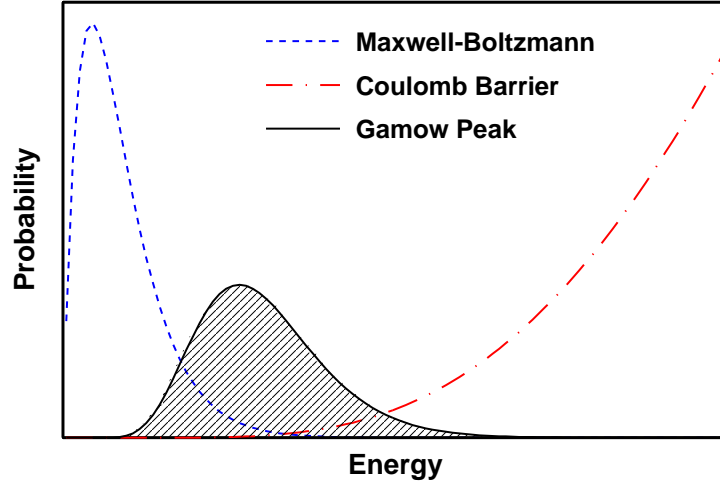


Figure 2.3: The tail of the Maxwell-Boltzmann distribution of particle energies $\exp(-E/kT)$ combined with the probability of charged particles to penetrate through the Coulomb barrier $\exp(-2\pi\eta)$ gives rise to the Gamow peak (not drawn to scale). The Gamow peak defines the energy window over which the majority of nuclear reactions take place inside of stellar environments.

The width of the Gamow peak can be estimated by approximating the shape as a Gaussian function. The $1/e$ width of the Gaussian is found to be [16]:

$$\Delta = 4 \sqrt{\frac{E_{max}kT}{3}}. \quad (2.17)$$

It has been pointed out by Ref. [54], that the energy and width of the Gamow window in the two previous equations rely on the cross section being dominated by the probability to penetrate through the Coulomb barrier. However, this is not always the case and a more accurate Gamow window can be determined by evaluating the integrand of Eq. 2.10.

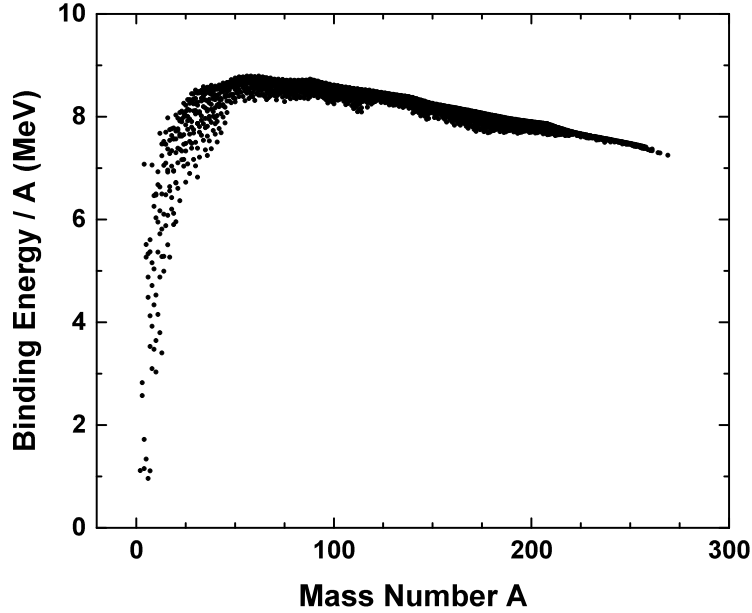


Figure 2.4: Binding energies per nucleon based on the data from [55]. The maximum occurs around the iron region.

2.5 Q value

The mass of a nucleus is one of its most fundamental properties. Since the 1920's [56, 57] it has been known that the measured mass of an atomic nucleus is less than the sum of its building blocks. From Einstein's mass-energy equivalence [58], the missing mass of a nucleus is equivalent to the energy released when building up the nucleus from free nucleons. Alternatively the missing mass is equal to the energy required to break a nucleus into free nucleons, thus it is referred to as the binding energy. The binding energy of a nucleus is given by

$$B.E./c^2 = Zm_p + Nm_n - m_x \quad (2.18)$$

where m_p , m_n , and m_x are the masses of the protons, neutrons, and nucleus, respectively. The plot of binding energy per nucleon in Fig. 2.4 shows that the maximum binding occurs around the iron region. Energy can be released by combining nuclei lighter than the iron

region in fusion or breaking up nuclei heavier than the iron region in fission.

For a nuclear reaction $1 + 2 \rightarrow 3 + 4$, the energetics can be quantified by the reaction Q value

$$Q = (m_{initial} - m_{final})c^2 = (m_1 + m_2)c^2 - (m_3 + m_4)c^2 . \quad (2.19)$$

Reactions with $Q > 0$ are exothermic and release energy, while reactions with $Q < 0$ are endothermic and require an input of energy to occur.

Chapter 3

Theoretical Considerations

3.1 Resonant Reactions

Nuclei live in the quantum world and therefore have discrete physical states at discrete energies with a lowest energy ground state and higher lying excited states. The excited states typically live for less than 10^{-12} seconds before releasing their energy through the emission a γ ray or nucleons from the nucleus. Excited states that live longer before deexciting are called metastable or isomeric states. Due to the Heisenberg uncertainty principle in quantum mechanics, the excited states have energy fluctuations about their mean energy with a certain width (Γ), and this width is related to the lifetime (τ) of the state by $\Gamma = \hbar/\tau$

In a nuclear reaction, two nuclei collide to form a new nucleus often in an excited state. The state is populated through the entrance channel and deexcites through the exit channel. The notation that will be used in the remainder of this chapter is



where $A + a$ is the entrance channel and $B + b$ is the exit channel. Like the state itself, the entrance and exit channel of a reaction have widths, which are related to the energy range over which the reaction can occur. These widths are called partial widths Γ_i and they are related to the total width by $\Gamma = \Gamma_1 + \Gamma_2 + \Gamma_3 + \dots$. The probability that the state decays

through a particular reaction channel is given by the branching ratio Γ_i/Γ .

If the energetics of a nuclear collision match the energy of an excited state of the new nucleus, then the reaction probability is enhanced in a resonance. The presence of a resonance in the reaction is also influenced by the angular momentum of the excited state. The shape of the resonance in the reaction cross section is given by the Breit-Wigner lineshape (see the top panel of Fig. 3.1):

$$\sigma(E) = \frac{\lambda^2}{4\pi} \omega \frac{\Gamma_1 \Gamma_2}{(E - E_r)^2 + (\Gamma/2)^2} . \quad (3.2)$$

The variable λ is the de Broglie wavelength, E_r and Γ are the energy and width of the resonance, Γ_1 and Γ_2 are the partial widths of the entrance and exit channel, and ω is the statistical factor of the entrance channel for total nuclear angular momentum (J) given by

$$\omega = \frac{2J_r + 1}{(2J_A + 1)(2J_a + 1)} . \quad (3.3)$$

3.1.1 In Stars

We can see how a resonance influences the stellar reaction rate by plugging Eq. 3.2 into Eq. 2.10 to obtain

$$\langle \sigma v \rangle = \sqrt{\frac{8}{\pi \mu (kT)^3}} \int_0^\infty \frac{\lambda^2}{4\pi} \omega \frac{\Gamma_1 \Gamma_2}{(E - E_r)^2 + (\Gamma/2)^2} E \exp\left(\frac{-E}{kT}\right) dE . \quad (3.4)$$

Noting that $\lambda^2/(4\pi) = \pi \hbar^2/(2\mu E)$, ignoring any energy dependence of Γ_i , and noticing that the narrow Breit-Wigner resonance will be like a delta function so that we can replace the

energy term in the exponential with the resonance energy E_r , the reaction rate becomes

$$\langle \sigma v \rangle = \sqrt{\frac{2\pi}{(\mu kT)^3}} \hbar^2 \omega \Gamma_1 \Gamma_2 \exp\left(\frac{-E_r}{kT}\right) \int_0^\infty \frac{1}{(E - E_r)^2 + (\Gamma/2)^2} dE . \quad (3.5)$$

The integral is equal to

$$\int_0^\infty \frac{1}{(E - E_r)^2 + (\Gamma/2)^2} dE = \frac{2\pi}{\Gamma} \quad (3.6)$$

so that the final reaction rate is given by

$$\langle \sigma v \rangle = \left(\frac{2\pi}{\mu kT}\right)^{3/2} \hbar^2 \omega \gamma \exp\left(\frac{-E_r}{kT}\right) \quad (3.7)$$

with the resonance strength $\omega \gamma$ defined as

$$\omega \gamma = \frac{2J_r + 1}{(2J_1 + 1)(2J_2 + 1)} \frac{\Gamma_1 \Gamma_2}{\Gamma} . \quad (3.8)$$

Thus the reaction rate due to a resonance in a stellar environment depends on the resonance strength, the resonance energy, and the temperature of the stellar material. This dissertation contains the experimental measurement of several resonance strengths. The method used to obtain this quantity will be introduced in the following section.

3.1.2 In the Laboratory

In the laboratory, we cannot reproduce the conditions inside of a stellar environment and instead experiments are done by impinging a nuclear beam of particles onto target nuclei.

The yield of the reaction is determined by

$$Y = \frac{\text{number of reactions}}{\text{number of beam particles}} . \quad (3.9)$$

For a thin target with thickness dx , the yield can be calculated as a simple extension of Eq. 2.3:

$$Y = \sigma \frac{N_t}{A} = \sigma n_t dx \quad (3.10)$$

where N_t/A is the areal target density and n_t is the volume target density in nuclei per unit volume. As the nuclear beam travels through the target, the charged projectiles interact with the target nuclei and electrons and slow down due to a loss in energy. The amount of energy loss depends on the initial energy of the beam as well as the abundance and Z of the target nuclei. Thus, a convenient way to quantify the energy loss is through the definition of the stopping power

$$\zeta(E) = \frac{1}{n_t} \frac{dE}{dx} . \quad (3.11)$$

For a thick target, the yield can be found by integrating the expression for a thin target of Eq. 3.10 over each slice dx . If the initial energy of the beam is E_0 and the energy loss through the target is ΔE , then the yield of a thick target is given by

$$Y = \int \sigma n_t dx = \int_{E_0-\Delta E}^{E_0} \sigma(E) \frac{1}{\zeta(E)} dE . \quad (3.12)$$

For a Breit-Wigner resonance (Eq. 3.2) the expression for the yield is

$$Y = \int_{E_0-\Delta E}^{E_0} \frac{\lambda^2}{4\pi} \omega \frac{\Gamma_1 \Gamma_2}{(E - E_r)^2 + (\Gamma/2)^2} \frac{1}{\zeta(E)} dE . \quad (3.13)$$

In our consideration of a narrow resonance, the de Broglie wavelength, partial widths, and stopping power can be taken as their resonance values and factored out of the integral. Thus, the integral has an analytic solution

$$Y = \frac{\lambda_r^2}{2\pi} \frac{\omega\gamma}{\zeta_r} \left[\arctan\left(\frac{E_0 - E_r}{\Gamma/2}\right) - \arctan\left(\frac{E_0 - E_r - \Delta E}{\Gamma/2}\right) \right]. \quad (3.14)$$

In the case of an infinitely thick target ($\Delta E \rightarrow \infty$), the maximum yield for the resonance is reached

$$Y_{\max} = \frac{\lambda_r^2}{2} \frac{\omega\gamma}{\zeta_r}. \quad (3.15)$$

The bottom panel of Fig. 3.1 shows the resulting excitation function for different target thicknesses using Eq. 3.14. In an experiment, the excitation function is created by changing the beam energy between different experimental runs and plotting yield against energy. This dissertation contains experiments measuring resonances with both thin targets (Chap. 7) and thick targets (Chap. 11). Typically it is easiest to extract resonance strengths using a target whose energy loss is much larger than the width of the resonance so that the thickness appears infinite. In this way, the resonance strength can be calculated by determining the maximum yield of the excitation function and using Eq. 3.15.

There is an additional way to extract the resonance strength using the area under the excitation function. Here I will follow the derivation of Iliadis [16]. First we need to introduce two normalized functions to take into account some experimental factors. The first function $g(E_0 - E_i)$ is to account for the beam energy resolution and it is the probability that a particle has energy E_i when the mean beam energy is E_0 . The second function $f(E_i - E, E')$ is to account for beam energy straggling inside of the target and it is the probability that when a particle hits the target with energy E_i it will have an energy E at a depth E' . Folding these

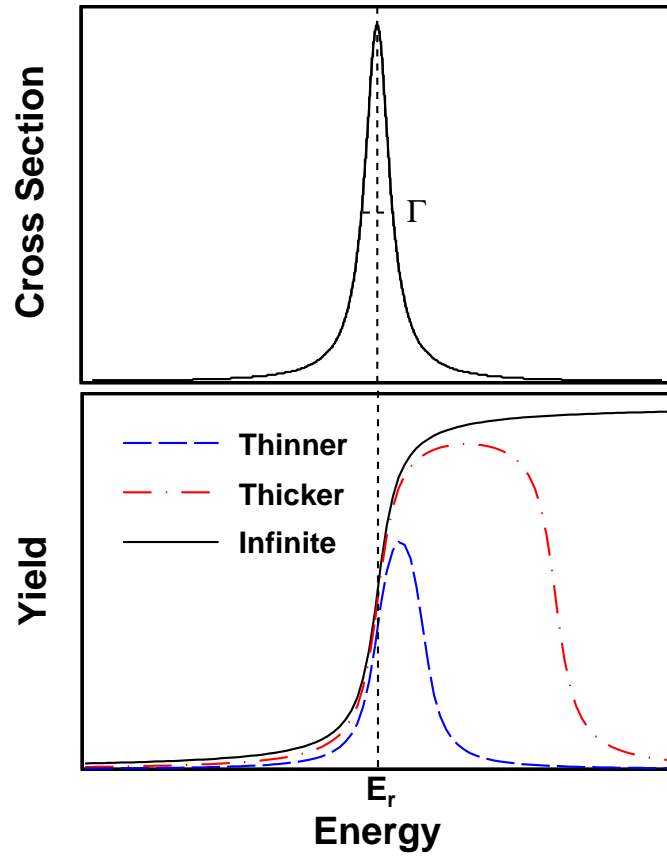


Figure 3.1: A Breit-Wigner lineshape with resonance energy E_r and width Γ (top panel). Expected excitation functions for the measurement of the resonance with different target thicknesses (bottom panel).

functions into Eq. 3.12, we get the general yield equation

$$Y(E_0) = \int_{E_0-\Delta E}^{E_0} dE' \int_0^\infty dE_i \int_0^{E_i} dE \left[\sigma(E) \frac{1}{\zeta(E)} g(E_0 - E_i) f(E_i - E, E') \right] . \quad (3.16)$$

To calculate the area underneath the excitation curve we put this entire expression inside of another integral:

$$A_Y = \int_0^\infty Y(E_0) dE_0 . \quad (3.17)$$

First, we factor out the stopping power assuming it is constant over the resonance. Second, the integral over E_0 is unity because from $g(E_0 - E_i)$, the probability of finding a beam particle with energy between 0 and ∞ is 1. Third, the integral over E_i is unity because from $f(E_i - E, E')$, the probability that a beam particle with initial energy E_i has energy between 0 and ∞ in the target is 1. This leaves

$$A_Y = \frac{1}{\zeta_r} \int_{E_0-\Delta E}^{E_0} dE' \int_0^\infty dE [\sigma(E)] = \frac{1}{\zeta_r} \Delta E \frac{\lambda_r^2}{2} \omega \gamma . \quad (3.18)$$

Thus, the area underneath the excitation function due to a resonance is independent of beam energy resolution and straggling. In fact, by substituting that the areal target density is equal to $n_t = \Delta E/\zeta$, it is not necessary to know the stopping power directly. The final result is

$$A_Y = n_t \frac{\lambda_r^2}{2} \omega \gamma . \quad (3.19)$$

3.2 Nuclear Statistical Model

At low excitation energies the levels of a nucleus are well spaced and their properties may be experimentally known. However, for capture reactions the states that are populated are typically at high excitation energies where there are many levels that overlap. Thus, instead of treating each level separately it becomes advantageous to take a statistical average over the resonances. Averaging over an energy region ΔE that contains many Breit-Wigner resonances, an energy averaged cross section can be calculated by

$$\langle \sigma_{12}(E) \rangle = \frac{1}{\Delta E} \int_{E-\Delta E}^E \sum_i \frac{\lambda^2}{4\pi} \omega \frac{\Gamma_1 \Gamma_2}{(E' - E_r)^2 + (\Gamma/2)^2} dE' \quad (3.20)$$

where the sum is over the number of Breit-Wigner resonances (n_{res}) of a specific total angular momentum J and parity Π . The sum over all J and Π will be put in at the end for the full solution. Manipulating this equation a little gives

$$\langle \sigma_{12}(E) \rangle = \frac{\lambda^2}{4\pi} \omega \frac{n_{res}}{\Delta E} \int_{E-\Delta E}^E \frac{\Gamma_1 \Gamma_2}{(E' - E_r)^2 + (\Gamma/2)^2} dE' . \quad (3.21)$$

First we can make note that the average level spacing is equal to the energy region divided by the number of resonances ($D = \Delta E/n_{res}$). Also, because the width of the resonances is much narrower than the energy region we are safe to take the limits of integration from 0 to ∞ and use the result of Eq. 3.6 to obtain

$$\langle \sigma_{12}(E) \rangle = \frac{\lambda^2}{4\pi} \omega \frac{2\pi}{D} \left\langle \frac{\Gamma_1 \Gamma_2}{\Gamma} \right\rangle . \quad (3.22)$$

It is important that the energy averaged cross section does not depend on the average of the individual widths $\langle \Gamma_i \rangle$ but depends on the average quantity $\langle \Gamma_1 \Gamma_2 / \Gamma \rangle$. Because of correlation between the widths of the entrance and exit channel it is necessary to introduce a width fluctuation correction defined by

$$\left\langle \frac{\Gamma_1 \Gamma_2}{\Gamma} \right\rangle = W_{12} \frac{\langle \Gamma_1 \rangle \langle \Gamma_2 \rangle}{\langle \Gamma \rangle} \quad (3.23)$$

with $\langle \Gamma \rangle = \sum_i \langle \Gamma_i \rangle$. This leaves an energy averaged cross section

$$\langle \sigma_{12}(E) \rangle = \frac{\lambda^2}{4\pi} \omega \frac{2\pi}{D} W_{12} \frac{\langle \Gamma_1 \rangle \langle \Gamma_2 \rangle}{\langle \Gamma \rangle} . \quad (3.24)$$

We are headed towards making a connection between the total reaction cross section obtained from averaging over many Breit-Wigner resonances to the cross section obtained from solving the nuclear scattering problem. To do this we need to first sum Eq. 3.2 over all exit channels $\sum_i \Gamma_i = \Gamma$ and take the energy average. The result is the total reaction cross section

$$\left\langle \sigma_1^{\text{tot}}(E) \right\rangle = \frac{\lambda^2}{4\pi} \omega \frac{2\pi \langle \Gamma_1 \rangle}{D} . \quad (3.25)$$

Next, for the sake of comparison we take the projectile and target to have $J = 0$ so that the statistical factor is simply related to the orbital angular momentum of the resulting state $\omega = 2\ell + 1$. This gives

$$\left\langle \sigma_1^{\text{tot}}(E) \right\rangle = \frac{\lambda^2}{4\pi} (2\ell + 1) \frac{2\pi \langle \Gamma_1 \rangle}{D} . \quad (3.26)$$

As mentioned, the total reaction cross section can also be obtained by solving the Schrödinger equation describing the interaction of the projectile nucleus and target. Much like light can be

refracted or absorbed upon striking a medium, the projectile can be scattered or absorbed by the target. This motivates the writing of the nuclear potential in the form of an optical model with a Coulomb term, a real term for elastic scattering, and an imaginary term for all other reaction channels. Solving the Schrödinger equation with this nuclear optical model potential gives the total reaction cross section as

$$\langle \sigma_1^{\text{tot}}(E) \rangle = \frac{\lambda^2}{4\pi} (2\ell + 1) \mathcal{T}_\ell \quad (3.27)$$

where \mathcal{T} is the transmission coefficient specifying the probability that the projectile will penetrate the potential barrier. Comparing the two equations we see that the relationship between the transmission coefficient and average partial width is given by

$$\mathcal{T}_i = \frac{2\pi \langle \Gamma_i \rangle}{D} . \quad (3.28)$$

Thus we can rewrite the average cross section of Eq. 3.24 to obtain the Hauser-Feshbach [59] formula with width fluctuation corrections:

$$\langle \sigma_{12}(E) \rangle = \frac{\lambda^2}{4\pi} \omega W_{12} \frac{\mathcal{T}_1 \mathcal{T}_2}{\sum_i \mathcal{T}_i} . \quad (3.29)$$

The Hauser-Feshbach reaction model is based on the independence hypothesis of Bohr [60], in which he proposed that the entrance channel and the exit channel are completely separate from each other. The idea is that the projectile and the target form a compound nucleus in an excited state and the nucleons of the compound nucleus share the energy. Due to the sharing of energy amongst the nucleons, compound nucleus reactions take place over a longer timescale than direct reactions and the nucleus “forgets” how it was formed. The

deexcitation of the nuclear state is therefore independent of the entrance channel and only depends on the exit channel branching ratios. However, this independence hypothesis is only true when the width fluctuation factor is equal to 1. There are several different models that estimate values of W_{12} and usually W_{12} differs from 1 only at low energies where only a few reaction channels are open [61]. At high excitation energies where many reaction channels are open, the cross section of Eq. 3.29 is safely factored into a production cross section and a decay probability given by the Hauser-Feshbach branching ratio $\mathcal{T}_2/\Sigma_i\mathcal{T}_i$.

As mentioned, nuclei have discrete experimentally known states at lower excitation energies and a continuum of states at higher energy. For a reaction channel to a discrete level the transmission coefficient simply equals \mathcal{T} , but for a reaction channel in the continuum there is an effective transmission coefficient about a region ΔE given by

$$\langle \mathcal{T} \rangle = \int_{E-\Delta E/2}^{E+\Delta E/2} \mathcal{T}(E') \rho(E') dE' \quad (3.30)$$

where ρ is the density of levels within the energy region with a specific J and Π . Thus to account for all energetically available states, the total transmission coefficient is given by

$$\mathcal{T} = \sum_i^{\nu} \mathcal{T}_i + \sum_j \int_{E^{\nu}}^{E^{max}} \mathcal{T}_j(E') \rho(E') dE' \quad (3.31)$$

where ν is the level up to which the experimental knowledge is complete and the integral goes up to the maximum state allowed. The reaction channels include the emission of particles and γ rays and their transmission coefficients are found using different methods. The transmission coefficients for particles are calculated by solving the Schrödinger equation with the proper nuclear optical model potential, and the transmission coefficients for emission

of γ rays are calculated using a radiative strength function $f_{X\lambda}(E_\gamma)$:

$$\mathcal{T}_{X\lambda}(E_\gamma) = 2\pi f_{X\lambda}(E_\gamma) E_\gamma^{2\lambda+1} . \quad (3.32)$$

The variable X describes the type of transition and is labelled E for an electric transition and M for a magnetic transition, and λ is the transition multipolarity equal to the amount of angular momentum that the γ ray carries away. There are various models for the radiative strength function and the models relevant to this thesis are described in Chapter 10.

So far we have limited ourselves to resonances with only a specific total angular momentum and parity. The result of Eq. 3.29 should include a sum over all possible resonances in the reaction to get the full cross section in the nuclear statistical model. Also, we will now introduce the explicit sums over angular momentum ℓ and spin s states available using the selection rules of angular momentum coupling. This gives the final Hauser-Feshbach formula with width fluctuation corrections:

$$\langle \sigma_{12}(E) \rangle = \frac{\lambda^2}{4\pi} \sum_{J\pi} \omega W_{12} \frac{[\sum_{\ell s} \mathcal{T}_1] [\sum_{\ell' s'} \mathcal{T}_2]}{\sum_i \sum_{\ell'' s''} \mathcal{T}_i} . \quad (3.33)$$

There are many inputs that go into the Hauser-Feshbach formulism, including nuclear properties such as masses, radii, and level densities, as well as the additional inputs of the optical model parameters and the radiative strength functions. Three of the most critical inputs for the production of the p nuclei in this thesis are the optical model potentials, nuclear level densities, and radiative strength functions, which all have an influence on the calculation of transmission coefficients. Further discussion of these three key quantities can be found in the chapters presenting the results of individual nuclear reactions.

3.3 Reciprocity Theorem

As mentioned in Sec. 1.4, the majority of reactions relevant for the production of the p nuclei are (γ, n) , (γ, p) , and (γ, α) reactions. While there are scientists who measure the photodisintegration reactions directly using photon beams [62], it is often simpler and more advantageous to experimentally measure the inverse capture reactions (n, γ) , (p, γ) , and (α, γ) . The cross sections of the forward and reverse reactions are related through the energy and number of states available in each channel. If we consider an arbitrary nuclear reaction $A + a \rightarrow B + b$, the relationship is given by the reciprocity theorem [63] also known as detailed balance:

$$\frac{(2J_A + 1)(2J_a + 1)}{1 + \delta_{Aa}} k_{Aa}^2 \sigma_{Aa \rightarrow Bb} = \frac{(2J_B + 1)(2J_b + 1)}{1 + \delta_{Bb}} k_{Bb}^2 \sigma_{Bb \rightarrow Aa} \quad (3.34)$$

where k is the wave number related to the de Broglie wavelength by $k = 2\pi/\lambda$. For a γ ray, the factor $(2J_\gamma + 1)$ is equal to 2 because there are two polarization states for photons.

In a typical experiment the target and projectile are both in their ground states, meaning that only the ground state cross section and the ground state reaction rate (Eq. 2.10) are measured. However, in the stellar environment particles may also be found in any of their low-lying excited states. The probability of finding a nucleus in an excited state i is given by the Boltzmann distribution

$$P_i = \frac{(2J_i + 1) e^{-E_i/kT}}{\sum_j (2J_j + 1) e^{-E_j/kT}} = \frac{(2J_i + 1) e^{-E_i/kT}}{G} \quad (3.35)$$

where G is the partition function. Using this Boltzmann distribution, the stellar reaction rate $\langle \sigma v \rangle^*$ can be calculated from the experimentally measured ground state reaction rate

$\langle\sigma v\rangle^{\text{g.s.}}$ using theoretical models such as the nuclear statistical model (Sec. 3.2) [64]. The ratio is given by the stellar enhancement factor

$$f^* = \frac{\langle\sigma v\rangle^*}{\langle\sigma v\rangle^{\text{g.s.}}} . \quad (3.36)$$

After using the stellar enhancement factor to turn the experimentally measured ground state reaction rate into the stellar reaction rate, detailed balance can be used to calculate the desired inverse reaction rate. The result is [16, 64]:

$$\frac{\langle\sigma v\rangle_{Bb\rightarrow Aa}^*}{\langle\sigma v\rangle_{Aa\rightarrow Bb}^*} = \frac{(2J_A + 1)(2J_a + 1)(1 + \delta_{Bb})}{(2J_B + 1)(2J_b + 1)(1 + \delta_{Aa})} \frac{G_A^n G_a^n}{G_B^n G_b^n} \left(\frac{M_A M_a}{M_B M_b}\right)^{3/2} e^{-Q/kT} \quad (3.37)$$

where M_i is the mass, Q is the reaction Q -value, and G_i^n is the partition function normalized to the ground state spin $G_i^n = G_i/(2J_i^{\text{g.s.}} + 1)$. For reactions where one of the particles is a photon, the decay constant λ_γ for the photodisintegration reaction is related to the inverse capture reaction by

$$\frac{\lambda_{B\gamma\rightarrow Aa}^*}{\langle\sigma v\rangle_{Aa\rightarrow B\gamma}^*} = \frac{(2J_A + 1)(2J_a + 1)}{(2J_B + 1)(1 + \delta_{Aa})} \frac{G_A^n G_a^n}{G_B^n} \left(\frac{M_A M_a}{M_B}\right)^{3/2} \left(\frac{\mu_{Aa} kT}{2\pi\hbar^2}\right)^{3/2} e^{-Q/kT} \quad (3.38)$$

where μ_{Aa} is the reduced mass of channel $A + a$.

A general level scheme of a capture reaction is shown in Fig. 3.2. The nuclei consist of discrete energy levels at low excitation energy and many levels in the continuum at high excitation energy. The ground state of the nuclei in the entrance and exit channel are offset by the Q value of the reaction. As previously mentioned, in the stellar environment nuclei can be present in any of their excited states. However due to the Q value of the reaction, more excited states are energetically accessible to the nuclei in the $B + b$ channel than the

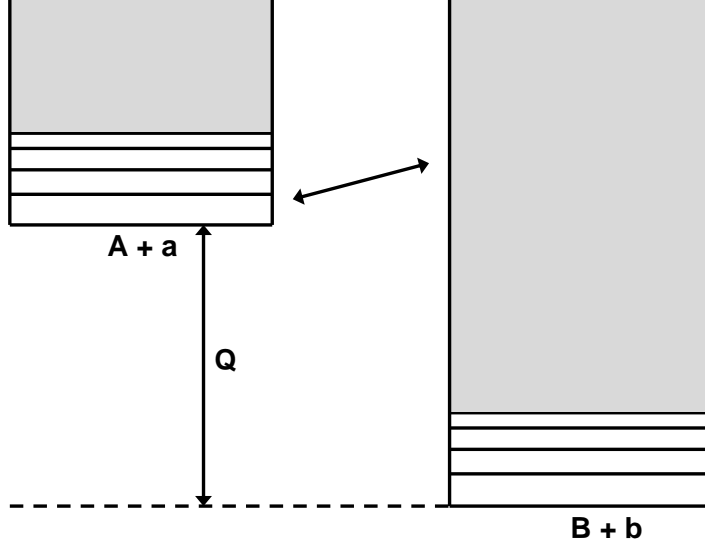


Figure 3.2: General level scheme for a forward and reverse reaction with a certain reaction Q value. The nuclei have discrete states at lower excitation energy and a continuum of states and higher excitation energy.

nuclei in the $A + a$ channel. This means that the stellar enhancement factor (Eqn. 3.36) will be larger for reactions in the direction of negative Q value. Since experimental measurements are done on nuclei on the ground state, it is more advantageous to measure reactions in the direction of positive Q value where the ground state contribution to the stellar reaction rate is largest. For reactions in the p process, the capture reactions typically have positive Q values and the photodisintegration reactions have negative Q values. Therefore, measuring the p process capture reactions provide a closer representation of the stellar rate, and then the inverse photodisintegration rate can be determined by Eqn. 3.38.

Another factor contributing to the stellar enhancement factor being closer to 1 in the direction of positive Q value is the relative energy of the particles after photodisintegration. The lower the relative energy of the particles, the higher the excitation energy of the level in the daughter nucleus that is populated. However for (γ, p) and (γ, α) reactions, there must be a high enough relative energy to penetrate through the Coulomb barrier. This means that

the proton or α particle carries away most of the energy, and the ground state of nucleus A is populated more often than any of the excited states. By measuring (p,γ) and (α,γ) reactions from this ground state of nucleus A , an accurate representation of the stellar rate can be obtained in laboratory.

Chapter 4

Experimental Techniques

Although the production of the p nuclei has remained a major open question in the field of nuclear astrophysics for nearly 60 years, very little experimental data exists for reactions relevant to the p process. Less than 40 (p, γ) and 20 (α , γ) reaction cross sections have been measured to date, and all of these measurements have been performed on stable nuclei [36]. For an improved understanding of the p process, additional data on (p, γ) and (α , γ) reactions and their inverse photodisintegration reactions is required, especially for reactions involving radioactive nuclei. This chapter contains a discussion of existing methods for measuring capture cross sections followed by the experimental techniques and procedures used in this thesis work.

4.1 Measuring the Cross Section

As discussed in Sec. 2.1, the cross section of a reaction is calculated by

$$\sigma = \frac{N_{\text{reactions}}}{N_{\text{projectiles}} n_{\text{targets}}} . \quad (4.1)$$

Methods of determining both the number of projectiles impinging on the target and the areal target density will be discussed later in this chapter, and for now we will focus on the various techniques for measuring the number of reactions that occurred.

4.1.1 Activation

The vast majority of the measured (p,γ) and (α,γ) reaction cross sections relevant for the p process have been performed using the activation technique (for example Ref. [65]). In activation, determining the number of reactions that occurred is done through the offline detection of the γ rays or X rays [66] emitted when the reaction products decay. This means that the target material is first irradiated with a beam of protons or α particles to create radioactive reaction products and then moved to a separate setup to detect the decay radiation. As evident by its popular use, there are many benefits to using the activation technique to measure a capture cross section. First, because the detection is done outside of the irradiation there is no beam induced background or complicated deexcitation level schemes to consider. Also, the detectors can be placed in a closely packed geometry around the target material to maximize detection efficiency and shielded by lead walls to reduce the background radiation. Finally, each reaction product decays with radiation at unique energies, so it is possible to do several cross section measurements in one irradiation [67, 68].

Although the activation technique has been very successful, it is limited in its application to reactions that meet a certain set of requirements. First of all, it is necessary to use target nuclei that are stable or long-lived so that they can be properly irradiated. This constraint alone is enough to rule out measuring many of the important reactions relevant for the p process. It is also required that the reaction products are radioactive and that their decay radiation is well-known with intense enough γ rays or X-rays to allow for detection. In addition, the half-lives of the reaction products must be long enough to allow for the transition from irradiation to detection but short enough that decays occur within the timescale of the experiment. If the half-life of the reaction products is too long for traditional detec-

tion methods, the number of reaction products can still be determined by combining the activation technique with accelerator mass spectrometry (AMS), for example Ref. [69].

4.1.2 γ -Induced Reactions

Experimental measurements of reaction cross sections relevant to the p process can also be performed using γ -ray beams to measure the photodisintegrations directly. The γ rays may be produced by Compton scattering laser light off of an electron beam to create an approximately monoenergetic beam of γ rays [70] or by decelerating an electron beam in a target to create Bremsstrahlung radiation. [71]. Due to the difficulty of measuring the protons or α particles freed by photodissociation, the number of reactions that occurred is typically determined by offline counting as is done in the activation technique [72].

The photodissociations that take place in the laboratory occur on nuclei in their ground state, which may be only a small contribution to the stellar environment where nuclei may photodissociate from any of their low lying excited states. As mentioned in Sec. 3.3, the ground state contribution to the stellar rate is much higher in the direction of positive Q value and therefore it is oftentimes more advantageous to measure the capture reactions instead of the photodisintegration reaction in laboratory. However, measuring reactions with γ beams still provides constraints for theoretical models.

4.1.3 In-Beam Methods

The number of capture reactions that occurred can also be measured by surrounding the target with γ -ray detectors to detect the prompt γ rays emitted in the reaction. Hence the term *in-beam* methods. When the capture occurs, the projectile and target form a new

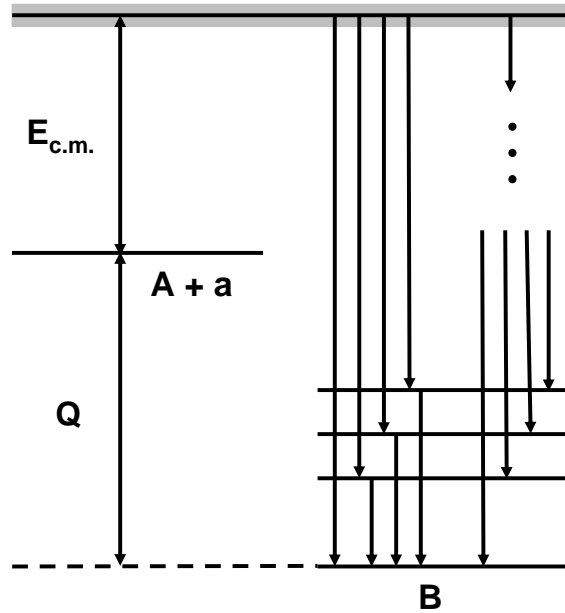


Figure 4.1: In a capture reaction, the projectile and target form an excited state in the produced nucleus equal to the Q value of the reaction plus the center of mass energy of the projectile and target system. The populated state is often at high excitation energies where many resonances overlap.

nucleus in an excited state with energy $E_x = E_{c.m.} + Q$, where $E_{c.m.}$ is the center of mass of the projectile and target system and Q is the reaction Q value (Eqn. 2.19). As discussed in Chap. 3, the excited state will deexcite in less than 10^{-12} seconds through the emission of γ rays and possibly particles if it is at an energy above the particle emission threshold. The deexcitation will continue until the final nucleus is in its ground state or long-lived isomeric state. By surrounding the target position with γ -ray detectors, it is possible to deduce how many times the reaction product of interest was produced.

For (p,γ) and (α,γ) reactions relevant to the p process, the populated excited state is typically at high energies where many resonances overlap (see Fig. 4.1). The deexcitation of the populated excited state occurs through any of the available γ -ray cascades, and the energy and intensity of all the γ rays are typically not known beforehand. If there is one

particular transition that all the γ -ray cascades pass through or if the percentage of cascades that pass through a particular transition is known, then simply detecting and analyzing this dominant transition will provide how many times the reaction product of interest was produced [73]. However, this is most often not the case and instead it is necessary to detect all of the transitions to deduce the number of reactions.

4.1.3.1 Angular Distributions Method

One in-beam method of calculating the (p,γ) and (α,γ) reaction cross section is by determining the number of transitions originating from the entry state, or alternatively determining the number of transitions populating the ground state. Because of incomplete knowledge of the γ -ray cascades before performing the experiment, it may be necessary to analyze all of the γ -ray transitions to build up a level scheme of nuclear excited states. This analysis can be quite complex as a typical spectrum often has a few hundred transitions to consider, including room background and beam-induced γ rays [74]. Once all ground-state transitions are identified, the angular distribution of each transition is fit with a sum of Legendre polynomials given by

$$A_0 \sum_l c_l P_l(\cos\theta) \quad (4.2)$$

where P_l are the Legendre polynomials and c_l are their coefficients. The A_0 term is unique for each transition to the ground state and is used to scale the fitting function to match the data. Once all scaling factors are determined, the reaction yield is calculated by

$$Y = \frac{N_{\text{reactions}}}{N_{\text{projectiles}}} = \sum_{i=1}^N A_0^i \quad (4.3)$$

where the sum i corresponds to the transition from excited state i to the ground state. The angular distribution method has been successfully used in several measurements [73, 74, 75] but it relies on the detection and correct assignment of each γ -ray transition. Any transition that is not detected or misidentified may lead to an incorrect value of the cross section. This may be especially problematic for high energy γ rays emitted from the entry state which have low efficiency for being detected.

4.1.3.2 γ -Summing Technique

In this dissertation, the reaction yield was experimentally determined by an in-beam method known as the γ -summing technique [76, 77]. As opposed to using several smaller detectors that can distinguish individual γ -ray transitions, the γ -summing technique implements a large volume γ -ray detector that covers as much of the 4π solid angle around the target as possible. The large size and angular coverage of the detector provide a high efficiency for detecting γ rays so that when the populated state deexcites (see Fig. 4.1), any γ ray that is emitted has a high probability of being detected. The goal of the γ -summing technique is to detect each γ ray regardless of the deexcitation cascade and angular distribution, and sum them up to the full energy of the populated state. This creates a “sum peak” at an energy $E_{\Sigma} = E_{c.m.} + Q$. Fig. 4.2 shows the difference between using a small-sized detector (top panel) and a large 4π detector (bottom panel) for a simplified level scheme. By using a large volume detector, the individual transitions are summed into a single sum peak that can be analyzed. The number of counts in the sum peak is directly related to the number of reactions that occurred through the detector’s γ -summing efficiency. A discussion of the γ -summing efficiency can be found in Chap. 6.

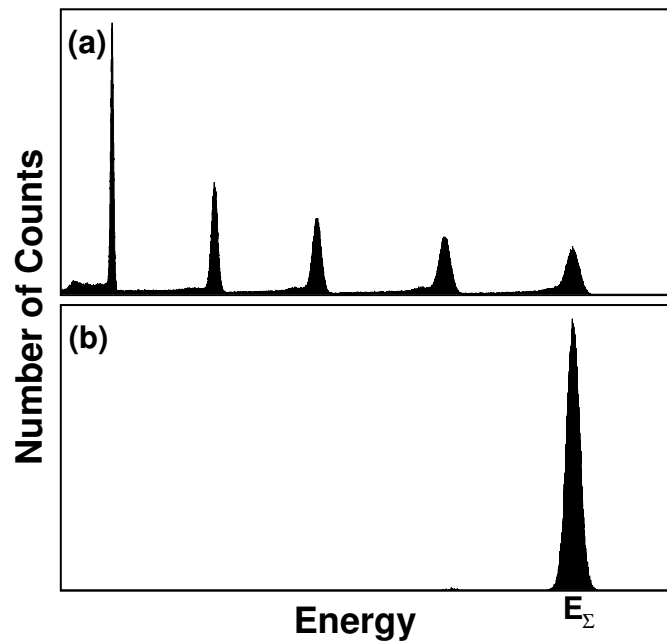


Figure 4.2: Difference in γ -ray spectra between a (a) small-sized detector and (b) large 4π detector for a simplified level scheme. The result of using a large 4π detector is the summation of all γ rays into a single sum peak whose intensity is directly related to the number of reactions that occurred.

4.1.4 Techniques in Inverse Kinematics

Techniques using proton, α , and γ beams are limited to reactions involving long-lived isotopes that have chemical properties favorable for creating a target. To overcome this limitation, reactions can be performed in inverse kinematics with heavy isotope beams impinging onto targets containing protons, α particles, or virtual γ rays in the field of a heavy target nucleus (Coulomb dissociation [78]). With the advancement of accelerator technologies and the development of radioactive isotope beams, measurements in inverse kinematics are now feasible and crucial for extending the experimental scope of capture reaction measurements. Whereas in regular kinematics the low energy protons or α particles lead to a negligible recoil velocity of the produced nucleus after capture, in inverse kinematics the momentum of the heavy projectile leads to a significant recoil velocity.

Thus far, the majority of proton and α capture reactions measured in inverse kinematics have been measured using recoil mass separators [79, 80, 81, 82, 83]. In this technique, the heavy isotope beam passes through a target, typically a hydrogen or helium gas, and a recoil separator comprised of a series of magnets and electric fields is used to separate the reaction products from the incoming beam. Successful (p,γ) and (α,γ) measurements using recoil separators have been performed for lighter masses where mass separation is easier to achieve. Only recently have efforts been made to expand the capability to measurements on heavier nuclei [84].

Additionally, storage rings have been used to measure (p,γ) and (α,γ) relevant to the p process in inverse kinematics [85]. This technique involves injecting the heavy isotope beam into a ring that maintains the nuclei in a large orbit. Somewhere along the storage ring there is a proton or α target where the capture reaction may occur. Since the reaction products

have a different charge and mass than the incoming beam they are not suited for orbiting the ring and can be detected with the proper placement of a detector.

The in-beam γ -ray detection methods discussed in Sec. 4.1.3 can also be used to measure (p,γ) and (α,γ) reactions in inverse kinematics. As in regular kinematics, the reaction product will be formed at the position of the target and the deexcitation γ rays promptly emitted. However, due to the recoil velocity of the produced nucleus in inverse kinematics, the γ rays are emitted from a moving source. As with any waves emitted from a moving source, the detected γ ray frequencies, and hence their energies, are subject to the Doppler effect. A γ ray detected in the forward direction has a higher energy than if emitted at rest, and a γ ray detected in the backward direction has a lower energy than if emitted at rest. The difference in energies is given by the Doppler shift

$$E_0 = \frac{1 - \beta \cos \theta}{\sqrt{1 - \beta^2}} E \quad (4.4)$$

where E_0 is the energy of the emitted γ ray, E is the detected energy in the laboratory, $\beta = v/c$ is the velocity of the recoil compared to the speed of light, and θ is the angle between the direction of the recoil velocity and the detector. Taking the velocity of the recoil and the position of the detector into account, it is possible to convert the detected energy into the actual emitted γ -ray energy.

4.2 Target Production and Characterization

4.2.1 Evaporation

This dissertation contains measurements of (p,γ) and (α,γ) reactions on 11 different targets. Most of the targets used were borrowed from previous nuclear science experiments and did not have to be fabricated. However, the ^{27}Al targets and isotopically enriched ^{74}Ge target did not exist beforehand and were produced through the process of evaporation. The general procedure of evaporation involves the heating of material until it evaporates and travels in gaseous form to a surface where it cools and condenses into a thin film. Before performing the procedure it is necessary to put the evaporation chamber under vacuum by pumping out the gas molecules to obtain a low pressure. This allows the evaporated material to travel without interaction to the deposition surface. Typical pressures used in this dissertation were 10^{-6} Torr.

When performing the evaporation, it is advantageous to track the amount of material that is being deposited to control the thickness of the target being created. To do this, evaporators are typically equipped with thickness monitors that deduce the thickness of deposited material based on the oscillation frequency of a quartz crystal. The general idea is that as evaporated material builds up on the quartz crystal, the oscillation frequency of the crystal decreases. The exact mathematical relationship between the change in frequency and change in mass depends on the properties of quartz and the area of the crystal, as well as the density and acoustic impedance of the evaporated material [86, 87]. The acoustic impedance is a property of the material itself and quantifies the opposition of the material to wave propagation. If the acoustic impedance of the material is different from the quartz crystal, there will be reflection of the wave which will impact the oscillation frequency. Thus,

for accurate target thickness measurements the user should input the density of the material and the ratio of the acoustic impedances between the material and quartz to the thickness monitor. There are useful tables of density and acoustic impedance ratios (Z-ratios), for example in Ref. [88].

The oscillation frequency of the quartz crystal provides a measure of the amount of material deposited on the crystal, but this may be different than the thickness of the evaporated target. To obtain the correct target thickness, the quartz crystal may be placed the same distance from the evaporation source as the target, or a calibration “tooling” factor can be used to make the correction. The tooling factor can be calculated by assuming the evaporation is occurring at a point source and estimating the ratio in solid angle covered by the quartz crystal and the target.

The evaporation of the ^{27}Al targets was performed at the NSCL’s detector lab. The evaporation was done onto 3” by 2” glass microscope slides coated with a mixture of 50% water and 50% Teepol. Aluminum pellets were placed in the evaporator crucible and heated with an electron gun until they melted and evaporated. Passing electric current through a tungsten filament causes the filament to heat and emit electrons. The electrons are then accelerated and directed in an arc onto the aluminum material through the use of electric and magnetic fields. Water cooling was used outside of the crucible to carry away excess heat. As mentioned in the preceding paragraphs, the target thickness was monitored with an oscillating quartz crystal taking into account the properties for aluminum with a density of 2.7 g/cm^3 and Z-ratio of 1.08. The evaporation was done at an approximately steady rate of 8 \AA/s until the desired thickness of 3 k\AA was reached, at which point the current to the filament was turned off.

After venting the evaporation chamber with nitrogen air and removing the glass slides,

it was necessary to transfer the thin layer of aluminum from the glass slides to the target frames. The target frames used in this thesis were aluminum rectangles, approximately 20mm by 17mm in size with a 12mm diameter hole in the center. Transferring the thin evaporated aluminum layer onto the target frames was done by floating the aluminum layer onto the surface of distilled water and then “fishing” them out with the target frames. First, a sharp blade is used to divide the evaporated aluminum into the desired size rectangles while still on the glass microscope slides. Then, slowly inserting the glass slide at an angle into a container of distilled water, the aluminum gradually peels back from the glass slide and floats on the water’s surface. The reason the aluminum does not stick to the glass slide is because of the thin layer of Teepol underneath coating the slide. While performing the floatation, it is helpful to be patient and use a stand to hold the glass slide in place and a lab jack to slowly raise the water level. Once the aluminum square breaks free along the cut lines and is floating on the surface of the water, it can be guided to a target frame, mounted, and removed from the water. In order to avoid ripping the aluminum, it is helpful to remove it at an approximately 90 degree angle from the water’s surface. It is also important to try to avoid wrinkling the aluminum as it is mounted on the target frame to maintain a layer of uniform thickness. Upon drying, the aluminum will cling to the target frame and the result is a self-supporting aluminum target for use in experiments. Ref. [89] contains more details and pictures of the use of an electron gun evaporator and the floatation of targets.

On the other hand, the ^{74}Ge target was produced from 97.55% enriched germanium powder using the University of Notre Dame’s evaporator. Due to the limited supply of enriched powder, the procedure was first performed multiple times with natural germanium powder to test the setup. Approximately 100 mg of the germanium powder was placed in a tungsten boat and heated by passing electric current through the tungsten material. The

germanium was simultaneously evaporated onto aluminum, carbon, and tantalum backings. The evaporation was carried out until all of the germanium powder was evaporated and based on the change in oscillation frequency of the quartz crystal, the thickness was estimated to be approximately $470 \mu\text{g}/\text{cm}^2$. A more accurate and detailed analysis of the target thicknesses is discussed in the following section.

4.2.2 Thickness Measurements

It is necessary to know the number of target nuclei per unit area in order to determine a reaction cross section. This quantity can be determined by impinging an ion beam onto the target. As ions travel through the target material, they will lose energy through interactions with electrons in the target as well as by scattering off of target nuclei. By measuring the outgoing energy of the incident ions or scattered particles at a well-defined scattering angle, it is possible to deduce what elements are present in the target, how many atoms of each element there is, and how the elemental abundances change with depth.

The energy loss due to electrons depends on the initial ion energy as well as the number of electrons in the target. Since the number of electrons depends on a combination of the Z and abundance of nuclei in the target, a measurement of the energy loss of the incident ion or scattered particle provides information on how many target nuclei are present. On the other hand when scattering off of a target nucleus, the incident ion will impart some of its momentum to the nucleus, and both nuclei will recoil at an angle. After the collision, the energy of both particles is related to the two masses of the colliding nuclei and the scattering angle. As expected, a head-on collision will result in a larger transfer of momentum than a more glancing collision. Thus, the energy of each particle after a collision provides information on the mass of the target nucleus. Finally, the scattering cross section is different

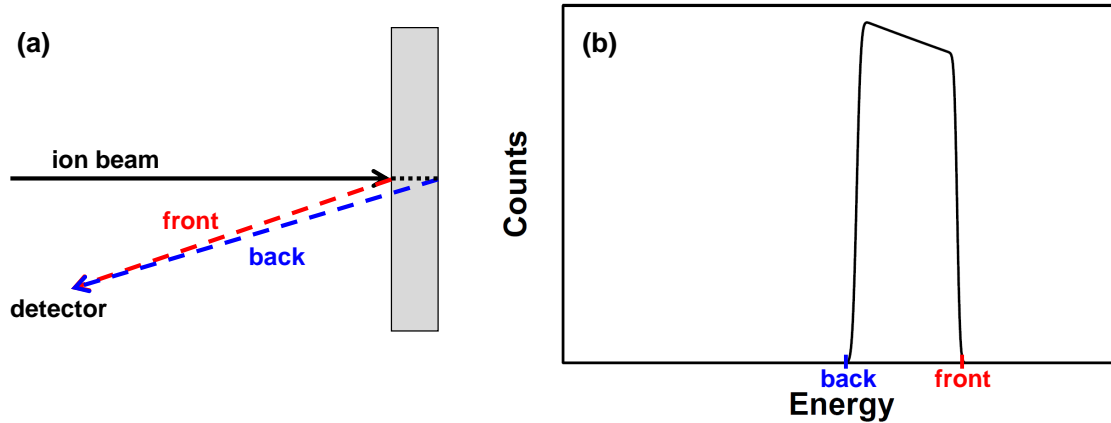


Figure 4.3: Schematic drawing of the RBS technique with (a) an ion beam backscattering off of target nuclei and (b) the energy spectrum of backscattered particles detected by the detector.

for each element, so the number of scatters off of each element provides information on the relative abundance of various components in the target.

The most widely used technique of ion beam analysis is Rutherford Backscattering Spectrometry (RBS) [90], named for the famous experiments by Ernest Rutherford and collaborators in which they deduced the presence of the positively charged nucleus by measuring the backscattering of α particles off of metal foils [91]. In the same way, RBS consists of bombarding a target with an ion beam with MeV energy and measuring the energy of the backscattered ions. As mentioned, the backscattered ions have an energy related to the energy immediately before the collision multiplied by a kinematical factor determined by the masses of the two nuclei participating in the collision and the scattering angle. Ions that backscatter off of the front surface of the target will be detected at the maximum backscattered energy, but ions that backscatter off of nuclei in the interior of the target will be detected at lower energy because the ions lose energy both on the way in and out of the target, mostly through interactions with target electrons. Therefore, there will be a spread in detected energies from the maximum corresponding to backscattering off of nuclei at the

front of the target to a minimum corresponding to backscattering off of nuclei at the rear of the target. The width of the energy spread is the energy loss of the ion through the target and provides the thickness of the target. See Fig. 4.3 for a schematic drawing of the RBS technique.

One drawback of the RBS technique is that it is not very sensitive to light elements in the target. This is due to the kinematics of the collision, in which heavier incident ions do not backscatter off of light nuclei. Instead of using backwards angles, light target nuclei can be characterized by measuring the incident ions and scattered particles at forward scattering angles in the elastic recoil detection (ERD) technique [92]. By rotating the target so that the ion beam has a small incident angle to the surface of the target (see Fig. 4.4), the greatest depth sensitivity can be achieved with scatterings at the front of the target having maximum detected energy and scatterings at the rear of the target having minimum detected energy.

4.2.2.1 Experimental Details

The target thickness measurements were carried out at the Hope College Ion Beam Analysis Laboratory (HIBAL) on five separate days over the course of two years. Both RBS and ERD methods were used, and the general layout of the two methods can be seen in Fig. 4.4. A ^4He ion beam with current between 1.5 and 20 enA was accelerated to energies between 2.9 and 5.4 MeV using the Pelletron accelerator and impinged onto the surface of the target at the center of the HIBAL scattering chamber. The scattered particles were detected by two 50 mm^2 silicon surface barrier detectors, one fixed at a backwards angle of $\theta = 168.20^\circ$ a distance of 4" from the target, and one that was rotated to a forward angle of $\theta = 30.0^\circ$ a distance of 2.75" from the target. Collimators 0.2" in diameter were placed in front of both detectors to reduce the solid angle coverage as well as to shield the edge of the silicon detectors

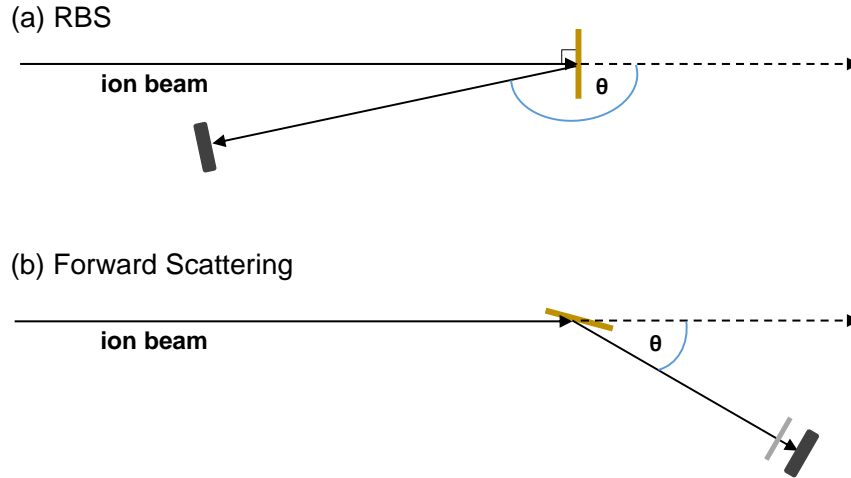


Figure 4.4: General layout of the HIBAL scattering chamber. (a) The RBS detector is located at $\theta = 168.20^\circ$, a distance 4.0" from the target, with a 0.2" diameter collimator in front of it. (b) The rotating detector was placed at a scattering angle of $\theta = 30.0^\circ$, a distance 2.75" from the target, with a 0.2" diameter collimator in front of it. The target was then rotated 75.0° and a 15.0μ aluminum foil placed in front of the detector.

where the response may be irregular. The RBS detector had a resolution of approximately 30 keV and the ERD detector had a resolution of approximately 40 keV in the energy region of interest.

The RBS technique was used to characterize all of the targets, whereas the ERD technique was only used for the titanium hydride foil. For the RBS measurements only scattered helium nuclei are detected as all other scatterings are kinematically prohibited. However, for the ERD measurements of the titanium hydride foil, forward scattering of helium, titanium, and hydrogen into the detector is possible. Therefore, a $15 \mu\text{m}$ thick aluminum foil was placed in front of the silicon detector to completely stop the helium and titanium nuclei, only allowing hydrogen nuclei knocked out of the titanium hydride foil to be detected. In order to provide a profile of how the H concentration in the foil was changing with depth, the foil was rotated 75° so that the beam was incident at 15° to the surface.

The analysis of the data was performed using SIMNRA software [93]. SIMNRA was

Table 4.1: ^4He beam energies and silicon surface barrier detector energy calibrations used at HIBAL over the course of five different experiments.

Experiment	Beam Energies (keV)	Detector	Slope (keV/ch)	Offset (keV)
I	2946	RBS	5.889	6.854
II	2977, 3484, 5195	RBS	5.930	8.881
III	2969	RBS	5.928	-0.301
IV	3486, 5282	RBS	5.930	3.837
V	3465, 4059, 3804	RBS	5.892	-0.576
V	3465, 4059, 3804	ERD	6.612	0.245

specifically developed for ion beam analysis of thin foils and contains the necessary kinematics, energy loss, energy straggling, and scattering cross sections to fit the data. The user simply needs to input the experimental information such as the scattering geometry, beam properties, detector response, and a best guess of the composition and thickness of the target. Then SIMNRA can be used to fit the simulated composition and thickness to the experimental data using a chi-square minimization routine.

4.2.2.2 Calibrations

The energy calibration of the silicon detectors was done with a quadruple α source consisting of α particles emitted from the decay of ^{148}Gd , ^{239}Pu , ^{241}Am , and ^{244}Cm , with energies of 3.183, 5.157, 5.486, 5.805 MeV, respectively. The α calibration measurements were typically performed the morning before and evening after the RBS and ERD measurements. The slope and offset of the calibrations used in the analysis can be found in Table 4.1.

After performing the detector energy calibration, the ^4He beam energy was precisely determined by measuring the scattering off of a heavy target with known composition. The majority of the time the beam energy determination was performed with a layer of gold on glass, but for convenience it was once performed with a thick piece of tantalum. By using a

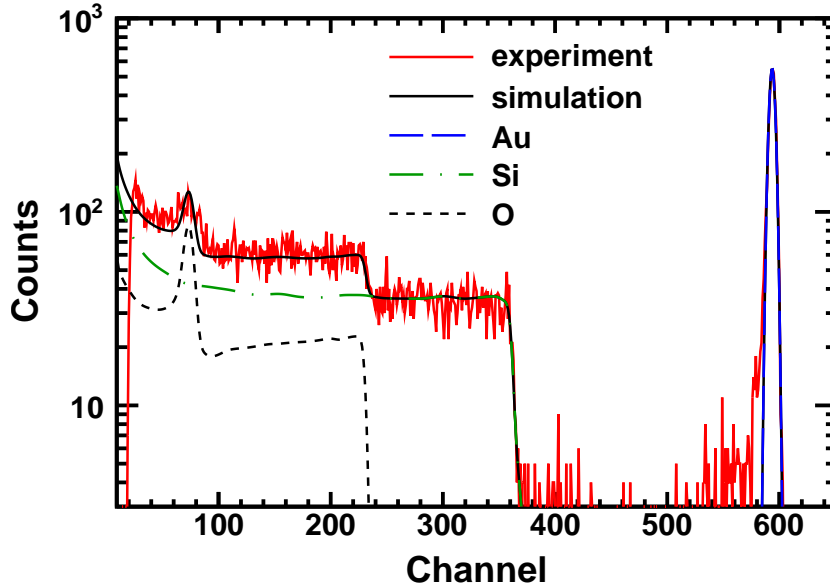


Figure 4.5: Comparison of the SIMNRA fit to an experimental gold-on-glass measurement. The precise beam energy of $E_{\alpha} = 3804$ keV was determined by fitting the front edge of the gold peak in the spectrum.

known heavy nucleus, the maximum energy of the scattered ions off of the front surface is well known and can be used to deduce the beam energy. This method is more precise than reading off the terminal voltage of the electrostatic accelerator. An example SIMNRA fit for a gold-on-glass run is shown in Fig. 4.5, where the beam energy was determined by fitting the front edge of the gold peak in the spectrum. The beam energies used in the various experiments are contained in Table 4.1.

4.2.2.3 RBS Analysis

After obtaining the beam energy, the RBS spectra can be fit to obtain the target thickness and composition. Spectra for nine of the targets can be seen in Fig. 4.6. The spectra are dominated by a large plateau corresponding to the target layer of interest, and the width of the plateau determines the thickness of the target. Some of the spectra also have contributions from other layers or impurities in the target. It was determined that many of

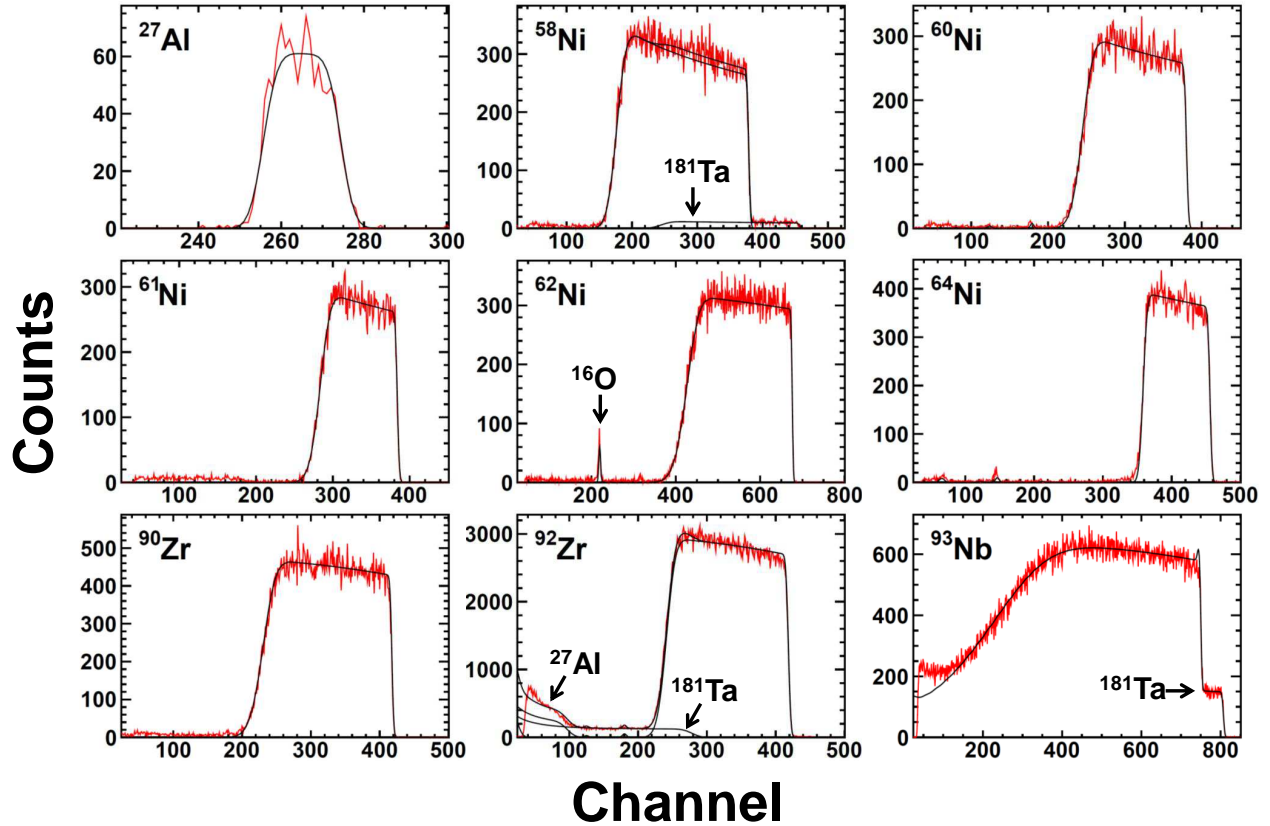


Figure 4.6: SIMNRA fits to RBS spectra of nine of the targets used in this dissertation. The resulting thicknesses are given in Table 4.2.

the targets have a very thin layer of oxygen and carbon on their surface, for example the spike at lower energies in the ^{62}Ni spectrum corresponds to ^4He scattering off of ^{16}O on the front surface of the target. Other contaminants seen were ^{27}Al and ^{181}Ta , for example in the ^{58}Ni , ^{92}Zr , and ^{93}Nb spectra.

One of the more difficult spectra to fit was the RBS measurement taken with the enriched ^{74}Ge layer evaporated onto a tantalum backing. The thickness of the germanium layer caused the germanium plateau to overlap with the contribution from tantalum in the spectrum. Also there was an unexpected plateau corresponding to tungsten, which was attributed to the accidental evaporation of some of the tungsten boat during the evaporation of the enriched ^{74}Ge powder. The best fit to the spectrum can be seen in Fig. 4.7 and was obtained with

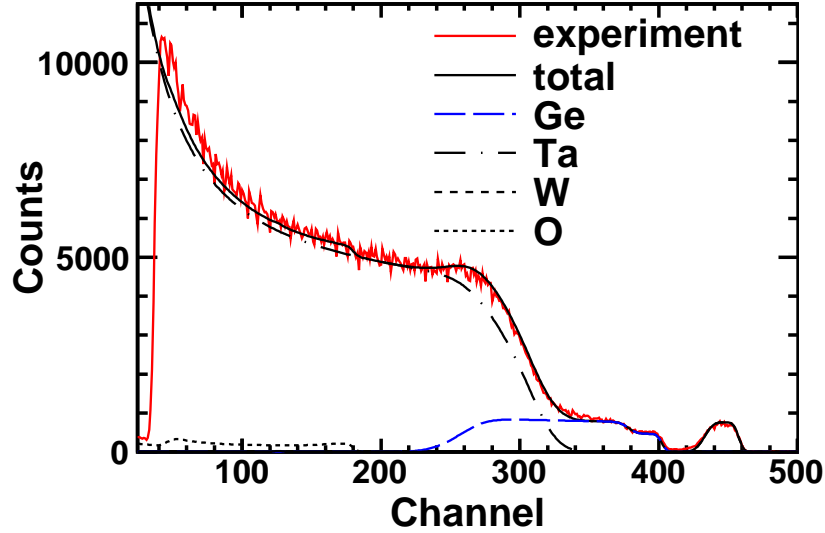


Figure 4.7: SIMNRA fit to the RBS spectrum of enriched ^{74}Ge on a tantalum backing.

a tantalum backing, a layer of germanium, and thin layer of germanium and tungsten on the surface. This indicates that the evaporation of the tungsten boat occurred towards the end of the evaporation procedure. The final values for all the target thicknesses used in this thesis can be found in Table 4.2.

4.2.2.4 ERD Analysis

The composition and thickness of the titanium hydride foil was determined by using both RBS and ERD techniques. The RBS measurements are more sensitive to the number of titanium nuclei in the target and the ERD measurements are more sensitive to the number of hydrogen nuclei in the target, so combining the two techniques provides the full composition of the target. The measurements were taken at three different locations on the foil and then added together for maximum statistics. By taking into account the difference in solid angle of the two detectors, the same target thickness and composition should be able to describe both the RBS and ERD spectra. The solid angle coverage of one of the detectors is approximately $\Omega \approx A/d^2$, where A is the active area of the detector and d is the distance of

Table 4.2: Target thickness values.

Isotope	Number of Nuclei in Target ($\times 10^{18}$ nuclei/cm 2)	Total Target Thickness ($\mu\text{g}/\text{cm}^2$)
^{27}Al	1.574 ± 0.079	70.5 ± 3.5
^{58}Ni	9.665 ± 0.483	930 ± 47
^{60}Ni	6.693 ± 0.335	666 ± 33
^{61}Ni	5.060 ± 0.253	512 ± 26
^{62}Ni	15.748 ± 0.787	1619 ± 81
^{64}Ni	5.260 ± 0.263	558 ± 28
^{74}Ge	2.703 ± 0.135	340 ± 17
^{90}Zr	6.472 ± 0.324	966 ± 48
^{92}Zr	6.199 ± 0.310	946 ± 47
^{93}Nb	21.485 ± 1.074	3315 ± 166
^1H	3.581 ± 0.358	232 ± 23

the detector from the target. Since the detectors have identically sized collimators in front of them, they have identical active areas and the difference in solid angles of the two detectors is approximately

$$\Omega_{ERD} \approx \frac{d_{RBS}^2}{d_{ERD}^2} \Omega_{RBS} \quad (4.5)$$

where the experimental distances of $d_{RBS} = 4''$ and $d_{ERD} = 2.75''$ provide a scaling factor of 2.1157.

Fig. 4.8 shows the resulting fit for both the RBS and ERD spectra. To achieve this fit, the target was broken down into 4 layers with different ratios of titanium and hydrogen. The outside layers have a hydrogen concentration down to 49.5% and the inner layers have a hydrogen concentration up to 64%, indicating that there is more H in the interior of the target. The total hydrogen thickness from the fit is 3.581×10^{18} nuclei/cm 2 . To determine an uncertainty in the number density of hydrogen nuclei, the standard uncertainty from SIMNRA of 5% was combined with the uncertainty from the experimental beam current between the

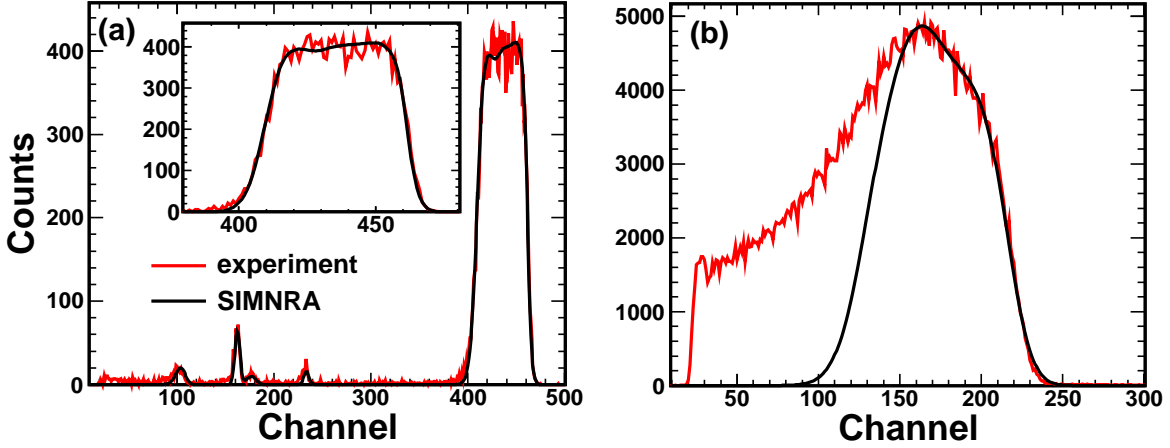


Figure 4.8: SIMNRA calculations compared to experimental data for (a) RBS and (b) ERD spectra of the titanium hydride foil.

RBS and ERD measurements. This extra uncertainty arises because the experimental setup at Hope College at the time of the measurements could only record one detector at a time, so the RBS and ERD measurements had to be taken at separate times. This in itself is not a problem, but there was no direct measure of the beam current so comparison of the RBS and ERD measurements could have been difficult if there were large fluctuations in the beam. However, there was multiple signs of beam current stability during the measurements. One indication of beam stability was that two gold-on-glass runs at $E_{\alpha} = 3804$ keV taken approximately 40 minutes apart show only a 2.5% difference in the beam current. Also, there was charge collection and integration performed at the back of the scattering chamber which had a maximum difference of 3.0% for the RBS measurements. Therefore, even though the first RBS and last ERD measurements were taken approximately 40 minutes apart, we do not expect the beam current to change by more than 5%. Fitting the spectra for the expected beam current $\pm 5\%$ led to a hydrogen thickness of $3.580 \pm 0.360 \times 10^{18}$ nuclei/cm².

As seen in Fig. 4.8, the fit of the ERD spectrum matches the height and shape of the experimental data well, but does not match the data at lower energies at all. As previously

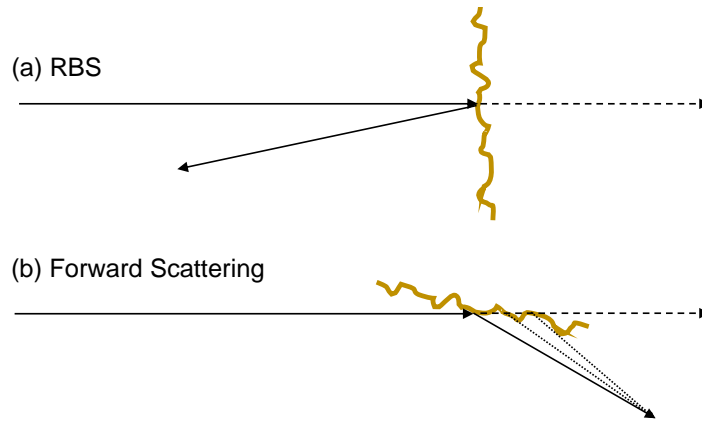


Figure 4.9: Diagram depicting how wrinkles in the titanium hydride foil may lead to a seemingly larger thickness in the ERD spectra than in the RBS spectra.

mentioned, the width of the spectrum is determined by the energy loss through the target, which in this case is dominated by the energy loss due to the titanium. Due to the fit of the RBS spectrum, the amount of titanium in the target is well known and thus the width of the spectrum in the ERD spectrum is well constrained. Therefore, the difference between simulation and experimental data for the ERD spectrum is expected to be due to another hydrogen source.

A possible explanation for the extra hydrogen contribution in the ERD spectrum is that the many wrinkles in the foil, which are clearly visible to the naked eye, and the small incident angle of the beam combine to make an effectively thicker target. Instead of scattering off of a smooth target and producing the expected result, the beam scatters off a target with many creases that has a larger effective thickness. Figure 4.9 shows how the wrinkles and small scattering angle of ERD measurements may add extra contributions to the spectrum. Because the RBS data is taken with the beam at 90° to the target, the wrinkles in the target do not change the RBS spectrum. Simply by adding a titanium hydride layer that is less than the deduced thickness of the foil, the result in Figure 4.10 is obtained. Adding

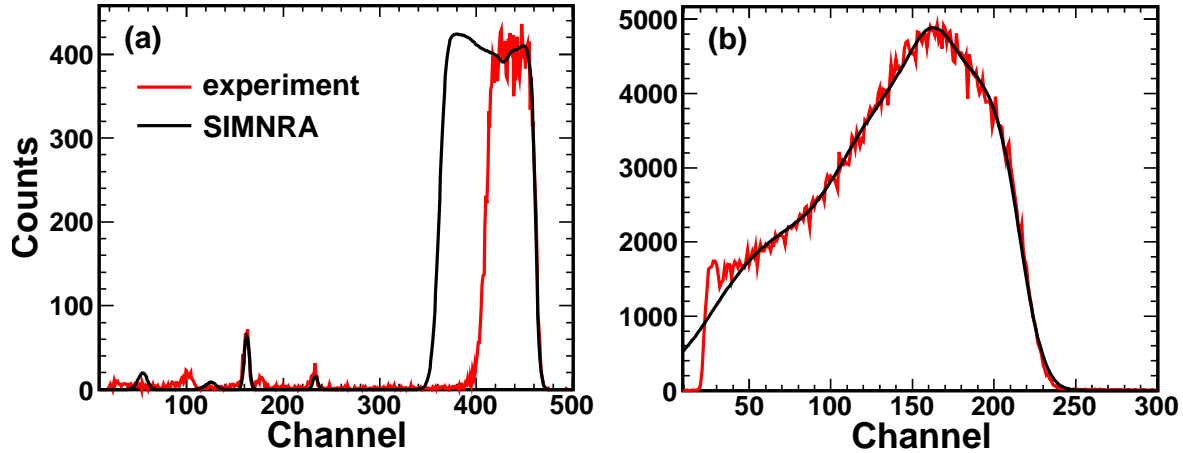


Figure 4.10: Same as Fig. 4.8 with the minimum additional titanium hydride material needed to match the ERD spectrum.

additional titanium hydride does not change the result.

4.3 Experimental Setup

Since the goal of this dissertation was the measurement of (p,γ) and (α,γ) reactions at astrophysical energies, it was necessary to use a facility that provides ion beams at astrophysical energies. Although Michigan State University has recently developed the capability to provide lower energy beams, at the time of these measurements the only beams available traveled at approximately 40% the speed of light and would be far too energetic for capture reactions in astrophysics. The idea of slowing these fast beams down with a series of degraders was considered, but the spread in both beam position and energy as a result of using the degraders was deemed too large for a measurement. Therefore, the experiments were performed at the Nuclear Science Laboratory of the University of Notre Dame instead. A layout of the laboratory at Notre Dame can be seen in Fig. 4.11 with the beams originating from the ion sources (labels 1 and 2), accelerated by the Tandem Van de Graaff accelerator



Figure 4.11: Layout of the Nuclear Science Laboratory at the University of Notre Dame.

(label 3), and sent into the experimental area where the capture reactions were measured (label 6). The important operating principles of these main experimental components will be discussed in the rest of this chapter.

4.3.1 Beam Production

Two different ion sources were used at the University of Notre Dame. One is exclusively used to produce beams of helium nuclei, while the second ion source is used for all other available beams. For injection into the FN Tandem accelerator, the nuclei must initially be negatively charged in order to be accelerated towards the positive terminal. The two sources achieve these negative ion beams through different methods.

The Helium Ion Source (HIS) consists of a cavity known as the duoplasmatron and a charge exchange canal filled with lithium. First, neutral helium atoms are fed into the

duoplasmatron from a gas cylinder. Also inside of the duoplasmatron is a tungsten filament that emits electrons when heated as a result of passing electric current through it. The electrons emitted from the filament ionize the helium into positive ions, ${}^3\text{He}^+$ and ${}^4\text{He}^+$, which are extracted and sent into the lithium charge exchange region. The lithium exchange region is filled with a lithium reservoir which is heated to produce lithium vapor. Since lithium has a low ionization energy and gives up its valence electron easily, some of the ${}^3\text{He}^+$ and ${}^4\text{He}^+$ ions that pass through the lithium vapor pick up two electrons to become negative ions ${}^3\text{He}^-$ and ${}^4\text{He}^-$. These negative ions can then be injected and accelerated by the FN Tandem accelerator.

On the other hand, the Multi-Cathode Source of Negative Ions by Cesium Sputtering (MC-SNICS) [94] is used for all other nuclear beams. The desired material is first packed into a small disk cavity known as the cathode. In principle, any material that can be packed into a cathode can be accelerated and hence the wide variety of beams that originate from this source. As many as 40 cathodes can be loaded at one time and rotated into place when needed. As the source's name indicates, the negative ions are produced by cesium sputtering. This is accomplished by heating a reservoir of cesium to produce cesium vapor in the same region as the cathode. Like lithium, cesium has a low ionization energy and loses its valence electron easily to form a positive ion. These positive cesium ions are accelerated towards the cathode and cause some of the cathode material to sputter upon striking it. A thin layer of cesium condenses and builds up on the cathode so that when the cathode material is sputtered it passes through the cesium layer and can pick up an electron to become negatively charged. The negatively charged ions can then be injected into the FN Tandem accelerator. The beams produced with this ion source in this dissertation were ${}^1\text{H}$, ${}^{27}\text{Al}$, and ${}^{58}\text{Ni}$.

4.3.2 Acceleration

Once the ions of interest leave the source, they are accelerated to the desired energies using the FN Tandem accelerator. The accelerator consists of a metal electrode called the terminal at its center which can be charged up to a maximum of +10 MV, surrounded by a large tank of gas which helps to insulate the terminal to prevent electrical sparking. The initial acceleration is from the negatively charged ions being attracted to the large positive terminal voltage and accelerating towards it. Once inside of the terminal, the ions pass through a thin carbon foil which strips some of the electrons and leaves a positively charged ion beam. The positively charged ion beam is repelled by the large positive voltage of the terminal and this creates the secondary acceleration. The dual acceleration towards and away from the terminal is why it is referred to as a “tandem” accelerator. Initially the ion has a charge of -1 and it leaves the accelerator in some charge $+q$ so that the total energy after the FN Tandem accelerator is

$$E = E_{\text{source}} + 1V + qV \quad (4.6)$$

where E_{source} is the small injection energy from the ion source and V is the terminal voltage. The charge $+q$ can take on a range of values from a charge state distribution as the ion beam passes through the carbon stripper foil.

The charging of the terminal is done with Pelletron chains that move electrically isolated metal pellets in a loop from a terminal pulley to a grounded drive pulley located near the outer part of the accelerator. By charging the metal pellets by induction both at the terminal pulley and at the drive pulley, it is possible to create a system where the metal pellets are positively charged as they enter the terminal and negatively charged when they leave the terminal. This allows for more efficient charging of the terminal. The FN Tandem accelerator

uses two Pelletron chains on either side of the terminal to create a large positive voltage. A more detailed description of the Pelletron charging system is found in Ref. [95].

The large voltage drop from the positively charged terminal to the grounded outer tank is broken down into steps through the use of resistors with large resistances of 300 M Ω that are evenly spaced. Because they are evenly spaced, there is a uniform voltage drop and the ions experience a uniform acceleration as they move along the acceleration tubes. During the experiment, it is necessary to maintain a constant terminal voltage so that there are no fluctuations in beam energy. This is done with the use of metal needles called corona points that can be brought closer or farther from the terminal to control the amount of charge on the terminal. The distance of the corona points to the terminal can be automatically adjusted to maintain constant terminal voltage. More details can be found in Ref. [96].

4.3.3 Ion Selection

After leaving the FN Tandem accelerator, the beam consists of a mixture of ions due to the various materials originating from the ion source, as well as different charge states due to the effect of passing through the carbon stripper foil. The selection of the ion beam of interest is done through the use of an analyzing magnet. For any charged particle moving perpendicular to a uniform magnetic field, the Lorentz force deflects the particle into a circular arc. Combining the Lorentz force ($F = qvB$) and centripetal force ($F = pv/r$), the radius of the circular arc is given by

$$r = \frac{p}{qB} \tag{4.7}$$

where r is the radius, p is the momentum of the ion, q is the charge of the ion, and B is the strength of the magnetic field. To make it to the experimental endstation, the ion must

travel the radius defined by the geometry of the beam pipe passing through the analyzing magnet. Since the momentum of the ion is given by the desired beam energy, and the charge state is typically selected to maximize the number of ions, the strength of the magnetic field must be adjusted so that the ion can make it to the experimental endstation. Once the field of the analyzing magnet is set, ions with the correct momentum to charge ratio make it through, while ions with too low or too high of a ratio get bent in a circular arc that is too small or too large, respectively. Slits at the end of the analyzing magnet can be open and closed to help select the ion of interest as well as to control the total number of beam particles making it to the experimental endstation.

At the University of Notre Dame, the magnetic field strength of the analyzing magnet is measured with Nuclear Magnetic Resonance (NMR) [97]. NMR works on the principle that when particles with magnetic moments and angular momentum are placed in a magnetic field, their magnetic moment precesses around the applied magnetic field with a frequency called the Larmor frequency given by

$$f = \gamma B \tag{4.8}$$

where f is the precession frequency, γ is the gyromagnetic ratio, and B is the magnetic field. With a gyromagnetic ratio of 42.576 MHz/T, protons are ideal for measuring magnetic field strengths up to 2.0 T (for example Ref. [98]), and that is what was used for this dissertation. Measuring the proton NMR frequency in the field of the analyzing magnet provides the very precise beam energy equal to (assuming $c = 1$ units)

$$KE = \sqrt{p^2 + m^2} - m \quad \text{and} \quad p = \frac{f r q}{\gamma} \tag{4.9}$$

where Eqn. 4.7 and Eqn. 4.8 were combined to determine the momentum p , and m is the

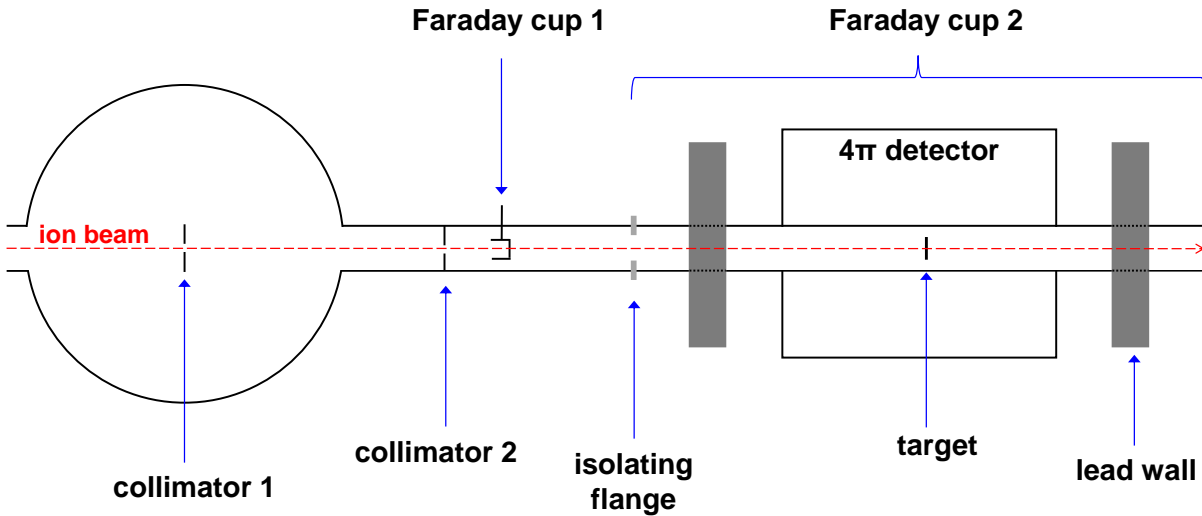


Figure 4.12: Experimental setup for the cross section measurements performed in this dissertation. The dimensions are not to scale.

rest mass of the ion beam. Typical uncertainties in this beam energy with the FN Tandem accelerator and analyzing magnet are around 2 keV.

4.3.4 Experimental Endstation

Upon leaving the analyzing magnet, the ion beam is directed into the experimental hall along any one of the experimental beam lines. For all of the measurements contained in this thesis, the ion beam was sent to the beam line where the “R2-D2” scattering chamber is housed (label 6 of Fig. 4.11). The experimental setup can be seen in Fig. 4.12 with the ion beam moving through the various components from left to right. For beam tuning purposes, two circular collimators were used. The collimator at the center of the R2-D2 scattering chamber was on an adjustable drive with options for a collimation to a beam diameter of 3, 6, or 10 mm. Further downstream was the second collimator with options for diameters of 3 or 10 mm. By reading the beam current deposited on the collimators it was possible to steer the beam until the minimum amount of current was deposited on both collimators. In

this scenario, the beam would be passing through the center of both collimators and thus would also hit the center of the target.

Besides measuring the beam current on the collimators, the beam current was also measured with two Faraday cups. The first Faraday cup was located immediately after the second collimator and could be inserted and removed from the beam line to both stop the ion beam if necessary as well as measure the current. The second Faraday cup was the entire last 1.2 m of the beam line, and therefore was electrically isolated with an insulating flange from the rest of the beam line. When the ion beam impinged on the target, electrons were emitted from the target position so that any charge collected only from the target frame was not equal to the charge carried in the beam. However, by using a long Faraday cup, all of the charge including the secondary electrons was collected to ensure an accurate beam current reading. The collected charge from the second Faraday cup was sent to the input of a digital current integrator that emitted an output pulse every time that 10^{-10} C in charge was deposited by the beam. Using the output of the digital current integrator and knowing the charge state of the ion beam, it is possible to calculate the total number of beam nuclei by

$$N_{\text{projectiles}} = N_{\text{pulses}} \frac{10^{-10} \text{ C}}{1 \text{ pulse}} \frac{1 \text{ projectile}}{q * e} \quad (4.10)$$

where q is the charge state of the beam and e is the elementary charge.

As previously mentioned, the reaction yield was determined by surrounding the target with a large 4π detector to implement the γ -summing technique. More details on this detector will be discussed in Chap. 5. To shield the detector from beam induced γ rays emitted from the beam striking an upstream collimator or the downstream beam stop, two lead walls were constructed on either side of the detector.

Chapter 5

The SuN Detector

5.1 Design

The major goal of this dissertation was the development of a new experimental program to measure (p,γ) and (α,γ) reactions using the γ -summing technique (Sec. 4.1.3.2) at the National Superconducting Cyclotron Laboratory (NSCL) at Michigan State University. Although there were already several existing γ -ray detectors at the NSCL, through GEANT4 simulations (see Sec. 5.5) it was determined that no configuration of the existing detectors was ideal for implementing the γ -summing technique. Thus, it was decided to design a new detector to meet the requirements.

When designing the detector, several important factors needed to be considered. First, the γ -summing technique relies on having a high γ -ray detection efficiency. This means having a large volume of material that can be used to detect γ rays while covering as much of the 4π solid angle as possible. Also, because many of the reactions of interest involve radioactive nuclei, it was necessary to have the capability of performing the measurements in inverse kinematics where the γ rays are emitted in-flight due to the velocity of the produced nucleus. As mentioned in Sec. 4.1.4, this creates a Doppler shift in the γ -ray energy with the energy of the γ rays emitted in the forward direction getting enhanced by the Doppler factor and the energy of the γ rays emitted in the backward direction getting reduced. Therefore, the second constraint on the detector was that it was necessary to introduce segmentation

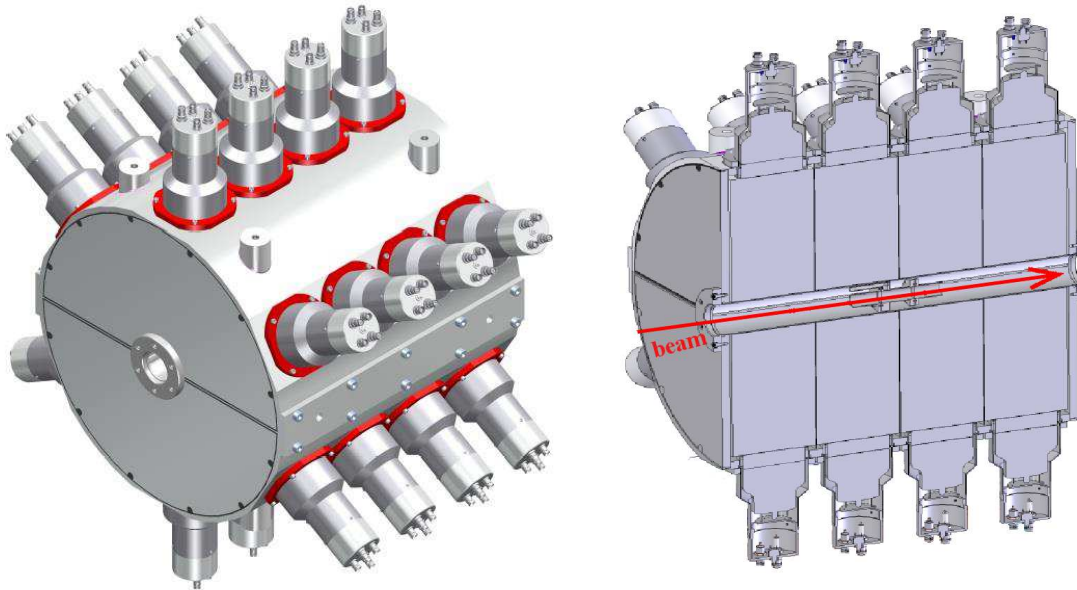


Figure 5.1: The Summing NaI (SuN) detector.

in the design to identify which direction a γ ray was emitted to perform a successful Doppler reconstruction of the energy. The third constraint was simply to stay within the project's budget.

Although other materials have better energy resolution, higher intrinsic efficiency, and better timing properties, sodium iodide with trace amounts of thallium is a highly-efficiency, cost-effective material for the detection of γ -rays and it can be built into unique shapes and sizes [99]. Cesium iodide has similar efficiency at a similar cost, however there is not much experience in making large volume crystals of CsI. Therefore, the final design was built with NaI(Tl), which is similar to other 4π detectors that have been used in nuclear physics experiments before (for example Ref. [100]). Balancing segmentation with detection efficiency, it was decided to have a total of eight segments with four on the top and four on the bottom. The detector was named the *Summing NaI (SuN)* detector, constructed by SCIONIX, and arrived at the NSCL in February 2011.

As seen in Fig. 5.1, SuN is a cylindrical detector with 16 inches of NaI(Tl) in length and 16 inches in diameter. There is a 4.5cm borehole along the axis so that the beam can enter and impinge on a target mounted at the center of the detector. It is comprised of eight large semicylindrical crystals that are each completely surrounded by a reflective layer of polytetrafluoroethylene 0.25 mm in thickness. Each crystal is also encased in an aluminum frame with the verticle plates having a thickness of 0.5 mm and the horizontal plates having a thickness of 0.75 mm. These dimensions mean that the four crystals in each half of the detector are separated by a total distance of 1 mm, and the flat surfaces of the crystals in the top and bottom halves of the detector are separated by a total distance of 2 mm. Therefore, each of the eight segments is optically isolated from its neighbor and can operate as an individual detector. The crystals are read out by three photomultiplier tubes to maximize light collection, which creates a total of 24 photomultiplier tubes in the design. As mentioned, the detector consists of a top half and a bottom half, which allows for easier mounting onto the beam line for experiments.

5.2 Detection

The nearly 4π angular coverage of SuN allows the vast majority of γ rays emitted from the target to interact with one or more of the eight crystals. Upon interacting with a crystal, the γ -ray energy is turned into electron energy in the NaI(Tl) in one of three ways: the photoelectric effect, pair production, or Compton scattering. At low energies, it is most probable that photoelectric absorption will occur, where the γ -ray energy is completely used to free a bound electron from an atom and give the electron some kinetic energy. The empty orbital left by the free electron is quickly filled, and an X-ray or Auger electron is

emitted. At energies larger than twice the rest mass of an electron, it is most probable that pair production will occur, where all of the γ -ray energy is used to create an electron and positron pair plus their kinetic energy in the electric field of the nucleus. The positron will quickly annihilate with an electron and emit two 511 keV γ rays which may or may not also interact with the crystals. Lastly, at intermediate energies, it is most probable that Compton scattering will occur, where the γ ray scatters off an electron at a random angle and imparts some of its energy to the electron. Both the electron and scattered γ ray can continue to interact with the crystal. In any case, the end result of all three important interactions is the transfer of γ -ray energy to the kinetic energy of free electrons. Ideally, all of the γ -ray energy will be deposited in SuN's crystals but sometimes energy is lost, for example if an annihilation or Compton scattered γ ray leaves SuN undetected, or if a γ ray interacts with the inactive reflector and aluminum layers.

As the free electrons move around the crystal, their negative charge causes them to interact with the atoms in the crystal and lose kinetic energy. Additional electrons are excited from their bound sites in the lattice (valence band) to an energy high enough to freely move about the crystal (conduction band). This process is known as exciting electrons across the band gap and it leaves a positively charged hole in the lattice. By doping the sodium iodide crystal with thallium, impurities are introduced to the crystal that have lower ionization energies than the other sites in the lattice. Because these impurities lose their valence electrons more easily, any hole in the lattice drifts to the site of the impurity. When an electron in the conduction band recombines with the hole in the valence band in a neutral configuration, visible light is emitted. In NaI(Tl) the visible light is emitted with a distribution in wavelengths centered at 415nm. Because the states in the impurity are at a lower energy than the other sites in the lattice, the light is at a wavelength that passes

through the crystal mostly without interaction.

Because NaI(Tl) turns radiation into visible light, it is classified as a scintillator. This important property was discovered in 1948 [101] and since that time it has remained an important material in the detection of radiation. As with many other scintillators, there is an interesting feature of NaI(Tl) detectors known as phosphorescence. This feature arises when instead of immediately emitting light upon recombination, the electron and hole recombine into an excited electronic state which cannot immediately transition to the ground state. Instead, these states rely on thermal excitations to move the electron up to a higher state that can transition to the ground state. Thus, phosphorescence increases the total detection time and it can be a problem in high count rate experiments.

By surrounding the NaI(Tl) crystals with a reflective layer, the light travels about the crystal until it impinges upon one of the three photomultiplier tubes (PMTs). The PMTs are capped with a thin material called the photocathode that emits electrons when hit by the light via the photoelectric effect. By applying a voltage to create an electric field inside of the PMT, the newly freed electrons can be accelerated to hit a dynode which emits several more secondary electrons. Using a series of dynodes allows a few electrons produced in the photocathode to be multiplied to a large number of electrons. The SuN detector uses Photonis' XP6342 PMTs which have 10 stages of electron multiplication. For the average voltage applied to the XP6342 PMT a gain of 2.4×10^5 is achieved. Thus, by collecting the electrons after the last multiplication stage, there is a significant electrical current that can be processed by the acquisition system.

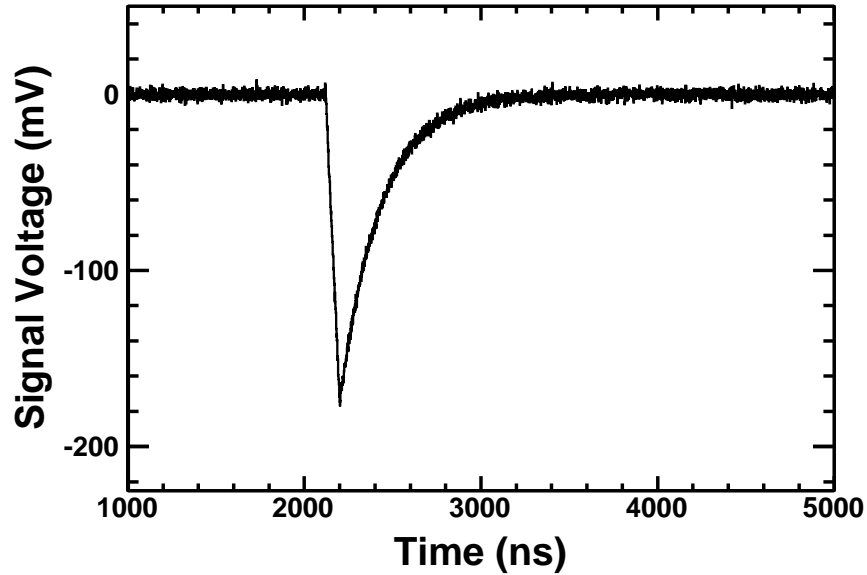


Figure 5.2: Typical signal from one of SuN's PMTs.

5.3 Data Acquisition

The main goal of any data acquisition system is to extract and record the important information carried in each detector signal, most notably the time and deposited energy of an event in the detector. A data acquisition system should also provide the capability to group information that corresponds to the same physical event together, and may include the possibility to reject information that does not meet a user-defined requirement. As with all detectors, the electric signal from each of SuN's PMTs is a continuous distribution of voltage as a function of time. When there is no energy deposited in SuN the signal is at its baseline value. However, there are always some fluctuations from the baseline value, referred to as noise. Noise can have a number of sources, for example from random thermal emission of electrons inside of the PMT. When some form of radiation deposits energy in SuN, scintillation light will be produced that is collected by the PMT and converted into a large number of electrons. The current of electrons causes the voltage of the signal to rise

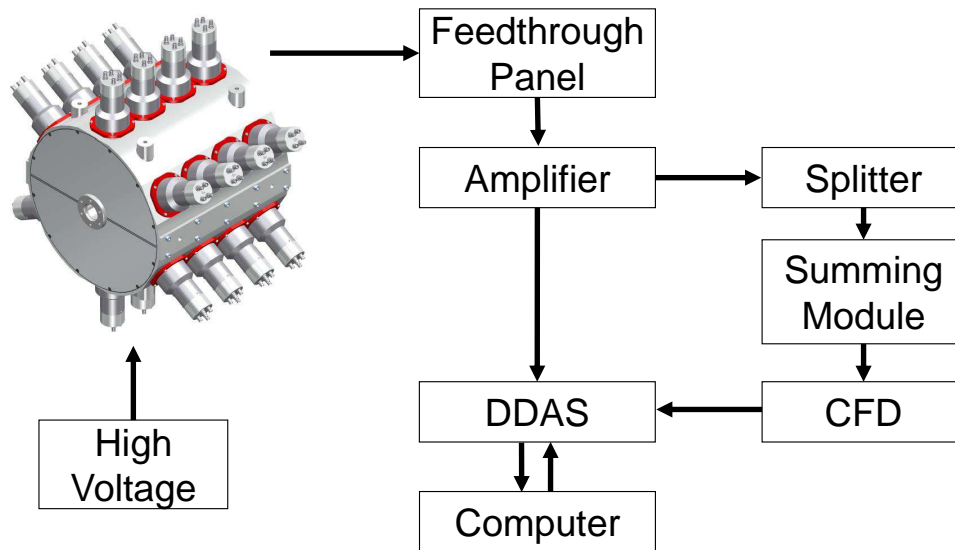


Figure 5.3: Diagram of SuN’s data acquisition system.

in a “pulse” (see Fig. 5.2). The signal pulse has a characteristic rise time followed by an exponential decay back to the baseline value. In SuN the pulse rise time is approximately 80ns and the decay constant of the exponential decay is approximately 230ns. Both the height and area underneath the pulse depend on the amount of energy deposited in SuN, and the front edge of the pulse contains important timing information. A general schematic for SuN’s data acquisition system is shown in Fig. 5.3, and the processing of SuN’s signals with this data acquisition system will now be discussed in more detail.

5.3.1 PMT signals

First of all, the voltage to each of the 24 photomultiplier tubes is applied through a WIENER MPOD crate with two ISEG high voltage modules. The crate is connected to an ethernet cable with a unique IP address so that it can be controlled through a webpage using SNMP commands. Communicating to the crate through a webpage is user friendly and provides

detailed information on each channel. The use of the webpage is also advantageous because it provides a convenient way for the user to power the crate on and off, change the voltage of individual PMTs, and control the voltage ramping speed. The use of SNMP commands allows for the use of automatic procedures to control the voltages applied to the PMTs, for example an automatic gain matching procedure. Although SuN's PMTs can withstand a maximum voltage of +1200V, typical experimental values for this thesis were approximately +800V.

The signals from each PMT get sent to an amplifier built by Pico Systems. However, before reaching the amplifier the 24 individual cables pass through a feedthrough panel with the purpose of sending the signals into two ribbon cables. It is most convenient to arrange the setup so that signals from the top half of SuN pass through one ribbon cable and signals from the bottom half of SuN pass through the other. These ribbon cables are plugged into the input of the amplifier and the signals get split into three different outputs. One of the outputs provides prompt unattenuated signals, while the remaining two outputs provide signals that are delayed and attenuated. In this thesis, one of the outputs was fed directly into the NSCL Digital Data Acquisition System (DDAS), while another output was used to create an external trigger signal.

5.3.2 NSCL DDAS

As mentioned, signals from the amplifier get fed directly into the NSCL Digital Data Acquisition System (DDAS). In this thesis, both the attenuated and unattenuated outputs were used at different times for this purpose. A nice description of the NSCL DDAS can be found in Ref. [102] and the most relevant information will be repeated here. The DDAS setup for SuN consists of three PIXIE-16 modules that are housed in an XIA crate. Each module

has 16 channels that take the continuous signal coming from a PMT and converts it into its digital representation through the use of an analog-to-digital convertor (ADC). The ADCs in SuN's setup are Analog Devices AD9432 12-bit 100 MSPS ADCs. The acronym MSPS stands for mega-samples per second and it means that the voltage of the signal gets converted to a digital number 100 million times every second, or equivalently that the conversion takes place every 10×10^{-9} seconds (10ns). The ADCs have two gain settings that allow for a maximum voltage height of 0.50V and 2.22V [103]. Since the ADC has 12-bits, the digital voltage value can take on any one of $2^{12} = 4096$ different possible values between 0V and 0.50V or 2.22V depending on the gain setting. For maximum resolution, it is best to have the signal pulses take up as much of the ADC range as possible, which is why SuN uses the 0.50V full-scale gain setting. NSCL DDAS requires positive signals for processing, so the original negative polarity signal from SuN first gets inverted.

Signal triggering and energy extraction in NSCL DDAS is done using digital trapezoidal filters. The general idea of extracting the energy carried in a signal pulse using a trapezoidal filter is shown in Fig. 5.4 using a signal step function. Because the height of the voltage step is directly related to the energy deposited in the detector, the goal is simply to find the height of the pulse. However, due to random fluctuations in the signal, better energy resolution is achieved by averaging over many digitized points on the top of the voltage step and subtracting an average over many digitized points at the bottom of the voltage step. Thus, there are three time windows to consider; the time range to average over on the top of the voltage step, the time range to average over at the bottom of the voltage step, and the time gap between the two regions. In NSCL DDAS, the user can define two timing parameters t_{peak} and t_{gap} , so that the averaging over the top and bottom of the voltage step take place in a time window t_{peak} and they are separated by the time t_{gap} . For any digitized

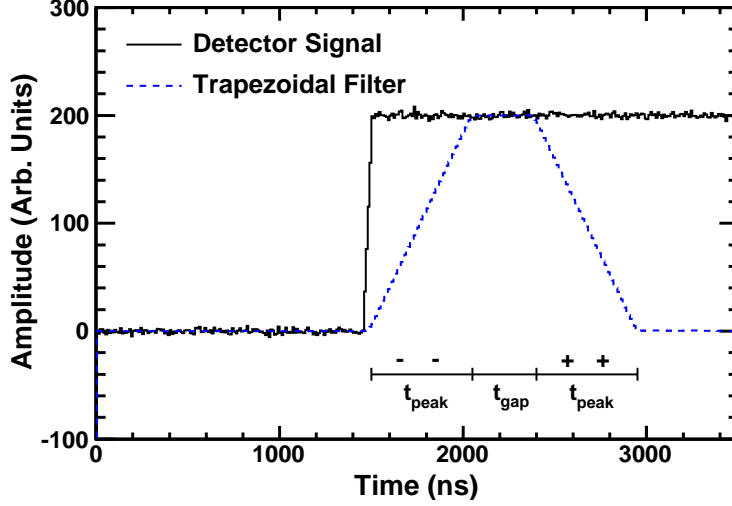


Figure 5.4: Illustrating the use of a digital trapezoidal filter using a signal step function. For every digitized point, the average value of points in the “-” t_{peak} region get subtracted from the average value of points in the “+” t_{peak} region. The two t_{peak} regions are separated by a time t_{gap} . For a step function, the response is a trapezoidal shape and the height of the trapezoidal filter contains the energy information of the signal.

point i , the difference in average voltage in the two t_{peak} regions is calculated as

$$\Delta V_i = \left(\sum_{j=i-P}^i V_j - \sum_{j=i-2P-G}^{i-P-G} V_j \right) / P \quad (5.1)$$

where P is the number of digitized points in time window t_{peak} and G is the number of digitized points in time window t_{gap} . This calculation gets implemented for every point in the detector signal and for a step function the result is the trapezoidal shape in Fig. 5.4, hence the name trapezoidal filter. The energy extraction is done by recording the value of the trapezoidal filter at some point on the flat top.

The signal pulses from SuN are not a step function; instead they exponentially decay with time constant $\tau = 230\text{ns}$. Thus, even though the digital filters implement the same algorithm as Eq. 5.1, they are not trapezoidal in shape. Fig. 5.5 shows the response of SuN’s trapezoidal filters to a typical pulse. The filter parameters used for the experiments in this

thesis were $t_{peak} = 100\text{ns}$ and $t_{gap} = 30\text{ns}$ for the trigger filter, and $t_{peak} = 600\text{ns}$ and $t_{gap} = 200\text{ns}$ for the energy filter.

The arrival time of each pulse is determined by the trigger filter. When the value of the trigger filter is above a user-defined threshold the time is recorded. The energy extraction from the energy filter occurs at a time $t_{peak} + t_{gap} = 800\text{ns}$ later based on the value of the energy filter at that time. By setting the user-defined τ parameter for the decay constant of the pulse, NSCL DDAS corrects for the exponential decay to obtain a corrected value of the energy using the algorithm of Ref. [104] (see Appendix A). Additionally, if another pulse satisfies the trigger filter threshold within $t_{peak} + t_{gap} = 800\text{ns}$ of the first pulse, both are rejected as pile-up. NSCL DDAS monitors the number of pulses accepted and number of pulses rejected due to pile-up to return a value for the data acquisition dead-time. In this thesis, typical values of the dead-time were less than 2% of the total acquisition time, but this small factor was taken into consideration in the analysis nonetheless.

Obtaining the time when a certain threshold level is reached is known as leading-edge triggering and it leads to time variation that depends on the height of the pulse. Larger pulses reach the threshold level sooner than smaller pulses, even though they occur at the same time. Thus, NSCL DDAS also implements more accurate timing using a constant fraction discrimination (CFD) algorithm. The general idea is that even though pulses have various heights, all pulses reach a certain fraction of their maximum height at the same time. Thus, by recording the time at which a pulse reaches a set fraction of its maximum height, more accurate timing information can be obtained. Since timing resolution was not critical to the experiments in this thesis, no further discussion will be included here. More information on the CFD algorithm implemented in NSCL DDAS can be found in Ref. [103, 105].

The end result of using NSCL DDAS is a raw experimental file which contains a time-

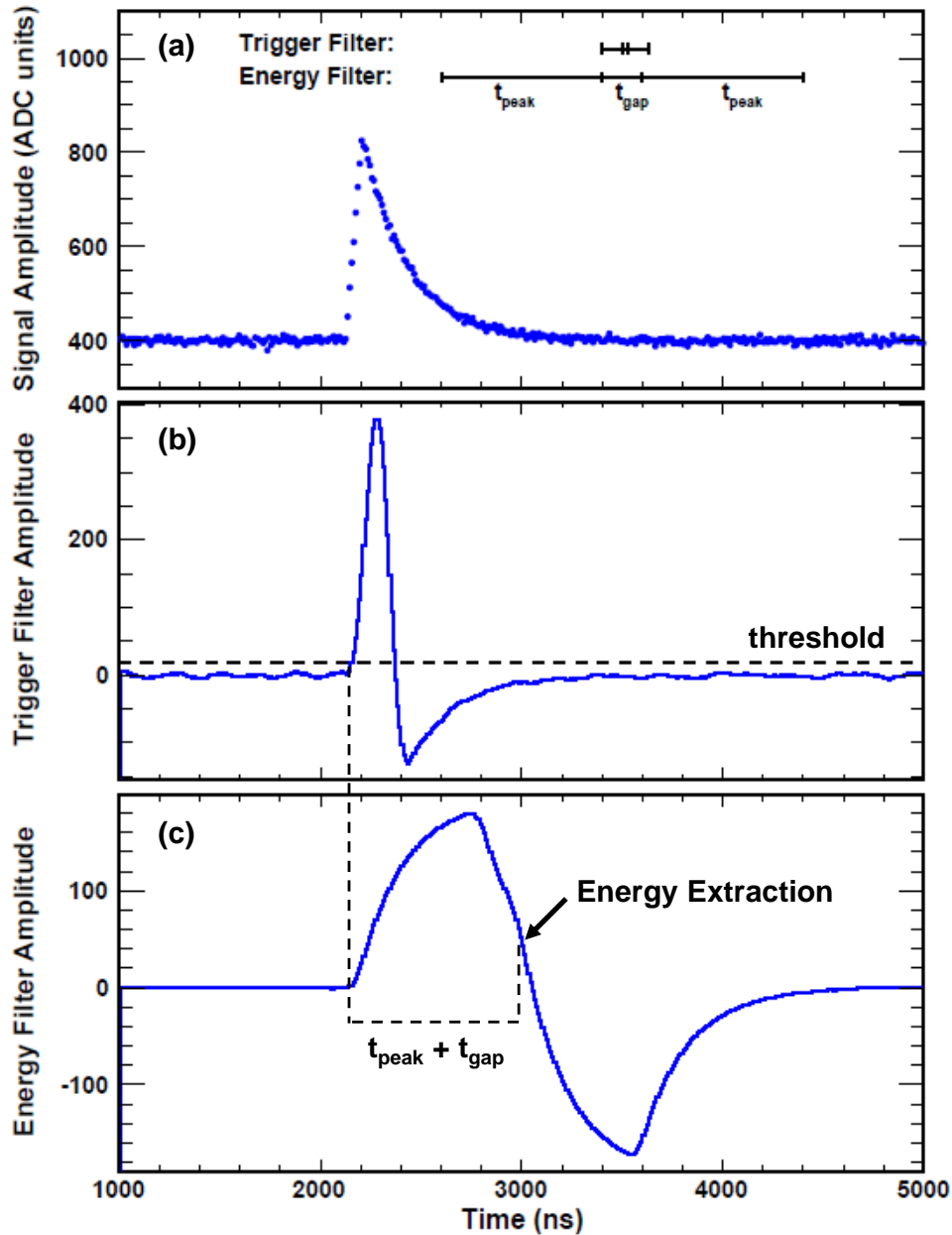


Figure 5.5: (a) Digitized representation of a signal from SuN’s PMT after passing through 100 MSPS ADC. (b) Response of SuN’s trigger filter. The arrival time of the pulse is obtained when the trigger filter passes above a user-defined threshold. (c) Response of SuN’s energy filter. The energy extraction is performed at a time $t_{peak} + t_{gap} = 800\text{ns}$ after the arrival of the pulse, with a correction to the decay constant applied as in Ref. [104].

ordered list of events with the energy, time, PIXIE-16 module number, and channel number that was triggered. Through the use of C++ computer coding, the events are extracted from this raw experimental file one-by-one and grouped according to their time. In this thesis a 300ns time window was used to put events into a group. This means that the first event opens a 300ns time window and every other detector that fired in that time window corresponds to the same physical event. In the case of measuring a reaction using the γ -summing technique, the physical event was a γ -ray cascade. The first detector that fired outside of the 300ns time window starts a new 300ns grouping, and so on and so forth. When studying the arrival time of pulses from SuN's PMTs, pulses originating from the same γ -ray cascade typically arrive within 10ns of each other, so the 300ns is a very conservative number for grouping the PMTs together. However if a γ -ray cascade populates a isomeric state that is longer lived than 300ns, its deexcitation will occur outside of the 300ns time window and it will not be grouped with the other γ rays of the cascade. More details on the impact of isomeric states for the γ -summing technique will be discussed in Chap. 6.

5.3.3 External Triggering

While one output from the amplifier gets processed by NSCL DDAS, another gets used to create an external trigger signal (see Fig. 5.3). The goal of an external trigger is to cut down on some of the data that gets saved to disk by checking to see if it satisfies a user-defined requirement first. Because SuN uses the γ -summing technique, this requirement is simply that a sum of the signals is above a threshold, which cuts down on the amount of data at lower energies that has no impact on the sum peak region. If the sum of the signals is large enough, then the information of all NSCL DDAS channels that fired in coincidence with the valid external trigger signal is recorded. The use of the external trigger signal allows the

threshold of individual PMTs to be lowered to ensure that all γ rays are recorded.

To implement external triggering into SuN's acquisition system, multiple electronics modules were needed. First, the ribbon cables from the amplifier pass into a splitter where their signals are divided into 24 individual channels. Taking only the eight channels which correspond to the eight central PMTs of SuN's segments, the signals are sent into a summing module. The reason for choosing the central PMT of each segment is that it typically has the best light collection of the three PMTs and is therefore representative of the total energy deposited in a segment. As its name indicates, the summing module takes the eight signals and sums them together into one output signal which is fed into CAEN V812 CFD module.

From the previous section, CFDs determine the arrival time of a pulse when the height is a certain fraction of its maximum height. The CAEN V812 module takes this value to be 20% of the pulse height at which time a logic signal is emitted. The advantage of using the CAEN CFD module is that it can be controlled through a computer graphical user interface to define a reproducible threshold from -1mV to -255mV in 1mV steps. The pulse height must be above the user-defined threshold level for a logic signal to be emitted. Therefore, if the height of the signal from the summing module is larger than the threshold, a valid external trigger signal is sent into NSCL DDAS and the data is recorded to disk.

Sending the signals through a splitter, a summing module, and a CFD takes a finite time, which causes a time delay between the arrival of SuN's signals and the potential arrival of the external trigger signal (if the CFD threshold is satisfied). This time delay must be taken into account when setting up a successful external trigger system. Conveniently, NSCL DDAS includes a "fast-trigger delay" variable which is user-defined so that the arrival of the detector signals is delayed to overlap with the external trigger signal. For this thesis a fast-trigger delay of 100ns was used.

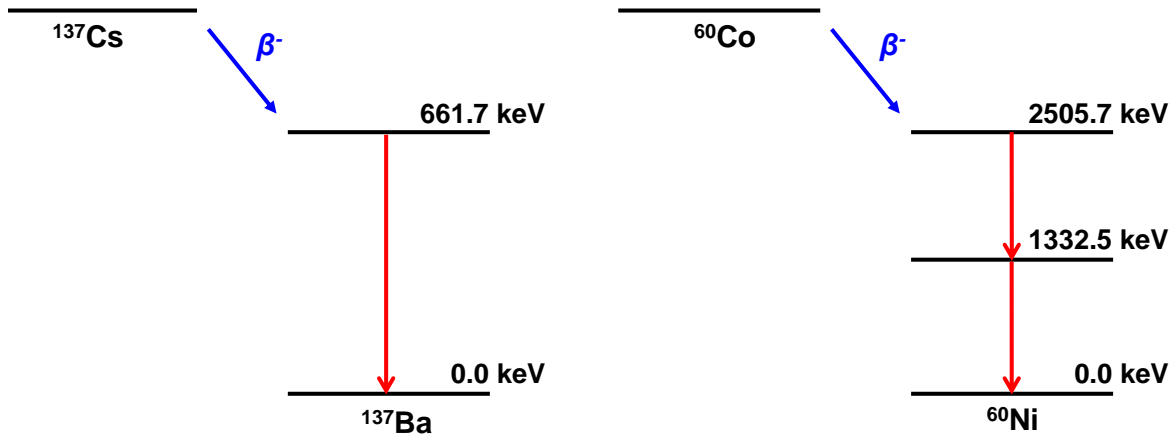


Figure 5.6: Simplified decay scheme showing the dominant decay radiation for the radioactive sources ^{137}Cs (left) and ^{60}Co (right).

5.4 Radiation Source Testing

Once the SuN detector arrived at the NSCL and the data acquisition system was set up, the initial testing of the detector was done using standard radioactive sources. The majority of the tests were done with two γ -ray sources; ^{137}Cs which β^- decays into ^{137}Ba with the emission of a single γ ray at 661.7 keV 94.7% of the time, and ^{60}Co which β^- decays into ^{60}Ni and then emits two sequential γ rays at 1173.2 keV and 1332.5 keV over 99% of the time. The general decay scheme of these two sources can be seen in Fig. 5.6.

The first feature of SuN to test was the energy resolution of the NaI(Tl) crystals. In any detector, the energy resolution quantifies the spread in detected energies for monoenergetic radiation. The distribution in detected energies is typically a Gaussian shape of the form

$$G(E) = A \exp\left(-\frac{(E - E_0)^2}{2\sigma^2}\right) \quad (5.2)$$

where A is the height, E_0 is the centroid, and σ is the standard deviation related to the width of the Gaussian. The energy resolution is defined as the full width at half maximum

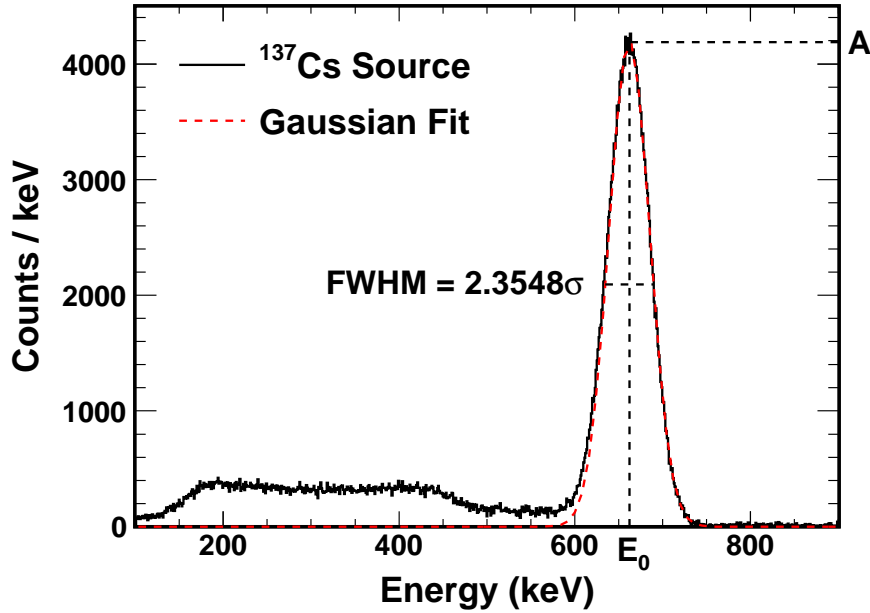


Figure 5.7: Experimental spectrum for a segment of SuN taken with a ^{137}Cs source with room background subtracted. Also shown is the result of a Gaussian fit to the 661.7 keV γ -ray line.

divided by the centroid energy, which for a Gaussian is

$$\text{Resolution} = \frac{\text{FWHM}}{E_0} = \frac{2\sqrt{2\ln 2} \sigma}{E_0} \approx \frac{2.3548 \sigma}{E_0}. \quad (5.3)$$

Fig. 5.7 shows the energy spectrum and Gaussian fit to the 661.7 keV line of a ^{137}Cs source for one of SuN's segments. The creation of the experimental spectrum will be discussed in Chap. 6. The standard deviation of the 661.7 keV line was determined to be 17.2 keV, which gives an energy resolution of 6.1% [77]. This is typical for a NaI(Tl) crystal and was the first proof that the SuN detector worked and met expectations. The energy resolution of SuN for the 1173.2 keV and 1332.5 keV ^{60}Co γ -ray lines was determined in a similar manner with standard deviations of 33.2 keV and 34.8 keV giving resolutions of 6.7% and 6.1%, respectively.

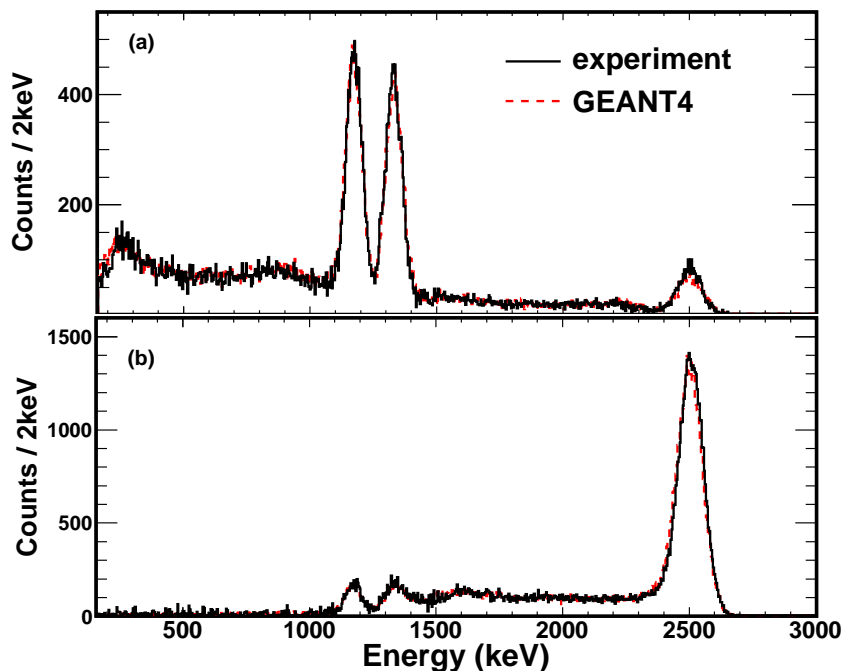


Figure 5.8: Experimental spectrum of SuN taken with a ^{60}Co source with room background subtracted. The result for (a) a segment of SuN and (b) all eight segments are in excellent agreement with GEANT4 simulations. When including the entire volume of SuN, the two sequential γ rays get summed together and the sum peak dominates the spectrum.

Since the decay of ^{60}Co emits two sequential γ -rays, it offers a nice test of the γ -summing technique. The energy spectrum obtained with a ^{60}Co placed at the center of SuN is shown in Fig. 5.8. For an individual segment of SuN, the spectrum is dominated by the two individual γ -ray lines with a smaller sum peak from when both γ rays simultaneously deposit their energy in the segment. However, when including the full volume of the detector the sum peak increases in intensity and dominates the spectrum. There are still two smaller peaks at 1173.2 keV and 1332.5 keV corresponding to when only one of the sequential γ rays is detected and the other one does not deposit any energy. By integrating the number of counts in the sum peak, the γ -summing efficiency for ^{60}Co was determined to be 62.4(1.2)% with no beam pipe and 51.5(1.0)% with a 1.5 mm thick stainless steel beam pipe.

The effect of the source position on the γ -summing efficiency was also investigated by

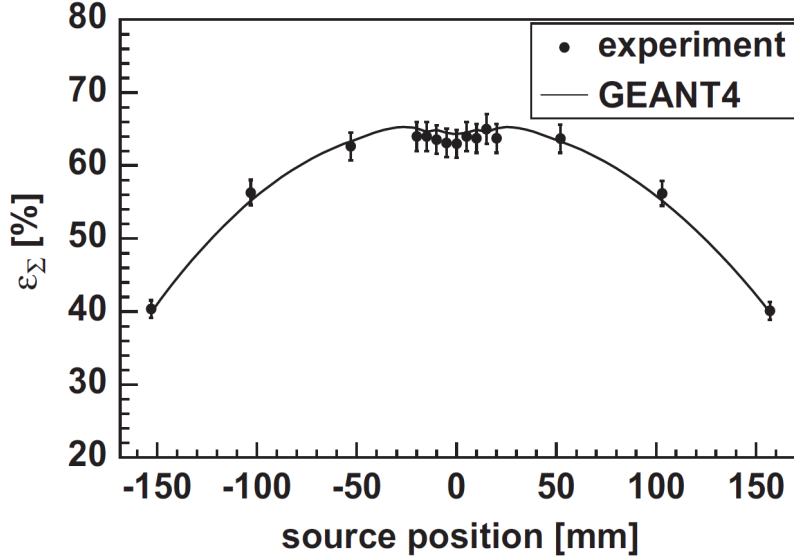


Figure 5.9: Figure from Ref. [77] showing the effect of the location of a ^{60}Co source inside of SuN on the γ -summing efficiency.

moving a ^{60}Co source to various locations along SuN's borehole, and the result is shown in Fig. 5.9. Although a small dip in the efficiency at the very center of SuN was discovered due to the thin layer of aluminum and reflector between the central segments, overall the efficiency was fairly constant at the center of the detector. This was encouraging because it showed that the position of the target in the center of SuN when performing experiments was not so crucial. As the source was moved further from the center, the γ -summing efficiency decreased as expected due to the decreased angular coverage and amount of NaI(Tl) near the source. See Ref. [77] for more details.

5.5 GEANT4 Simulation

In order to analyze the data in this thesis and make predictions of how the SuN detector will behave under various experimental conditions, it was necessary to develop a working and reliable computer simulation of the detector. As with many applications that involve the

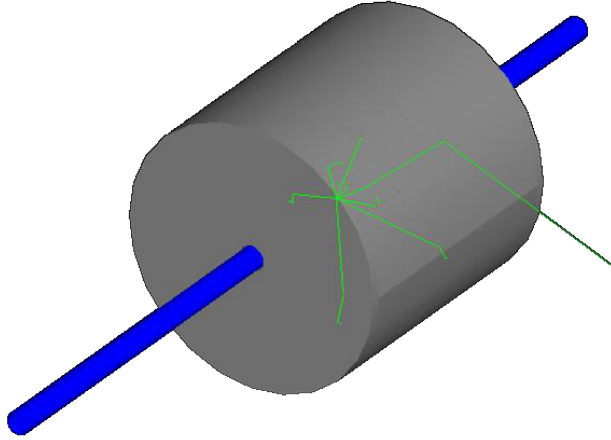


Figure 5.10: Visualization of the GEANT4 SuN detector simulation. The lines inside of SuN are several γ -ray tracks. The one track that scatters outside of SuN does not deposit all of its energy inside of the detector.

detection of radiation, the GEANT4 software package was used which implements Monte Carlo methods to simulate how particles interact with matter [106]. In the case of SuN, this means repeatedly sampling how a cascade of γ rays interacts with SuN to obtain the detector response. GEANT4 is an ideal tool for this purpose because it already has the physics of how γ rays interact with matter built in to its physics libraries, and the implementation has been shown to be reliable for many other applications.

The successful adaptation of GEANT4 for use with the SuN detector involved a few important steps. First, SuN was constructed in the simulation by inputting each component with the correct dimensions, composition, and location within SuN's geometry. The construction of the SuN detector can be found in Appendix B. It was also important to include experimental equipment such as the beam pipe and target holder in the design for maximum accuracy. Second, the capability to specify the location, energy, and direction for the emission of γ rays was introduced. In most cases the γ rays are simply emitted in a random direction from the center of SuN with an input file listing the γ -ray cascades to

Table 5.1: Standard deviation (σ) of a Gaussian function fit to various experimental γ -ray peaks, along with the corresponding energy resolution.

E (keV)	σ (keV)	Res. (%)	Source	E (keV)	σ (keV)	Res. (%)	Source
511	24.4	11.2		6129	92.7	3.56	$^{19}\text{F}(\text{p},\alpha\gamma)^{16}\text{O}$
1173	33.2	6.66	^{60}Co	9394	119	2.98	$^{27}\text{Al}(\text{p},\gamma)^{28}\text{Si}$
1332	34.8	6.15	^{60}Co	10509	126	2.82	$^{27}\text{Al}(\text{p},\gamma)^{28}\text{Si}$
1779	42.1	5.57	$^{27}\text{Al}(\text{p},\gamma)^{28}\text{Si}$	12420	138	2.62	$^{27}\text{Al}(\text{p},\gamma)^{28}\text{Si}$
2839	54.8	4.55	$^{27}\text{Al}(\text{p},\gamma)^{28}\text{Si}$				

simulate. An optional Doppler shift in energy was introduced for γ rays emitted in flight for comparison to experiments performed in inverse kinematics. Third, the simulation was set up so that for each simulated γ -ray cascade the energy deposited in each segment, the total energy deposited in the detector, and the number of segments that detected energy were extracted and saved. A visualization of the GEANT4 SuN detector simulation can be seen in Fig. 5.10.

Additionally, the resolution of SuN's NaI(Tl) crystals had to be input into the simulation. This resolution was experimentally determined by fitting the peak of several individual γ -ray lines, including measurements taken with a γ -ray sources as well as γ rays emitted from the deexcitation of well-known resonances in the $^{27}\text{Al}(\text{p},\gamma)^{28}\text{Si}$ reaction. Table 5.1 lists the γ -ray energies and the standard deviation of a Gaussian fit to the peak in the spectrum, which was used for the resolution function of SuN. This information is also plotted in Fig. 5.11 along with the best fit function that was implemented in the GEANT4 simulation. The GEANT4 simulation of SuN agrees excellently with the experimental data contained in this thesis. Validation of the code can be found in comparison to γ -ray sources (Fig. 5.8 and 5.9) and well-known resonances in the $^{27}\text{Al}(\text{p},\gamma)^{28}\text{Si}$ and $^{58}\text{Ni}(\text{p},\gamma)^{59}\text{Cu}$ reactions (Chap. 7 and 11). Although the resolution function worked well for this thesis and described the

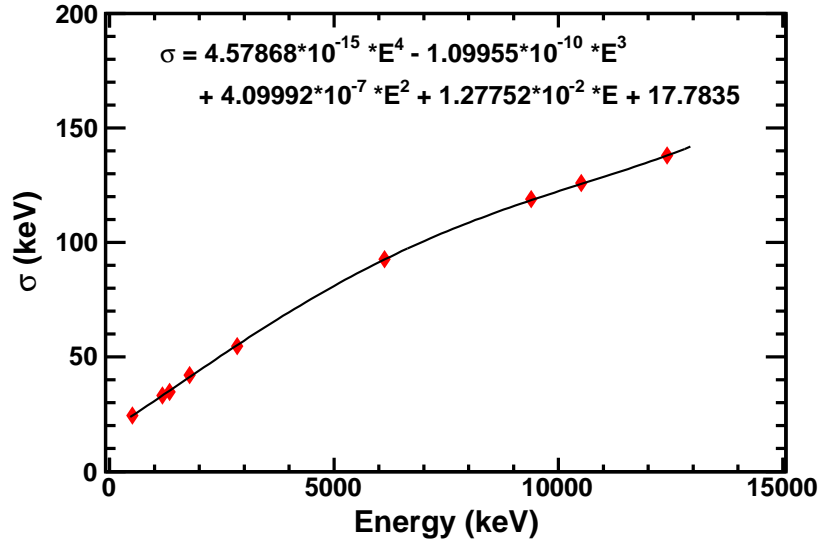


Figure 5.11: Standard deviation in the detected energy of the SuN detector as a function of the γ -ray energy. The points correspond to experimental data and the curve is the best fit function that was implemented in the GEANT4 simulation.

experimental data up to γ -ray energies above 12 MeV, it has been seen in more recent SuN experiments that the extrapolation of σ to low energies of a few hundred keV does not match experimental values. Thus, future scientists should take note that the resolution function of SuN was based on the available experimental data at the time and may be altered and improved with additional γ -ray lines.

As mentioned in Sec. 5.1, GEANT4 simulations were used to aide in creating the final design of SuN. By simulating well-known γ -ray cascades, the γ -summing efficiency was determined for various possible geometries by taking the ratio of the number of counts in the sum peak to the total number of cascades simulated. Fig. 5.12 shows sample efficiency results for the SuN detector, a solid cylindrical detector of the same dimensions, and the existing CAESAR detector at the NSCL [107]. CAESAR consists of 192 CsI crystals and the standard configuration of the crystals is shown in the inset of Fig. 5.12. By arranging the 192 crystals of CAESAR into different configurations it was possible to improve the efficiency,

however it was still too low for the ideal implementation of the γ -summing technique. It was decided that it was best to go with a cylindrical detector and that eight segments was the best compromise between segmentation and efficiency. The simulated efficiency of SuN for the detection of a single γ ray up to 15 MeV is shown in Fig. 5.13. The efficiency decreases from 82% for a 1 MeV γ ray to 45% for a 15 MeV γ ray. When using the stainless steel beam pipe and aluminum target holder in experiments, the efficiencies drop to 71% for a 1 MeV γ ray to 42% for a 15 MeV γ ray.

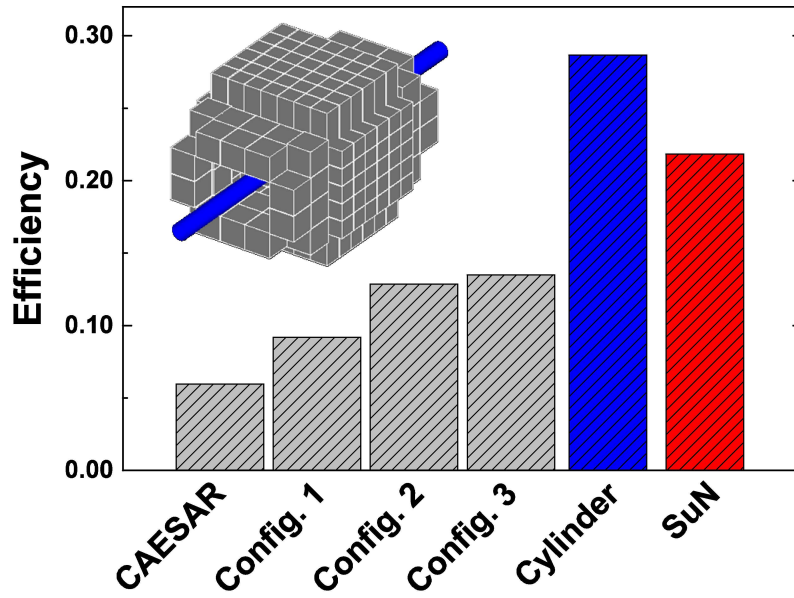


Figure 5.12: γ -summing efficiencies for various configurations of the CAESAR detector (standard configuration inset), a solid cylindrical detector, and the SuN detector for the resonance at a proton energy of $E_p = 1118\text{keV}$ in the $^{27}\text{Al}(p,\gamma)^{28}\text{Si}$ reaction. This resonance deexcites through the emission of 3.2 γ rays on average.

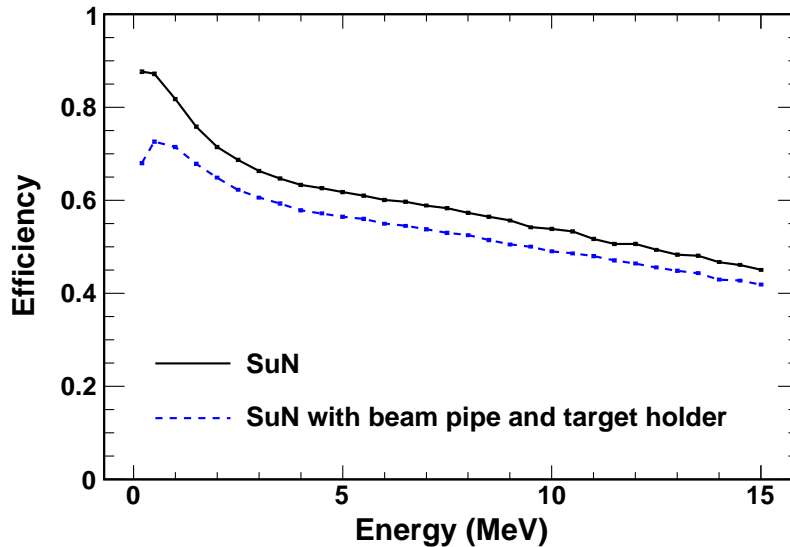


Figure 5.13: SuN's efficiency for the detection of a single γ ray as a function of energy both with and without the beam pipe and target holder used in experiments.

Chapter 6

Analysis

The raw output of the experimental measurements with the SuN detector included in this thesis were files containing a time-ordered list of entries. Each entry contained the PIXIE-16 module number and channel number that fired, along with the time and energy information extracted from the signal pulse that caused the entry. As discussed in Sec. 5.3.2, the time and energy were calculated with digital filter algorithms, and entries occurring within the same 300ns time window were grouped together as originating from a single γ -ray cascade. This chapter contains the procedures to analyze the data, the bulk of which was performed using the C++ programming language and the ROOT software package.

6.1 Gain Matching and Calibration

The first step in the analysis procedure is to make sure that SuN's PMTs have the same response when collecting the scintillation light originating from γ -rays of the same energy. This procedure is called gain matching and it can be done in two separate ways. One method is to adjust the amount of high voltage applied to a PMT to alter the number of electrons produced in the different electron multiplication stages. In this way, the PMTs themselves are adjusted to create similar output signals so that the energy extracted by the data acquisition system is consistent for every PMT. The 1460.8 keV γ -ray line from the room background decay of ^{40}K is well suited for this purpose. Therefore, the voltage on

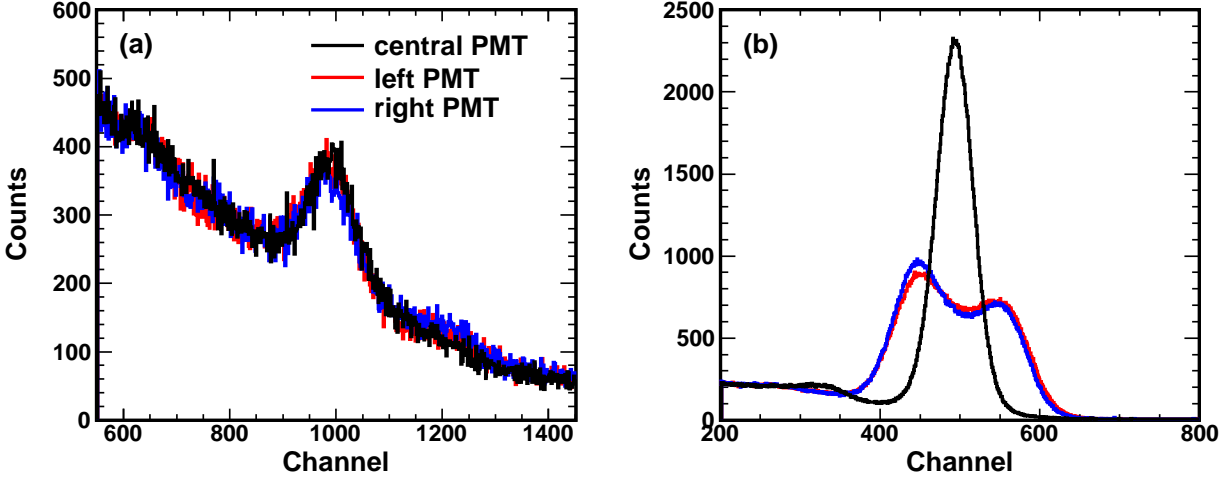


Figure 6.1: (a) Room background and (b) ^{137}Cs source spectra from the three PMT's in a single segment of SuN after gain matching the voltages applied to each PMT. Since the ^{137}Cs source emits γ rays from the center of SuN, the outer two PMTs show a double peak in their spectrum.

each PMT was adjusted so that the energy extracted from the 1460.8 keV γ -ray line was approximately the same for each PMT before performing the measurements of this thesis.

Fig. 6.1 shows the result after altering the PMT voltages in one of SuN's segments for both a room background measurement and a measurement taken with a ^{137}Cs source. In the room background spectra there is a single peak from the ^{40}K line for each PMT, and the peaks are aligned to the same channel number as expected. However, the ^{137}Cs spectra shows a single peak for the 661.7 keV transition only for the central PMT. Instead of single peaks as one might expect, the outer two PMTs show a double peak in their energy spectra.

It was concluded that the double peak for γ rays emitted from the center of SuN is due to the geometry of the segments, where the semicylindrical shape of the crystal and the placement of the three PMTs causes a position dependence on the light collection of the outer two PMTs. This position dependence is further illustrated in Fig. 6.2, which contains a plot of the left PMT against the right PMT for a ^{60}Co source. The two γ -ray transitions in the decay of ^{60}Co show up as the two strong bands around channel 1000 in each PMT.

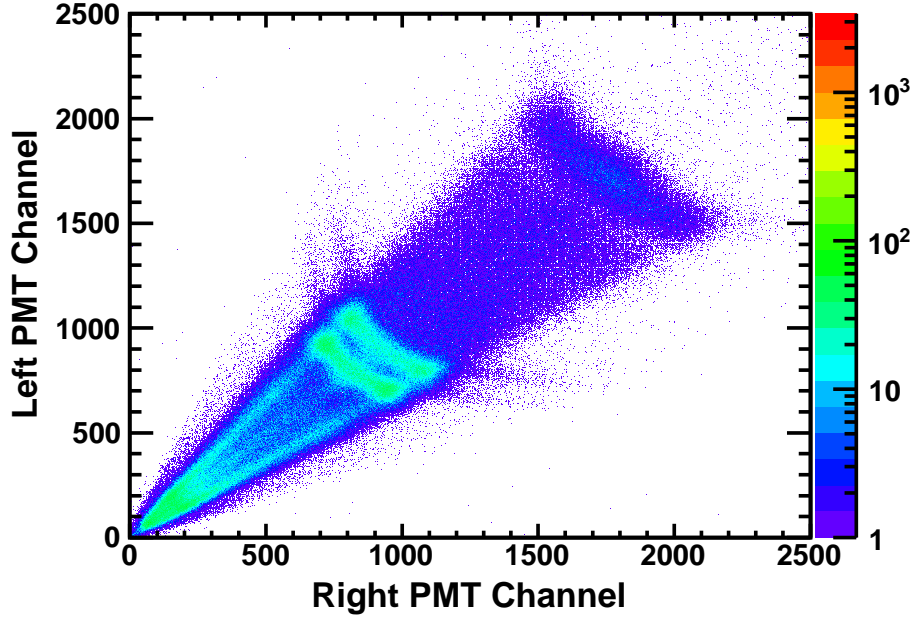


Figure 6.2: Two-dimensional plot showing the response of the left PMT against the response of the right PMT for a ^{60}Co source. The two bands in the spectrum around channel 1000 in each PMT correspond to the two γ -ray transitions in the decay of ^{60}Co . The slope of these bands indicates that the response of the outer two PMTs is affected by where the γ ray deposits energy in the crystal.

Depending on where the γ ray interacts with the crystal, the light collection of the outer two PMTs is affected. For instance, if the γ ray deposits energy near the left PMT, the left PMT collects more light than the right PMT, and vice versa. This creates a spread in the amount of light collected by the outer two PMTs for a single energy, which corresponds to a poor energy resolution. However when adding the two outer PMTs together, good energy resolution is achieved. Contrary to the outer PMTs, the location of the central PMT allows for uniform light collection regardless of where the emitted γ ray interacts with the crystal, and hence the single peak in the spectrum and why it was used to create the external trigger signal (see Sec. 5.3.3). Since the ^{40}K γ -ray line originates outside of the detector and deposits its energy near the outside of the NaI(Tl) crystals, all PMTs receive uniform light collection and there is a single peak in all PMTs.

As mentioned, there is also an additional method of gain matching SuN's PMTs. The second method of gain matching is to apply a correction to the PMT energies in software after the data is taken. By multiplying the energy extracted from a PMT by a numerical multiplication factor it is possible to more precisely align the energy spectra for every PMT. In this thesis, different methods of aligning the energy spectra from the three PMTs in a segment were investigated to see which method provides the best energy resolution when summing the PMTs together to create a total energy spectrum for the segment. During a reaction measurement, the γ rays are emitted from the center of SuN so the energy spectra of the outer two PMTs have a double peak for each γ ray. Three different gain matchings were considered; aligning the γ -ray peak to the left of the double peaks, to the right of the double peaks, and in the center of the double peaks. The results are shown in Fig. 6.3 for a ^{137}Cs source, a ^{60}Co source, and the ^{40}K background line. In this figure, the top row of three panels are aligning the spectra to the left, the second row is aligning to the center, and the third row is aligning to the right. The three PMTs in each alignment are summed together to create a total energy spectrum for the segment, and the result is then calibrated. The result of calibrating the total segment spectrum is shown in the bottom row of three panels in the figure. Surprisingly, there is no noticeable difference in resolution between the three methods. Therefore, it is often easiest to gain match to the center, so that the single peak in the energy spectrum from the central PMT is aligned at the center of the double peaks in the energy spectra of the outer two PMTs. This can be done by fitting the 1460.8 keV γ -ray line from the room background decay of ^{40}K in each PMT with a Gaussian to determine the centroid, and then calculating the multiplication factor necessary for precise alignment.

After gain matching the three PMTs in each segment, their energies can be added for each

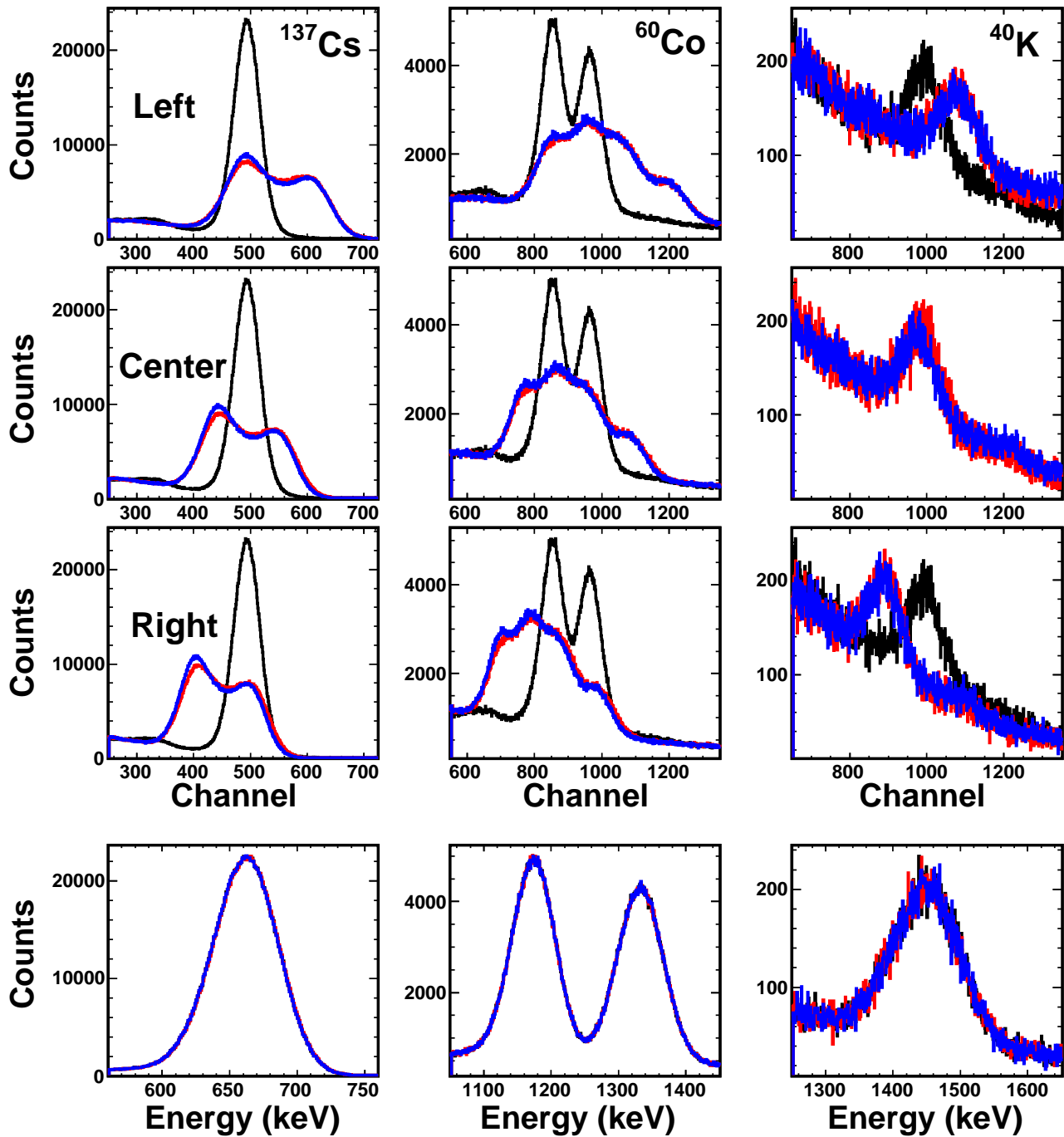


Figure 6.3: Result of applying gain matching multiplication factors in software to align the central PMT in a segment to the left (first row), center (second row), and right (third row) of the double peaks in spectra of the outer two PMTs. This was done for a ^{137}Cs source (left column), a ^{60}Co source (central column), and the ^{40}K background line (right column). After summing the three PMTs in a segment together, the end result is that there is no noticeable difference in the method of gain matching.

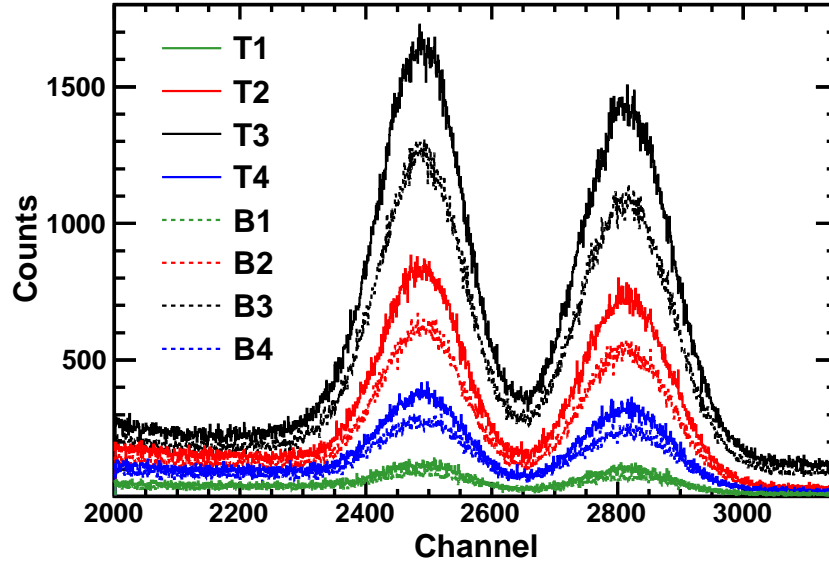


Figure 6.4: The result of gain matching SuN's segments using a ^{60}Co source. The label T is for the top of the detector and B is for the bottom of the detector. Based on the spectra it can be deduced that the source was placed off-center under the third segment of SuN and closer to the top than the bottom.

γ -ray cascade to create an energy spectrum for the entire segment. As with the individual PMTs, it is necessary that SuN's segments have the same response when detecting γ rays of the same energy. This can be assured by fitting peaks in the energy spectrum of each segment with a Gaussian function to determine the centroid and then aligning each centroid. For creating source spectra like Fig. 5.7 and Fig. 5.8, the alignment of each segment was done using the γ -ray lines from the sources themselves. For example when creating the ^{60}Co spectrum, multiplication factors to align the 1173.2 keV and 1332.5 keV γ -ray lines were calculated for each segment and the average of the two values was used. A typical result of gain matching all of SuN's segments for ^{60}Co is shown in Fig. 6.4. After gain matching each segment, the energies can be added together to create the total γ -summed spectrum. This spectrum can then be calibrated so that each γ -ray line shows up at the correct energy in the spectrum. For source spectra, a linear calibration of the form $E = Ax + B$ is sufficient, where A is the slope and B is the intercept of the calibration.

Table 6.1: Energy and source of γ -ray transitions used to calibrate SuN's segments.

E (keV)	Source	E (keV)	Source
511		6129	$^{19}\text{F}(\text{p},\alpha\gamma)^{16}\text{O}$, $^{16}\text{O}(\alpha,\alpha')^{16}\text{O}$
596	$^{74}\text{Ge}(\alpha,\alpha')^{74}\text{Ge}$	6668	$^{27}\text{Al}(\text{p},\gamma)^{28}\text{Si}$
1173	^{60}Co decay	8938	$^{27}\text{Al}(\text{p},\gamma)^{28}\text{Si}$
1332	^{60}Co decay	9394	$^{27}\text{Al}(\text{p},\gamma)^{28}\text{Si}$
1779	$^{27}\text{Al}(\text{p},\gamma)^{28}\text{Si}$	10509	$^{27}\text{Al}(\text{p},\gamma)^{28}\text{Si}$
2839	$^{27}\text{Al}(\text{p},\gamma)^{28}\text{Si}$	10762	$\text{p}(^{27}\text{Al},\gamma)^{28}\text{Si}$
4438	$^{12}\text{C}(\alpha,\alpha')^{12}\text{C}$	12420	$^{27}\text{Al}(\text{p},\gamma)^{28}\text{Si}$

Initially when analyzing the (p,γ) and (α,γ) measurements, it was thought that the same procedure as used to create the source spectra could be used to create the reaction γ -summed spectra. However, because the reactions measured in this thesis produced compound nuclei at high excitation energy, it turns out that this method was not satisfactory. A multiplication factor that gain matched SuN's segments using γ rays with energies between 1 and 2 MeV misaligned γ -ray lines at energies above 5 MeV, and vice versa. For the proper summation of all eight segments in this thesis, the response of each segment needed to be gain matched up to γ -ray energies of approximately 15 MeV. Therefore, it was decided to calibrate each segment individually before summing them all together. The calibration points for each segment came from single γ -ray transitions from standard radioactive sources, the $^{27}\text{Al}(\text{p},\gamma)^{28}\text{Si}$ reaction, and various beam induced reactions. Due to the large energy range, it was necessary to use a quadratic function of the form $E = Ax^2 + Bx + C$ to achieve the best calibration. Table 6.1 lists the γ -ray energies used to calibrate SuN's segments in this thesis.

In an experiment, it is possible that the PMT responses may drift over time, which causes a shift in the energy spectrum from a PMT despite the maintaining of a constant applied voltage. This would lead to different gain matching and calibration values over the course of an experiment. The drift may be due to factors such as shifting high voltages, fluctuating

Table 6.2: Gain matching multiplication factors for each PMT in the three different experiments at the University of Notre Dame.

PMT	Exp. I	Exp. II	Exp. III	PMT	Exp. I	Exp. II	Exp. III
T11	1.00453	0.99467	1.02591	B11	1.00014	1.00689	1.04008
T12	1.00000	1.00000	1.00000	B12	1.00000	0.97160	1.00000
T13	0.99230	1.00715	1.05147	B13	1.00245	1.00000	1.04778
T21	1.00607	1.00764	1.04427	B21	0.98698	1.00078	1.00872
T22	1.00000	0.96076	1.00000	B22	1.00000	0.99070	1.00000
T23	0.98970	1.00000	1.03669	B23	0.98800	1.00000	0.97929
T31	0.99193	0.97883	1.02639	B31	1.01521	1.03585	1.01702
T32	1.00000	1.00000	1.00000	B32	1.00000	1.00000	1.00000
T33	0.99233	1.01458	1.05110	B33	1.00682	0.98628	0.97929
T41	0.98590	0.99266	0.98726	B41	1.00403	0.98217	0.95456
T42	1.00000	1.00797	1.00000	B42	1.00000	1.01543	1.00000
T43	0.99113	1.00000	0.99374	B43	0.99396	1.00000	0.98351

temperatures or magnetic fields in the experimental area, or perhaps the ageing of a PMT with use. During the (p,γ) and (α,γ) measurements at the University of Notre Dame, room background runs were taken at least a few times a day and oftentimes many more. By monitoring the location of the 1460.8 keV γ -ray line in the room background spectrum for each PMT, it was possible to determine whether or not the response of the PMTs were changing with time. Over the course of the three separate, week-long experiments, no significant drift in the PMTs was discovered. Therefore, it was possible to perform a single gain matching and calibration procedure for each experiment. The values used for the analysis of the data in this thesis can be found in Table 6.2 and Table 6.3.

6.2 Thresholds

As will be described later in this chapter, the complete analysis of SuN's experimental data requires an accurate simulation of the detector that matches existing experimental data

Table 6.3: Energy calibrations of the form $E = Ax^2 + Bx + C$ for each segment in the three different experiments at the University of Notre Dame.

	Segment	A	B	C
Exp. I	T1	1.08547×10^{-06}	0.47770	-38.8211
	T2	1.06741×10^{-06}	0.48932	-45.3902
	T3	1.39848×10^{-06}	0.47533	-23.1084
	T4	1.17564×10^{-06}	0.48355	-28.8541
	B1	2.18739×10^{-06}	0.46264	-2.88832
	B2	1.41779×10^{-06}	0.48360	-43.1425
	B3	1.11948×10^{-06}	0.46897	-46.4133
	B4	1.51094×10^{-06}	0.46840	-23.2460
Exp. II	T1	5.64057×10^{-06}	1.09818	-21.0829
	T2	7.00597×10^{-06}	1.14240	-21.6076
	T3	6.44751×10^{-06}	1.12545	-35.0943
	T4	7.40063×10^{-06}	1.12614	-5.59329
	B1	7.86493×10^{-06}	1.11152	-6.65785
	B2	7.15952×10^{-06}	1.13639	-43.1837
	B3	7.17831×10^{-06}	1.10718	-37.0146
	B4	8.35966×10^{-06}	1.09061	-11.0828
Exp III	T1	3.08654×10^{-06}	1.04165	-42.4995
	T2	1.16270×10^{-06}	1.08097	-54.4708
	T3	5.40427×10^{-06}	1.04891	-27.7781
	T4	5.40296×10^{-06}	1.09220	-30.9802
	B1	3.65558×10^{-06}	1.06209	-44.4285
	B2	3.29566×10^{-06}	1.12088	-49.5915
	B3	4.40908×10^{-06}	1.05076	-38.5224
	B4	7.81034×10^{-06}	1.07178	-25.6977

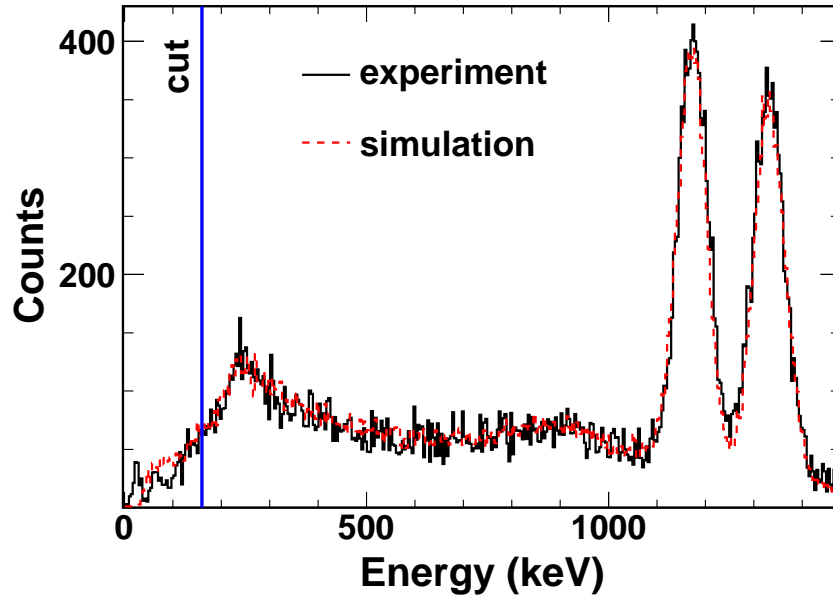


Figure 6.5: Experimental data and GEANT4 simulation for one of SuN’s central segments for a ^{60}Co source. In the analysis, a hard cut at 160 keV was applied for each segment in order to use the same threshold in both experiment and simulation.

and makes accurate predictions. The simulation should match the experimental data for all energies, including the low energy part of SuN’s spectra which is directly affected by the experimental threshold. As discussed in Sec. 5.3.2, NSCL DDAS applies a threshold based on the trigger filter response to SuNs PMT signals. After applying the energy filter to signals satisfying the threshold requirement, the result is not a sharp cut in the PMT energy spectrum but instead the low energy part of the spectrum has a positive slope.

The GEANT4 simulation of the SuN detector developed in this thesis does not include the response of individual PMTs, but instead calculates the response of all eight of SuN’s segments. Therefore it is necessary to compare an experimental spectrum of a segment to a simulated spectrum of the segment to view the effect of the threshold. Fig. 6.5 shows the difference between simulation and experimental data for one of SuN’s central segments for a ^{60}Co source. Overall the simulated spectrum matches the experimental data well for

the energies shown. However for the energies below a few hundred keV, there are some discrepancies between the two spectra due to the experimental threshold. Because of the difficulty in correctly implementing the effect of NSCL DDAS's threshold in simulation, it was decided to apply a hard cut in both experimental and simulated spectra. A conservative value of 160 keV was chosen based on the energy spectra of SuN's 24 PMTs. If the total energy deposited in a segment was below the hard cut at 160 keV, it was ignored in the analysis.

6.3 Sum Peak Analysis

After performing the gain matching, calibration, and threshold steps described in the previous sections, the energy deposited in each of SuN's eight segments was added together to create a total γ -summed energy. In this way, the detected energy of all the γ -rays emitted in deexcitation of the produced nuclei in the (p,γ) and (α,γ) reactions were summed together to create a sum peak at $E_{\Sigma} = E_{c.m.} + Q$. At this point in the analysis, the effects of detection dead time (less than 2% for all measurements) and room background were also taken into account. Both the total γ -summed reaction spectrum and total γ -summed room-background spectrum were scaled by their corresponding live-time ratios. After this scaling, the room background spectrum was further scaled by normalizing to the same run time as the reaction spectrum. By subtracting the normalized room background spectrum from the reaction spectrum, the final result was achieved. Fig. 6.6 shows a typical sum peak after the dead-time corrections and room-background subtraction, in this case for the $^{60}\text{Ni}(\alpha,\gamma)^{64}\text{Zn}$ reaction.

As discussed in the γ -summing technique in Sec. 4.1.3.2, the cross section of a reaction

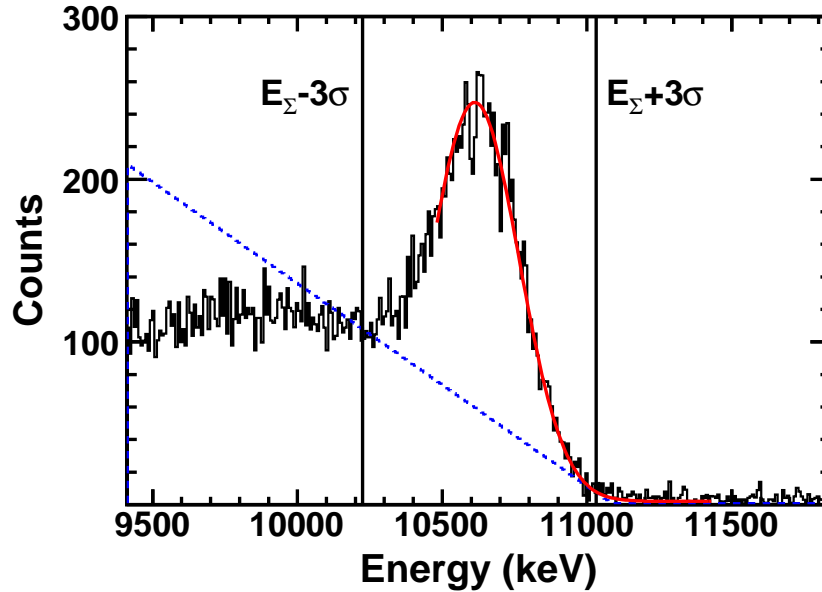


Figure 6.6: Zoomed in view of a typical sum peak from the γ -summing technique with the SuN detector, in this case for the $^{60}\text{Ni}(\alpha,\gamma)^{64}\text{Zn}$ reaction. A Gaussian fitting function is used to define a sum-peak region of $(E_\Sigma-3\sigma, E_\Sigma+3\sigma)$ and then a linear background is determined from an average of the region's boundary values. The sum peak integral is taken to be the number of counts above the linear background.

is directly related to the number of counts in the sum peak. Because this thesis contains the first ever implementation of the γ -summing technique with the SuN detector, the method of integrating the number of counts in the sum peak was not yet determined and several methods were initially considered. When deciding which method to use, it was desirable to find a technique that was reproducible and provided a reasonable estimate of the background underneath the sum peak. The sum peaks contained in this thesis were typically fairly large and it was possible to describe the background with a polynomial function if necessary, although some of the (α,γ) sum peaks did have low statistics. In addition, future measurements with the SuN detector are expected to utilize low intensity radioactive beams and low cross sections with a corresponding low count rate in the sum peak. Therefore, it was decided that a linear background would be easiest to implement for sum peaks of all shapes and sizes.

The γ -summing technique tends to produce sum peaks that are asymmetric with the low energy side of the peak extending outwards in a “tail”. This low energy tail is a result of incomplete summation of the γ -ray energy when not all of the energy is deposited into the detection crystal. Instead, some of the energy may be deposited in an inactive layer of the detector or scattered outside of the detector. Therefore, the total γ -summed energy for these events is less than the energy of the sum peak, creating the asymmetric shape. Because the size and shape of the low energy tail may be different for each sum peak depending on the number and energy of the γ rays being summed together, it was necessary to use a technique independent of the low energy side of the sum peak when determining the bounds of integration. Therefore, only the high energy side of the sum peak was fit with a Gaussian fitting function (Eq. 5.2) to determine the centroid (E_{Σ}) and standard deviation (σ) of the peak. Using the values of E_{Σ} and σ , the sum-peak region was defined from an energy of $E_{\Sigma}-3\sigma$ on the left to an energy of $E_{\Sigma}+3\sigma$ on the right. To create a linear background beneath the sum peak an average of the number of counts on both the left and right boundaries of the sum-peak region was taken. A line was then drawn between the average values. The number of counts in the sum peak was calculated as the total number of counts in the sum-peak region subtracted by the number of counts in the linear background spectrum within the sum-peak region. Fig. 6.6 shows a typical Gaussian fit as well as the linear background determination from a typical sum peak in the $^{60}\text{Ni}(\alpha,\gamma)^{64}\text{Zn}$ reaction. The vertical lines in the spectrum denote the location of the sum-peak region.

6.3.1 Isomeric states

An important consideration to take into account when performing the sum-peak analysis is whether or not there are any isomeric states in the produced nuclei. The presence of

an isomeric state that has a lifetime close to or longer than the data acquisition system's event window requires additional analysis. In this thesis an event window of 300ns was used. Therefore, if any excited state produced in the (p,γ) and (α,γ) reactions lived longer than 300ns before deexciting, the γ rays emitted from this longer lived state would be outside of the event window and not grouped with the other γ rays from the same cascade. When populating an isomeric state, this separate grouping of the γ rays creates a total γ -summed energy that is less than the total energy of the reaction. Thus, multiple sum peaks would be observed in the γ -summed spectrum. One peak would correspond to the full energy of the reaction when the isomeric state is not populated in a γ -ray cascade. A second peak would also be present, corresponding to when the isomeric state is populated. This second peak would be found at an energy equal to the full energy of the reaction minus the energy of the isomeric state.

Since the total radiative capture cross section depends on the total number of γ -ray cascades, including ones that populate and ones that do not populate the isomeric state, it is necessary to integrate both peaks in the spectrum. For example, the $^{74}\text{Ge}(p,\gamma)^{75}\text{As}$ reaction discussed in Chap. 8 includes a 304 keV isomeric state in ^{75}As with a half-life of 17.62 ms [108], which is much longer than the 300ns event window. The 304 keV energy is small compared to the full energy of the reaction of approximately 10 MeV studied in Chap. 8, and the integral of events populating the isomeric state was included in the analysis by expanding the sum-peak region to $(E_{\Sigma}-3\sigma-304\text{keV}, E_{\Sigma}+3\sigma)$. As mentioned, for isomeric states at higher energies, it may be necessary to completely analyze separate peaks in the total γ -summed spectrum.

6.3.2 Doppler reconstruction

An additional consideration to take into account is that reactions measured in inverse kinematics have deexcitation γ rays emitted from a moving source, which creates a shift in the detected energy by the Doppler factor (Eq. 4.4). Therefore, the analysis of measurements in inverse kinematics require the additional step of Doppler reconstruction of the γ -ray energy. The Doppler reconstruction is done separately for each of SuN's segments before summing the energy of the segments together. Since the shift in γ -ray energy depends on the angle of emission, it is important to choose the correct angle to use for the Doppler reconstruction for each segment. For the analysis in this thesis, three different angles were investigated for each segment. The first angle was simply the angle from the center of the target position to the geometrical center of the NaI crystal. However, it is possible that this angle is incorrect because it does not take into account that there are different thicknesses of NaI crystal available at different angles in a segment. The greater the thickness of the NaI crystal, the more likely it is that γ rays emitted at the corresponding angle will interact and deposit energy. Therefore, the second angle was calculated by weighing each emission angle by the path-length through the NaI crystal. Lastly, SuN's GEANT4 simulation was used to determine the average emission angle for the γ rays that deposit energy in each crystal.

The calculated angles for each segment using the three different methods are listed in Table 6.4 and drawn in Fig. 6.7. Overall, the three methods return approximately the same angle to use in the Doppler reconstruction. It was also found that the GEANT4 angles are closer to the geometrical center of the crystals for the central two segments, but closer to the weighted center for the outer two crystals. Because the GEANT4 simulation has been shown to provide reliable results for the SuN detector, it was decided to use the GEANT4

Table 6.4: Average emission angle in radians for the different segments of the SuN detector calculated from the geometrical center of the NaI crystals, by weighting the angles by the path-length through the crystals, and from SuN’s GEANT4 simulation.

Segment	Crystal Center	Weighted Center	GEANT4 Center
1	2.510	2.559	2.550
2	1.999	2.082	2.024
3	1.142	1.059	1.118
4	0.632	0.582	0.592

Table 6.5: Doppler correction factors used for each segment in this thesis.

Segment	^{27}Al ($\beta = 0.0459$)	^{58}Ni ($\beta = 0.0550$)
1	1.0395	1.0476
2	1.0212	1.0256
3	0.9800	0.9762
4	0.9629	0.9558

angles in the analysis. However, it should be mentioned the angles provided by the three methods are close enough that they do not demonstrate any significant differences in the sum-peak resolution.

In this thesis, it was necessary to perform Doppler corrections for the $p(^{27}\text{Al},\gamma)^{28}\text{Si}$ and $p(^{58}\text{Ni},\gamma)^{59}\text{Cu}$ reactions measured in inverse kinematics (see Chap. 11). The $p(^{27}\text{Al},\gamma)^{28}\text{Si}$ reaction was measured at a resonance energy of $E_{\text{c.m.}} = 956$ keV, which corresponds to a ^{27}Al projectile velocity of $\beta = 0.0459$. On the other hand, the $p(^{58}\text{Ni},\gamma)^{59}\text{Cu}$ reaction was measured at a resonance energy of $E_{\text{c.m.}} = 1400$ keV, which corresponds to a ^{58}Ni projectile velocity of $\beta = 0.0550$. Using these values of β and the GEANT4 angles listed in Table 6.4, the Doppler correction factors were obtained. The final values are listed in Table 6.5.

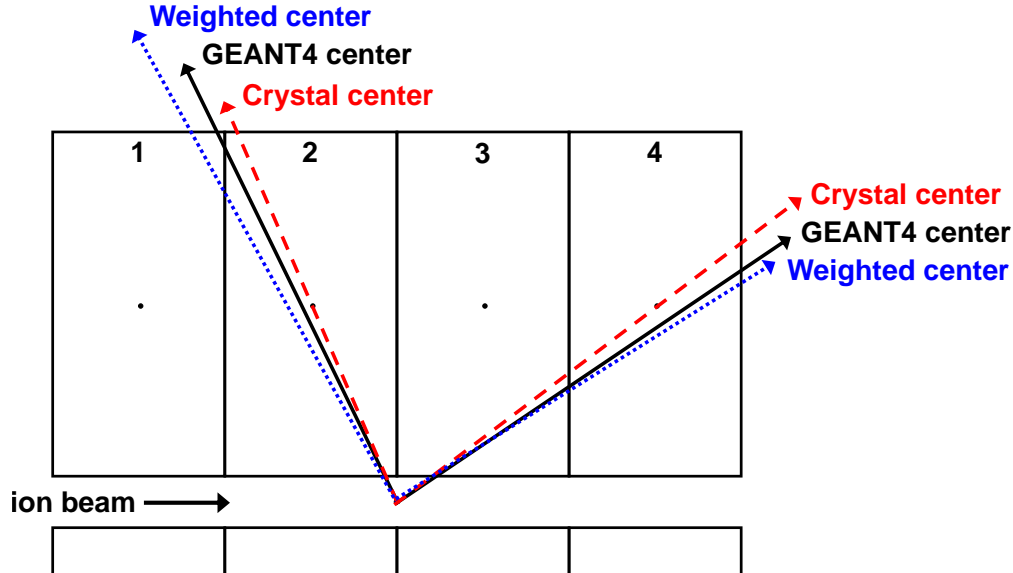


Figure 6.7: Cross-sectional view of the SuN detector showing the different angles used in the Doppler reconstruction. The different angles are to the geometrical center of the NaI crystals, to the weighted center based on the path-length through the crystals, and from SuN’s GEANT4 simulation.

6.4 γ -Summing Efficiency

SuN’s γ -summing efficiency depends not only on the total energy of the deexcitation γ rays, but also on the number of γ rays in the deexcitation cascade. SuN’s efficiency of detecting a single γ ray from the entry state to the ground state is very different than the efficiency of detecting multiple γ rays whose total energy is equal to the entry state. In fact, the efficiency even varies depending on how those multiple γ rays split up the total energy. During an experiment, the capture reaction and subsequent deexcitation of the produced nucleus is happening many times through many different possible γ -ray cascades. Therefore, the average γ -ray multiplicity, or the average number of γ -rays that are emitted in the deexcitation of the entry state, is considered in the analysis. For the majority of (p,γ) and (α,γ) reactions measured with the SuN detector, the average γ -ray multiplicity is not known beforehand and correspondingly, the γ -summing efficiency is not known before

performing the experiment. Therefore, it is necessary to use the information obtained during the measurement of a reaction to determine the average γ -ray multiplicity.

In previous applications of the γ -summing technique, the authors made use of the “in/out ratio” method to determine the average γ -ray multiplicity. This method relies on comparing the number of sum-peak counts for the full 4π solid angle coverage of the detector (“in”) to those with only half of the full solid angle coverage (“out”). For a single γ ray, the ratio of detected counts for half the solid angle compared to the full solid angle is expected to be $1/2$. This means that a sum peak with average multiplicity $\langle M \rangle$ is expected to have an in/out ratio of $(1/2)^{\langle M \rangle}$. While successful, this method can be difficult in low count rate experiments because a small number of counts in the sum peak becomes even tinier when considering only half of the solid angle coverage.

Fortunately, the unique design of the SuN detector provides a new method of determining the average γ -ray multiplicity during an experiment by making use of SuN’s eight segments. This new method is based on the expectation that the higher the γ -ray multiplicity of a cascade, the larger the number of SuN’s segments that will detect γ -ray energy on average. Fig. 6.8 illustrates this concept using GEANT4 simulations of a 10 MeV sum peak for γ -ray multiplicities of two and three. For these calculations, the total 10 MeV excitation energy is divided equally among the emitted γ rays. By selecting the events in the sum-peak region, a histogram of the number of SuN’s segments that detected energy is drawn. This histogram is known as the “hit pattern” of the sum peak. By fitting the hit pattern plots in Fig. 6.8 with a Gaussian, it is clear that the GEANT4 simulation with a multiplicity of three has a higher centroid value than the GEANT4 simulation with a multiplicity two. This means that the average number of SuN’s segments that detected energy for multiplicity three is larger than the average number of SuN’s segments that detected energy with multiplicity two, as

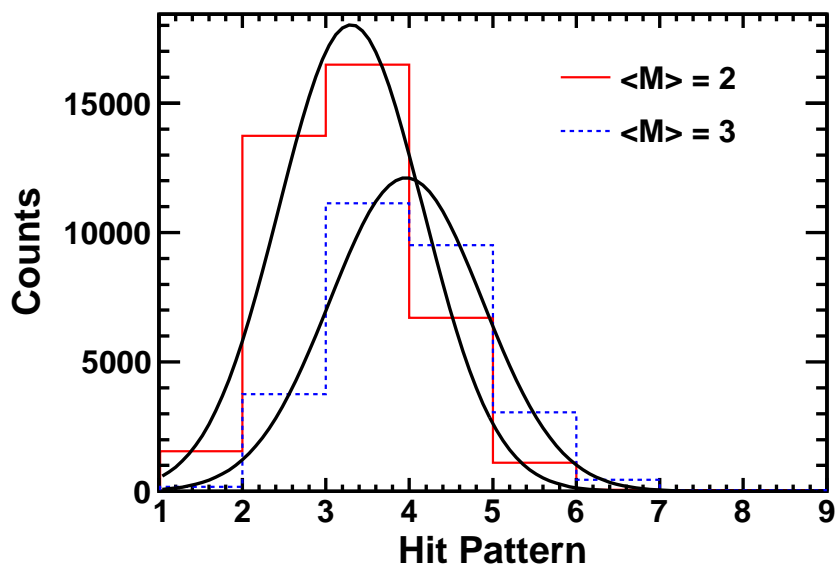


Figure 6.8: Histogram of the number of SuN’s segments that detect energy for events in the sum peak (the “hit pattern”). The spectra are from simulations of the deexcitation of a 10 MeV state with γ -ray multiplicities of $\langle M \rangle = 2$ and $\langle M \rangle = 3$ with the emitted γ rays having equal energy. The spectra are fit with a Gaussian function to determine the hit pattern centroid, and it is shown that the higher the γ -ray multiplicity the higher the average number of SuN’s segments that detect energy.

expected. Through GEANT4 simulations of the SuN detector, the relationship between hit pattern centroids and the average multiplicity is well known. This was verified using resonances of known strength and average multiplicity (see Chap. 7).

When analyzing a reaction, the total γ -summed spectrum is created and the sum-peak region is identified as described in the previous section. For each event within the sum-peak region, the number of segments that detected energy is calculated and used to create the hit pattern spectrum. In cases when the sum peak is sitting on top of a beam-induced background, it is necessary to subtract this background out of the hit pattern spectrum. In certain situations, it may also be advantageous to narrow the bounds of the sum-peak region when creating the hit pattern. Overall, the main goal is to obtain a hit pattern for SuN that is representative of the events in the sum peak of the reaction of interest. Once the desired spectrum is obtained, a Gaussian fitting function is used to determine the hit

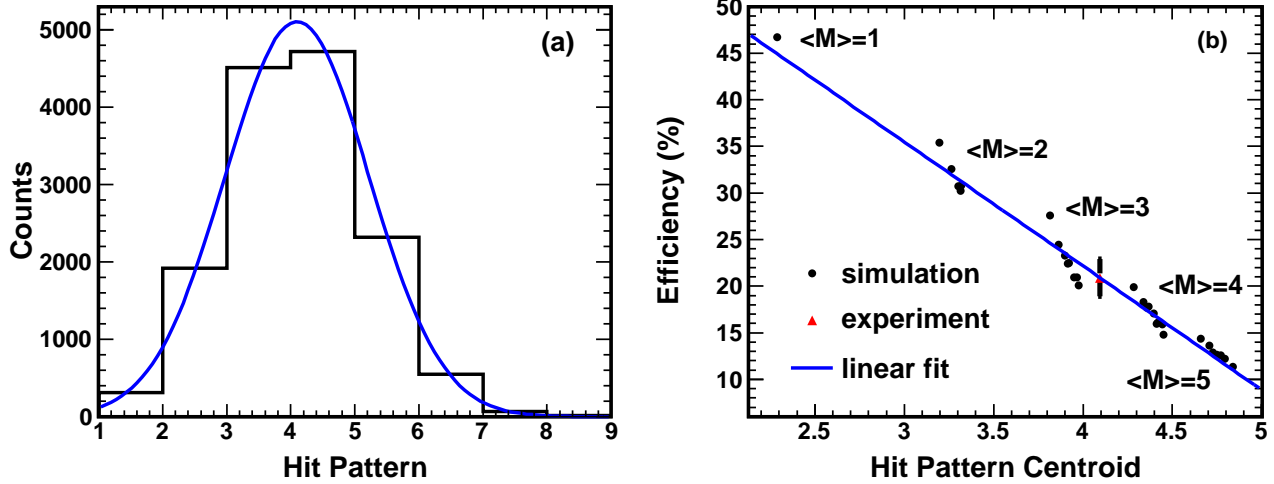


Figure 6.9: Method of determining the experimental γ -summing efficiency for the $^{60}\text{Ni}(\alpha,\gamma)^{64}\text{Zn}$ sum peak shown in Fig. 6.6. Panel (a) shows the hit pattern spectrum for events in the sum peak region and the corresponding Gaussian fit to determine the hit pattern centroid. Panel (b) shows the efficiency and hit pattern centroids from GEANT4 simulations with various γ -ray multiplicities and transitions. The best fit line is also shown, which is used to determine the experimental efficiency.

pattern centroid. The left panel of Fig. 6.9 shows the hit pattern spectrum and its Gaussian fit for the $^{60}\text{Ni}(\alpha,\gamma)^{64}\text{Zn}$ sum peak in Fig. 6.6.

The next step in determining the γ -summing efficiency is to run a series of GEANT4 simulations with the total deexcitation energy equal to the experimental sum-peak energy. The simulations should be performed for a variety of γ -ray multiplicities and transitions to provide a good basis for comparison to the experimental data. The γ -summing efficiency of each simulation is determined by the ratio of number of counts in the sum peak to total number of γ -ray cascades simulated. In addition, the hit pattern centroid is determined using the events in the simulated sum-peak region. After determining the γ -summing efficiency and hit pattern centroid for each simulation, a plot of the results is made. The right panel of Fig. 6.9 contains a plot of γ -summing efficiency versus hit pattern centroid based on the results of 30 simulations with the same total energy as the sum peak of Fig. 6.6. On this plot, the simulations are grouped in order according to their γ -ray multiplicity, with multiplicity 1

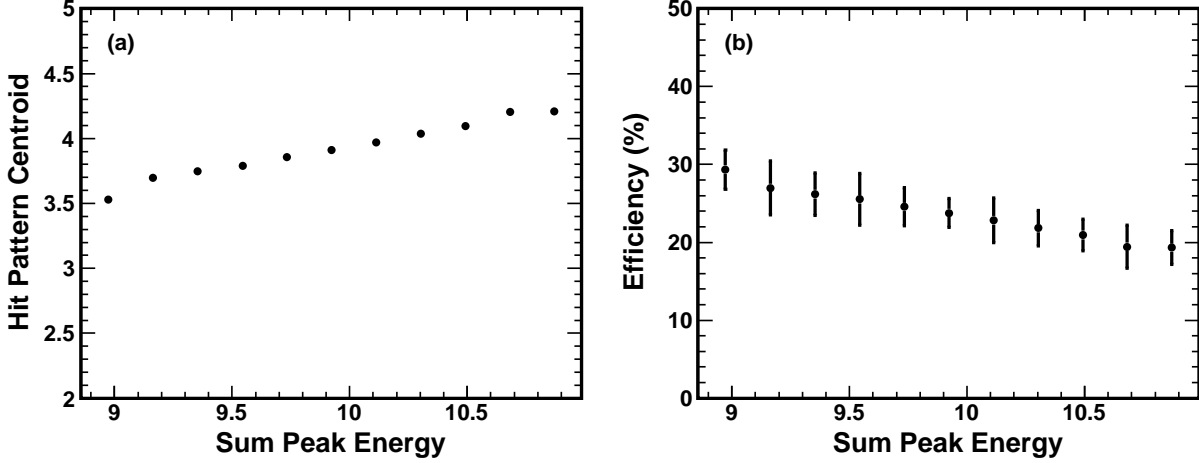


Figure 6.10: Values of (a) hit pattern centroid and (b) γ -summing efficiency plotted against sum-peak energy for the $^{60}\text{Ni}(\alpha,\gamma)^{64}\text{Zn}$ reaction. For the reactions measured in this thesis, the hit pattern centroid and therefore the average γ -ray multiplicity increase with energy, and the γ -summing efficiency decreases with energy.

having a much higher efficiency than multiplicity 5. The various data points in the multiplicity groupings correspond to different possible γ -ray cascades with the same total energy but different transitions between excited states. Next, all of the GEANT4 simulations are used to create a linear fit describing the relationship between hit pattern centroid and γ -summing efficiency. Using the best-fit line and the experimental value of the hit pattern centroid, the experimental γ -summing efficiency and its uncertainty are immediately obtained. Typical uncertainties of the γ -summing efficiency using the hit pattern technique are approximately 10%.

Because the majority of (p,γ) and (α,γ) reactions studied in this thesis produce nuclei in high-lying excited states where many resonances overlap, it can be interesting to look at systematic trends in the hit pattern centroid (and therefore average γ -ray multiplicity) as well as the γ -summing efficiency. Typically as the excitation energy increases in a nucleus, the average γ -ray multiplicity increases and the corresponding γ -summing efficiency decreases. Results for the $^{60}\text{Ni}(\alpha,\gamma)^{64}\text{Zn}$ reaction are shown in Fig. 6.10.

Chapter 7

$^{27}\text{Al}(p,\gamma)^{28}\text{Si}$

The first measurements with the SuN detector at the University of Notre Dame were of the $^{27}\text{Al}(p,\gamma)^{28}\text{Si}$ reaction. This reaction was chosen because it has been measured many times previously and was therefore a well-understood benchmark for comparison of SuN's results. The measurements of the $^{27}\text{Al}(p,\gamma)^{28}\text{Si}$ reaction served as an excellent proof-of-principle of the γ -summing technique with the SuN detector, as well as a check on the analysis procedures of the data.

As discussed in Sec. 4.2, the aluminum target was produced by evaporation at the NSCL and its thickness of $74.7(3.7) \mu\text{g}/\text{cm}^2$ was measured with the RBS technique at Hope College. The target was mounted at the center of the SuN detector, and the energy of the proton beam was changed in small steps, typically 1-2 keV, to scan well-known resonances within $E_p = 2 - 4$ MeV of the $^{27}\text{Al}(p,\gamma)^{28}\text{Si}$ reaction. Fig. 7.1 shows a typical γ -summed spectrum, in this case for the resonance at $E_p = 2517.7$ keV. The spectrum is dominated by the sum peak at 14.012 MeV with additional peaks in the spectrum corresponding to incomplete summation of the γ rays. From previous measurements of the $E_p = 2517.7$ keV resonance, the corresponding entry state in ^{28}Si is known to deexcite to the ground state with the emission of three γ rays of energy 9394, 2839, and 1779 keV 88.2% of the time [109] (see Fig. 7.2 for a simplified level scheme). Therefore, the smaller peaks observed in Fig. 7.1 are found at energies 4.618, 11.173, and 12.233 MeV from when two of the γ rays are detected but the third γ ray escapes undetected. Additionally, a GEANT4 simulation of the $E_p = 2517.7$

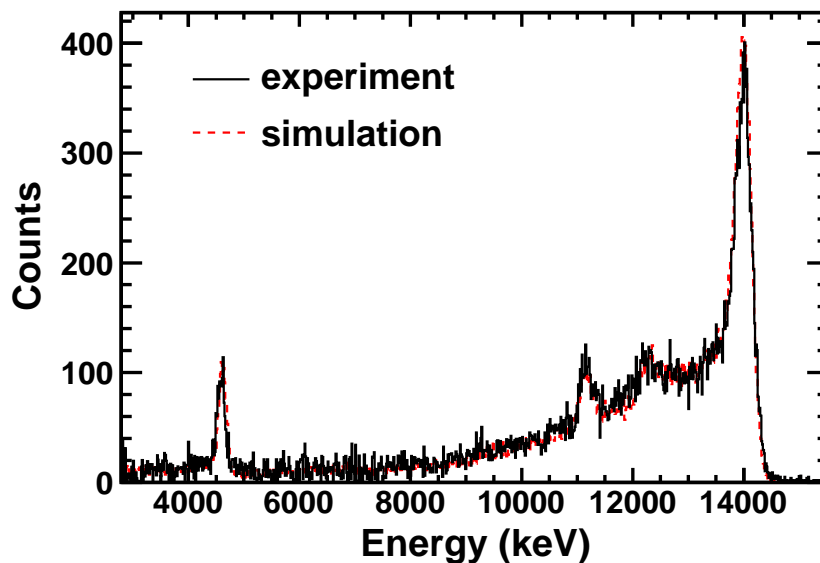


Figure 7.1: Total γ -summed spectrum for the $E_p = 2517.7$ keV resonance in the $^{27}\text{Al}(p,\gamma)^{28}\text{Si}$ reaction. Plotted are the experimental spectrum taken with the SuN detector and the result of GEANT4 simulations.

keV resonance was performed using the known deexcitation γ -ray cascades of ^{28}Si . Fig. 7.1 demonstrates that the GEANT4 simulation accurately matches the experimental data for the SuN detector all the way up to a total energy of above 14 MeV. Excellent agreement between GEANT4 simulations and experimental data was obtained for all of the measured resonances, with subtle differences for some of the higher-energy resonances which could be attributed to incorrect deexcitation cascades in the literature.

In addition to creating a total γ -summed spectrum, the SuN detector also provides insight into the deexcitation cascades through the energy spectra of the eight segments. By drawing the energy spectrum of individual segments for events that have the full sum-peak energy in the γ -summed spectrum, the individual γ -ray transitions can be identified. For example, Fig. 7.3 shows the spectrum of a central segment for the $E_p = 2517.7$ keV resonance for events that lie in the sum-peak region. The dominant γ -ray transitions at 9394, 2839, and 1779 keV are clearly visible, along with an intense peak at 511 keV from an electron-positron

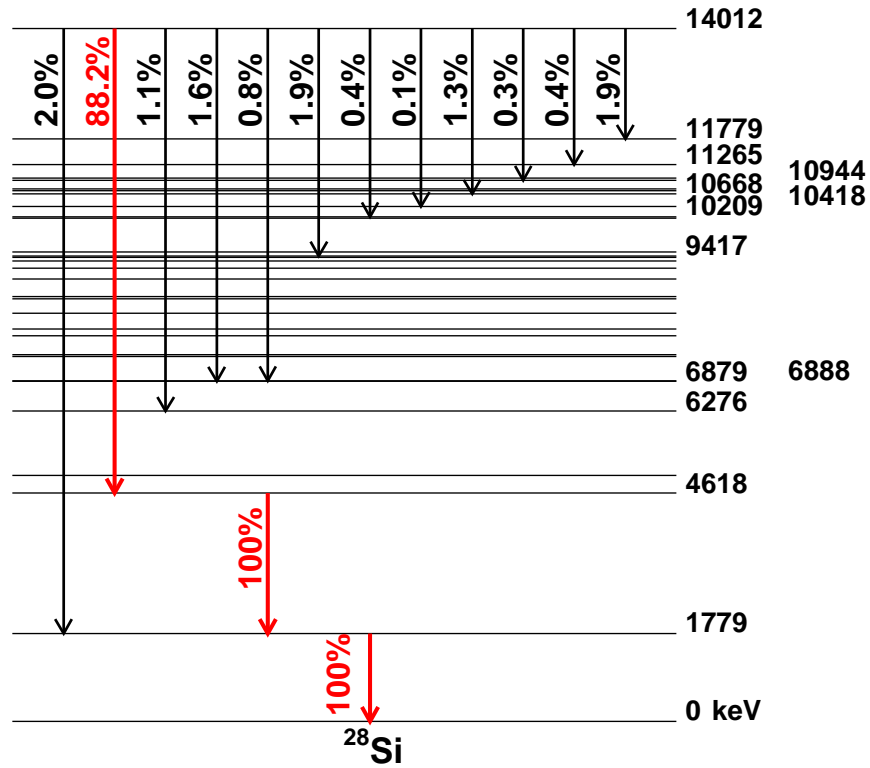


Figure 7.2: Level scheme of ^{28}Si for the $E_p = 2517.7$ keV resonance in the $^{27}\text{Al}(p,\gamma)^{28}\text{Si}$ reaction. For simplicity, only the energy levels and intensities for the primary γ -ray transitions are labeled. The unlabeled levels also participate in the cascades based on their transition probabilities. The most dominant cascade is highlighted and consists of the emission of γ rays with energy 9394, 2839, and 1779 keV.

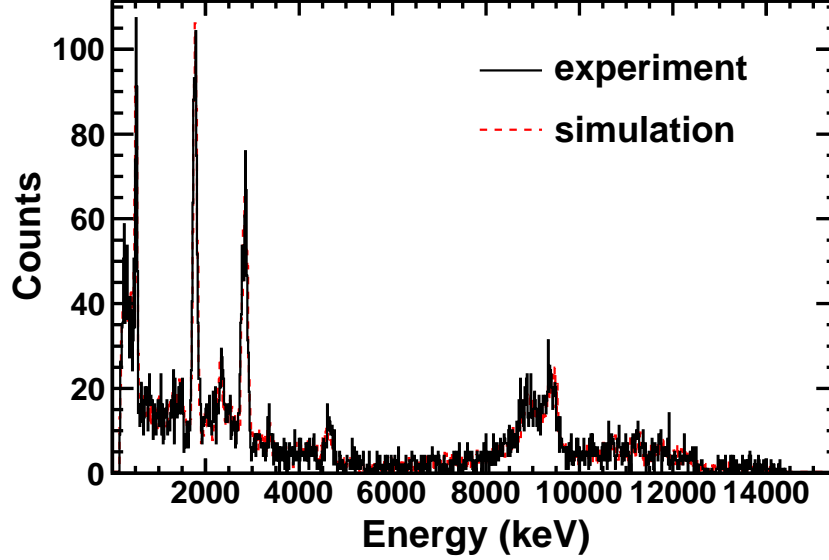


Figure 7.3: Spectrum from one segment of the SuN detector for events in the sum-peak region of the $E_p = 2517.7$ keV resonance in the $^{27}\text{Al}(p,\gamma)^{28}\text{Si}$ reaction. Plotted are the experimental spectrum taken with the SuN detector and the result of GEANT4 simulations.

annihilation occurring in a different segment. Similarly, sometimes a 511 keV γ ray escapes from the plotted segment, which creates the peaks visible 511 keV below the energy of the γ -ray transitions at 8883, 2328, and 1268 keV. The experimental spectrum is matched well by GEANT4 simulation, indicating that the detector response in simulation is correct and that the intensities of all the γ -ray transitions in literature are accurate.

For each measurement, the sum peak was integrated and the γ -summing efficiency determined by the techniques discussed in Chap. 6. The yield of each measurement was determined as the ratio of number of times the $^{27}\text{Al}(p,\gamma)^{28}\text{Si}$ reaction occurred to the number of incoming protons. Fig. 7.4 shows the measured excitation function for all of the data included in the analysis. Additionally, the inset of the figure shows a zoomed-in view of the resonance at $E_p = 3674.9$ keV and its comparison to the theoretical yield of a Breit-Wigner resonance of Eq. 3.14. For each resonance in the excitation function, the area was determined and the resonance strength calculated using Eq. 3.19. Due to lack of experimental data scanning the

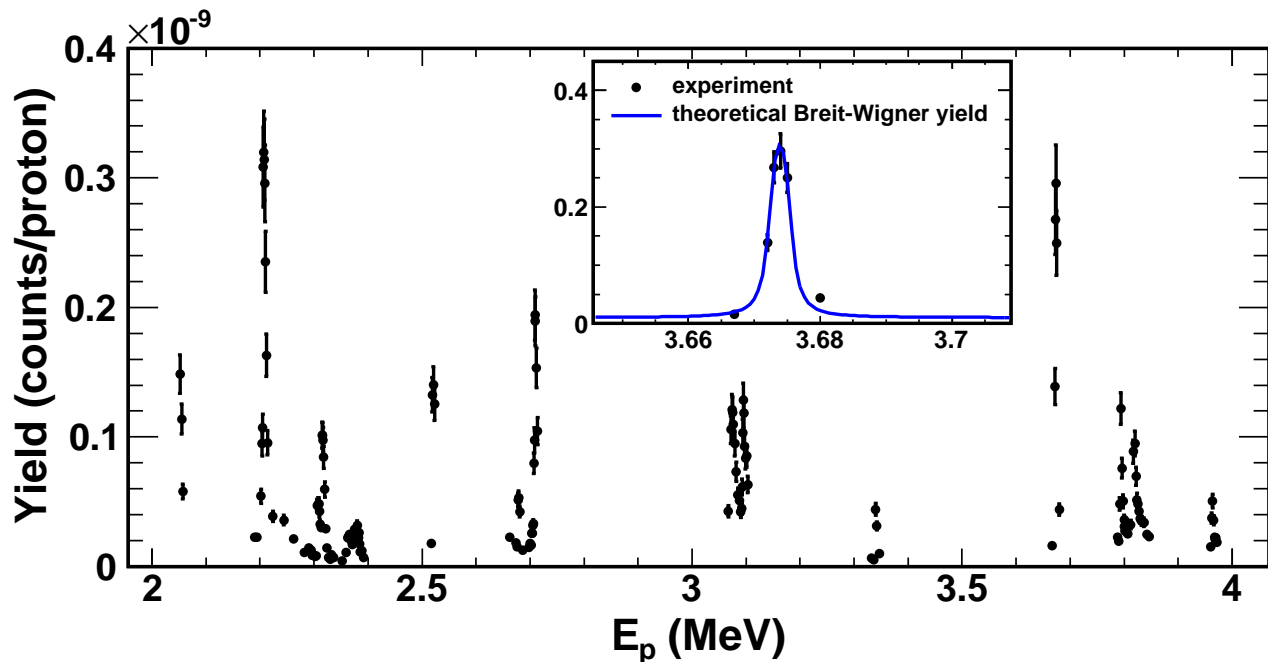


Figure 7.4: Measured excitation function in the region $E_p = 2 - 4$ MeV of the $^{27}\text{Al}(p,\gamma)^{28}\text{Si}$ reaction. The inset shows a zoomed in view around the resonance at $E_p = 3674.9$ keV and a comparison to the theoretical Breit-Wigner yield.

full resonance or the overlap of many resonances, not all of the data could be used to extract a resonance strength. In total, 11 resonances were completely scanned and their resonance strengths compared to previous measurements. The literature values for comparison came from Ref. [110] and Ref. [53, 111], which contain compilations and evaluations of all previous data sets for the $^{27}\text{Al}(p,\gamma)^{28}\text{Si}$ reaction.

The final results for the measurement of the $^{27}\text{Al}(p,\gamma)^{28}\text{Si}$ reaction with the SuN detector are listed in Table 7.1 and plotted in Fig. 7.5. The values of S_p shown are calculated by

$$S_p = \omega\gamma (2J_p + 1) (2J_t + 1) \quad (7.1)$$

where $J_p = 1/2$ is the spin of the proton and $J_t = 5/2$ is the ground-state spin of the ^{27}Al target nuclei. Overall, there is good agreement between the SuN results and the previous measurements. In the case of the $E_p = 2374$ keV resonance, there was a discrepancy between

Table 7.1: Measured resonance strengths for the $^{27}\text{Al}(p,\gamma)^{28}\text{Si}$ reaction for the SuN detector and previous results.

E_p (keV)	SuN	Endt [110]	NACRE [53, 111]
2303.1	3.3 (0.6)	1.6 (0.48)	2.6 (1.3)
2311.9	10.1 (1.8)	6.7 (1.3)	6.72 (0.84)
2359.9	2.8 (0.5)	5.4 (1.62)	1.32 (0.48)
2373.8	3.9 (0.7)	26 (7.8)	4.2 (1.2)
2517.7	14.6 (2.1)	16 (3)	17.2 (1.9)
2675.5	4.7 (1.0)	7.2 (1.4)	7.32 (0.84)
2711.7	16.1 (2.2)	14 (3)	15.5 (3)
3338.4	3.6 (0.7)	4.3 (0.9)	4.2 (8)
3674.9	32.3 (4.5)	35 (7)	33.5 (6.7)
3791.7	11.9 (1.6)	7.3 (1.5)	7.1 (1.7)
3960.8	5.4 (0.8)	3.3 (0.7)	3.2 (0.6)

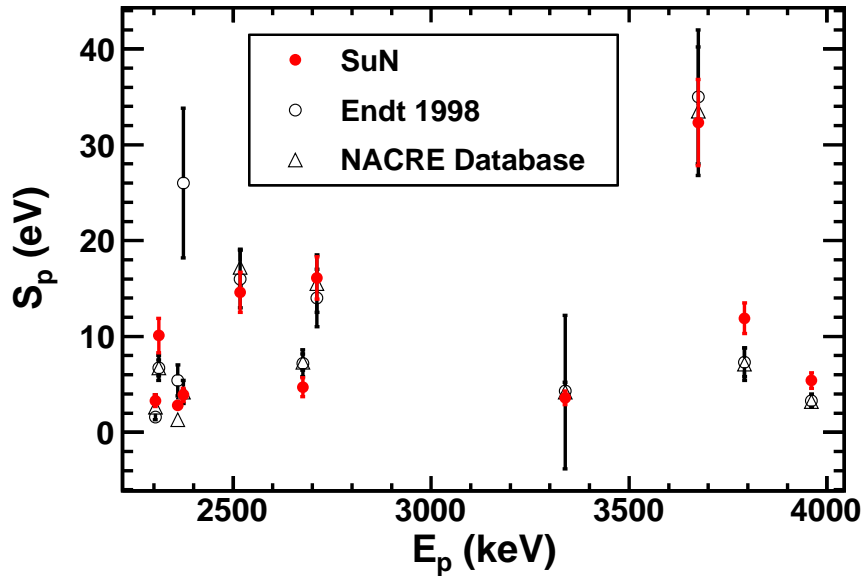


Figure 7.5: Resonance strengths of the $^{27}\text{Al}(p,\gamma)^{28}\text{Si}$ reaction measured with the SuN detector compared to previous results. Overall good agreement is achieved.

the resonance strength values listed in Ref. [110] and Ref. [111] and the SuN results agree nicely with the value given in Ref. [111]. The agreement of the $^{27}\text{Al}(p,\gamma)^{28}\text{Si}$ resonance strengths between SuN results and previous measurements demonstrated the validity of measurements with the SuN detector. The same techniques that gave these results are also used in the more astrophysically interesting measurements contained in the following chapters.

Chapter 8

$^{74}\text{Ge}(p,\gamma)^{75}\text{As}$

One of the significant results obtained during the SuN experimental campaign at the University of Notre Dame was the measurement of the $^{74}\text{Ge}(p,\gamma)^{75}\text{As}$ reaction and its role in p-process nucleosynthesis. The motivation for measuring the $^{74}\text{Ge}(p,\gamma)^{75}\text{As}$ reaction was that it was previously identified in a p-process sensitivity study by Rapp et al. [37] as playing an important role in the production of the lightest of the p nuclei, ^{74}Se . The authors found that varying the $^{74}\text{Ge}(p,\gamma)^{75}\text{As}$ reaction rate within its theoretical uncertainty had a direct impact on the production of ^{74}Se and therefore deemed this reaction “particularly important” to experimentally measure.

^{74}Se is produced in the high-temperature layers of type II supernovae (SNII) which are undergoing p-process nucleosynthesis. The higher temperatures of the stellar environment allow for charged particle capture reactions on less massive seed nuclei, and (p, γ) and (p,n) reactions can dominate over the typical photodisintegration scenario. The dominant reaction chain for the production of ^{74}Se is $^{74}\text{Ge}(p,\gamma)^{75}\text{As}(p,n)^{75}\text{Se}(\gamma,n)^{74}\text{Se}$, which is shown in Fig. 8.1. The main destruction reaction is $^{74}\text{Se}(\gamma,\alpha)^{70}\text{Ge}$ with smaller contributions from $^{74}\text{Se}(\gamma,p)^{73}\text{As}$. Prior to the measurement, most of the other reaction rates had been well constrained by previous experiments. The $^{74}\text{Se}(n,\gamma)^{75}\text{Se}$ reaction rate was well known through several measurements and in particular by the measurement of Dillmann et al. [112] focusing on p-process relevant energies. Similarly, the cross section of the $^{75}\text{As}(p,n)^{75}\text{Se}$ reaction had been measured down to the reaction threshold ($Q = -1.646$ MeV) [113, 114], and the

^{73}Br	^{74}Br	^{75}Br	^{76}Br	^{77}Br	^{78}Br
^{72}Se	^{73}Se	^{74}Se	^{75}Se	^{76}Se	^{77}Se
^{71}As	^{72}As	^{73}As	^{74}As	^{75}As	^{76}As
^{70}Ge	^{71}Ge	^{72}Ge	^{73}Ge	^{74}Ge	^{75}Ge
^{69}Ga	^{70}Ga	^{71}Ga	^{72}Ga	^{73}Ga	^{74}Ga

Figure 8.1: A zoomed in section of the nuclear chart showing the dominant reaction flow producing ^{74}Se in the p process.

$^{70}\text{Ge}(\alpha,\gamma)^{74}\text{Se}$ reaction had been measured at p-process energies covering the majority of the Gamow window [115]. Therefore, the $^{74}\text{Ge}(\text{p},\gamma)^{75}\text{As}$ reaction was the remaining reaction to measure in the production chain of ^{74}Se .

Investigating the production of ^{74}Se is significant because, unlike the majority of the light p nuclei, ^{74}Se is surprisingly overproduced by approximately a factor of 3 (see Fig. 1.7). A similar, but not as pronounced, behavior is observed for the second lightest p nucleus, ^{78}Kr . As mentioned, the lighter p nuclei are the only ones influenced by the (p, γ) and (p,n) reactions taking place at high temperatures, and it is therefore crucial to constrain the involved nuclear reaction rates and reduce the relevant nuclear physics uncertainties to provide deeper insight into this alternative reaction mechanism. Since the $^{74}\text{Ge}(\text{p},\gamma)^{75}\text{As}$ reaction was the last unconstrained reaction in the production chain of ^{74}Se , it could perhaps explain the overproduction of ^{74}Se and be an important step towards understanding the discrepancy in the overall production of the puzzling light p nuclei.

The measurements were performed with proton energies in the range $E_p = 1.6 - 4.2$ MeV

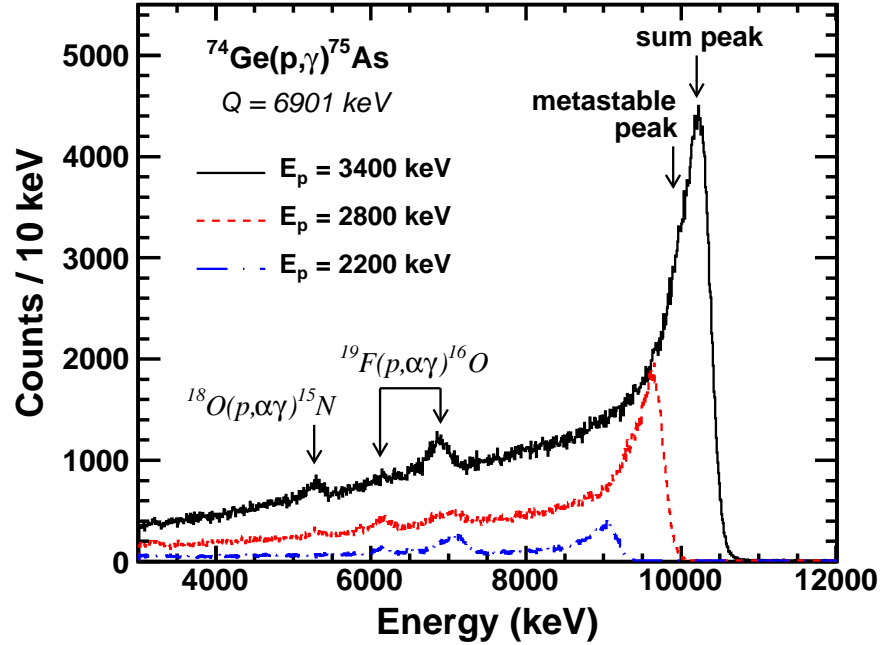


Figure 8.2: Sum peak spectra for three different proton energies E_p normalized to the same number of incoming protons. The location of the sum peak and the metastable peak are indicated for $E_p = 3400$ keV.

and an enriched ^{74}Ge target. As discussed in Sec. 4.2, the target was made by evaporating 97.55% enriched ^{74}Ge powder onto a thick tantalum backing, and the thickness of $340(17)$ $\mu\text{g}/\text{cm}^2$ was determined through RBS analysis. For the measurement of the $^{74}\text{Ge}(p,\gamma)^{75}\text{As}$ reaction, the beam intensity was maintained below 10 enA to ensure minimal dead time in the SuN detector. The resulting total γ -summed spectra from the SuN detector are shown in Fig. 8.2 for three different energies. Above 3 MeV the spectra are dominated by the sum peak of the $^{74}\text{Ge}(p,\gamma)^{75}\text{As}$ reaction. The shift in location of the sum peak is due to the changing center of mass energy, and the different intensities of the sum peaks give indication that the cross section is increasing with energy. Small signatures of the contaminants in the target can be observed around 7 MeV coming from the $^{19}\text{F}(p,\alpha\gamma)^{16}\text{O}$ reaction, and around 5.3 MeV from the $^{18}\text{O}(p,\alpha\gamma)^{15}\text{N}$ reaction caused by a small amount of oxygen present in the target.

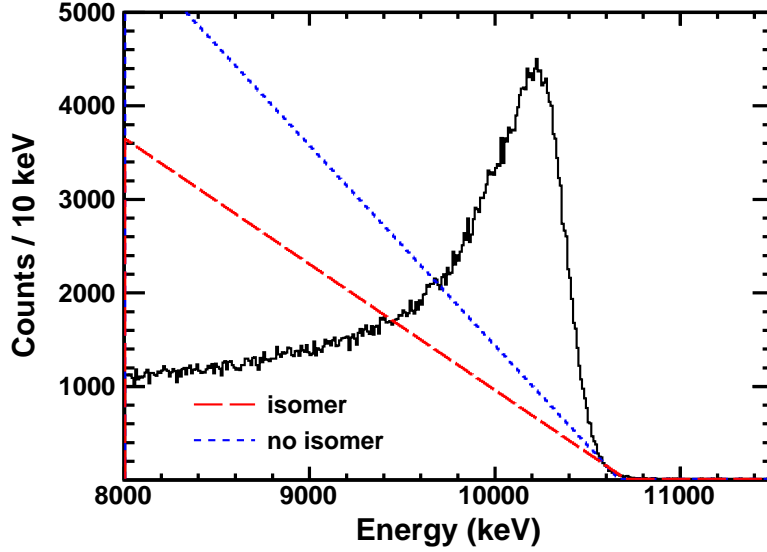


Figure 8.3: Total γ -summed spectrum for the $^{74}\text{Ge}(p,\gamma)^{75}\text{As}$ measurement at $E_p = 3400$ keV. Also plotted is the linear background with and without including the 304 keV isomer.

When determining the number of counts in the sum peak, it was necessary to take into account the 304 keV isomeric state in ^{75}As with a half-life of 17.62 ms [108]. As this half-life was much longer than the 300 ns event window used in the analysis, any deexcitation to the isomeric state does not get summed into the sum peak. Instead, these events are found 304 keV below the sum peak energy (E_Σ). To include the events populating the isomeric state in the analysis, it was decided to expand the sum-peak region to $(E_\Sigma - 3\sigma - 304 \text{ keV}, E_\Sigma + 3\sigma)$. Once the sum-peak region was defined, a linear background was subtracted and the total number of counts above the linear background was determined as discussed in Sec. 6.3. Fig. 8.3 shows the difference in linear backgrounds with and without including the 304 keV isomeric state. The γ -summing efficiencies (Sec. 6.4) ranged from 28.1(2.3)% at $E_p = 1.6$ MeV to 21.8(1.7)% at $E_p = 4.2$ MeV. Using the number of sum-peak counts and SuN's summing efficiency, the total number of reaction products was determined and the total (p,γ) cross sections and astrophysical S-factors were calculated using Eq. 2.3 and Eq. 2.13. The results are listed in Table 8.1.

Table 8.1: Cross sections and astrophysical S-factors for the $^{74}\text{Ge}(p,\gamma)^{75}\text{As}$ reaction.

$E_{\text{c.m.}}$ (MeV)	σ (mb)	S-factor (GeV b)	$E_{\text{c.m.}}$ (MeV)	σ (mb)	S-factor (GeV b)
1.554	0.045 ± 0.005	6251 ± 708	3.246	15.5 ± 1.7	2005 ± 218
1.763	0.19 ± 0.02	6464 ± 714	3.345	17.5 ± 1.9	1799 ± 196
1.961	0.51 ± 0.06	5796 ± 637	3.444	15.5 ± 1.7	1279 ± 139
2.159	1.11 ± 0.12	4910 ± 540	3.543	13.0 ± 1.4	875 ± 95
2.357	2.17 ± 0.24	4196 ± 463	3.642	6.08 ± 0.66	334 ± 36
2.554	3.78 ± 0.41	3534 ± 387	3.741	5.46 ± 0.59	247 ± 27
2.752	6.23 ± 0.68	3062 ± 333	3.839	3.68 ± 0.40	138 ± 15
2.950	10.5 ± 1.1	2914 ± 317	3.938	2.96 ± 0.32	94 ± 10
3.049	11.6 ± 1.3	2468 ± 268	4.037	2.93 ± 0.32	78 ± 9
3.148	13.2 ± 1.4	2177 ± 237	4.136	3.13 ± 0.34	71 ± 8

The uncertainties reported in Table 8.1 include both statistical and systematic errors. The primary sources of error are the 5% uncertainty in target thickness, 5% uncertainty in beam charge collection, and the 8% uncertainty in summing efficiency. There is also an uncertainty in the integral of the sum peak due to a possible contribution from the $^{73}\text{Ge}(p,\gamma)^{74}\text{As}$ reaction with a Q-value of 6852 keV, only 49 keV below the Q-value of the $^{74}\text{Ge}(p,\gamma)^{75}\text{As}$ reaction. However, the cross section of the $^{73}\text{Ge}(p,\gamma)^{74}\text{As}$ reaction is predicted to be lower by a factor of 1.5 to 25 throughout the energy range measured [116], and the isotopic composition of ^{73}Ge in the target was only 1.9%. Thus, an upper bound contribution of 1.5% to the sum peak from the $^{73}\text{Ge}(p,\gamma)^{74}\text{As}$ reaction was estimated.

As the analysis of the $^{74}\text{Ge}(p,\gamma)^{75}\text{As}$ reaction cross section measurement was nearing completion, a research group in Köln, Germany published their results on the same reaction [74]. A comparison of values in this dissertation to the Köln data set is shown in Fig. 8.4. The two separate measurements agree within the uncertainty, with the Köln data giving systematically slightly lower cross sections, 6% to 21% below the present results. This systematic effect could be attributed to the two different measurement techniques. The Köln

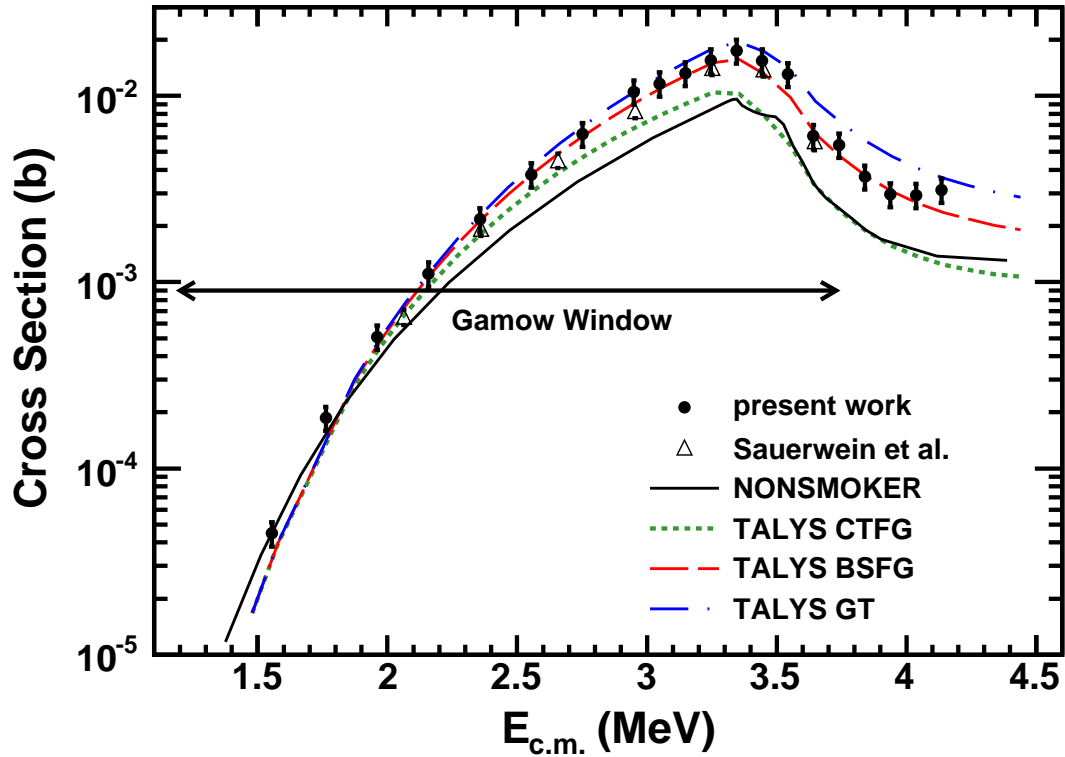


Figure 8.4: Cross section vs. center of mass energy plot for the $^{74}\text{Ge}(p,\gamma)^{75}\text{As}$ reaction. The measurements of this dissertation (solid circles) and previous data of Ref. [74] (open triangles) are compared to theoretical calculations using NON-SMOKER and TALYS 1.4 nuclear reaction codes. The most accurate reproduction of the data is the TALYS back-shifted Fermi gas model (BSFG).

group performed the measurement using the in-beam method (Sec. 4.1.3), where four high-purity germanium detectors were used to detect the individual ^{75}As deexcitation γ -rays and their angular distribution. This method may underestimate the total cross section if there are low intensity γ -rays that are below the detectable limits or high energy γ -rays that have a low efficiency for being detected. In Fig. 8.4 both data sets show an increase in cross section values until an energy around $E_{\text{c.m.}} = 3.3$ MeV where the (p,n) reaction channel opens. The SuN measurements extend to both higher and lower energies than the Köln data. At the lower energies this allows for a better characterization of the energy dependence of the cross section. At the higher energies, above the energy where the (p,n) channel opens, the larger energy coverage allows for a more sensitive selection of the appropriate nuclear level density model.

The theoretical calculations of the Köln group. [74] were done using the statistical model code SMARAGD [117]. The authors conclude that the best description of the data was one which used the standard microscopic optical model potential of Jeukenne, Lejeune, and Mahaux (JLM) [118] with the proton width multiplied by two. In Fig. 8.4, the solid black curve represents standard NON-SMOKER [116] statistical model calculations, which is the predecessor code to SMARAGD and is therefore representative of the Köln calculations. The NON-SMOKER calculations do not reproduce the energy dependence of the cross section, as an incorrect slope in the curve leads to an underestimation of the cross section at higher energies and an overestimation of the cross section at lower energies. Scaling the proton widths by two, as done in Ref. [74], would better match the data at higher energies, but then further overestimate the cross section at lower energies. This large difference at lower energies, up to 70% at 1.55 MeV, is only noticeable with the new data presented here.

Therefore, aiming at an improved description of the data, additional theoretical calcu-

lations were performed using the TALYS 1.4 nuclear reaction code [119]. The remaining three curves in Fig. 8.4 are TALYS calculations for different nuclear level densities. All were performed using the semimicroscopic optical model of Bauge, Delaroche, and Girod [120], which is a reparametrization of the JLM optical model to cover a wider energy range of scattering data. TALYS calculations were performed using level densities from the constant temperature and Fermi gas model (CTFG) [121, 122], back-shifted Fermi gas model (BSFG) [123], generalized superfluid model (GSM) [124, 125], and the microscopic level densities from Goriely’s table (GT) [126] and Hilaire’s table (HT) [127]. The calculations using level densities from GSM and HT are left off of Fig. 8.4, as they produce results similar to CTFG for the present reaction. Default parameter values were used in TALYS 1.4 except for options for the JLM potential and different nuclear level densities. As seen in Fig. 8.4 the best description of the $^{74}\text{Ge}(p,\gamma)^{75}\text{As}$ reaction is achieved when using the back-shifted Fermi gas model (BSFG). The BSFG model uses the Fermi gas model down to zero energy with a shift in energy to account for nucleon pairing. This shift attempts to correct for the fact that the Fermi gas model is based on non-interacting fermions. In TALYS, the BSFG model uses the modification of Ref. [128] to fix the divergence of the nuclear level density at zero energy.

Using the BSFG nuclear level density and JLM optical model potential, new astrophysical reaction rates were calculated with TALYS 1.4 and their values are shown in Table 8.2. Furthermore, in Fig. 8.5 the ratio of the new reaction rate calculations compared to the reaction rates presented in the Köln paper [74] and to the standard REACLIB [129] rates used in astrophysical calculations is shown. Within the relevant temperature window for the p process, 1.8 - 3.3 GK, the new rates are higher than the standard REACLIB rates with a maximum increase of 27%, but below the rates proposed by the Köln group with a

Table 8.2: Reaction rates for the $^{74}\text{Ge}(p,\gamma)^{75}\text{As}$ reaction from TALYS 1.4 calculations with the JLM optical model potential and BSFG nuclear level density which provide the most accurate reproduction of experimental data.

T (GK)	Rate ($\text{cm}^3 \text{mol}^{-1} \text{s}^{-1}$)	T (GK)	Rate ($\text{cm}^3 \text{mol}^{-1} \text{s}^{-1}$)
0.10	4.629×10^{-31}	1.50	6.228×10^0
0.15	4.310×10^{-21}	2.00	1.369×10^2
0.20	4.173×10^{-16}	2.50	1.101×10^3
0.25	4.429×10^{-13}	3.00	4.742×10^3
0.30	5.130×10^{-11}	3.50	1.345×10^4
0.40	2.638×10^{-8}	4.00	2.845×10^4
0.50	1.556×10^{-6}	5.00	6.961×10^4
0.60	3.055×10^{-5}	6.00	9.787×10^4
0.70	3.146×10^{-4}	7.00	9.502×10^4
0.80	2.130×10^{-3}	8.00	7.379×10^4
0.90	1.073×10^{-2}	9.00	5.182×10^4
1.00	4.338×10^{-2}	10.00	3.600×10^4

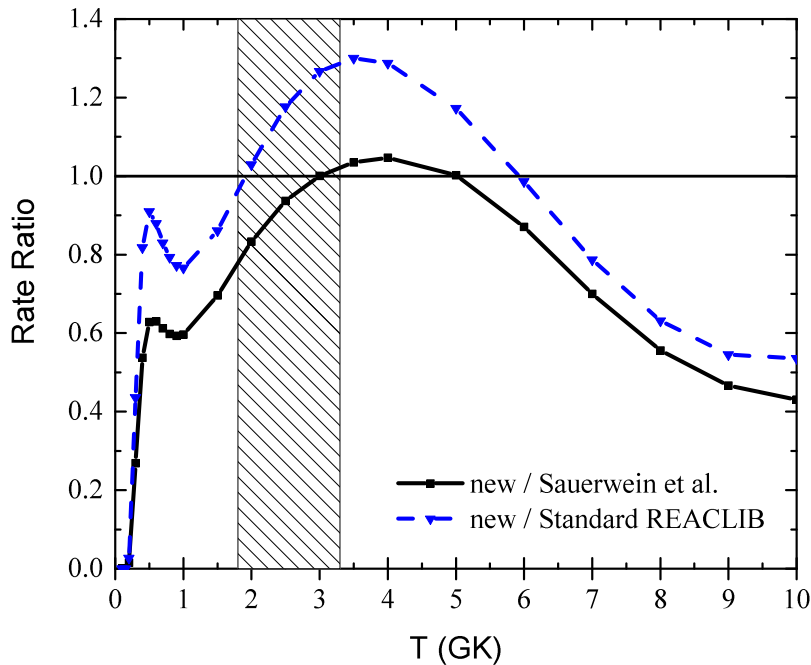


Figure 8.5: Ratio of reaction rates in Table 8.2 to those presented in Ref. [74] and to the standard REACLIB [129] rates. The shaded area indicates the p-process relevant temperatures of 1.8 - 3.3 GK.

maximum decrease of 20%. The large change in the new reaction rates at low T compared to the other two data sets can be attributed to the different description of cross section at low energies. Because the TALYS model gives a more accurate reproduction of the energy dependence of the experimental data, the reaction rates in Table 8.2 are new recommended rates for the $^{74}\text{Ge}(p,\gamma)^{75}\text{As}$ reaction.

The impact of the experimental cross sections on the final abundance of the p nuclei was investigated using the post-processing code NucNet Tools [130] to follow the reaction network of a $25M_{\odot}$ SNII when the shock front passes through the O/Ne layer. In this model, the initial seed abundances and temperature and density profiles were taken to be the same as Rapp et al. [37]. The p process was then followed through 11 different mass layers and the final abundances of the p nuclei were summed for all the included layers. This reaction network uses reactions that are all based on theoretical cross sections from REACLIB [129], whose uncertainty arises from uncertainties in the optical model potential and nuclear level density models used. The theoretical uncertainty of the $^{74}\text{Ge}(p,\gamma)^{75}\text{As}$ reaction cross section was investigated using TALYS 1.4, and the spread in predicted cross sections can be seen in Fig. 8.4. An uncertainty up to a factor of three was determined based on the difference between the constant temperature Fermi gas model (CTFG) and the microscopic level densities taken from Goriely’s Table (GT). In Fig. 8.6, the impact of the $^{74}\text{Ge}(p,\gamma)^{75}\text{As}$ reaction on the final abundance of the lightest p nucleus, ^{74}Se , is shown for the $25M_{\odot}$ SNII model. The cumulative mass fraction for ^{74}Se is plotted against the maximum temperature of the mass layer. The maximum temperature of the mass layer decreases along the abscissa, corresponding to integrating the mass fraction from the inside layer to the outside layer of the supernova. The majority of ^{74}Se is produced in the inner (hotter) layers, as the mass fraction does not increase when including layers with a maximum

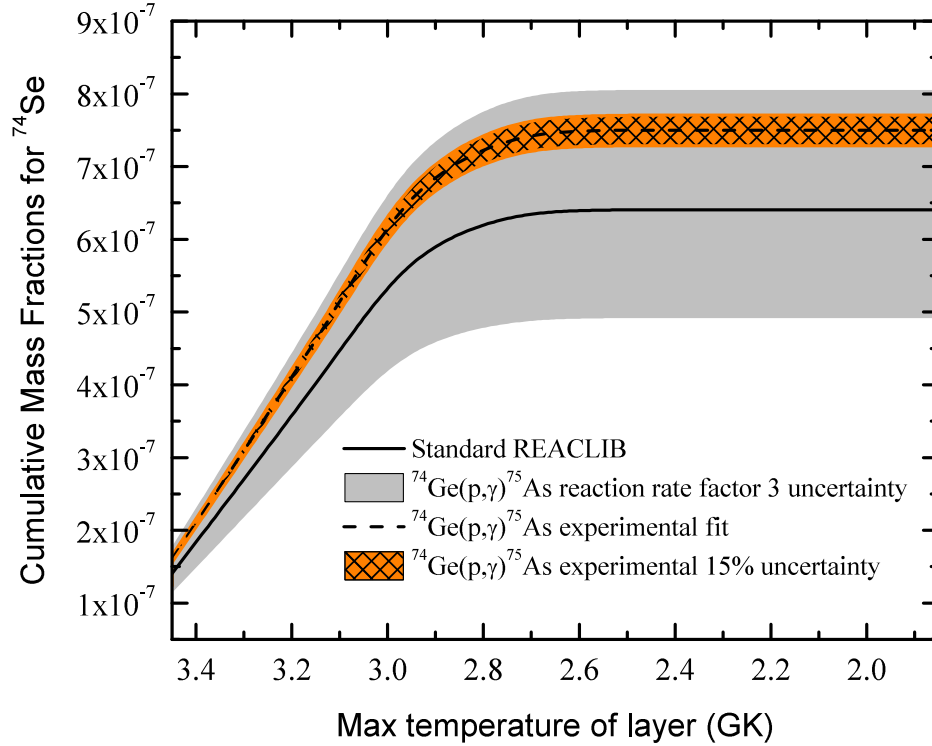


Figure 8.6: Cumulative mass fraction of ^{74}Se from a model of the p process in a type II supernova, plotted as a function of the maximum temperature of the mass layer included. See text for details.

temperature below 2.6 GK. The solid black line and shaded grey area represent the results for ^{74}Se using the standard REACLIB $^{74}\text{Ge}(p,\gamma)^{75}\text{As}$ reaction rate and a factor of three increase and decrease, respectively. Increasing the reaction rate by 3 leads to a 25% increase in the production of ^{74}Se , while decreasing the reaction rate by 3 leads to a 23% decrease in the production of ^{74}Se . The overall spread in the final cumulative mass fraction of ^{74}Se when relying on the theoretical predictions and uncertainties of the $^{74}\text{Ge}(p,\gamma)^{75}\text{As}$ reaction spans from 4.94×10^{-7} to 8.03×10^{-7} , which is a factor of 1.6.

Also in Fig. 8.6, the impact of the new experimental reaction rates on the final mass fraction of ^{74}Se is shown. The dashed black line and shaded hatched area show the ^{74}Se mass fraction when performing the network calculation with experimental values and un-

certainties for the $^{74}\text{Ge}(p,\gamma)^{75}\text{As}$ reaction. The uncertainty in the production of ^{74}Se from the $^{74}\text{Ge}(p,\gamma)^{75}\text{As}$ reaction is reduced to a factor of 1.05 with the reaction rates presented here, with an overall increase in the mean mass fraction from 6.4×10^{-7} to 7.5×10^{-7} . As mentioned previously, ^{74}Se is strongly overproduced in p-process models, and this overproduction is further enhanced with the experimental results reported here. Thus, the end result of the $^{74}\text{Ge}(p,\gamma)^{75}\text{As}$ measurement contained in this chapter is that the uncertainty in the production of ^{74}Se in the p process is greatly reduced, but the general overproduction of ^{74}Se compared to its observed abundance remains.

Chapter 9

$^{58}\text{Ni}(\alpha,\gamma)^{62}\text{Zn}$

The story of the $^{58}\text{Ni}(\alpha,\gamma)^{62}\text{Zn}$ reaction is unique to this thesis in that the astrophysical motivation for its measurement is different from the other reactions contained here. Rather than playing an important role in the p process of type II supernovae, the $^{58}\text{Ni}(\alpha,\gamma)^{62}\text{Zn}$ reaction instead contributes to the nucleosynthesis inside of a type Ia supernovae (SNIa). Its importance was first discovered by Bravo and Martínez-Pinedo [131] when performing a sensitivity study quantifying the influence of individual reaction rates on the nucleosynthesis in SNIa. For the study, the authors used a one-dimensional model of a Chandrasekhar-mass white dwarf and varied the reaction rates up and down by a factor of 10. Overall, the authors concluded that nucleosynthesis was relatively insensitive to the change of individual reaction rates, but many reactions were identified as relevant for having a direct impact on the final abundance of particular isotopes. One such reaction was the $^{58}\text{Ni}(\alpha,\gamma)^{62}\text{Zn}$ reaction, which was selected for its impact on the production of ^{62}Ni , ^{63}Cu , and ^{64}Zn . The relation of the $^{58}\text{Ni}(\alpha,\gamma)^{62}\text{Zn}$ reaction to these isotopes is shown in the nuclear chart of Fig. 9.1.

The astrophysical scenario in which the $^{58}\text{Ni}(\alpha,\gamma)^{62}\text{Zn}$ reaction is expected to play an important role is during the α -rich freeze-out from nuclear statistical equilibrium (NSE) (see Sec. 1.3.4). In the innermost layers of SNIa, temperatures and densities are sufficiently high to reach NSE, and a large portion of the material in NSE is expected to undergo α -rich freeze-out. For the Chandrasekhar-mass white dwarf studied in Ref. [131] it was noticed that the inner $0.4M_{\odot}$ reached NSE, of which $0.24M_{\odot}$ underwent α -rich freeze-out. After

^{59}Ga	^{60}Ga	^{61}Ga	^{62}Ga	^{63}Ga	^{64}Ga	^{65}Ga	^{66}Ga
^{58}Zn	^{59}Zn	^{60}Zn	^{61}Zn	^{62}Zn	^{63}Zn	^{64}Zn	^{65}Zn
^{57}Cu	^{58}Cu	^{59}Cu	^{60}Cu	^{61}Cu	^{62}Cu	^{63}Cu	^{64}Cu
^{56}Ni	^{57}Ni	^{58}Ni	^{59}Ni	^{60}Ni	^{61}Ni	^{62}Ni	^{63}Ni
^{55}Co	^{56}Co	^{57}Co	^{58}Co	^{59}Co	^{60}Co	^{61}Co	^{62}Co
^{54}Fe	^{55}Fe	^{56}Fe	^{57}Fe	^{58}Fe	^{59}Fe	^{60}Fe	^{61}Fe

Figure 9.1: A zoomed in section of the nuclear chart showing the $^{58}\text{Ni}(\alpha,\gamma)^{62}\text{Zn}$ reaction and the isotopes most influenced by its reaction rate in SNIa (^{62}Ni , ^{63}Cu , ^{64}Zn).

α -rich freeze-out, the composition of the layer is dominated by isotopes in the iron region and α -particles that did not reassemble into heavier nuclei. Thus it is expected that α -induced reactions on nuclei in the iron region are important for the final abundance pattern, including the $^{58}\text{Ni}(\alpha,\gamma)^{62}\text{Zn}$ reaction.

The $^{58}\text{Ni}(\alpha,\gamma)^{62}\text{Zn}$ reaction has been measured three times previously, all over 50 years ago. Morinaga [132] and Ball et al. [133] performed cross section measurements using the activation technique (Sec. 4.1.1) with energies $E_\alpha = 10.6 - 31.0$ MeV. After irradiation, both measurements included an additional step of chemically separating zinc from other elements before counting the decay of ^{62}Zn with Geiger counters. McGowan and collaborators [134] extended the measurements to lower energies by using thick-target yields from enriched ^{58}Ni targets. The yield was determined every 100 keV within the beam energy range of $E_\alpha = 4.9 - 6.1$ MeV and the cross section determined by differentiating the yield curve.

The measurement of the $^{58}\text{Ni}(\alpha,\gamma)^{62}\text{Zn}$ reaction cross section was performed using the SuN detector and the γ -summing technique. The FN Tandem Van de Graaff Accelerator at

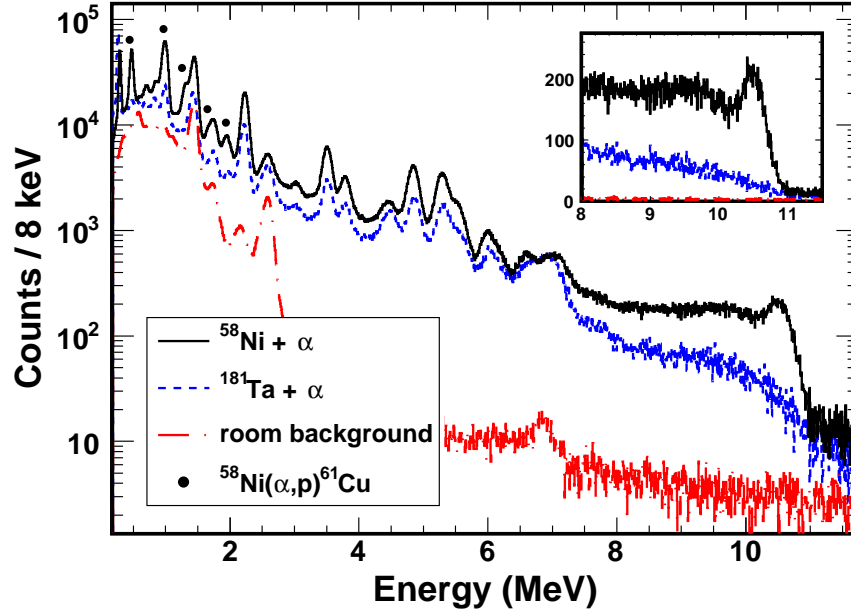


Figure 9.2: Experimental spectra from the SuN detector for measurements at $E_\alpha = 7.7$ MeV. The spectra correspond to ^{58}Ni (solid black), thick tantalum backing (dotted blue), and normalized room background (dot-dashed red). The inset shows a zoom around the sum-peak region of the $^{58}\text{Ni}(\alpha,\gamma)^{62}\text{Zn}$ reaction.

the University of Notre Dame was used to accelerate $^4\text{He}^{2+}$ nuclei to energies $E_\alpha = 5.5 - 9.5$ MeV. The beam current was varied between 4 – 60 enA in order to balance count rate with minimal detection dead time. For the present work the dead time was kept below 1.2%. For each data run the total charge collected from the $^4\text{He}^{2+}$ beam was between 7 – 159 μC . The ^{58}Ni target was isotopically enriched to 95(5)% and its thickness of $930 \pm 46 \mu\text{g}/\text{cm}^2$ was measured using the RBS technique. Trace amounts of carbon and oxygen on the front and back surfaces of the target were revealed during the RBS measurements. The target thickness corresponded to a beam energy loss of 0.42 MeV and 0.30 MeV at $E_\alpha = 5.5$ MeV and $E_\alpha = 9.5$ MeV, respectively [135].

A total γ -summed spectrum from the SuN detector for the $^{58}\text{Ni}(\alpha,\gamma)^{62}\text{Zn}$ reaction with $E_{\text{c.m.}} = 7039$ keV and $Q = 3364.27$ keV is shown in Fig. 11.3 (solid black line). At

Table 9.1: Cross sections for the $^{58}\text{Ni}(\alpha,\gamma)^{62}\text{Zn}$ reaction.

$E_{\text{c.m.}}^{\text{max}}$ (MeV)	$E_{\text{c.m.}}^{\text{min}}$ (MeV)	$E_{\text{c.m.}}^{\text{eff}}$ (MeV)	σ (μb)
5.143	4.750	4.988	3.13 ± 0.44
5.330	4.946	5.171	4.70 ± 0.60
5.517	5.143	5.360	6.69 ± 1.04
5.704	5.337	5.548	9.65 ± 1.34
6.078	5.723	5.922	15.3 ± 2.4
6.452	6.112	6.298	22.2 ± 3.5
6.826	6.496	6.673	34.0 ± 6.1
7.201	6.883	7.051	52.4 ± 7.1
7.574	7.268	7.428	66.9 ± 9.7
7.949	7.649	7.805	92.8 ± 15.1
8.415	8.129	8.277	138.8 ± 22.1
8.884	8.606	8.749	158.9 ± 25.2

higher energies, both room background and beam-induced background contributions to the spectrum are reduced allowing the sum peak to be clearly visible at 10.4 MeV. The source of room background in the region of the sum peak comes from cosmic rays. During the experiment the ^{58}Ni target was mounted in front of a thick tantalum backing. Thus, the beam induced background was determined by taking data without the ^{58}Ni target in place so that the beam was impinging solely onto the tantalum backing. Additional peaks were visible in the low energy region of the ^{58}Ni spectrum that originate from the $^{58}\text{Ni}(\alpha,\text{p}\gamma)^{61}\text{Cu}$ reaction which has a higher cross section than the $^{58}\text{Ni}(\alpha,\gamma)^{62}\text{Zn}$ reaction at this energy by approximately two orders of magnitude [134, 136]. The additional nickel isotopes have (α,γ) Q values larger than the $^{58}\text{Ni}(\alpha,\gamma)^{62}\text{Zn}$ reaction, and thus do not contribute in the sum-peak region. Also, these additional nickel isotopes are present in very low amounts in the target and there was no indication of their (α,γ) reactions in the summed spectra.

The number of counts in the sum peak and the γ -summing efficiency were determined at each energy step, and then the reaction cross section was calculated using Eq. 2.3. SuN's γ -

summing efficiency ranged from 26.7(2.8)% at $E_{c.m.} = 4.943$ MeV to 17.4(2.3)% at $E_{c.m.} = 8.742$ MeV. The results of the cross section calculations are displayed in Table 9.1. In the table, the first two columns contain the maximum and minimum energies of the beam due to the thickness of the target. The third column contains the effective energy for each data point taking into account the variation of the cross section in the target. The last column lists the calculated cross sections. Of the uncertainty reported, roughly 3% comes from statistical uncertainties, 5% from the beam charge collection, 5% from the target thickness, 5% from the target enrichment, and 10% - 15% from the detection efficiency. The uncertainty in energy from the accelerator is 4 keV at all energies.

A plot of the $^{58}\text{Ni}(\alpha,\gamma)^{62}\text{Zn}$ reaction cross section is shown in Fig. 9.3. The present work is in agreement with the previous results of Ref. [134] and extends the measurements to higher energies. The increased energy coverage of the experimental cross section allows for a more sensitive study of the energy dependence of the cross section and provides a better test for theoretical models. The theoretical calculations of the $^{58}\text{Ni}(\alpha,\gamma)^{62}\text{Zn}$ reaction were performed using the code SMARAGD [137, 138] which is based on the nuclear statistical model (see Sec. 3.2). According to Ref. [139], the nuclear statistical model is expected to be valid down to 0.12 GK for the $^{58}\text{Ni}(\alpha,\gamma)^{62}\text{Zn}$ reaction. Since this is well below the relevant temperature range of 2-5 GK for which the $^{58}\text{Ni}(\alpha,\gamma)^{62}\text{Zn}$ reaction is expected to play a role in the nucleosynthesis of SNIa, the use of the nuclear statistical model is well founded. The Gamow window (see Sec. 2.4) for the $^{58}\text{Ni}(\alpha,\gamma)^{62}\text{Zn}$ reaction at 2 GK is from approximately 3 to 5 MeV with a maximum contribution to the rate at 4 MeV, and at 5 GK the Gamow window is from 4 to 7 MeV with a maximum contribution at 5.25 MeV [54]. As shown in Fig. 9.3, the experimental values cover only the upper part of this energy window, and theoretical predictions are required for the lower energies.

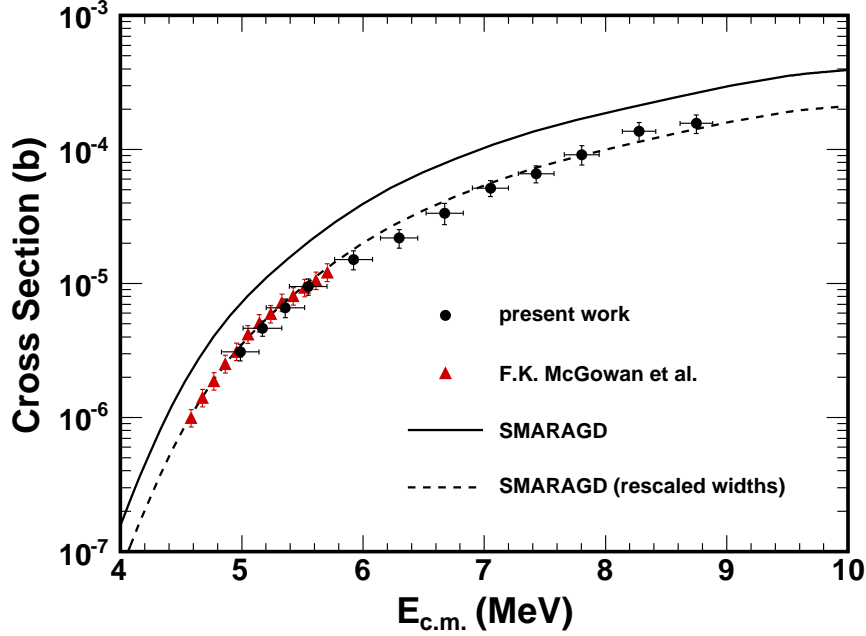


Figure 9.3: Cross section of the $^{58}\text{Ni}(\alpha,\gamma)^{62}\text{Zn}$ reaction for the present work (black circles), previous data of Ref. [134] (red triangles), and theoretical calculations from the SMARAGD code [137]. A good description of the data was obtained by modifying the α width and the γ -to-proton width ratio (dashed line).

The initial SMARAGD calculation systematically overestimated the cross section values by approximately a factor of 2, as shown with the solid line of Fig. 9.3. Since this theoretical value is representative of the standard value that gets used in nucleosynthesis calculations, the previously accepted reaction rate for the $^{58}\text{Ni}(\alpha,\gamma)^{62}\text{Zn}$ reaction was overestimated by approximately a factor of 2. The investigation of how to modify the theoretical calculation to best describe the data is summarized in Fig. 9.4, which shows the sensitivity of the $^{58}\text{Ni}(\alpha,\gamma)^{62}\text{Zn}$ cross section to variations in partial widths. For the energy range here, the emission of γ rays, neutrons, protons, and α particles was considered and therefore their partial widths were varied. The sensitivity is defined as [140]

$$\Omega_{S_q} = \frac{v_{\Omega} - 1}{v_q - 1} \quad (9.1)$$

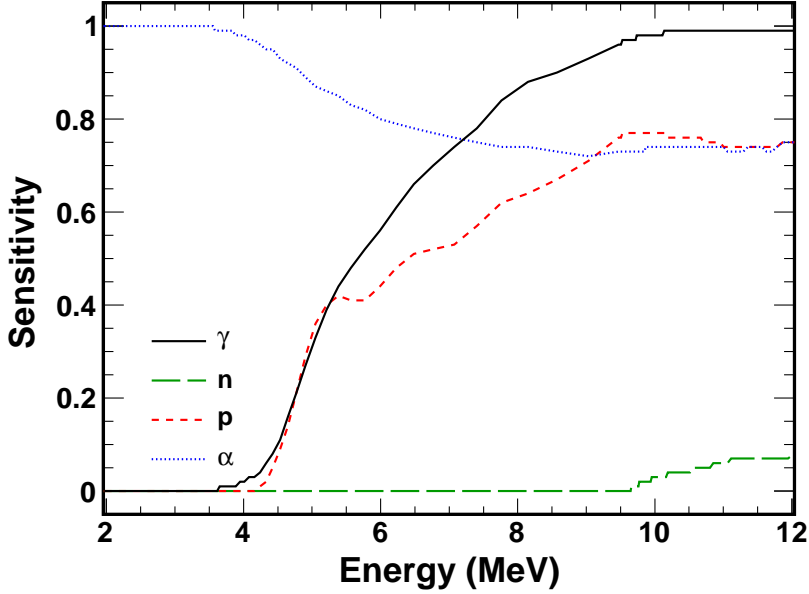


Figure 9.4: Absolute values of the sensitivity of the $^{58}\text{Ni}(\alpha,\gamma)^{62}\text{Zn}$ cross section as function of energy, when separately varying γ , neutron, proton, and α widths.

where q is the quantity being changed and Ω is the resulting quantity. A change in q is given by the factor $v_q = q_{new}/q_{old}$ and the subsequent change in Ω is given by the factor $v_\Omega = \Omega_{new}/\Omega_{old}$. In the current context, the quantity q is an averaged width used in the reaction model and the resulting quantity Ω is the reaction cross section. Using these definitions, the sensitivity $\Omega_{S_q} = 0$ when there is no change in the cross section after changing the partial width and $\Omega_{S_q} = 1$ when the cross section changes by the same factor as the change in the partial width.

Below 4 MeV the $^{58}\text{Ni}(\alpha,\gamma)^{62}\text{Zn}$ reaction cross section is exclusively sensitive to the α width with the sensitivity to the α width persisting throughout the energy region plotted. This low-energy region is also important for the calculation of the astrophysical reaction rate and reactivity [139]. Conversely, there is very little sensitivity to the neutron width even for energies above the neutron emission threshold at $E_{c.m.} = 9.526$ MeV. The remaining two parameters, the proton and γ widths, show an increasing effect on the cross section

with increasing energy in the region between 4 and 10 MeV. As mentioned, the default SMARAGD calculation overestimated the experimental data but accurately reproduced the energy dependence of the cross section. Because the energy dependence was reproduced well and the sensitivity to the α width was present for all energies, it was expected that rescaling the alpha width could provide a good description of the data. It was determined that the α width obtained with the optical potential of [141] has to be scaled by a factor 0.45 to match the low energy data below 6 MeV. However, at higher energies where the cross section sensitivity to the α width is reduced, there were still small deviations between the SMARAGD calculation and the experimental data. By increasing the γ -to-proton width ratio by 10%, an improved agreement with the data at the upper end of the measured energy range was achieved. The γ - and proton widths cannot be constrained separately with data from only this reaction and only the increase in ratio can be determined.

The SMARAGD calculation with the rescaled widths is shown as dashed line in Fig. 9.3, which matches the experimental data very well. Although the scaling factors for the α - width and γ -to-proton width ratio provide an excellent description of the $^{58}\text{Ni}(\alpha,\gamma)^{62}\text{Zn}$ cross section, calculations using these scaling factors underproduce the $^{58}\text{Ni}(\alpha,p)^{61}\text{Cu}$ experimental data [134, 136] by a factor of three. Further theoretical work is required to obtain a full understanding of α -induced reaction cross sections on ^{58}Ni , which was beyond the scope of this thesis.

Since there is no indication from the data that the energy dependence of the cross section changes towards even lower energies, the modified widths were used to calculate new stellar reactivities, which are shown in Table 9.2. These stellar reactivities are dominated by the ground-state cross sections with only small influence from thermally excited states in ^{58}Ni . The ground-state contributions are 100% at 2 GK and 95% at 5 GK and thus the

Table 9.2: Stellar reactivities for the $^{58}\text{Ni}(\alpha,\gamma)^{62}\text{Zn}$ reaction.

T (GK)	Reactivity ($\text{cm}^3 \text{mol}^{-1} \text{s}^{-1}$)	T (GK)	Reactivity ($\text{cm}^3 \text{mol}^{-1} \text{s}^{-1}$)
0.10	6.623×10^{-62}	2.00	2.268×10^{-7}
0.15	1.971×10^{-50}	2.50	2.045×10^{-5}
0.20	2.068×10^{-43}	3.00	5.000×10^{-4}
0.30	1.171×10^{-34}	3.50	5.407×10^{-3}
0.40	3.546×10^{-29}	4.00	3.399×10^{-2}
0.50	2.649×10^{-25}	4.50	1.461×10^{-1}
0.60	2.293×10^{-22}	5.00	4.755×10^{-1}
0.70	4.941×10^{-20}	6.00	2.812×10^0
0.80	4.070×10^{-18}	7.00	9.844×10^0
0.90	1.666×10^{-16}	8.00	2.443×10^1
1.00	4.020×10^{-15}	9.00	4.755×10^1
1.50	2.679×10^{-10}	10.00	7.688×10^1

reactivities are well constrained by experimental data. Table 9.3 contains a fit to the stellar reactivities using the standard 7 parameter REACLIB format [64], which is commonly used in astrophysical calculations.

After calculating new reactivities, their effect on the nucleosynthesis of SNIa was investigated. The reduction in the rate of $^{58}\text{Ni}(\alpha,\gamma)^{62}\text{Zn}$ is expected to translate into a decrease in the abundance of ^{62}Zn and other nuclei linked by subsequent reaction chains, e.g.

Table 9.3: REACLIB parameters for the $^{58}\text{Ni}(\alpha,\gamma)^{62}\text{Zn}$ reaction.

Parameter	Value
a_0	5.194217×10^1
a_1	– 2.314329×10^0
a_2	– 2.528868×10^1
a_3	– 5.651307×10^1
a_4	– 1.088296×10^0
a_5	1.763373×10^{-1}
a_6	3.858753×10^1

Table 9.4: Changes to the nucleosynthesis in SNIa models. (1) Chandrasekhar-mass delayed detonation model with $\rho_{\text{DDT}} = 3.9 \times 10^7 \text{ g/cm}^3$. (2) Explosion of a sub-Chandrasekhar white dwarf of $1.025 M_{\odot}$ C-O core surrounded by a $0.055 M_{\odot}$ He envelope.

$v_{\Omega} - 1$	Delayed detonation	Sub-Chandrasekhar
-0.05	^{64}Zn	^{62}Ni
-0.04	^{62}Ni	
-0.02	$^{63}\text{Cu}, ^{66}\text{Zn}$	$^{63}\text{Cu}, ^{66}\text{Zn}, ^{69}\text{Ga}$
-0.01		$^{64}\text{Zn}, ^{65}\text{Zn}, ^{73}\text{Ge}$

$^{62}\text{Zn}(\alpha, \gamma)^{66}\text{Ge}$, $^{62}\text{Zn}(p, \gamma)^{63}\text{Ga}(p, \gamma)^{64}\text{Ge}$, and so on. After the decay of the radioactive isotopes, the result is a decrease of the ejected abundances of ^{62}Ni , ^{66}Zn , ^{63}Cu , ^{64}Zn , and others. In the temperature range in which α -rich freeze-out takes place, namely from 2-5 GK, the new reaction rates given by Table 9.3 are smaller than the standard REACLIB [129] rates by a factor of 0.45. From Ref. [131], these lower rates correspond to an expected decrease in the ejected abundance of ^{62}Ni by approximately 6-7%.

Simulations of SNIa were performed with both the standard REACLIB [129] rates and the new rates following the same methodology and codes as described in Ref. [131]. Calculations were done for both a delayed detonation of a Chandrasekhar-mass white dwarf and a thermonuclear explosion of a sub-Chandrasekhar white dwarf. The relative change in the ejected abundances of the most sensitive species is listed in Table 9.4. The results agree with the prior estimate and have a maximum sensitivity of approximately 5% for the abundances of ^{62}Ni and ^{64}Zn . Additional calculations were performed with different sets of deflagration-to-detonation transition densities, ρ_{DDT} , and initial metallicities, but their effect is small and the maximum sensitivities never exceed the values reported in Table 9.4. It was found that in general, the sensitivities increase with metallicity and with ρ_{DDT} .

In summary, the $^{58}\text{Ni}(\alpha, \gamma)^{62}\text{Zn}$ reaction cross section results contained in this chapter

agree well with previous measurements and expand to energies not covered by prior experiments. The standard theoretical calculation by the SMARAGD code overproduced the measured cross section, but multiplying the α width by a factor of 0.45 accurately reproduced the data. New reactivities were reported, and the new reaction rates used in nucleosynthesis calculations for SNIa. It was determined that the new rates have at most a 5% effect on the ejected abundances of several isotopes, all in cases where a significant portion of the mass participates in α -rich freeze-out.

Chapter 10

Additional (α, γ) Measurements

This chapter contains the first ever measurements of the $^{90}\text{Zr}(\alpha, \gamma)^{94}\text{Mo}$, $^{92}\text{Zr}(\alpha, \gamma)^{96}\text{Mo}$, and $^{74}\text{Ge}(\alpha, \gamma)^{78}\text{Se}$ reaction cross sections, which are relevant for the production of the lightest p nuclei. As discussed in Sec. 1.4, this region is especially interesting to study due to the large discrepancies between astrophysical calculations and the observed abundances. Models of the p process predict a notable underproduction of the $^{92,94}\text{Mo}$ and $^{96,98}\text{Ru}$ isotopes of greater than a factor of 10, while simultaneously predicting a significant overproduction in the amount of ^{74}Se by approximately a factor of 3 [37].

In general, there is limited existing experimental data for (α, γ) reactions in the p process, with less than 20 of the relevant (α, γ) reactions being measured to date [36]. Due to this lack of experimental data, reaction networks of the p process rely heavily on theoretical reaction rates which typically have large uncertainties. The $^{90}\text{Zr}(\alpha, \gamma)^{94}\text{Mo}$, $^{92}\text{Zr}(\alpha, \gamma)^{96}\text{Mo}$, and $^{74}\text{Ge}(\alpha, \gamma)^{78}\text{Se}$ measurements in this chapter expand the existing experimental database for (α, γ) reactions and fit into the larger effort aimed at constraining the reaction theory relevant to the p process through systematic measurements across a large mass and energy range.

In addition to the global systematic studies, efforts have been made to identify a smaller list of reactions which have the largest impact on the final abundances of the p nuclei. Such sensitivity studies are valuable because they inform experimentalists which reactions are the most crucial to measure. One such sensitivity study by Rauscher [38] took the approach of

identifying the isotope of each element where the (γ, p) or (γ, α) photodisintegration rates are comparable to the (γ, n) rates. As discussed in Sec. 1.4, near stability the (γ, n) reactions dominate, but as the isotopes become more neutron-deficient, the (γ, p) or (γ, α) reactions may proceed with a higher rate. Accurately constraining the reaction rates at these “branching points” is critical for correctly modeling the mass flow of the p process. Because the locations of the branching points at a given temperature rely solely on the nuclear properties, it is possible to identify potentially critical reactions independently of the astrophysical model.

In Rauscher’s study [38], the branching point in the molybdenum isotopes was determined to be at ^{94}Mo , at which point the (γ, α) reaction is expected to proceed at a higher rate than the (γ, n) reaction for p-process temperatures. However, the two reaction channels have reaction rates that are within the theoretical uncertainty of each other, which makes the identification of ^{94}Mo as a branching point highly sensitive to the individual reaction rates. This is illustrated in Fig. 10.1, which shows REACLIB reaction rates [129] for the photodissociation of ^{94}Mo through the (γ, n) , (γ, p) , and (γ, α) channels as a function of temperature. The uncertainty in the rates was taken to be a factor of 10 for the (γ, α) reaction and a factor of 5 for the (γ, n) and (γ, p) reactions. Within the p-process window of 1.8 – 3.3 GK, the $^{94}\text{Mo}(\gamma, \alpha)^{90}\text{Zr}$ and $^{94}\text{Mo}(\gamma, n)^{93}\text{Mo}$ reactions are within the theoretical uncertainty of each other. If the actual $^{94}\text{Mo}(\gamma, \alpha)^{90}\text{Zr}$ reaction rate is towards the lower end of its uncertainty band, then the (γ, n) reaction would proceed with a higher rate, and the branching point in molybdenum would be shifted to more neutron deficient isotopes, potentially increasing the production of the isotope ^{92}Mo . Therefore, the $^{90}\text{Zr}(\alpha, \gamma)^{94}\text{Mo}$ was identified as one of the critical reactions to investigate experimentally to improve the understanding of the p-process mass flow in this mass region [38].

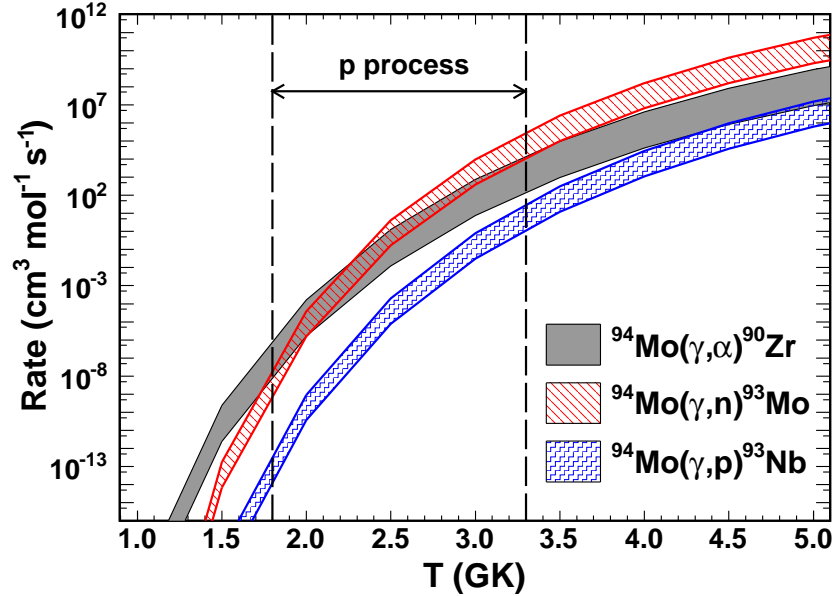


Figure 10.1: REACLIB reaction rates [129] as a function of temperature for the photodissociation of ^{94}Mo through the (γ,n) , (γ,p) , and (γ,α) channels. The width of the curves corresponds to a factor of 10 uncertainty in the (γ,α) reaction rate and a factor of 5 uncertainty in the (γ,n) and (γ,p) rates. Within the p-process window of 1.8 – 3.3 GK, the $^{94}\text{Mo}(\gamma,\alpha)^{90}\text{Zr}$ reaction may have a higher rate than the $^{94}\text{Mo}(\gamma,n)^{93}\text{Mo}$ reaction and could therefore be a branching point in the p process [38].

The measurements were performed at the University of Notre Dame and consisted of impinging α particles onto isotopically-enriched targets. The FN Tandem Van de Graaff accelerator was used to accelerate the $^4\text{He}^{2+}$ beam to energies between 9.5 to 12.0 MeV in 0.5 MeV steps. The beam intensity was set between 4.3×10^9 and 2.5×10^{10} pps as needed to maximize the count rate and minimize detection dead time. The dead time was below 1.8% for all measurements reported here. The ^{90}Zr and ^{92}Zr targets were self-supporting foils with thicknesses of 966(48) and 946(47) $\mu\text{g}/\text{cm}^2$, respectively, and both were isotopically enriched to 98(1)%. In order to eliminate scattered α particles from hitting the beam pipe after passing through the Zr foils, a tantalum backing was placed directly behind each foil during the measurements. In the $^{74}\text{Ge}(\alpha,\gamma)^{78}\text{Se}$ case, the ^{74}Ge was made through the evaporation of 97.55% enriched ^{74}Ge powder onto tantalum backing and had a thickness of 340(17)

$\mu\text{g}/\text{cm}^2$. Additional details on the fabrication of the ^{74}Ge target and the RBS thickness measurements can be found in Sec. 4.2.

The (α,γ) reactions on ^{90}Zr , ^{92}Zr , and ^{74}Ge reported here have Q values of 2064.2, 2758.9, and 6028.4 keV, respectively. When combined with the beam energy of $E_\alpha = 9.5 - 12.0$ MeV, these Q values produce sum peaks in SuN's total γ -summed spectrum from approximately 11 to 17 MeV. The sum peaks for these (α,γ) reactions had low intensities, and the statistical error associated with the sum-peak integral was 6 – 14%. The largest source of uncertainty in the measurements was the γ -summing efficiency, with uncertainty values of up to $\pm 17\%$.

10.1 $^{90}\text{Zr}(\alpha,\gamma)^{94}\text{Mo}$ Results

The $^{90}\text{Zr}(\alpha,\gamma)^{94}\text{Mo}$ reaction was measured in the energy range of $E_{\text{c.m.}} = 9.0 - 11.4$ MeV. The total γ -summed spectrum for an energy of $E_{\text{c.m.}} = 9.94$ MeV is shown in Fig. 10.2 along with the normalized room-background spectrum. The majority of low energy peaks in the spectrum can be attributed to contaminants in the tantalum backing used during the measurements. At an energy of approximately 12 MeV, the sum peak of the $^{90}\text{Zr}(\alpha,\gamma)^{94}\text{Mo}$ reaction is indicated. Also indicated is the peak around 9 MeV, which originates from neutrons released in the $^{90}\text{Zr}(\alpha,n)^{93}\text{Mo}$ reaction.

The cross section values (see Eq. 2.3) and corresponding S-factors (see Eq. 2.13) for the $^{90}\text{Zr}(\alpha,\gamma)^{94}\text{Mo}$ reaction are listed in Table 10.1. The effective energy of each data point was calculated by taking into account the variation in cross section through the ^{90}Zr target. In this calculation, the slope of the cross section was taken from the best-fit theoretical calculation to the data (see Sec. 10.4). The energy loss through the target was between 0.22 and 0.26 MeV for the measurements here.

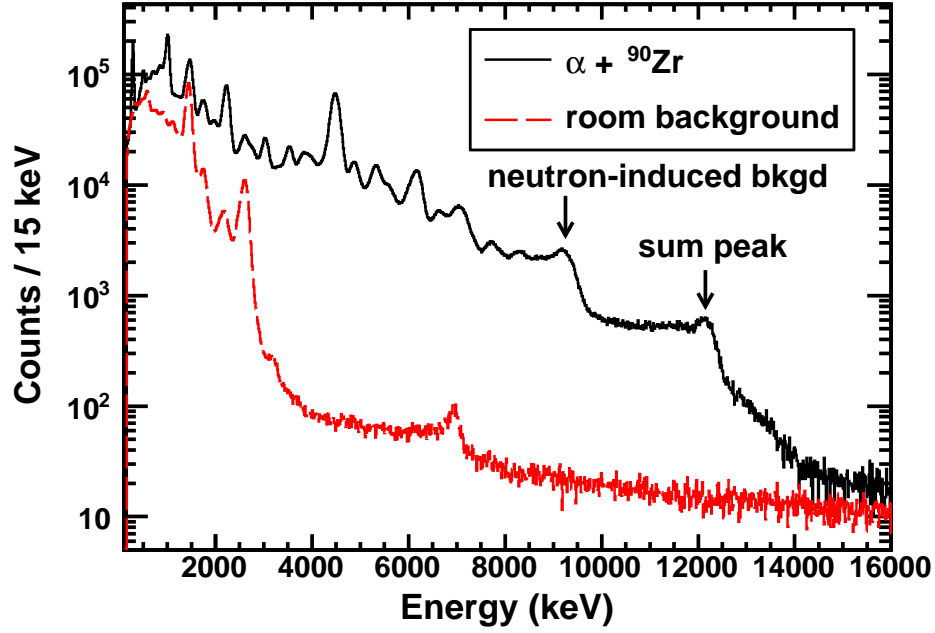


Figure 10.2: Total γ -summed spectrum for an α beam impinging onto the enriched ^{90}Zr target at $E_{\text{c.m.}} = 9.94$ MeV, with the $^{90}\text{Zr}(\alpha,\gamma)^{94}\text{Mo}$ sum peak at 12 MeV. The peak around 9 MeV in the spectrum comes from neutrons released in the $^{90}\text{Zr}(\alpha,n)^{93}\text{Mo}$ reaction. Also plotted is the normalized room background.

Table 10.1: Cross sections and S-factors for the $^{90}\text{Zr}(\alpha,\gamma)^{94}\text{Mo}$ reaction.

$E_{\text{c.m.}}$ (MeV)	σ (mb)	S (10^{15} eV b)
8.98 ± 0.03	0.060 ± 0.018	15500 ± 4600
9.46 ± 0.02	0.093 ± 0.024	6690 ± 1730
9.94 ± 0.02	0.155 ± 0.028	3420 ± 620
10.42 ± 0.02	0.171 ± 0.028	1260 ± 210
10.90 ± 0.02	0.207 ± 0.034	547 ± 60
11.39 ± 0.02	0.307 ± 0.051	306 ± 51

10.2 $^{92}\text{Zr}(\alpha,\gamma)^{96}\text{Mo}$ Results

The $^{92}\text{Zr}(\alpha,\gamma)^{96}\text{Mo}$ reaction was measured at energies $E_{\text{c.m.}} = 10.0 - 11.4$ MeV. Fig. 10.3 contains the experimental γ -summed spectrum for the measurement taken at $E_{\text{c.m.}} = 11.4$ MeV. The sum peak at 14.2 MeV is indicated on the plot, and is at an energy where the room background and beam-induced background are greatly reduced. In this case, the beam-induced background was determined by removing the ^{92}Zr target so that the α beam impinged solely onto the tantalum backing. The neutron-induced signature around 12 MeV is also indicated on the plot and comes from neutrons released in the $^{92}\text{Zr}(\alpha,n)^{95}\text{Mo}$ reaction. The inset of Fig. 10.3 shows a zoomed-in view of the sum-peak region, along with the linear background used to calculate the integral of the peak. The sum peaks for the $^{92}\text{Zr}(\alpha,\gamma)^{96}\text{Mo}$ reaction had the lowest intensity of the three measured reactions, and therefore carry the largest statistical uncertainty of up to 14%.

The energy loss through the ^{92}Zr target was $0.22 - 0.24$ MeV, and the small change in cross section through the target was taken into account in calculating the final energy value. To perform this effective energy calculation, the slope of the cross section was taken from the best-fit theoretical calculation (see Sec. 10.4). The final values for the center of mass energy, the cross sections, and the astrophysical S-factors are reported in Table 10.2.

Table 10.2: Cross sections and S-factors for the $^{92}\text{Zr}(\alpha,\gamma)^{96}\text{Mo}$ reaction.

$E_{\text{c.m.}}$ (MeV)	σ (mb)	S (10^{15} eV b)
9.96 ± 0.03	0.034 ± 0.008	732 ± 172
10.44 ± 0.03	0.057 ± 0.012	410 ± 86
10.92 ± 0.03	0.090 ± 0.018	233 ± 47
11.40 ± 0.03	0.116 ± 0.024	116 ± 24

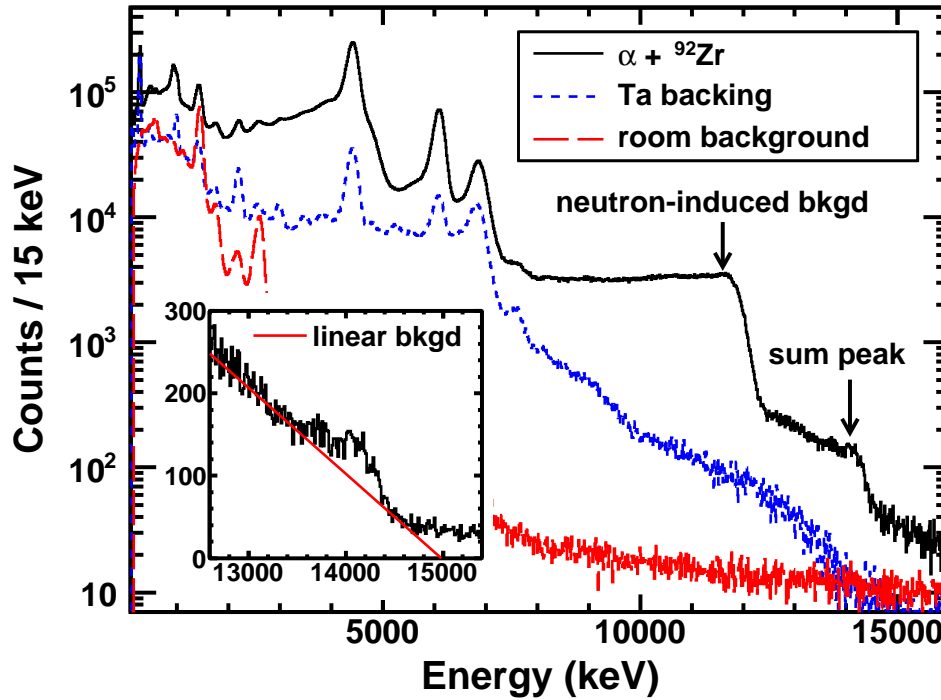


Figure 10.3: Total γ -summed spectrum for an α beam impinging onto the enriched ${}^{92}\text{Zr}$ target at $E_{\text{c.m.}} = 11.4$ MeV, with the ${}^{92}\text{Zr}(\alpha, \gamma){}^{96}\text{Mo}$ sum peak at 14.2 MeV. The peak around 12 MeV originates from neutrons emitted in the ${}^{92}\text{Zr}(\alpha, n){}^{95}\text{Mo}$ reaction. Also plotted are the normalized room background and the beam-induced background from the tantalum backing. The inset shows a zoomed in view of the sum peak and the linear background used when integrating the sum peak.

10.3 $^{74}\text{Ge}(\alpha,\gamma)^{78}\text{Se}$ Results

The measurements of the $^{74}\text{Ge}(\alpha,\gamma)^{78}\text{Se}$ reaction were carried out for energies $E_{\text{c.m.}} = 8.5 - 10.9$ MeV. The γ -summed spectrum for the measurement at $E_{\text{c.m.}} = 8.5$ MeV is shown in Fig. 10.4. The sum peak at 14.5 MeV is clearly visible above the normalized room background, and the peak around 10.5 MeV comes from the effect of neutrons released in the $^{74}\text{Ge}(\alpha,n)^{77}\text{Se}$ reaction. After integrating the sum peak and determining the γ -summing efficiency, the cross sections and the astrophysical S-factors were calculated. The final values are reported in Table 10.3 along with the center of mass energy of the measurement. The energy loss through the target was 0.08 – 0.10 MeV for the measured energies.

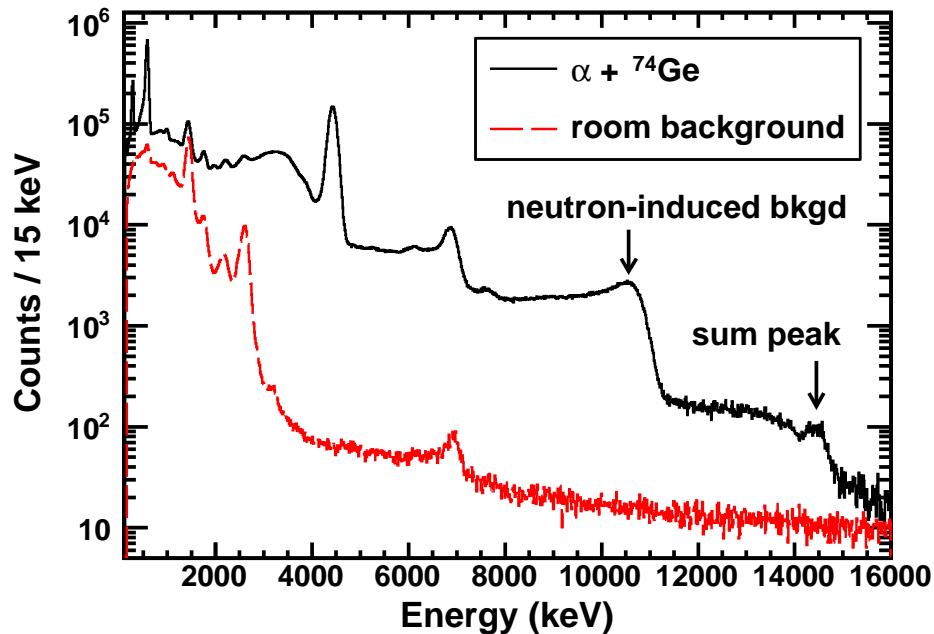


Figure 10.4: Total γ -summed spectrum for an α beam impinging onto the enriched ^{74}Ge target at $E_{\text{c.m.}} = 8.5$ MeV, with the $^{74}\text{Ge}(\alpha,\gamma)^{78}\text{Se}$ sum peak at 14.5 MeV. The neutron-induced peak around 10.5 MeV comes from neutrons emitted in the $^{74}\text{Ge}(\alpha,n)^{77}\text{Se}$ reaction. Also plotted is the normalized room background spectrum.

Table 10.3: Cross sections for the $^{74}\text{Ge}(\alpha,\gamma)^{78}\text{Se}$ reaction.

$E_{\text{c.m.}}$ (MeV)	σ (mb)	S (10^{12} eV b)
8.49 ± 0.01	0.048 ± 0.008	1010 ± 170
8.97 ± 0.01	0.075 ± 0.012	528 ± 84
9.44 ± 0.01	0.080 ± 0.014	210 ± 37
9.92 ± 0.01	0.113 ± 0.021	116 ± 22
10.39 ± 0.01	0.124 ± 0.026	55 ± 11
10.87 ± 0.01	0.169 ± 0.039	33 ± 8

10.4 Discussion

The experimental (α,γ) reaction cross sections contained in this chapter were compared to theoretical calculations using the TALYS 1.6 nuclear reaction software package [119]. Because the states populated in the α capture were at high excitation energy where there are many levels that overlap, the theoretical cross sections were calculated using the nuclear statistical model. TALYS 1.6 implements Hauser-Feshbach formalism for this purpose [59], which relies on the calculation of the transmission coefficients in the entrance channel and all exit channels. A discussion of the nuclear statistical model is contained in Sec. 3.2.

For the reactions considered here there are three ingredients that dominate the uncertainties in the theoretical cross sections; the nuclear optical model potential (OMP), the γ -ray strength function (GSF), and the nuclear level density (NLD). TALYS 1.6 has multiple options on its menu to choose from, including two OMPs for protons and neutrons, five OMPs for α particles, five GSFs for the dominant E1 transitions, and six NLDs. For details on all the models, the reader is directed to the TALYS 1.6 manual [142]. In the following paragraphs, only a brief description of the models with references to the original publications will be provided.

The two proton and neutron optical model potentials in TALYS are the phenomenolog-

ical OMP of Koning and Delaroche [143] constrained by experimental data across a large energy and mass range (KD OMP), and the semi-microscopic OMP of Jeukenne-Lejeune-Mahaux [118] reparametrized by Bauge, Delaroche, and Girod [120] (JLM OMP). For the α optical model potentials, the default option in TALYS is to take the KD OMP for protons and neutrons and combine them appropriately for the α particle. This concept of applying OMP for single nucleons to describe interactions of more complex nuclei was first done by Watanabe for deuterons [144]. TALYS also includes the α potential of McFadden and Satchler [141], as well as the three potentials provided by Demetriou, Grama, and Goriely [145] which differ in their description of the imaginary part of the OMP. The first α potential of Demetriou et al. used experimental data to constrain the imaginary part consisting of only a volume component, the second used a surface and volume component, and the third potential was determined using the dispersion relation to relate the imaginary part of the OMP to the real part.

The six nuclear level densities in TALYS are: the constant temperature and Fermi gas model [121, 122], the back-shifted Fermi gas model [123], the generalized superfluid model [124, 125], the microscopic level densities from Goriely's tables calculated with a Skyrme force [126], the microscopic level densities from Hilaire's table calculated with a Skyrme force [127], and the microscopic level density from Hilaire's table calculated with the Gogny interaction [146].

In TALYS, the γ -ray strength function for all transition types besides E1 are calculated with the Brink-Axel Lorentzian [147, 148]. However for the dominant E1 transitions, five different models can be used. These models are: the Kopecky-Uhl generalized Lorentzian [149], the Brink-Axel Lorentzian [147, 148], the microscopic option calculated from the Hartree-Fock BCS model [142], the microscopic option calculated from the Hartree-Fock-Bogolyubov

model [142], and Goriely’s hybrid model [150, 151].

In total, 300 TALYS calculations were performed for each reaction in an attempt to determine which combination of parameters best describes the data. In addition to the TALYS calculations, the cross section data was also compared to Hauser-Feshbach calculations from the NON-SMOKER code obtained through the NON-SMOKER web interface [116, 152]. Since the NON-SMOKER reaction rates are used in the REACLIB database [129], they are the reaction rates that are often used in astrophysical calculations.

10.4.1 $^{90}\text{Zr}(\alpha,\gamma)^{94}\text{Mo}$

A plot of the $^{90}\text{Zr}(\alpha,\gamma)^{94}\text{Mo}$ reaction cross sections as a function of center of mass energy is shown in Fig. 10.5. The relevant Gamow window is from 4.2 to 9.6 MeV for p-process temperatures of 1.8 – 3.3 GK [153]. Therefore, the data reaches the higher energies of the astrophysically relevant region and extrapolation is required for the lower energies. In addition to the data points, the result of four different theoretical calculations are shown. The upper and lower lines correspond to maximum and minimum of the TALYS calculations in this energy region, which represent the total theoretical uncertainty of up to a factor of 35. The upper TALYS limit was calculated using the JLM OMP [118], the first Demetriou α potential [145], the nuclear level density from Hilaire’s tables calculated with a Skyrme force [127], and the Brink-Axel Lorentzian γ -ray strength function [147, 148]. On the other hand, the minimum TALYS limit was calculated using the KD OMP [143], the third Demetriou α potential [145], the nuclear level density from the constant temperature plus Fermi gas model [121, 122], and the Kopecky-Uhl generalized Lorentzian γ -ray strength function [149]. The data presented here significantly reduces the uncertainty in the $^{90}\text{Zr}(\alpha,\gamma)^{94}\text{Mo}$ reaction cross section.

Also plotted in Fig. 10.5 is the NON-SMOKER theoretical cross section. In the en-

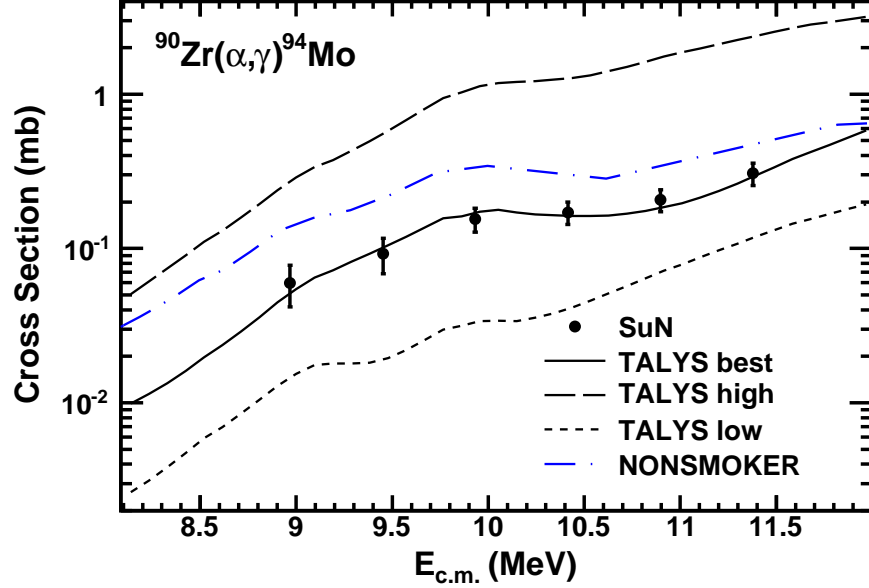


Figure 10.5: Experimental cross sections for the $^{90}\text{Zr}(\alpha,\gamma)^{94}\text{Mo}$ reaction compared to TALYS 1.6 and NON-SMOKER calculations. The three TALYS curves correspond to the upper limit, lower limit, and best-fit calculations (see text for details).

energy region plotted, the NON-SMOKER calculation overestimates the $^{90}\text{Zr}(\alpha,\gamma)^{94}\text{Mo}$ cross section by a factor of 1.6 – 2.3, with a larger discrepancy at the lower energies. Because NON-SMOKER calculations are used in the REACLIB database, it can be concluded that the standard REACLIB reaction rate for the $^{90}\text{Zr}(\alpha,\gamma)^{94}\text{Mo}$ reaction is too high as well. In order to extract a new reaction rate, the TALYS calculation that most accurately described the data was used. In this case, the best fit was achieved with the JLM OMP [118], the second Demetriou α potential [145], the microscopic level densities from Hilaire’s tables calculated with the Gogny force [146], and the microscopic γ -ray strength function from the Hartree-Fock BCS model [142]. The calculated reaction rates are listed in Table 10.4. As expected, these new rates are lower than the REACLIB rate by approximately a factor of 1.9 – 2.2 for p-process temperatures.

In order to investigate whether the reduction in the $^{90}\text{Zr}(\alpha,\gamma)^{94}\text{Mo}$ reaction rate has

Table 10.4: Reaction rates for the $^{90}\text{Zr}(\alpha,\gamma)^{94}\text{Mo}$ reaction.

T (GK)	Rate ($\text{cm}^3 \text{ mol}^{-1} \text{ s}^{-1}$)	T (GK)	Rate ($\text{cm}^3 \text{ mol}^{-1} \text{ s}^{-1}$)
0.4	6.385×10^{-42}	3.0	2.577×10^{-7}
0.5	2.962×10^{-36}	3.5	8.368×10^{-6}
0.6	2.955×10^{-32}	4.0	1.235×10^{-4}
0.7	3.762×10^{-29}	5.0	5.527×10^{-3}
0.8	1.374×10^{-26}	6.0	5.880×10^{-2}
0.9	2.189×10^{-24}	7.0	2.429×10^{-1}
1.0	1.867×10^{-22}	8.0	6.254×10^{-1}
1.5	8.485×10^{-16}	9.0	1.359×10^0
2.0	5.908×10^{-12}	10.0	2.760×10^0
2.5	2.662×10^{-9}		

an impact on the ^{94}Mo branching point in the p process, it is necessary to compare the inverse $^{94}\text{Mo}(\gamma,\alpha)^{90}\text{Zr}$ reaction rate to the $^{94}\text{Mo}(\gamma,n)^{93}\text{Mo}$ rate. The reaction rates for both reactions were taken from the REACLIB database [129] and the $^{94}\text{Mo}(\gamma,\alpha)^{90}\text{Zr}$ rate reduced by a factor of 2 as indicated by the experimental results here. Even with this reduction, the rate of photodissociating ^{94}Mo through the (γ,α) channel is still larger than the (γ,n) channel for temperatures below 2.5 GK. Therefore, ^{94}Mo appears to be the branching point in the molybdenum isotopic chain. However, this could change if a future measurement of the $^{93}\text{Mo}(n,\gamma)^{94}\text{Mo}$ reaction indicates that the rate is much higher than the current theoretical predictions.

10.4.2 $^{92}\text{Zr}(\alpha,\gamma)^{96}\text{Mo}$

The cross sections of the $^{92}\text{Zr}(\alpha,\gamma)^{96}\text{Mo}$ reaction are plotted in Fig. 10.6. The Gamow window is from 4.2 to 9.6 MeV for p-process temperatures [153], so the data reaches to just above the astrophysically relevant region. Also plotted in Fig. 10.6 are the results

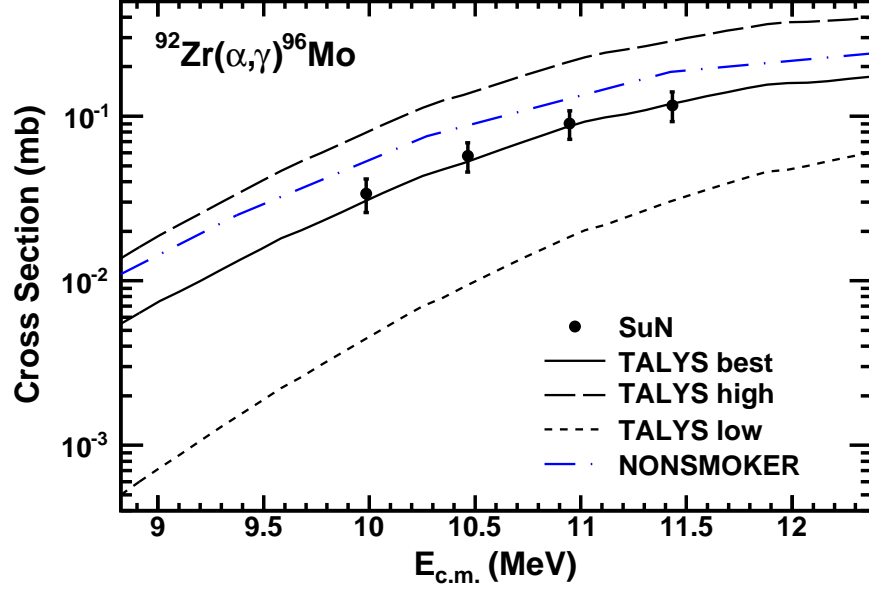


Figure 10.6: Experimental cross sections for the $^{92}\text{Zr}(\alpha,\gamma)^{96}\text{Mo}$ reaction compared to TALYS 1.6 and NON-SMOKER calculations. The three TALYS curves correspond to the upper limit, lower limit, and best-fit calculations (see text for details).

from theoretical calculations with the TALYS and NON-SMOKER codes. In the energy region plotted, NON-SMOKER describes the energy dependence of the cross section well, but overestimates the values by a factor of 1.5 – 1.7.

The three TALYS calculations that are plotted represent the upper limit, lower limit, and best description of the experimental results. The large spread between the maximum and minimum TALYS calculations show the total theoretical uncertainty of a factor of 6 at the highest energies and a factor of 29 at the lowest energies plotted. To achieve the upper limit, TALYS calculations were performed with the JLM OMP [118], the first Demetriou α potential [145], the nuclear level density from Hilaire’s tables calculated with a Skyrme force [127], and the Brink-Axel Lorentzian γ -ray strength function [147, 148]. On the other hand, the lower TALYS limit was calculated using the KD OMP [143], the second Demetriou α potential [145], the nuclear level density from the constant temperature plus

Fermi gas model [121, 122], and the Kopecky-Uhl generalized Lorentzian γ -ray strength function [149]. The experimental data greatly reduces the uncertainty in the cross section of the $^{92}\text{Zr}(\alpha,\gamma)^{96}\text{Mo}$ reaction to approximately 20%. Lastly, the TALYS calculation which most accurately describes the data was performed with the JLM OMP [118], the first Demetriou α potential [145], the generalized superfluid level density model [124, 125], and Goriely’s hybrid γ -ray strength function [150].

10.4.3 $^{74}\text{Ge}(\alpha,\gamma)^{78}\text{Se}$

A plot of the $^{74}\text{Ge}(\alpha,\gamma)^{78}\text{Se}$ cross section results compared to the TALYS and NON-SMOKER theoretical calculations is shown in Fig. 10.7. As in the case of the $^{90,92}\text{Zr}(\alpha,\gamma)^{94,96}\text{Mo}$ reactions, the experimental data is lower than the NON-SMOKER calculations. Here, NON-SMOKER is a factor of 1.6 – 2.3 larger. The Gamow window for the $^{74}\text{Ge}(\alpha,\gamma)^{78}\text{Se}$ reaction is 3.5 – 8.4 MeV [153] for p-process temperatures, so the data reaches to just above the astrophysically relevant region.

The upper TALYS limit corresponds to calculations with the JLM OMP [118], the default α potential [142], the nuclear level density from Hilaire’s tables calculated with a Skyrme force [127], and the Brink-Axel Lorentzian γ -ray strength function [147, 148]. The lower TALYS limit corresponds to calculations with the KD OMP [143], the second Demetriou α potential [145], the nuclear level density from Hilaire’s tables calculated with the Gogny force [146], and the Kopecky-Uhl generalized Lorentzian γ -ray strength function [149]. The total theoretical uncertainty between the upper and lower bounds is a factor of 11 at the higher energies and a factor of 21 at the lower energies plotted. The experimental uncertainty of 16 – 23% greatly constrains the cross section values in this energy region.

The experimental data was compared to the 300 TALYS calculations to determine what

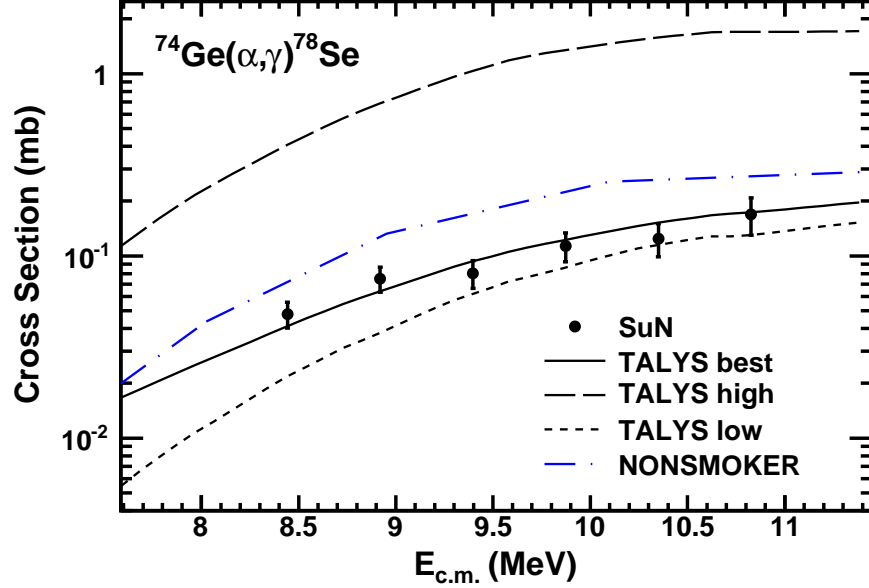


Figure 10.7: Experimental cross sections for the $^{74}\text{Ge}(\alpha,\gamma)^{78}\text{Se}$ reaction compared to TALYS 1.6 and NON-SMOKER calculations. The three TALYS curves correspond to the upper limit, lower limit, and best-fit calculations (see text for details).

combination of input parameters provided the best match. The best fit to the data was achieved with TALYS calculations performed with the KD OMP [143], the default α potential [142], the nuclear level densities from Goriely’s tables [126], and the microscopic γ -ray strength function calculated from the Hartree-Fock-Bogolyubov model [142].

10.5 Conclusions

In an effort to expand the very limited quantity of existing experimental data for (α,γ) reactions relevant in the astrophysical p process, the first ever measurements of the $^{90}\text{Zr}(\alpha,\gamma)^{94}\text{Mo}$, $^{92}\text{Zr}(\alpha,\gamma)^{96}\text{Mo}$, and $^{74}\text{Ge}(\alpha,\gamma)^{78}\text{Se}$ reaction cross sections were performed by implementing the γ -summing technique with the SuN detector at the University of Notre Dame. The measurements greatly reduce the uncertainty of the cross section values between energies of $E_\alpha = 9.5 - 12.0$ MeV from a theoretical uncertainty of larger than a factor of 10 to an exper-

imental uncertainty of approximately 20%. The nuclear reaction code TALYS was used to calculate theoretical cross sections to determine which input parameters provided the most accurate description of the data. The results of the $^{90}\text{Zr}(\alpha,\gamma)^{94}\text{Mo}$ reaction seem to confirm that ^{94}Mo is a branching point in the p process.

Chapter 11

Measurements in Inverse Kinematics

In this chapter, an alternative method to measure (p,γ) and (α,γ) reactions in inverse kinematics by utilizing the γ -summing technique is presented. The aim of this new experimental technique is to measure reaction cross sections at or near astrophysically relevant energies involving nuclei that cannot be studied in regular kinematics. The data obtained with this method, especially for reactions on radioactive nuclei, can help advance the field of nuclear astrophysics by expanding the nuclear physics input used in astrophysical models, particularly models of the p process. The feasibility of the γ -summing technique in inverse kinematics was demonstrated through the measurement of well-known resonances in the $p(^{27}\text{Al},\gamma)^{28}\text{Si}$ and $p(^{58}\text{Ni},\gamma)^{59}\text{Cu}$ reactions.

The experiments in inverse kinematics were performed at the University of Notre Dame using beams of $^{27}\text{Al}^{5+}$ and $^{58}\text{Ni}^{10+}$ with intensities of $2 - 5 \times 10^{10}$ pps. The beam energies were changed in small energy steps in order to scan well-known resonances in the $p(^{27}\text{Al},\gamma)^{28}\text{Si}$ and $p(^{58}\text{Ni},\gamma)^{59}\text{Cu}$ reactions. The target used during the measurements was a titanium hydride foil produced at Argonne National Laboratory using the method of Ref. [154]. The characterization of the target using RBS and ERD methods is described in detail in Sec. 4.2.2.4. The total measured thickness of the titanium hydride foil was $232(14) \mu\text{g}/\text{cm}^2$ with $3.58(36) \times 10^{18} \text{ cm}^{-2}$ hydrogen nuclei.

Using the SuN detector, the yield of each experimental run was determined as

$$Y = \frac{N_{\Sigma}}{N_b \varepsilon_{\Sigma}} \quad (11.1)$$

where N_{Σ} is the number of counts in the sum peak, N_b is the number of beam particles, and ε_{Σ} is the γ -summing efficiency. Because the measurements were performed in inverse kinematics, the recoil velocity caused the γ rays to be emitted in-flight and led to an energy broadening of the sum peak. Doppler corrections were applied using the segmentation of SuN and Eq. 4.4. After applying the Doppler corrections, the standard analysis procedures of this thesis were followed. Specifically, a Gaussian fitting function was used to define a sum-peak region of 3σ below to 3σ above the sum peak centroid, and then N_{Σ} was taken as the number of counts above a linear background in the sum-peak region and ε_{Σ} was taken based on the hit pattern analysis of the sum peak region.

A resonance yield curve was created for each reaction by changing the beam energies in small increments and determining the yield at each energy. By determining the integral under the resonance yield curve, the resonance strength can be determined from (see Sec. 3.1.2)

$$A_Y = n_H \frac{\lambda_r^2}{2} \omega \gamma . \quad (11.2)$$

Here A_Y is the integral under the resonance yield curve, n_H is the number of hydrogen nuclei in the target per unit area, λ_r is the center-of-mass de Broglie wavelength of the resonance, and $\omega \gamma$ is the resonance strength.

The first reaction measured was the $p(^{27}\text{Al}, \gamma)^{28}\text{Si}$ reaction ($Q = 11585$ keV) at the resonance energy of $E_{c.m.} = 956$ keV. A typical example of the Doppler corrected γ -summed

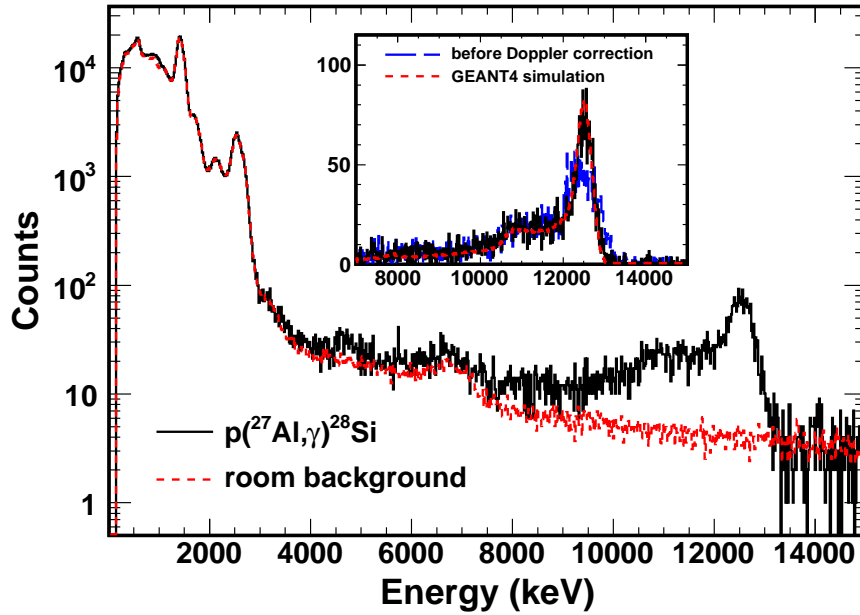


Figure 11.1: Doppler corrected γ -summed spectra for the $p(^{27}\text{Al}, \gamma)^{28}\text{Si}$ reaction plotted with the normalized room background. The inset shows a zoomed in view of the sum peak at $E_{\Sigma} = 12541$ keV. Additionally, the improvement due to applying the Doppler correction is demonstrated and the excellent agreement with GEANT4 simulations is shown.

spectrum is shown in Fig. 11.1. The sum peak at $E_{\Sigma} = 12541$ keV is clearly visible above the normalized room background. Additional peaks in the spectrum at 1461 keV and 2614 keV come from the room background decay of ^{40}K and the decay series of ^{232}Th , respectively. The inset of the figure is a comparison of the sum peak with and without Doppler corrections with the room background subtracted. By correcting for the velocity of the ^{28}Si recoil, the resolution of the sum peak is significantly improved. The inset of the figure also contains the result of GEANT4 simulations based on the known decay scheme of the resonance. Excellent agreement between the experimental data and simulation is obtained. For this $p(^{27}\text{Al}, \gamma)^{28}\text{Si}$ resonance, the summing efficiency was determined to be approximately 31(2)%.

The resonance yield curve from the $p(^{27}\text{Al}, \gamma)^{28}\text{Si}$ reaction is displayed in Fig. 11.2. In this plot, the experimental data is compared to estimated contributions from known reso-

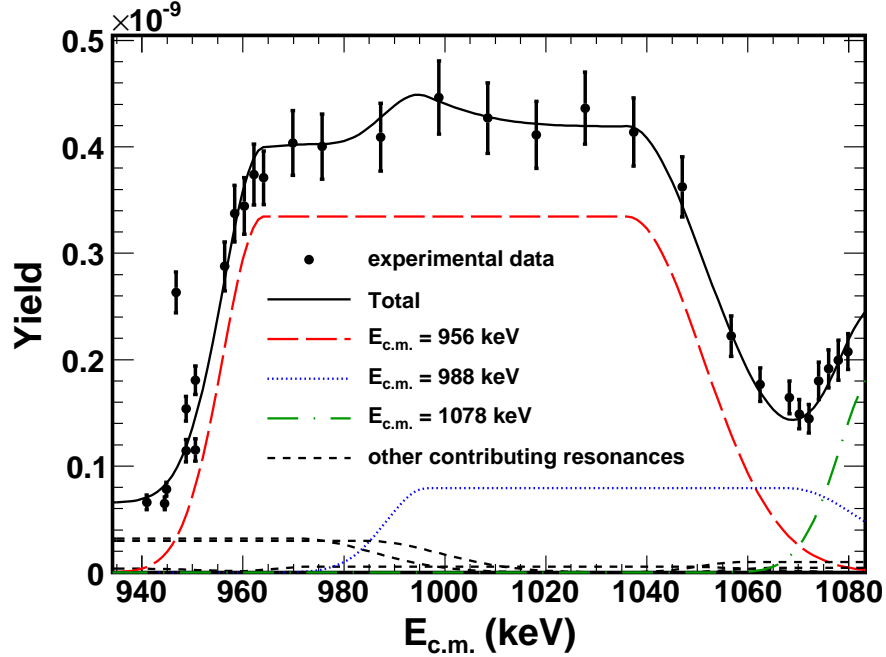


Figure 11.2: Yield curve for the $p(^{27}\text{Al},\gamma)^{28}\text{Si}$ reaction with the experimental data shown in solid circles. The spectrum is dominated by the $E_{c.m.} = 956$ keV resonance, with other large contributions from the $E_{c.m.} = 988$ keV and $E_{c.m.} = 1078$ keV resonances. In this energy region there are additional contributions from the $E_{c.m.} = 856, 890, 904, 966, 1051,$ and 1058 keV resonances [110]. The solid line shows the total yield from all resonances.

nances [110]. Due to the thickness of the target, many resonances can contribute at a given beam energy. The yield in this energy region is dominated by the $E_{c.m.} = 956$ keV resonance that was completely mapped out in this experiment. The integral underneath this resonance was determined by fitting the height and width on the resonance yield curve. The uncertainty in the integral of approximately 5% was calculated from the uncertainty in the fit. Using Eq. 11.2, the resulting resonance strength was determined to be $\omega\gamma = 2.05(23)$ eV.

A comparison between the present work and values in literature is shown in Table 11.1. The $E_{c.m.} = 956$ keV resonance of the $p(^{27}\text{Al},\gamma)^{28}\text{Si}$ reaction has been measured many times previously. Compilations and evaluations of earlier work by Endt [110] and Angulo et al. [53] provide adopted values of $\omega\gamma = 2.00(17)$ eV and $1.90(10)$ eV, respectively. In addition,

Table 11.1: Resonance strength measurements

Reaction	$E_{c.m.}$ (keV)	Present work $\omega\gamma$ (eV)	Other values $\omega\gamma$ (eV)	Ref.
$^{27}\text{Al}(p,\gamma)^{28}\text{Si}$	956	2.05 ± 0.23	1.93 ± 0.16	[110] ^a
			1.90 ± 0.10	[53]
			1.94 ± 0.07	[155]
			2.00 ± 0.15	[156]
$^{58}\text{Ni}(p,\gamma)^{59}\text{Cu}$	1400	0.58 ± 0.07	0.61	[157] ^a
			0.62 ± 0.10	[158] ^a
			0.687 ± 0.096	[84]

^a converted to center of mass frame for comparison

the resonance was measured more recently by Chronidou et al. [155] and Harissopulos et al. [156] using 4π NaI detectors in regular kinematics finding values of $\omega\gamma = 1.94(7)$ eV and $2.00(15)$ eV, respectively. The present value of $\omega\gamma = 2.05(23)$ eV agrees well with all values.

The second measurement was of the $E_{c.m.} = 1400$ keV resonance in the $p(^{58}\text{Ni},\gamma)^{59}\text{Cu}$ reaction. A Doppler corrected γ -summed spectrum is shown in Fig. 11.3. This reaction has $Q = 3419$ keV which leads to the sum peak found at $E_{\Sigma} = 4819$ keV. A zoomed in view of the sum peak is shown in the inset of the figure. The inset also demonstrates the improvement in sum-peak resolution after the Doppler corrections were applied, and shows the excellent agreement between experimental data and GEANT4 simulations. A summing efficiency of approximately 44(3)% was calculated for each energy and the yield determined with Eq. 11.1. The resulting experimental resonance yield curve is shown in Fig. 11.4 along with estimated contributions from known resonances in this energy region [157]. By fitting the height and width of the $E_{c.m.} = 1400$ keV resonance in the yield plot, the integral underneath the resonance was determined and the resonance strength was calculated using Eq. 11.2 to be $\omega\gamma = 0.58(7)$ eV.

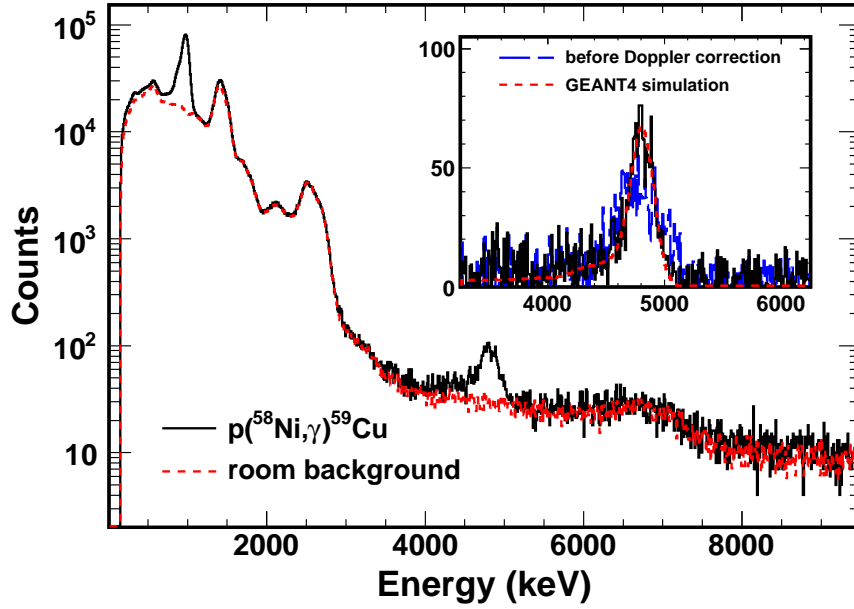


Figure 11.3: Doppler corrected γ -summed spectra for the $p(^{58}\text{Ni}, \gamma)^{59}\text{Cu}$ reaction with a comparison to the normalized room background. The inset shows a zoomed in view of the sum peak at $E_{\Sigma} = 4819$ keV as well as the summed spectrum without Doppler corrections. An excellent agreement with GEANT4 simulation is also observed.

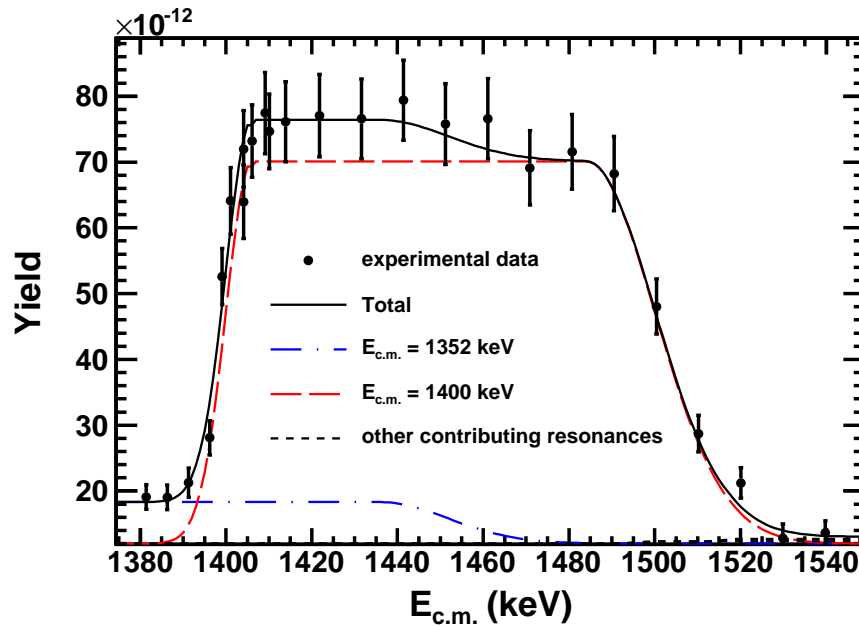


Figure 11.4: Yield curve for the $p(^{58}\text{Ni}, \gamma)^{59}\text{Cu}$ reaction. The spectrum is dominated by the $E_{c.m.} = 1400$ keV resonance, with an additional large contribution from the $E_{c.m.} = 1352$ keV resonance. In this energy region there are additional contributions from the $E_{c.m.} = 1496$ and 1514 keV resonances [157]. The solid line shows the total yield from all resonances.

The resonance strength of the $E_{c.m.} = 1400$ keV resonance of the $p(^{58}\text{Ni},\gamma)^{59}\text{Cu}$ reaction was published three times previously and the results are shown in Table 11.1. Carver and Jones [157] used the work of Butler and Gossett [159] to deduce $\omega\gamma = 0.62$ eV, although no uncertainty was given. The measurement by Tingwell et al. [158] reported a nearly identical value of $\omega\gamma = 0.63(10)$ eV. More recently Simon et al. [84] measured the resonance in inverse kinematics with the DRAGON recoil separator and determined $\omega\gamma = 0.687(96)$ eV. Overall, there is excellent agreement between the measurements of this thesis and the previous values since the present results are consistent with all literature values within the experimental uncertainty.

In summary, the first ever measurements utilizing the γ -summing technique in inverse kinematics were performed using the SuN detector at the University of Notre Dame. As a proof of principle, well-known resonances in the $p(^{27}\text{Al},\gamma)^{28}\text{Si}$ and $p(^{58}\text{Ni},\gamma)^{59}\text{Cu}$ reactions were measured with ^{27}Al and ^{58}Ni beams impinging onto a titanium hydride target. The deduced resonance strengths are in excellent agreement with previous values, illustrating the feasibility of the technique. The new method expands the experimental possibilities for measuring (p,γ) and (α,γ) reactions to additional nuclei, such as radioactive isotopes and stable isotopes that exist in a liquid or gas state. Future measurements with the γ -summing technique in inverse kinematics will contribute to an improved understanding of stellar nucleosynthesis.

Chapter 12

Summary and Outlook

Throughout history, humankind has searched for an explanation of the origin the world and of ourselves. Today we are closer to a full understanding than ever before. We know that our complex world is made up of less than 100 elements whose abundances in the universe are evolving due to various nucleosynthesis processes. Hydrogen and the majority of helium were produced immediately after the Big Bang, and the heavier elements are continually synthesized in various stellar environments. The bulk of isotopes beyond iron are synthesized via two neutron capture processes, although there is a group of 35 stable neutron-deficient p nuclei which must be produced by an alternative “p-process” nucleosynthesis scenario. Overall, the synthesis of the p nuclei remains a major open question in the field of nuclear astrophysics, with current state of the art p-process models failing to reproduce the observed solar abundance pattern.

The most studied scenario of synthesizing the p nuclei is from existing seed nuclei in the O/Ne layers of a type II supernovae, but this environment suffers from large uncertainties in the nuclear physics (in addition to the astrophysical uncertainties). A severe lack of experimental data means that models of this p-process scenario rely heavily on theoretical reaction rates and their corresponding large uncertainties. To reduce these nuclear physics uncertainties it is crucial to expand and develop new experimental techniques to measure the relevant reactions. It is especially important to develop experimental capabilities in inverse kinematics which allow for the investigation of reactions involving radioactive nuclei which

currently have the largest uncertainties of all.

To this end, this dissertation focused on the development of a new experimental program at the National Superconducting Cyclotron Laboratory (NSCL) to measure proton and α radiative capture reactions which are relevant for the astrophysical p process. To detect the radiation released in these reactions, a new γ -ray detector was designed which combines a large active volume and a nearly 4π angular coverage for the ideal implementation of the γ -summing technique. The Summing NaI (SuN) detector also was designed to include eight segments to allow for the Doppler reconstruction of γ -ray energy when performing measurements in inverse kinematics. After SuN's arrival to the NSCL, a digital data acquisition system was installed and testing and optimization was performed using standard radioactive γ -ray sources.

All (p, γ) and (α , γ) reaction measurements in this dissertation were performed at the University of Notre Dame using the FN Tandem Van de Graaff accelerator. Two of the targets had to be produced through evaporation, and all of the targets had their thicknesses measured with the RBS technique. The commissioning of the SuN detector was performed by measuring 11 known resonances in the $^{27}\text{Al}(p,\gamma)^{28}\text{Si}$ reaction. The measured resonance strengths were in good agreement with previously published values, demonstrating the validity of the experimental techniques and the analysis procedures. A new method of extracting the γ -summing efficiency was developed, which makes use of the segmentation of the SuN detector and requires comparison to a well-tested GEANT4 simulation.

Four reactions were measured to investigate the region of the light p nuclei, namely the $^{74}\text{Ge}(p,\gamma)^{75}\text{As}$, $^{90}\text{Zr}(\alpha,\gamma)^{94}\text{Mo}$, $^{92}\text{Zr}(\alpha,\gamma)^{96}\text{Mo}$, and $^{74}\text{Ge}(\alpha,\gamma)^{78}\text{Se}$ reactions. The measured cross sections were compared to theoretical calculations using the TALYS and NON-SMOKER nuclear reaction codes, and the TALYS parameters that most accurately described

the data were determined. New reaction rates were extracted for the $^{74}\text{Ge}(p,\gamma)^{75}\text{As}$ reaction which were approximately 20% higher than the standard REACLIB rates for p-process temperatures. The increase in reaction rates was found to enhance the production of ^{74}Se in the p process by 17% when performing calculations with a reaction network of a type II supernova. Additionally, the nuclear physics uncertainty in the production of ^{74}Se was reduced from 63% to 5% with the new measurements here. In the case of the $^{90}\text{Zr}(\alpha,\gamma)^{94}\text{Mo}$ reaction, the new reaction rates were lower than the standard REACLIB rates by approximately a factor of 2 for p-process temperatures. Even with the reduction in reaction rate, the inverse $^{94}\text{Mo}(\gamma,\alpha)^{90}\text{Zr}$ reaction was found to have a higher rate than the $^{94}\text{Mo}(\gamma,n)^{93}\text{Mo}$ reaction for temperatures below 2.5 GK, which tentatively confirms that ^{94}Mo is the branching point in the p process for the molybdenum isotopic chain. The results of the $^{92}\text{Zr}(\alpha,\gamma)^{96}\text{Mo}$ and $^{74}\text{Ge}(\alpha,\gamma)^{78}\text{Se}$ reactions greatly reduces the uncertainty in the reaction cross sections from larger than a factor of 10 to an uncertainty of less than 20%. These measurements expand the experimental database for (α,γ) reactions relevant for the p process, and can be used to place constraints on the nuclear reaction theory.

The $^{58}\text{Ni}(\alpha,\gamma)^{62}\text{Zn}$ reaction was measured for its role in the nucleosynthesis in the innermost layers of type Ia supernovae, in which α -rich freeze-out from nuclear statistical equilibrium is expected to occur. The measurements were approximately a factor of 2 below the default calculations of the SMARAGD code, but good agreement to the data was achieved by multiplying the α width by a factor of 0.45. The new reaction rates were found to have up to a 5% effect on the ejected abundances of several isotopes, including ^{64}Zn and ^{62}Ni .

The last measurements of this dissertation, the $p(^{27}\text{Al},\gamma)^{28}\text{Si}$ and $p(^{58}\text{Ni},\gamma)^{59}\text{Cu}$ reactions, were performed in inverse kinematics with ^{27}Al and ^{58}Ni beams impinging onto a

titanium hydride target. Well-known resonances in both reactions were measured, and the deduced resonance strengths were found to be in excellent agreement with previous literature values. The success of these measurements served as a proof of principle of using the γ -summing technique in inverse kinematics. This opens the door to studying (p,γ) and (α,γ) reactions on radioactive nuclei and other nuclei which are difficult to make targets out of.

Looking ahead, this dissertation is just the beginning of what should be a bright future of measuring (p,γ) and (α,γ) reactions with the SuN detector and the γ -summing technique. In the time since the initial measurements were performed with the SuN detector at the University of Notre Dame, the reaccelerator facility (ReA3) at the NSCL has been completed and commissioned. The ReA3 facility is just starting to provide radioactive beams with the intensities necessary to successfully perform cross section measurements. Combining the SuN detector with ReA3 beams will allow for the measurement of (p,γ) and (α,γ) reactions on radioactive nuclei at astrophysical energies which were previously not possible. These future experiments will be the pioneering experiments involving radioactive nuclei in the p process, and it will be fascinating to see what the findings will be and the impact that these findings will have on our understanding of the nucleosynthesis of the p nuclei.

Before performing experiments with the SuN detector and ReA3, however, the current experimental setup should be updated to increase the measurement sensitivity. The increase in sensitivity is necessary due to the fact that the best-case radioactive beam intensities provided by ReA3 facility are expected to be at least 3 orders of magnitude below the beam intensities utilized at the University of Notre Dame. The lower beam intensities will contribute to a significant decrease in the experimental count rate. To counteract this reduction, it is possible to increase the number of target nuclei by moving towards a gas cell. For example, a hydrogen gas cell with a pressure of 1 atm would have proton thickness

larger than 10 times that of the titanium hydride foils used in this dissertation.

In addition, most of the background in the total γ -summed spectrum in the region of the sum peak comes from cosmic rays depositing their energy in the SuN detector. An increase in the sum-peak signal can be achieved if this cosmic-ray background is somehow reduced. One solution is to develop an active volume to surround the SuN detector and detect cosmic rays so that their contribution is removed from SuN's spectra. Therefore, SuN's Scintillating Cosmic Ray Eliminating Ensemble (SuNSCREEN) was recently developed in collaboration with Hope College. SuNSCREEN consists of 9 plastic scintillator bars arranged in a roof-like configuration above SuN. It was shown that a reduction of the cosmic-ray background by up to a factor of 2 in SuN's total γ -summed spectrum was achieved when using SuNSCREEN.

An additional way to reduce the cosmic-ray background is to remove events in the data when the beam is not impinging onto the target. The ReA3 facility has the capability to provide bunched radioactive beams so that there are regular time intervals of no particles impinging on the target followed by a short burst of beam. By selecting only the small time intervals when the (p,γ) and (α,γ) reactions of interest might be occurring, the cosmic-ray background can be significantly reduced. It is recommended that the initial measurements with the SuN detector and ReA3 should start with the most sensible candidates to check the sensitivity of the experimental setup before moving onto even challenging measurements. The best candidates are reactions where the theoretical models predict a relatively large reaction cross section, as well as reactions with large Q-values that produce sum peaks at high energies where the background is reduced.

APPENDICES

Appendix A

Energy Filter Algorithm

This appendix contains the algorithm that NSCL DDAS implements to extract the energy of a pulse. This algorithm was introduced in Ref. [104] and it takes into account the exponential decay of the signal. Its implementation was not part of this thesis, but it may be useful for future experimenters who want to understand how the energy spectrum of the SuN detector is obtained. Also, Ref. [104] does not include the value of all the coefficients needed.

First of all, Fig. A.1 shows a typical digitized pulse from the SuN detector. Both the signal and its baseline are drawn. As discussed in Sec. 5.3.2, NSCL DDAS implements digital trapezoidal filter algorithms, which make use of a user-defined “peaking” time and “gap” time. In the figure, SuN’s energy filter peaking time of 600ns is equal to L_0 and L_1 , and SuN’s energy filter gap time of 200ns is equal to L_G . For each digitized point, the following sum is first calculated:

$$\text{Filter Sum} = a_0 (S_0 - B_0) + a_G (S_G - B_G) + a_1 (S_1 - B_1) \quad (\text{A.1})$$

where S_i is the integral of the signal in region i and B_i is the integral of the baseline in region i . This sum is straightforward to calculate with the only complication coming from the value of the coefficients. The coefficients depend on the decay constant τ of the signal

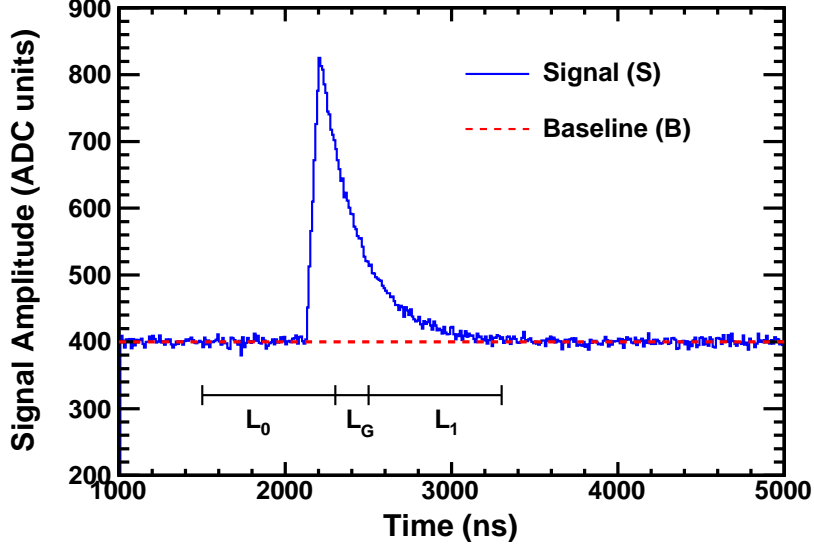


Figure A.1: A digitized signal from the SuN detector plotted along with its baseline. The lengths of the peaking time (L_0 and L_1) and gap time (L_G) are also drawn.

and the length L_i of each region. Their values are

$$a_0 = \frac{\exp(-2L_0/\tau)}{\exp(-2L_0/\tau) - 1} \quad a_G = 1 \quad a_1 = \frac{1}{\exp(-2L_1/\tau) - 1} . \quad (\text{A.2})$$

It should be mentioned that these coefficients are for an NSCL DDAS energy filter range of 1, and the value of the exponentials change slightly for energy filter ranges larger than 1.

After calculating the sum, the value is multiplied by a factor that depends on the decay constant τ . This factor is equal to

$$\frac{1}{1 - \exp(-1/\tau)} . \quad (\text{A.3})$$

A plot of the tau corrected energy filter using algorithm described here is plotted in Fig. A.2 compared to the uncorrected energy filter. It is shown that by using the coefficients in Eq. A.2, the energy filter successfully accounts for the exponential decay of the signal and

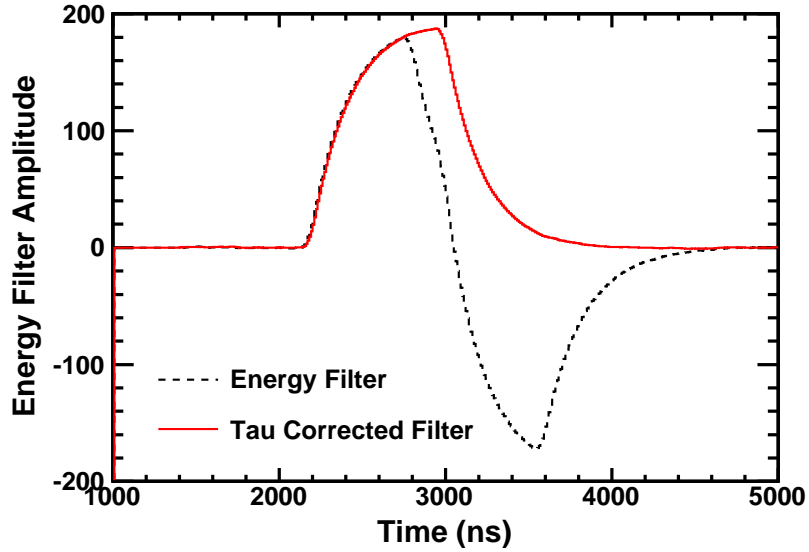


Figure A.2: The response of SuN’s tau-corrected energy filter compared to the uncorrected energy filter. By correcting for the exponential decay of the signal, the tau-corrected energy filter does not take on any negative values.

therefore does not take on negative values. The only additional step that NSCL DDAS takes is to multiply the result by a normalization factor to ensure that the extracted energy falls within the desired channel range of 0 to approximately 32000.

Appendix B

GEANT4 Detector Construction

Below is the code used to build the SuN detector in GEANT4:

```
////////////////////////////////////
// Author: Steve Quinn //
// //
// Description: This is the file where you build the detector. For now it consits //
// of the experimental setup for the SuN detector, but it can be modified by //
// following the syntax to build and place new materials. There is also many //
// useful examples online. //
// //
// Steps: 1. Define the elements that you need //
// 2. Use these elements to define the materials for the experimental setup //
// 3. Create an experimental room of air, vacuum, etc. //
// 4. Create your experimental setup and place it in the experimental room //
// 5. Apply the color scheme you want for the optional visualization //
// //
// Important: The way the code is currently set up, you are required to fill the //
// array called detectorName[i] with the name of the detectors you want to save //
// in your ROOT file. In this example the names are "T1", "B1", etc. //
// (see syntax below). //
////////////////////////////////////

#include "DetectorConstruction.hh"
#include "G4SDManager.hh"
#include "G4Element.hh"
#include "G4Material.hh"
#include "G4Box.hh"
#include "G4Tubs.hh"
#include "G4Cons.hh"
#include "G4Trd.hh"
#include "G4LogicalVolume.hh"
#include "G4ThreeVector.hh"
#include "G4PVPlacement.hh"
#include "G4SubtractionSolid.hh"
#include "G4UnitsTable.hh"
#include "globals.hh"
#include "G4VisAttributes.hh"
#include "G4Colour.hh"
#include <iostream>
#include <sstream>
#include "G4String.hh"
#include "G4ios.hh"
#include <stdio.h>
```

```

DetectorConstruction::DetectorConstruction()
: NaI(0), Al(0), N78021Ar1(0), Cr20Ni8Fe76(0), C2F4(0), C502H8(0)
{}

DetectorConstruction::~DetectorConstruction()
{}

G4VPhysicalVolume* DetectorConstruction::Construct()
{ DefineMaterials();
  return ConstructDetector();
}

void DetectorConstruction::DefineMaterials()
{
  // define Parameters
  G4String name, symbol;
  G4double a, z, density;
  G4int ncomponents, natoms;

  // define Elements

  a = 22.99*g/mole;
  G4Element* Na = new G4Element(name="Sodium" ,symbol="Na" , z= 11., a);

  a = 126.90*g/mole;
  G4Element* I = new G4Element(name="Iodine" ,symbol="I" , z= 53., a);

  a = 204.38*g/mole;
  G4Element* Tl = new G4Element(name="Thalium" ,symbol="Tl" , z= 81., a);

  a = 26.982*g/mole;
  G4Element* elAl = new G4Element(name="element_Aluminum",symbol="elAl",
                                z= 13., a);

  a = 14.00*g/mole;
  G4Element* N = new G4Element(name="Nitrogen",symbol="N" , z= 7., a);

  a = 16.00*g/mole;
  G4Element* O = new G4Element(name="Oxygen",symbol="O" , z= 8., a);

  a = 39.95*g/mole;
  G4Element* Ar = new G4Element(name="Argon",symbol="Ar" , z= 18., a);

  a = 51.996*g/mole;
  G4Element* Cr = new G4Element(name="Chromium" ,symbol="Cr" , z= 24., a);

  a = 58.69*g/mole;
  G4Element* Ni = new G4Element(name="Nickel" ,symbol="Ni" , z= 28., a);

  a = 55.847*g/mole;
  G4Element* Fe = new G4Element(name="Iron" ,symbol="Fe" , z= 26., a);

  a = 12.011*g/mole;
  G4Element* C = new G4Element(name="Carbon" ,symbol="C" , z= 6., a);

```

```

a = 18.998*g/mole;
G4Element* F = new G4Element(name="Fluorine" ,symbol="F" , z= 9., a);

a = 1.008*g/mole;
G4Element* H = new G4Element(name="Hydrogen" ,symbol="H" , z= 1., a);

// define Materials

//.....Stainless Steel.....
density = 8.0*g/cm3;
Cr20Ni8Fe76 = new G4Material(name="Stainless_Steel", density, ncomponents=3);
Cr20Ni8Fe76->AddElement(Cr, natoms=20);
Cr20Ni8Fe76->AddElement(Fe, natoms=76);
Cr20Ni8Fe76->AddElement(Ni, natoms=8);

//.....Polytetrafluorine (PTFE).....
density = 2.20*g/cm3;
C2F4 = new G4Material(name="PTFE", density, ncomponents=2);
C2F4->AddElement(C, natoms=2);
C2F4->AddElement(F, natoms=4);

//.....NaI.....
density = 3.67*g/cm3;
NaI = new G4Material(name="Sodium Iodine", density, ncomponents=3);
NaI->AddElement(Na, natoms=1000);
NaI->AddElement(I, natoms=1000);
NaI->AddElement(Tl, natoms=1);

//.....Al.....
density = 2.698*g/cm3;
Al = new G4Material (name="Aluminum", density, ncomponents=1);
Al->AddElement(e1Al, natoms=1);

//.....Air.....
density = 1.2927*mg/cm3;
N78021Ar1 = new G4Material (name="Air", density, ncomponents=3);
N78021Ar1->AddElement(N, natoms=78);
N78021Ar1->AddElement(O, natoms=21);
N78021Ar1->AddElement(Ar, natoms=1);

//.....Acrylic.....
density = 1.18*g/cm3;
C502H8 = new G4Material (name="Acrylic", density, ncomponents=3);
C502H8->AddElement(C, natoms=5);
C502H8->AddElement(O, natoms=2);
C502H8->AddElement(H, natoms=8);

// Print out Elements and Materials
G4cout << "\n\n ####-----##### \n";
G4cout << "\n\n\n\n\t\t #### List of elements used #### \n";
G4cout << *(G4Element::GetElementTable());
G4cout << "\n\n\n\n\t\t #### List of materials used #### \n";
G4cout << *(G4Material::GetMaterialTable());
}

```

```

G4VPhysicalVolume* DetectorConstruction::ConstructDetector()
{
// EXPERIMENTAL ROOM
G4Tubs* room_tube = new G4Tubs("room",0.0*cm,100.0*cm,300.0*cm,0.0*deg,360.0*deg);
G4LogicalVolume* room_log = new G4LogicalVolume(room_tube,N78021Ar1,"room",0,0,0);
G4VPhysicalVolume* room_phys = new G4PVPlacement(0,G4ThreeVector(0.0*cm,0.0*cm,
0.0*cm),"room",room_log,NULL,false,0);

// BEAM PIPE
G4double outerR_beam = 19.0*mm;           //radius of the beam pipe
G4double innerR_beam = outerR_beam - 1.5*mm; //thickness of the beam pipe
G4double halflength_beam = 720.0*mm;      //length of the beam pipe
G4double startAngle_beam = 0.*deg;
G4double spanAngle_beam = 360.*deg;

G4Tubs* beam_tube = new G4Tubs("beam_tube",innerR_beam,outerR_beam,halflength_beam,
startAngle_beam, spanAngle_beam);
G4LogicalVolume* beam_log = new G4LogicalVolume(beam_tube,Cr20Ni8Fe76,"beam_log",
0,0,0);
G4VPhysicalVolume* beam_phys = new G4PVPlacement(0,
G4ThreeVector(0.0*mm,0.0*mm,100.0*mm),beam_log,"beam_phys",room_log,false,0);

// DIMENSIONS OF SuN          *(changing these will scale the whole simulation)**
G4double innerR_scint = 22.5*mm;           // 45mm borehole
G4double outerR_scint = 203.0*mm;         // total of 406mm in diameter
G4double length_scint = 101.5*mm;         // total of 406mm in length
G4double width_Refl = 0.25*mm;            // width of reflector
G4double width_Al_vert = 0.50*mm;         // width of Al between each segment
G4double width_Al_horiz = 0.75*mm;        // width of Al between top and bot
G4double innerR_Al = 21.5*mm;             // 43mm in center
G4double outerR_Al = 222.5*mm;           // thick outer casing

// NaI SCINTILLATOR
G4double halflength_scint = 0.5*length_scint;
G4double startAngle_scint = 0.0*deg;
G4double spanAngle_scint = 180.0*deg;

G4Tubs* scint_tube = new G4Tubs("scint_tube",innerR_scint,outerR_scint,
halflength_scint,startAngle_scint,spanAngle_scint);
G4LogicalVolume* scint_log = new G4LogicalVolume(scint_tube,NaI,"scint_log",0,0,0);

// REFLECTOR
G4double innerR_Refl = innerR_scint - width_Refl;
G4double outerR_Refl = outerR_scint + 2.0*width_Refl;
G4double length_Refl = length_scint + 2.0*width_Refl;
G4double halflength_Refl = 0.5*length_Refl;

G4Tubs* refl_tube = new G4Tubs("refl_tube",innerR_Refl,outerR_Refl,
halflength_Refl,startAngle_scint,spanAngle_scint);
G4SubtractionSolid* refl_sub = new G4SubtractionSolid("refl_sub",refl_tube,
scint_tube,0,G4ThreeVector(0.0*mm,width_Refl,0.0*mm));
G4LogicalVolume* refl_log = new G4LogicalVolume(refl_sub,C2F4,"refl_log",0,0,0);

```

```

// ALUMINUM
G4double length_Al = length_Refl + width_Al_vert;
G4double halflength_Al = 0.5*length_Al;

G4Tubs* al_tube = new G4Tubs("al_tube",innerR_Al,outerR_Al,halflength_Al,
                             startAngle_scint,spanAngle_scint);
G4SubtractionSolid* al_sub = new G4SubtractionSolid("al_sub",al_tube,refl_tube,0,
                                                    G4ThreeVector(0.0*mm,width_Al_horiz,0.0*mm));
G4LogicalVolume* al_log = new G4LogicalVolume(al_sub,Al,"al_log",0,0,0);

G4double length_Al_side = 13.0*mm;
G4double halflength_Al_side = 0.5*length_Al_side;

G4Tubs* al_tube_side = new G4Tubs("al_tube_side",innerR_Al,outerR_Al,
                                   halflength_Al_side,0.0*deg,360.0*deg);
G4LogicalVolume* al_log_side = new G4LogicalVolume(al_tube_side,Al,
                                                    "al_log_side",0,0,0);

// ===== Placing the volumes =====//

G4RotationMatrix* rot_180 = new G4RotationMatrix();
rot_180->rotateZ(180*deg);

G4double Pos_x = 0.0*mm;
G4double Pos_y_Al = 0.0*mm;
G4double Pos_y_Refl = width_Al_horiz;
G4double Pos_y_Scint = Pos_y_Refl + width_Refl;
G4double Pos_z = -1.5*width_Al_vert - 3.0*width_Refl - 3.0*halflength_scint;

G4String topName;
G4String botName;

for (int i=1; i<=4; i++)
{
  if(i==1)
    { topName = "T1";
      botName = "B1"; }
  if(i==2)
    { topName = "T2";
      botName = "B2"; }
  if(i==3)
    { topName = "T3";
      botName = "B3"; }
  if(i==4)
    { topName = "T4";
      botName = "B4"; }

// TOP OF SUN
Pos_y_Al = 0.0*mm;
Pos_y_Refl = width_Al_horiz;
Pos_y_Scint = Pos_y_Refl + width_Refl;

```

```

//aluminum
  G4VPhysicalVolume* al_top = new G4PVPlacement(0,
    G4ThreeVector(Pos_x,Pos_y_Al,Pos_z),al_log,"al_top",room_log,false,0);
//reflector
  G4VPhysicalVolume* refl_top = new G4PVPlacement(0,
    G4ThreeVector(Pos_x,Pos_y_Refl,Pos_z),refl_log,"refl_top",room_log,false,0);
//scintillator
  G4VPhysicalVolume* scint_top = new G4PVPlacement(0,
    G4ThreeVector(Pos_x,Pos_y_Scint,Pos_z),scint_log,topName,room_log,false,0);

// BOTTOM OF SUN
Pos_y_Al = 0.0*mm;
Pos_y_Refl = -width_Al_horiz;
Pos_y_Scint = Pos_y_Refl - width_Refl;

//aluminum
  G4VPhysicalVolume* al_bottom = new G4PVPlacement(rot_180,
    G4ThreeVector(Pos_x,Pos_y_Al,Pos_z),al_log,"al_bottom",room_log,false,0);
//reflector
  G4VPhysicalVolume* refl_bottom = new G4PVPlacement(rot_180,
    G4ThreeVector(Pos_x,Pos_y_Refl,Pos_z),refl_log,"refl_bottom",room_log,false,0);
//scintillator
  G4VPhysicalVolume* scint_bottom = new G4PVPlacement(rot_180,
    G4ThreeVector(Pos_x,Pos_y_Scint,Pos_z),scint_log,botName,room_log,false,0);

  Pos_z = Pos_z + width_Al_vert + 2.0*width_Refl + length_scint;
}

// SIDES OF SUN
Pos_x = 0.0*mm;
Pos_y_Al = 0.0*mm;
Pos_z = 2.0*length_scint + 2.0*width_Al_vert + 4.0*width_Refl + halflength_Al_side;

G4VPhysicalVolume* al_sideA = new G4PVPlacement(0,
  G4ThreeVector(Pos_x,Pos_y_Al,Pos_z),al_log_side,"al_sideA",room_log,false,0);
G4VPhysicalVolume* al_sideB = new G4PVPlacement(0,
  G4ThreeVector(Pos_x,Pos_y_Al,-Pos_z),al_log_side,"al_sideB",room_log,false,0);

// *****
// TO PROPERLY SAVE THINGS TO ROOT, YOU NEED TO SPECIFY WHAT YOU NAMED THE DETECTORS
// *****
// The name of the detectors is in the G4VPhysicalVolume command
detectorName[0] = "T1";
detectorName[1] = "T2";
detectorName[2] = "T3";
detectorName[3] = "T4";
detectorName[4] = "B1";
detectorName[5] = "B2";
detectorName[6] = "B3";
detectorName[7] = "B4";
// *****

```

```

// VISUALIZATION STUFF

    room_log->SetVisAttributes (G4VisAttributes::Invisible);

//visualization for scintillators = GREEN
    G4VisAttributes *GreenAttr = new G4VisAttributes(G4Colour(0.,1.,0.));
    GreenAttr->SetVisibility(true);
    GreenAttr->SetForceSolid(true);

//visualization for reflector = PURPLE
    G4VisAttributes *PurpleAttr = new G4VisAttributes(G4Colour(1.,0.,1.));
    PurpleAttr->SetVisibility(true);
    PurpleAttr->SetForceSolid(true);

//visualization for aluminum = GREY
    G4VisAttributes *GreyAttr = new G4VisAttributes(G4Colour(0.5,0.5,0.5));
    GreyAttr->SetVisibility(true);
    GreyAttr->SetForceSolid(true);

//visualization for BLUE
    G4VisAttributes *BlueAttr = new G4VisAttributes(G4Colour(0.,0.,1.));
    BlueAttr->SetVisibility(true);
    BlueAttr->SetForceSolid(true);

//visualization for RED
    G4VisAttributes *RedAttr = new G4VisAttributes(G4Colour(1.,0.,0.));
    RedAttr->SetVisibility(true);
    RedAttr->SetForceSolid(true);

// applying the color scheme

    scint_log->SetVisAttributes(GreenAttr);
    refl_log->SetVisAttributes(PurpleAttr);
    al_log->SetVisAttributes(GreyAttr);
    al_log_side->SetVisAttributes(GreyAttr);
    beam_log->SetVisAttributes(BlueAttr);

    return room_phys;
}

```

Appendix C

Creating SuN's ROOT files

In the SuN group, the initial experimental data is saved in the .EVT file format. Converting the initial data into a format suitable for analysis with the ROOT software package currently involves two steps. First, the “ddasdumper” program written by members of the current NSCL data acquisition (DAQ) committee is used to create a raw output .ROOT file from the .EVT file. This raw .ROOT file consists of a time-ordered list of detectors that triggered above their threshold. The list contains the module number and channel number of the detector that fired, along with the corresponding timestamp and extracted energy. In the second step, the raw .ROOT file is used to create a new .ROOT file which hopefully contains events grouped together properly with the SuN detector. The code for the second step of the process is listed below:

```
////////////////////////////////////  
// Steve Quinn      October 2013                                     //  
////////////////////////////////////  
// PURPOSE: Take the output ROOT file from ddasdumper and turn it into another ROOT //  
// file with a pretty SuN tree.                                     //  
//                                                                 //  
// OPTIONS: Change the variable "timewindow" to the amount of time that you want to //  
// consider for coincidences. For example a time window of 30 clock ticks means //  
// that you group everything up to 300ns after the trigger as a single event. //  
// (This is assuming you are using the 100MSPS modules) //  
//                                                                 //  
// HOW TO RUN: //  
// 1. To uncompile <terminal> make clean //  
// 2. To compile <terminal> make //  
// 3. Before compiling, make sure that the timewindow, input file, and output file //  
// are what you want them to be. //  
////////////////////////////////////
```

```

#include "ddaschannel.h"
#include "DDASEvent.h"
#include <iostream>
#include <cmath>
#include <TFile.h>
#include <TTree.h>
#include <TBranch.h>

int main()
{
// *****
//           THE COINCIDENCE WINDOW (1 tick = 10ns for 100MSPS module)
// *****
    int timewindow = 30; //the coincidence window is set to 300ns

//Filenames
    TFile *fIn = new TFile("/pathway/to/the/ddasdumper/files/yourInputFile.root");
    TFile *fOut = new TFile("/pathway/to/wherevers/best/yourOutputFile.root","RECREATE");

//Variables for input file
    int crate;          //event crate number
    int slot;           //event slot number
    int chan;           //event channel number
    int energy;         //event energy
    double time;        //event time
    double refT=0.;    //placeholder for time of previous trigger
    double deltaT;     //difference in time between events
    int nEntries;      //number of entries
    int nEvents;       //number of events per entry

//Variables for output file
    int eSuN[2][5][4]={0}; //energy of SuNs PMTs
    int eExt=0;             //energy of raw external trigger signal
    int eExtG=0;           //energy of external trigger signal, after applying it
    int multi=0;           //multiplicity of SuNs segments
    int nPMT=0;            //multiplicity of SuNs PMTs
    int numPMT[8]={0};     //keeps track of the number of pmts fired in each segment
    double tSuN[2][5][4]={0}; //time of SuNs PMTs
    double tExt=0.;        //time of raw external trigger signal
    double tExtG=0.;       //time of raw external trigger signal, after applying it
    double tTrigger=0.;    //trigger time

    int counter=10; //counter for status bar

//Create tree and branches for output file
    TTree *tOut = new TTree("t","SuN Tree");
    tOut->Branch("energy",&eSuN,"E[2][5][4]/I");
    tOut->Branch("time",&tSuN,"t[2][5][4]/D");
    tOut->Branch("energy_ext",&eExt,"E_ext/I");
    tOut->Branch("time_ext",&tExt,"t_ext/D");
    tOut->Branch("energy_ext_G",&eExtG,"E_ext_G/I");
    tOut->Branch("time_ext_G",&tExtG,"t_ext_G/D");
    tOut->Branch("trigger",&tTrigger,"time/D:pos/I:segm:pmt");
    tOut->Branch("multiplicity",&multi,"multiplicity/I");

```

```

//Get DDAS tree from input file
fIn->cd();
TTree *tIn = (TTree*)fIn->Get("dchan");
DDASEvent *dEvent = new DDASEvent();
tIn->SetBranchAddresses("ddasevent",&dEvent);

nEntries = tIn->GetEntries();

//Read in data, entry-by-entry
for(int i=0; i<nEntries; i=i+1)
{
    tIn->GetEntry(i);

    //status bar
    if (i % (int)(0.1*nEntries) == 0)
        {std::cerr << counter << " ";
         if (counter==0) std::cerr << std::endl;
         counter--;}

    //Readout now has correlations, so entries may have multiple events
    nEvents = dEvent->GetNEvents();

    //Read in data event-by-event
    for(int j=0; j<nEvents; j++)
    {
        //Get all the input variables we need
        ddaschannel *dchan = dEvent->GetData()[j];
        crate = dchan->GetCrateID();
        slot = dchan->GetSlotID();
        chan = dchan->GetChannelID();
        energy = dchan->GetEnergy();
        time = dchan->GetTime();

        deltaT = time - refT;

        //If the new time is outside of the timewindow, calculate the multiplicities,
        // fill the tree, save the new timestamp, and set everything back to zero
        if (deltaT > timewindow)
        {
            for(int a=0;a<8;a++)
            { nPMT=nPMT+numPMT[a];
              if (numPMT[a]>0) {multi++;}
            }
            tOut->Fill();
            refT = time;

            for (int a=0;a<2;a++){
            for (int b=0;b<5;b++){
            for (int c=0;c<4;c++){
                eSuN[a][b][c]=0;
                tSuN[a][b][c]=0.0;}}
            for (int a=0;a<8;a++){
                numPMT[a]=0;
            }
        }
    }
}

```

```

        eExt=0;
        tExt=0.0;
        eExtG=0;
        tExtG=0.0;
        multi = 0;
        nPMT=0;
        tTrigger = 0.0;
    }

//.....Set SuN tree variables to correct values.....//
//Top of SuN
if (crate==0 && slot==2 && chan<12)
{ int seg = (chan / 3) + 1;
  int pmt = (chan % 3) + 1;
  eSuN[1][seg][pmt] = eSuN[1][seg][pmt] + energy;
  tSuN[1][seg][pmt] = time;
  numPMT[seg-1]++;
}
//Bottom of SuN
if (crate==0 && slot==3 && chan<12)
{ int seg = (chan / 3) + 1;
  int pmt = (chan % 3) + 1;
  eSuN[0][seg][pmt] = eSuN[0][seg][pmt] + energy;
  tSuN[0][seg][pmt] = time;
  numPMT[seg+3]++;
}
//External trigger stuff
if (crate==0 && slot==4 && chan==0)
{ eExt = eExt + energy;
  tExt = time;
}
if (crate==0 && slot==3 && chan==15)
{ eExtG = eExtG + energy;
  tExtG = time;
}
//Trigger time
tTrigger = refT;

} //finish loop over j=events

} //finish loop over i=entries

//Write to output file
fOut->cd();
tOut->Write();
fOut->Close();

return 0;
}

```

REFERENCES

REFERENCES

- [1] J. Erler, N. Birge, M. Kortelainen, W. Nazarewicz, E. Olsen, A. M. Perhac, and M. Stoitsov. *Nature*, 486:509, 2012.
- [2] W. Elsasser. *Journal de Physique et Le Radium*, 5:625, 1934.
- [3] M. Goeppert-Mayer. *Physical Review*, 75:1969, 1949.
- [4] J. H. D. Jensen O. Haxel and H. E. Suess. *Physical Review*, 75:1766, 1949.
- [5] C. R. Cowley. *An Introduction to Cosmochemistry*. Cambridge University Press, 1995.
- [6] M. Asplund, N. Grevesse, A. J. Sauval, and P. Scott. *Annual Review of Astronomy and Astrophysics*, 47:481, 2009.
- [7] K. Lodders. *The Astrophysical Journal*, 591:1220, 2003.
- [8] K. Lodders, H. Palme, and H. P. Gail. *Landolt-Börnstein, New Series in Astronomy and Astrophysics*, VI/4B:560, 2009.
- [9] K. J. R. Rosman and P. D. P. Taylor. *Journal of Physical and Chemical Reference Data*, 27:1275, 1998.
- [10] E. Anders and N. Grevesse. *Geochimica et Cosmochimica Acta*, 53:197, 1989.
- [11] H. E. Suess and H. C. Urey. *Reviews of Modern Physics*, 28(1):53, 1956.
- [12] K. M. Burbidge, G. R. Burbidge, W. A. Fowler, and F. Hoyle. *Reviews of Modern Physics*, 29:547, 1957.
- [13] A. G. W. Cameron. *Publications of the Astronomical Society of the Pacific*, 69:201, 1957.
- [14] G. Steigman. *Annual Review of Nuclear and Particle Science*, 57:463, 2007.
- [15] R. A. Alpher, H. Bethe, and G. Gamow. *Physical Review*, 73(7):803, 1948.

- [16] C. Iliadis. *Nuclear Physics of Stars*. Wiley-VCH, Weinheim, 2007.
- [17] H.-Th. Janka, K. Langanke, A. Marek, G. Martínez-Pinedo, and B. Müller. *Physics Reports*, 442:38, 2007.
- [18] P. Höflich. *Nuclear Physics A*, 777:579, 2006.
- [19] F. E. Clifford and R. J. Tayler. *Memoirs of the Royal Astronomical Society*, 69:21, 1965.
- [20] D. Bodansky, D. D. Clayton, and W. A. Fowler. *The Astrophysical Journal Supplement Series*, 16(148):299, 1968.
- [21] F. Käppeler, R. Gallino, S. Bisterzo, and W. Aoki. *Review of Modern Physics*, 83:157, 2011.
- [22] M. Arnould, S. Goriely, and K. Takahashi. *Physics Reports*, 450:97, 2007.
- [23] J. Audouze and J. W. Truran. *The Astrophysical Journal*, 202:204, 1975.
- [24] C. Fröhlich, G. Martínez-Pinedo, M. Liebendörfer, F. K. Thielemann, E. Bravo, W. R. Hix, K. Langanke, and N. T. Zinner. *Physical Review Letters*, 96:142502, 2006.
- [25] J. Pruet, R. D. Hoffman, S. E. Woosley, H. T. Janka, and R. Buras. *The Astrophysical Journal*, 644:1028, 2006.
- [26] S. Wanajo. *The Astrophysical Journal*, 647:1323, 2006.
- [27] R. K. Wallace and S. E. Woosley. *The Astrophysical Journal Supplement Series*, 45:389, 1981.
- [28] S. Wanajo, H-T Janka, and S. Kubono. *The Astrophysical Journal*, 729:46, 2011.
- [29] H. Schatz, A. Aprahamian, J. Görres, et al. *Physics Reports*, 294:167, 1998.
- [30] H. Schatz, A. Aprahamian, V. Barnard, L. Bildsten, A. Cumming, M. Ouellette, T. Rauscher, F. K. Thielemann, and M. Wiescher. *Physical Review Letters*, 86(16):3471, 2001.

- [31] N. N. Weinberg, L. Bildsten, and H. Schatz. *The Astrophysical Journal*, 639:1018, 2006.
- [32] M. Arnould. *Astronomy and Astrophysics*, 46:117, 1976.
- [33] T. Rauscher, A. Heger, R. D. Hoffman, and S. E. Woosley. *The Astrophysical Journal*, 576:323, 2002.
- [34] S. E. Woosley and W. M. Howard. *The Astrophysical Journal Supplement Series*, 36:285, 1978.
- [35] M. Arnould and S. Goriely. *Physics Reports*, 384:1, 2003.
- [36] T. Rauscher, N. Dauphas, I. Dillmann, C. Fröhlich, Zs. Fülöp, and Gy. Gyürky. *Reports on Progress in Physics*, 76:066201, 2013.
- [37] W. Rapp, J. Görres, M. Wiescher, H. Schatz, and F. Käppeler. *The Astrophysical Journal*, 653:474, 2006.
- [38] T. Rauscher. *Physical Review C*, 73:015804, 2006.
- [39] M. Rayet, N. Prantzos, and M. Arnould. *Astronomy and Astrophysics*, 227:271, 1990.
- [40] M. Rayet, M. Arnould, M. Hashimoto, N. Prantzos, and K. Nomoto. *Astronomy and Astrophysics*, 298:517, 1995.
- [41] I. Dillmann, T. Rauscher, M. Heil, F. Käppeler, W. Rapp, and F. K. Thielemann. *Journal of Physics G: Nuclear and Particle Physics*, 35:014029, 2008.
- [42] Zs. Németh, F. Käppeler, C. Theis, T. Belgya, and S. W. Yates. *The Astrophysical Journal*, 426:357, 1994.
- [43] I. Dillmann, F. Käppeler, T. Rauscher, F. K. Thielemann, R. Gallino, and S. Bisterzo. *Proceedings of Science*, NIC X:091, 2008.
- [44] S. E. Woosley, D. H. Hartmann, R. D. Hoffman, and W. C. Haxton. *The Astrophysical Journal*, 356:272, 1990.
- [45] A. Heger, E. Kolbe, W. C. Haxton, K. Langanke, G. Martínex-Pinedo, and S. E. Woosley. *Physics Letters B*, 606:258, 2005.

- [46] W. M. Howard, B. S. Meyer, and S. E. Woosley. *The Astrophysical Journal*, 373:L5, 1991.
- [47] M. Kusakabe, N. Iwamoto, and K. Nomoto. *Nuclear Physics A*, 758:459c, 2005.
- [48] M. Kusakabe, N. Iwamoto, and K. Nomoto. *The Astrophysical Journal*, 726:25, 2011.
- [49] C. Travaglio, F. K. Röpke, R. Gallino, and W. Hillebrandt. *The Astrophysical Journal*, 739:93, 2011.
- [50] V. Costa, M. Rayet, R. A. Zappala, and M. Arnould. *Astronomy and Astrophysics*, 358:L67, 2000.
- [51] M. Rayet, V. Costa, and M. Arnould. *Nuclear Physics A*, 688:74c, 2001.
- [52] G. R. Caughlan and W. A. Fowler. *Atomic Data and Nuclear Data Tables*, 40:283, 1988.
- [53] C. Angulo, M. Arnould, M. Rayet, et al. *Nuclear Physics A*, 656:3, 1999.
- [54] T. Rauscher. *Physical Review C*, 81:045807, 2010.
- [55] M. Wang, G. Audi, A.H. Wapstra, F.G. Kondev, M. MacCormick, X. Xu, and B. Pfeiffer. *Chinese Physics C*, 36(12):1603, 2012.
- [56] F. W. Aston. *Nature*, 105(2646):617, 1920.
- [57] F. W. Aston. *Proceedings of the Royal Society of London. Series A*, 115(772):487, 1927.
- [58] A. Einstein. *Annalen der Physik*, 323(13):639, 1905.
- [59] W. Hauser and H. Feshbach. *Physical Review*, 87(2):366, 1952.
- [60] N. Bohr. *Nature*, 137:344, 1936.
- [61] S. Hilaire, Ch. Lagrange, and A. J. Koning. *Annals of Physics*, 306:209, 2003.
- [62] H. Utsunomiya, P. Mohr, A. Zilges, and M. Rayet. *Nuclear Physics A*, 777:459, 2006.

- [63] J. M. Blatt. *Theoretical Nuclear Physics*. Wiley, New York, 1952.
- [64] T. Rauscher F. K. Thielemann. *Atomic Data and Nuclear Data Tables*, 75:1, 2000.
- [65] T. Sauter and F. Käppeler. *Physical Review C*, 55:3127, 1997.
- [66] G. G. Kiss, T. Rauscher, T. Szücs, et al. *Physics Letters B*, 695:419, 2011.
- [67] Gy. Gyürky, E. Somorjai, Zs. Fülöp, S. Harissopulos, P. Demetriou, and T. Rauscher. *Physical Review C*, 64:065803, 2001.
- [68] Gy. Gyürky, G. G. Kiss, Z. Elekes, et al. *Physical Review C*, 74:025805, 2006.
- [69] G. Rugel, I. Dillmann, T. Faestermann, et al. *Nuclear Instruments and Methods in Physics Research B*, 259:683, 2007.
- [70] H. Utsunomiya, H. Akimune, S. Goko, et al. *Physical Review C*, 67:015807, 2003.
- [71] K. Vogt, P. Mohr, M. Babilon, J. Enders, T. Hartmann, C. Hutter, T. Rauscher, S. Volz, and A. Zilges. *Physical Review C*, 63:055802, 2001.
- [72] C. Nair, A. R. Junghans, M. Erhard, et al. *Journal of Physics G*, 35:014036, 2008.
- [73] S. Harissopulos, E. Skreti, P. Tsagari, et al. *Physical Review C*, 64:055804, 2001.
- [74] A. Sauerwein, J. Endres, L. Netterdon, et al. *Physical Review C*, 86:035802, 2012.
- [75] S. Galanopoulos, P. Demetriou, M. Kokkoris, et al. *Physical Review C*, 67:015801, Jan 2003.
- [76] A. Spyrou, H. W. Becker, A. Lagoyannis, S. Harissopulos, and C. Rolfs. *Physical Review C*, 76:015802, 2007.
- [77] A. Simon, S. J. Quinn, A. Spyrou, et al. *Nuclear Instruments and Methods in Physics Research A*, 703:16, 2013.
- [78] O. Ershova, P. Adrich, H. Alvarez-Pol, et al. Coulomb dissociation reactions on mo isotopes for astrophysics applications. In *PoS(NIC XI) 232*. Proceedings of Science, 2010.

- [79] D.A. Hutcheon, S. Bishop, L. Buchmann, et al. *Nuclear Instruments and Methods in Physics Research A*, 498:190, 2003.
- [80] M. Couder, C. Angulo, W. Galster, J.-S. Graulich, P. Leleux, P. Lipnik, G. Tabacaru, and F. Vanderbist. *Nuclear Instruments and Methods in Physics Research A*, 506:26, 2003.
- [81] D. Rogalla, D. Schurmann, F. Strieder, et al. *Nuclear Instruments and Methods in Physics Research A*, 513:573, 2003.
- [82] R. Fitzgerald, E. Abbotoy, D.W. Bardayan, et al. *Nuclear Physics A*, 748:351, 2005.
- [83] M. Couder, G.P.A. Berg, J. Gorres, P.J. LeBlanc, L.O. Lamm, E. Stech, M. Wiescher, and J. Hinnefeld. *Nuclear Instruments and Methods in Physics Research A*, 587:35, 2008.
- [84] A. Simon, J. Fallis, A. Spyrou, et al. *The European Physics Journal A*, 49:60, 2013.
- [85] Q. Zhong, T. Aumann, S. Bishop, et al. *Journal of Physics: Conference Series*, 202:012011, 2010.
- [86] G. Sauerbrey. *Zeitschrift für Physik*, 155:206, 1959.
- [87] C. S. Lu and O. Lewis. *Journal of Applied Physics*, 43:4385, 1972.
- [88] INFICON, East Syracuse, NY USA. *SQM-160 Rate/Thickness Monitor User's Guide*, 4.09 edition, 2008.
- [89] A. H. F. Muggleton. *Vacuum*, 37(11-12):785, 1987.
- [90] W. K. Chu, J. W. Mayer, and M. A. Nicolet. *Backscattering Spectrometry*. Academic Press, New York, 1978.
- [91] E. Rutherford. *Philosophical Magazine*, 21:669, 1911.
- [92] J. L'Ecuyer, C. Brassard, C. Cardinal, J. Chabbal, L. Deschênes, J. P. Labrie, B. Terreault, J. G. Martel, and R. St. Jacques. *Journal of Applied Physics*, 47:381, 1976.
- [93] M. Mayer. *SIMNRA User's Guide, Report IPP 9/113*. Max-Planck-Institut für Plasmaphysik, Garching, Germany, 1997.

- [94] G. A. Norton. Multi cathode snics ion source. In *Proceedings of 25th Symposium of North Eastern Accelerator Personnel*, page 295, Santa Fe, NM, USA, October 1991. World Scientific.
- [95] National Electrostatics Corporation. <http://www.pelletron.com/charging.htm>. 2014.
- [96] FN Tandem Van de Graaff Accelerator. http://isnap.nd.edu/html/research_FN.html. 2014.
- [97] P. T. Callaghan. *Principles of Nuclear Magnetic Resonance Microscopy*. Clarendon Press, Oxford, 1991.
- [98] X. Fei, V. W. Hughes, and R. Prigl. *Nuclear Instruments and Methods in Physics Research A*, 394:349, 1997.
- [99] G. F. Knoll. *Radiation Detection and Measurement*. John Wiley & Sons Inc., Hoboken, NJ, 4th edition, 2010.
- [100] K. Spyrou, C. Chronidou, S. Harissopulos, S. Kossionides, T. Paradellis, C. Rolfs, W. H. Schulte, and L. Borucki. *The European Physics Journal A*, 7:79, 2000.
- [101] R. Hofstadter. *Physical Review*, 74:100, 1948.
- [102] C. J. Prokop, S. N. Liddick, B. L. Abromeit, A. T. Chemey, N. R. Larson, S. Suchyta, and J. R. Tompkins. *Nuclear Instruments and Methods in Physics Research A*, 741:163, 2014.
- [103] XIA LLC, Hayward, CA USA. *Digital Gamma Finder (DGF) PIXIE-16 Manuals*, 1.40 edition, October 2009.
- [104] H. Tan, M. Momayezi, A. Fallu-Labruyere, Y. Chu, and W. K. Warburton. *IEEE Transactions on Nuclear Science*, 51:1541, 2004.
- [105] A. Fallu-Labruyere, H. Tan, W. Hennig, and W. K. Warburton. *Nuclear Instruments and Methods in Physics Research A*, 579:247, 2007.
- [106] S. Agostinelli, J. Allison, K. Amako, et al. *Nuclear Instruments and Methods in Physics Research A*, 506:250, 2003.
- [107] D. Weisshaar, A. Gade, T. Glasmacher, et al. *Nuclear Instruments and Methods in Physics Research A*, 624:615, 2010.

- [108] Ameenah R. Farhan and Balraj Singh. *Nuclear Data Sheets*, 86:785, 1999.
- [109] J. Brenneisen, D. Grathwohl, M. Lickert, R. Ott and H. Röpke, J. Schmälzlin, P. Siedle, and B. H. Wildenthal. *Zeitschrift für Physik A*, 352:149, 1995.
- [110] P. M. Endt. *Nuclear Physics A*, 663:1, 1998.
- [111] NACRE Database. http://pntpm.ulb.ac.be/Nacre/nacre_d.htm. 2015.
- [112] I. Dillmann, M. Heil, F. Käppeler, T. Rauscher, and F.-K. Thielemann. *Physical Review C*, 73:015803, 2006.
- [113] C. H. Johnson, A. Galonsky, and J. P. Ulrich. *Physical Review*, 109:1243, 1958.
- [114] C. H. Johnson, C. C. Trail, and A. Galonsky. *Physical Review*, 136:B1719, 1964.
- [115] Zs. Fülöp, Á.Z. Kiss, E. Somorjai, C.E. Rolfs, H.P. Trautvetter, T. Rauscher, and H. Oberhummer. *Zeitschrift für Physik A*, 355:203, 1996.
- [116] T. Rauscher and F. K. Thielemann. *Atomic Data and Nuclear Data Tables*, 79:47, 2001.
- [117] T. Rauscher. code *SMARAGD*, version 0.8.4s (2012).
- [118] J. P. Jeukenne, A. Lejeune, and C. Mahaux. *Physical Review C*, 15:10, 1977.
- [119] A. J. Koning, S. Hilaire, and M. C. Duijvestijn. "TALYS-1.0" *Proceedings of the International Conference on Nuclear Data for Science and Technology*, April 22-27, Nice, France, editors O. Bersillon and F. Gunsing and E. Bauge and R. Jacqmin and S. Leray and EDP Sciences, p 211-214 (2008).
- [120] E. Bauge, J. P. Delaroche, and M. Girod. *Physical Review C*, 63:024607, 2001.
- [121] A. Gilbert, F. S. Chen, and A. G. W. Cameron. *Canadian Journal of Physics*, 43:1248, 1965.
- [122] A. Gilbert and A. G. W. Cameron. *Canadian Journal of Physics*, 43:1446, 1965.
- [123] W. Dilg, W. Schantl, H. Vonach, and M. Uhl. *Nuclear Physics A*, 217:269, 1973.

- [124] A. V. Ignatyuk, K. K. Istekov, and G. N. Smirenkin. *Soviet Journal of Nuclear Physics*, 29:450, 1979.
- [125] A. V. Ignatyuk, J. L. Weil, S. Raman, and S. Kahane. *Physical Review C*, 47:1504, 1993.
- [126] S. Goriely, F. Tondeur, and J. M. Pearson. *Atomic Data and Nuclear Data Tables*, 77:311, 2001.
- [127] S. Goriely, S. Hilaire, and A. J. Koning. *Physical Review C*, 78:064307, 2008.
- [128] M. K. Grossman and H. Feldmeier. *Nuclear Physics A*, 444:113, 1985.
- [129] R. H. Cyburt, A. M. Amthor, R. Ferguson, et al. *The Astrophysical Journal Supplement Series*, 189:240, 2010.
- [130] <http://sourceforge.net/projects/nucnet-tools/>, 2013.
- [131] E. Bravo and G. Martínez-Pinedo. *Physical Review C*, 85:055805, 2012.
- [132] H. Morinaga. *Physical Review*, 101(1):100, 1956.
- [133] J. B. Ball, A. W. Fairhall, and I. Halpern. *Physical Review*, 114(1):305, 1959.
- [134] F. K. McGowan, P. H. Stelson, and W. G. Smith. *Physical Review*, 133(4B):907, 1964.
- [135] O. B. Tarasov and D. Bazin. *Nuclear Instruments and Methods in Physics Research B*, 266:4657, 2008.
- [136] A. E. Vlieks, J. F. Morgan, and S. L. Blatt. *Nuclear Physics A*, 224(3):492, 1974.
- [137] T. Rauscher. code *SMARAGD*, version 0.9.0s (2012).
- [138] T. Rauscher. *International Journal of Modern Physics E*, 20:1071, 2011.
- [139] T. Rauscher, F. K. Thielemann, and K.-L. Kratz. *Physical Review C*, 56:1613, 1997.
- [140] T. Rauscher. *The Astrophysical Journal Supplement Series*, 201:26, 2012.

- [141] L. McFadden and G. R. Satchler. *Nuclear Physics*, 84:177, 1966.
- [142] Arjan Koning, Stephane Hilaire, and Stephane Goriely. *TALYS 1.6 a nuclear reaction program: User Manual*. Nuclear Research and Consultancy Group, Westerduinweg 3, P.O. Box 25, NL-1755 ZG, Petten, The Netherlands, Dec. 2013.
- [143] A. J. Koning and J. P. Delaroche. *Nuclear Physics A*, 713:231, 2003.
- [144] S. Watanabe. *Nuclear Physics*, 8:484, 1958.
- [145] P. Demetriou, C. Grama, and S. Goriely. *Nuclear Physics A*, 707:253, 2002.
- [146] S. Hilaire, M. Girod, S. Goriely, and A. J. Koning. *Physical Review C*, 86:064317, 2012.
- [147] D. M. Brink. *Nuclear Physics*, 4:215, 1957.
- [148] P. Axel. *Physical Review*, 126(2):671, 1962.
- [149] J. Kopecky and M. Uhl. *Physical Review C*, 41:1941, 1990.
- [150] S. Goriely. *Physical Letters B*, 436:10, 1998.
- [151] R. Capote, M. Herman, P. Oblozinsky, et al. *Nuclear Data Sheets*, 110(12):3107, 2009.
- [152] T. Rauscher. Non-smoker database, February 2015. nuastro.org/nonsmoker.html.
- [153] Kadonis. Karlsruhe astrophysical database of nucleosynthesis in stars, March 2015. www.kadonis.org/pprocess/gamow.php.
- [154] J. P. Greene, H. Y. Lee, and H-W Becker. *Nuclear Instruments and Methods in Physics Research A*, 613:462, 2010.
- [155] C. Chronidou, K. Spyrou, S. Harissopulos, S. Kossionides, and T. Paradellis. *The European Physics Journal A*, 6:303, 1999.
- [156] S. Harissopulos, C. Chronidou, K. Spyrou, T. Paradellis, C. Rolfs, W. H. Schulte, and H. W. Becker. *The European Physics Journal A*, 9:479, 2000.
- [157] J. H. Carver and G. A. Jones. *Nuclear Physics*, 19:184, 1960.

- [158] C. I. W. Tingwell, L. W. Mitchell, M. E. Sevier, and D. G. Sargood. *Nuclear Physics A*, 439:371, 1985.
- [159] J. W. Butler and C. R. Gossett. *Physical Review*, 108:1473, 1957.